Structure and Dynamics of Model Fluids with Anisotropic Interactions

DISSERTATION

der Mathematisch-Naturwissenschaftlichen Fakultät
der Eberhard Karls Universität Tübingen
zur Erlangung des Grades eines
Doktors der Naturwissenschaften
(Dr. rer. nat.)

vorgelegt von
DANIEL STOPPER
aus Herrenberg

Tübingen
2019

Gedruckt mit Genehmigung der Mathematisch-Naturwissenschaftlichen Fakultät der Eberhard Karls Universität Tübingen.

Tag der mündlichen Qualifikation:	08.11.2019
Dekan:	Prof. Dr. Wolfgang Rosenstiel
1. Berichterstatter:	Prof. Dr. Roland Roth
2. Berichterstatter:	Prof. Dr. Martin Oettel
3. Berichterstatter:	Prof. Dr. Matthias Schmidt

Zusammenfassung

In dieser Promotionsarbeit untersuchen wir die statistische Physik von kolloidalen Flüssigkeiten mit stark-richtungsabhängigen Teilchenwechselwirkungen, was Relevanz für viele reale Systeme hat. So spielen auf der molekularen Ebene anisotrope Teilchenwechselwirkungen zum Beispiel in Wasser eine entscheidende Rolle, wohingegen auf der Skala der weichen und biologischen Materie anisotrope Wechselwirkungen insbesondere das Phasenverhalten von Proteinen in wässriger Lösung bestimmen.
Ein wichtiges Fundament zur theoretischen Beschreibung von Systemen mit stark-richtungsabhängigen Wechselwirkungen bilden *patchy particles*. Dieses Modell ist im Prinzip einfach zu verstehen: Es beschreibt harte Kugeln, welche über attraktive Wechselwirkungszentren (*patches*) auf ihren Oberflächen miteinander interagieren können. Interessanterweise kann dieses einfache Modell bereits sehr viele Eigenschaften von realen Flüssigkeiten mit anisotropen Wechselwirkungen beschreiben.
Diese Dissertation fußt auf einem erfolgreichen theoretischen Modell für *patchy particles*, welches von M. Wertheim in den 1980er Jahren im Rahmen der Statistischen Mechanik formuliert wurde. Die Wertheim'sche Theorie kann das Phasenverhalten von *patchy particles* in vielen Facetten äußerst erfolgreich beschreiben. Die Beschreibung von strukturellen Eigenschaften wie der Dichteverteilung in einem externen Feld oder die Berechnung von Korrelationsfunktionen stellt die statistische Physik jedoch vor Herausforderungen. In dieser Arbeit nutzen wir klassische Dichtefunktionaltheorie (DFT) sowie Computersimulationen um Paarkorrelationsfunktionen und deren asymptotischen Zerfall, oder die Adsorptionseigenschaften von *patchy particles* an einer Oberfläche (z.B. einer harte Wand) zu berechnen. Weiterhin werden wir auch dynamischen Eigenschaften wie z.B. das Diffusionsverhalten untersuchen.
Neben grundlegenden und fundamentalen Betrachtungen aus dem Blickwinkel der theoretischen statistischen Physik werden wir auch ein experimentelles System in welchem stark-richtungsabhängige Wechselwirkungen auftreten ausführlicher behandeln: Protein-Salz-Mischungen. In diesen Systemen können Salzionen stark-richtungsabhängige Wechselwirkungen zwischen den Proteinen hervorrufen. Aufbauend auf einem einfachen Modell, welches Proteine als *patchy particles* basierend auf der Wertheim'schen Theorie beschreibt, zeigen wir mithilfe von DFT-Rechnungen, dass das experimentelle Adsoprtionsverhalten von Proteinen an festen Oberflächen verstanden werden kann, was für viele interdisziplinäre Gebiete wie der Biotechnologie oder Humanmedizin von Relevanz ist.

Abstract

In this thesis we investigate the statistical physics of model fluids with anisotropic particle interactions, i.e. interactions that depend on the relative orientation of the fluid particles to each other. In the fields of soft matter and biophysics, anisotropic interactions occur for instance in many protein solutions or can explicitly be designed in colloidal fluids in order to achieve certain desired material properties. Orientation-depend interparticle forces arise also in many atomic fluids; for instance, the directional interactions between the oxygen and hydrogen atoms in water are responsible for many of its anomalies, most notably the fact that the liquid phase is denser than the solid.

A widely employed framework to describe directional interactions is the model of patchy particles, which consists of hard spheres decorated with a specific number of attractive interaction sites (patches). If two sites of distinct particles overlap, a bond between the latter is formed. Detailed studies based on theoretical considerations and computer simulations have revealed that this rather simple model is capable of describing many features of the thermodynamic phase behavior, structure and dynamics of real fluids with anisotropic interactions.

Seminal work by Wertheim has paved the way towards a theoretical understanding of the rich bulk phase behavior of uniform patchy fluids. Determining structural properties, such as correlation functions, however, is still a challenge for liquid-state theories. In this work we employ classical density functional theory (DFT) and computer simulations in order to investigate structural properties of patchy fluids, which includes bulk pair correlation functions or density profiles in the vicinity of solid surfaces such as a hard planar wall. In addition, we also put attention to the dynamic properties of patchy fluids.

Besides fundamental considerations from the perspective of liquid-state theory, we shall focus explicitly on an experimental system in which patchy interactions are believed to play a crucial role: protein solutions in the presence of multivalent metal ions. In these systems, the latter can bind to the protein surfaces and thereby act as mediator of a highly-directional interaction between the proteins. Building up on an existing simple model for the protein bulk phase behavior, we for instance demonstrate that experimentally observed protein adsorption at substrates attracting the proteins can successfully be understood with a DFT formulation of this protein model. The results are relevant for many interdisciplinary fields such as biology and medical sciences.

Contents

Chapter 1

Introduction

„Assume that a group of intelligent theoretical physicists had lived in closed buildings from birth such that they never had occasion to see any natural structures [...]. Given a fundamental knowledge in quantum mechanics, they probably would predict the existence of atoms, of molecules, of solid crystals, both metals and insulators, but most likely not the existence of liquids.“
V. Weisskopf in ‘About liquids’, Trans. N.Y. Acad. Sci. II, **38**, 202 (1977)

1.1 Liquid-state theory

Liquid-state theory is concerned with describing and connecting the macroscopic behavior of a fluid, i.e. the existence of gaseous, liquid, and solid phases, to its microscopic structural and dynamical properties, which, in turn, are controlled by the underlying interparticle forces. A classical fluid is an interacting many-body system consisting of N particles confined to a volume $\mathcal{V}$, in which quantum mechanical effects can be neglected. As a result, it suffices to employ classical theories that are based on Newtonian mechanics. However, it is important to recognize that the *existence* of certain kinds of particle interactions can often be only understood within quantum mechanics – for example, the strong repulsion that atoms or molecules feel when their electron orbitals overlap is due to Pauli's principle.

In order to estimate whether a system can be described with a classical approach it is helpful to consider the thermal de Broglie wavelength λ_{th}. It is given by

$$\lambda_{\mathrm{th}} = \frac{h}{\sqrt{2\pi m k_B T}}\,, \tag{1.1}$$

where m denotes the mass of a particle, h is Planck's constant, k_B Boltzmann's constant and T is the temperature. Quantum effects cannot be omitted if the value of λ_{th} is comparable to that of the particle mean distance $a = \rho_b^{-1/3}$, where $\rho_b = N/\mathcal{V}$ is the average (bulk) particle density. On the other hand is a classical description justified and sufficient if $a \gg \lambda_{\mathrm{th}}$. This certainly is satisfied in the gaseous phase, where the

mean distance is typically much larger than the effective atomic diameter σ_s, $a \gg \sigma_s$. By contrast, in a liquid or solid the mean distance typically is of the order of σ_s, $a \sim \sigma_s$. Thus, a classical description of a liquid (or solid) is a good one if the particles are sufficiently massive and the temperature is sufficiently high such that $\lambda_{\rm th} \ll \sigma_s$; a good example is liquid argon. In general it turns out that the interactions between nearly all heavier atoms and molecules (i.e. except H_2 and He) can be treated well in a classical picture at 'moderate' conditions.

Let us consider the Hamiltonian H of a classical N-particle system, where all particles have equal mass m:

$$H = \underbrace{\sum_{i=1}^{N} \frac{|\mathbf{p}_i|^2}{2m}}_{\equiv T_{\rm kin}} + \underbrace{\Phi(\mathbf{r}_1, ..., \mathbf{r}_N)}_{\equiv U} + \underbrace{\sum_{i=1}^{N} V_{\rm ext}(\mathbf{r}_i)}_{\equiv V} \,, \tag{1.2}$$

where $\mathbf{p}_i = m\,\dot{\mathbf{r}}_i$ is the momentum of particle i and $V_{\rm ext}(\mathbf{r}_i)$ denotes a time-independent external potential acting on the latter. The interactions among the particles are encoded within the function $U \equiv \Phi(\mathbf{r}_1, ..., \mathbf{r}_N)$. The Hamilton function separates naturally into kinetic ($T_{\rm kin}$) and potential energy contributions. The latter in turn splits into internal contributions due to particle interactions (U) and external fields (V). For many fluids it turns out that to a good approximation $\Phi(\mathbf{r}_1, ..., \mathbf{r}_N)$ may be written as the sum over an isotropic and pairwise additive potential $\phi(r)$:

$$\Phi(\mathbf{r}_1, ..., \mathbf{r}_N) = \frac{1}{2} \sum_{i=1}^{N} \sum_{i \neq j}^{N} \phi(|\mathbf{r}_{ij}|) \,, \tag{1.3}$$

where $|\mathbf{r}_{ij}|$ is the absolute value of the center-to-center vector $\mathbf{r}_{ij} \equiv \mathbf{r}_i - \mathbf{r}_j$ between two particles i and j. The physics of a classical system is governed by Hamilton's equations of motion:

$$\dot{\mathbf{r}}_i = \frac{\partial H}{\partial \mathbf{p}_i} \quad ; \quad \dot{\mathbf{p}}_i = -\frac{\partial H}{\partial \mathbf{r}_i} \,, \quad i = 1, ..., N \,, \tag{1.4}$$

which, of course, are equivalent to Newton's second law:

$$m\,\ddot{\mathbf{r}}_i = \mathbf{f}_i^{\,\rm int} + \mathbf{f}_i^{\,\rm ext} \,, \quad i = 1, ..., N \,, \tag{1.5}$$

where we have discriminated between external forces $\mathbf{f}_i^{\,\rm ext} = -\nabla_i V_{\rm ext}(\mathbf{r}_i)$ and the internal forces $\mathbf{f}_i^{\,\rm int} = -\nabla_i\, \Phi(\mathbf{r}_1, ..., \mathbf{r}_N)$. For given initial configurations $\{\mathbf{r}_1(0), ..., \mathbf{r}_N(0)\}$ and $\{\mathbf{p}_1(0), ..., \mathbf{p}_N(0)\}$ there exists only one unique solution to Eqs. (1.4) or (1.5). Structural, dynamical as well as thermodynamic properties of the system would be fully determined if we knew the phase-space trajectories $\mathbf{r}_i(t)$ and $\mathbf{p}_i(t)$ at all times $t > 0$. Clearly, for a macroscopic number of particles, $N \sim 10^{23}$, this is an exceedingly difficult challenge. Moreover, explicit knowledge of all the trajectories is not desirable at all: all relevant (i.e. experimentally measurable) fluid properties such as the pressure

p, the compressibility χ, or the static structure factor $S(k)$, are inevitably the result of a time-averaged collective behavior. No experimental setup exists that can resolve the dynamics of $\sim 10^{23}$ particles on atomistic time scales ($\sim 10^{-13}\,\mathrm{s}$)[1]. Besides that, the produced amount of data would probably exceed all to date available world-wide digital storage capabilities. The only sensible possibility to theoretically describe the relevant physical properties of a fluid is thus to expect that the ergodicity theorem holds true and apply classical statistical mechanics. This precisely is what equilibrium[2] liquid-state theory does.

1.2 Simple fluids, Colloids and Soft Matter

Simple fluids

The existence of gases, metals, semiconductors, and insulators can be understood rather straightforwardly from fundamental principles of many-body quantum mechanics. For the third state of matter, that we experience in daily life, the liquid phase, this is much less clear. In 1977 Weisskopf argued in his essay 'About liquids' [1] that the existence of the liquid phase is not at all self-evident; this was rephrased by Evans in a 2019 anniversary essay in Physics Today [2]: *„It is not obvious that a state of matter, other than gas and solid, should exist that is dense, disordered, and strongly spatially correlated"*. In fact, by the end of the 1950s no theoretical framework had existed to describe dense liquids due to their aforementioned properties. In a gas, the bulk density ρ_b is small and perturbation approaches employing ρ_b as an order parameter are likely to succeed. On the other hand, in a solid one can employ spatial symmetries which is not possible in a disordered liquid.

In the 1940s, Kirkwood [3] probably was the first who realized that the structure of the hard-sphere fluid shares remarkable similarities with that of simple atomic fluids such as argon. The hard-sphere pair potential is defined as:

$$\beta\phi_{\mathrm{HS}}(r) = \begin{cases} \infty & ; \quad r < \sigma \\ 0 & ; \quad r \geq \sigma\,, \end{cases} \tag{1.6}$$

where $\beta = 1/(k_B T)$ is the inverse temperature and σ the hard-core diameter. In the 1950s, Kirkwood's findings were confirmed by early computer simulations carried out by Wood and Wainright [4, 5]. Catalyzed by these simulation results, in the 1960s and 70s a quantitative theoretical understanding of the liquid state emerged which had been lacking before. In particular, Widom [6] and Weeks, Chandler and Andersen [7] elaborated in seminal papers the role of repulsive packing effects in determining the characteristic short-range order of (dense) liquids, which in 1976 was reviewed

[1] This is different for colloidal fluids as is discussed subsequently.

[2] Note that a time-independent external potential implies that a well-defined equilibrium state exists so that the system as a whole does not move (no net flows etc). In a dynamical picture, this means that in equilibrium on average the external forces are balanced by the internal forces. In this thesis we will only consider fluids that are in equilibrium.

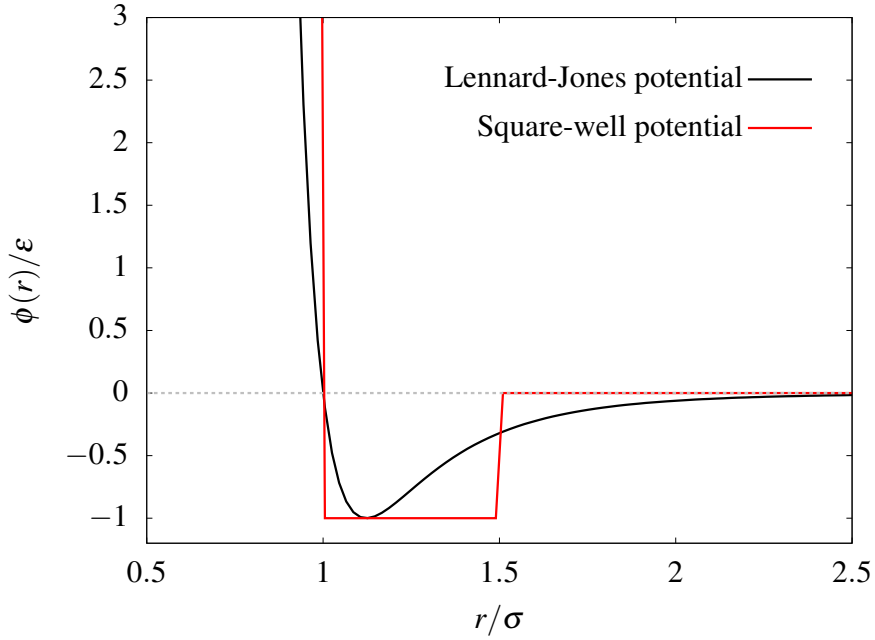

Figure 1.1 The Lennard-Jones pair potential (black line) in comparison to the square-well model (red line) with well-width $\delta = 0.5$. The gray dashed line is a guide to the eye.

by Barker and Henderson in the beautiful work: 'What is liquid? Understanding the states of matter' [8].

The simulation results by Wood and Wainright also suggested that hard spheres crystallize on a regular lattice at packing fractions

$$\eta = \frac{\pi}{6}\rho_b\sigma^3 \tag{1.7}$$

well below the point at which random close packing is reached ($\approx 62\%$). These observations raised controversial debates [9]: it was not clear how crystallization processes could occur in systems purely driven by entropy. The mystery was solved by realizing that a regular ordering of spheres allows for much higher packing fractions up to 74%, compared to random closed packing. The latter has indeed a higher configurational entropy than an ordered arrangement of particles on a lattice; however, this is counterbalanced by the so-called vibrational entropy. Broadly speaking, the latter measures the amount of accessible volume per sphere, which is much higher on a regular lattice compared to a random closed packing situation where the particles are jammed by surrounding neighbors.

The hard-sphere model is a crude yet justified approximation for atoms that feel a harsh repulsion on distances $r < \sigma_s$, but do not attract or repel each other on larger distances, which is a reasonable assumption at sufficiently high temperatures. However, the hard-sphere model has its limitations. The absence of attractive forces implies that there will be no phase separation into gaseous and liquid phases. If in a real system the density and temperature are sufficiently low, attraction can dominate over repulsion and lead to gas-liquid phase separation (i.e. the coexistence of gas and liquid

on a macroscopic scale). Nowadays, the hard-sphere pair potential $\phi_{\rm HS}(r)$ is often supplemented by an additional attractive portion $\phi_{\rm att}(r)$ for $r > \sigma$, which then leads to the existence of gaseous, liquid, and solid phases in computer simulations. By contrast, the prediction of all three states of matter on equal footing has been challenging liquid-state theories for many decades. Remarkably, the concept of separating the effects of repulsion and attraction was already realized in 1867 by Johannes van der Waals. He introduced the distinction between effects of attraction and volume-excluded repulsion by modifying the ideal-gas equation of state. This idea led to a simple theory that was capable of predicting gas-liquid phase separation, but, however, could not describe the liquid-solid transition.

The attractive part of the pair potential, $\phi_{\rm att}(r)$, typically depends on a parameter ε, measuring the strength of the attraction, and another parameter δ defining the distance for which the attraction between two particles acts. A widely considered model system is the square-well (SW) fluid, where $\phi_{\rm SW}(r)$ reads

$$\phi_{\rm SW}(r) = \phi_{\rm HS}(r) + \phi_{\rm att}^{\rm SW}(r) = \begin{cases} \infty & ; \quad r < \sigma \\ -\varepsilon & ; \quad \sigma < r < \sigma(1+\delta) \\ 0 & ; \quad r > \sigma(1+\delta)\,, \end{cases} \tag{1.8}$$

which is displayed as the red line in Fig. 1.1 for $\delta = 0.5$. It approximates the more realistic Lennard-Jones (LJ) pair potential (black line):

$$\phi_{\rm LJ}(r) = 4\varepsilon \left[\left(\frac{\sigma_s}{r}\right)^{12} - \left(\frac{\sigma_s}{r}\right)^{6} \right], \tag{1.9}$$

where the repulsive part in Eq. (1.9) models the Pauli repulsion and the attractive bit describes van der Waals forces (induced dipole-induced dipoole interactions between molecules).

In Fig. 1.2 (a) the generic phase diagram of a fluid with a longer-ranged attraction ($\gtrsim 50\%$ of the hard-core diameter σ) is sketched in the temperature-density plane. Qualitatively, it applies to most atomic fluids such as argon and is not very sensitive to the precise form of the interaction potential. At very high particle densities, $\gtrsim 60\%$ packing fraction, the system is most likely in a solid phase (S). At lower densities, above the gas-liquid critical point (circle), the fluid is in a so-called supercritical state where gas and liquid phases cannot be distinguished. We call such state points simply 'fluid' (F). Below the critical point, stable gaseous (G) can occur at low, and liquid phases (L) at higher densities. These one-phase regions are separated by the binodal, the line at which the latter can coexist. Inside of the binodal no single phase of gas or liquid can be thermodynamically stable and so there are always coexisting domains of gaseous and liquid phases. The typical values for the critical density (in terms of the packing fraction η_c) are in the range of ~ 15 – 30%. The packing fractions at the triple point (coexistence of gas, liquid and solid) are roughly in the range of ~ 40 – 45%.

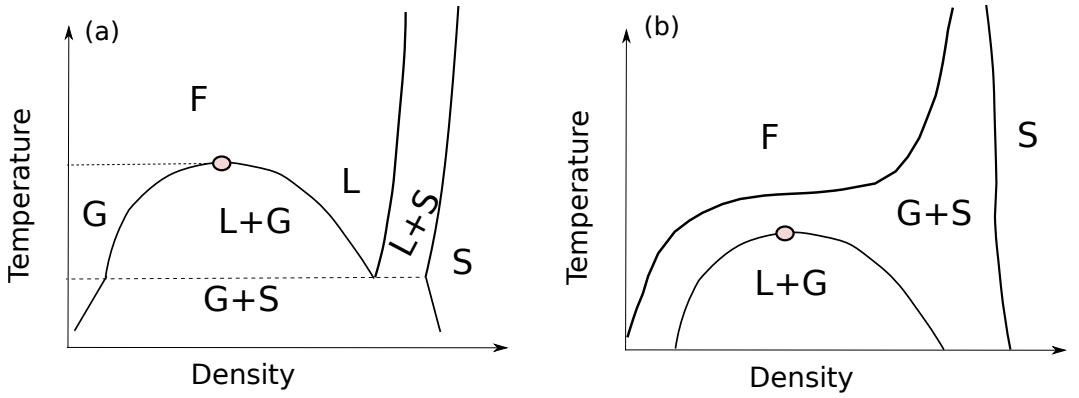

Figure 1.2 (a) Schematic equilibrium phase diagram in the temperature-density plane of a simple atomic fluid, including the gas (G), liquid (L), and solid phases (S). The interparticle attraction is sufficiently long-ranged so that the gas-liquid coexistence region is thermodynamically stable. The dashed lines are guides to the eye indicating the critical temperature (upper line) and triple point (lower line). Above the critical point (red dot) no phase separation occurs. (b) Phase diagram of a colloidal fluid where the interparticle attraction is short-ranged so that the gas-liquid coexistence region becomes metastable with respect to the solid phase. Note that this is not possible for atomic fluids.

At temperatures below the triple point, gas and solid are the only stable equilibrium phases.

Colloids and Soft Matter

Besides simple atomic fluids, there are molecules and structures that can consist of up to thousands of individual atoms, such as polymers, surfactants, proteins, or even cells in living organisms, that may (or may not) exhibit gaseous, liquid, and solid phases. Very often these kinds of systems form states of matter that differ fundamentally from what is known from atomic fluids. This includes for instance gels and glasses, highly stable non-equilibrium cluster phases or liquid crystals. All such exotic structures are the result of considerably more involved interparticle forces. Predicting the thermodynamic phases, structure and dynamics of such complex fluids defines soft-matter science [2]. The physics of colloidal suspensions does also belong to the field of soft matter providing a crucial link to simple fluids. In what follows we will briefly outline the basic principles of colloid physics as it is important for this thesis to keep in mind the differences between atomic and colloidal fluids; a detailed and excellent introduction is given by J. Dhont in the text book entitled *An Introduction to Dynamics of Colloids* [10].

A colloidal fluid consists of mesoscopic particles, with diameters varying between 10^{-7} – 10^{-4} m, that are immersed in a atomic solvent, where the particle size is of the order of $\sim 10^{-10}$ m. In the most simple case these colloids are spherical particles, which we shall assume in what follows. In addition to differences in their size, the colloidal mass M is much larger than that of the solvent molecules m, i.e. $M \gg m$. This, in turn, implies that the time scales between the motion of a colloid and that of the solvent particles is completely separated; as mentioned earlier, the latter is of the

order of 10^{-13} s whereas the microscopic colloidal dynamics take place on time scales of about 10^{-9} – 10^{-5} s. Furthermore, one learns that the motion of the colloidal particles is of a stochastic nature, as they undergo Brownian motion due to frequent random collisions with the solvent molecules. For instance, it takes a colloidal particle of diameter ~ 100 nm roughly 10^{-3} s to diffuse over a distance comparable to its diameter (which defines the Brownian time τ_B). Note also that a colloidal trajectory is due to its stochastic character not smooth, in contrast to those in atomic systems. An illustration is displayed in Fig. 1.3 (a) (image from Ref. 11).

The equations of motion for a colloidal suspension may be described by the (overdamped) Langevin equations [12]:

$$\gamma \dot{\mathbf{r}}_i = -\nabla_i \Phi(\mathbf{r}_1, ..., \mathbf{r}_N) - \nabla_i V_{\text{ext}}(\mathbf{r}_i) + \boldsymbol{\xi}_i(t)\,, \quad i = 1, ..., N\,, \tag{1.10}$$

where γ is a solvent-dependent friction constant. In the colloidal picture, $\Phi(\mathbf{r}_1, ..., \mathbf{r}_N)$ denotes an *effective* colloid-colloid interaction potential, which, in general, does also contain solvent-mediated forces. Furthermore, $\boldsymbol{\xi}_i(t)$ is an uncorrelated stochastic white-noise term that satisfies

$$\langle \boldsymbol{\xi}_i(t) \rangle = 0\,, \quad \forall\, t\,, \tag{1.11}$$

$$\langle \boldsymbol{\xi}_i^a(t) \boldsymbol{\xi}_j^b(t') \rangle = 2 k_B T \gamma \delta_{ij} \delta_{ab} \delta(t - t')\,, \tag{1.12}$$

and arises from the random kicks of the solvent molecules exerted on the colloids. Here, brackets $\langle \cdot \rangle$ denote averages over different initial conditions of the solvent-induced noise, δ_{ij} denotes the Kronecker-symbol, and $\delta(\cdot)$ the Dirac distribution. Despite their fundamentally different equations of motion (deterministic versus stochastic) atomic fluids and colloidal suspensions share important common physical grounds: both are realizations of classical statistical mechanics systems. Thus, for equal pair potentials, the equilibrium structure and phase diagrams are expected to be similar, but occur on different length- and time scales. The interactions between atoms and molecules are fixed and cannot be changed; this is different for colloids, where it is, for instance, possible to alter their surface chemistry, or if the colloidal particles carry surface charges, their pair interactions can be tuned upon the addition of salts. In 1986, Pusey and van Megen [13] were the first who synthesized nearly bare hard-sphere interactions in colloidal suspensions and showed that the experimental phase behavior is in extraordinary agreement with predictions from classical statistical mechanics. Their work paved the way towards experimentally determining the hard-sphere equation of state [14] and towards measuring the structure of hard-sphere crystals [15]. These accomplishments have also been boosting the development and establishment of novel theoretical frameworks such as classical density functional theory [16, 17], where experimental data serves as an important benchmark for theoretical results. For example, recent experimental work on two-dimensional hard disks has impressively confirmed predictions of liquid-state theory and simulations [18–20].

Experimentally, advances in imaging and tracking of mesoscopic sized colloids opened

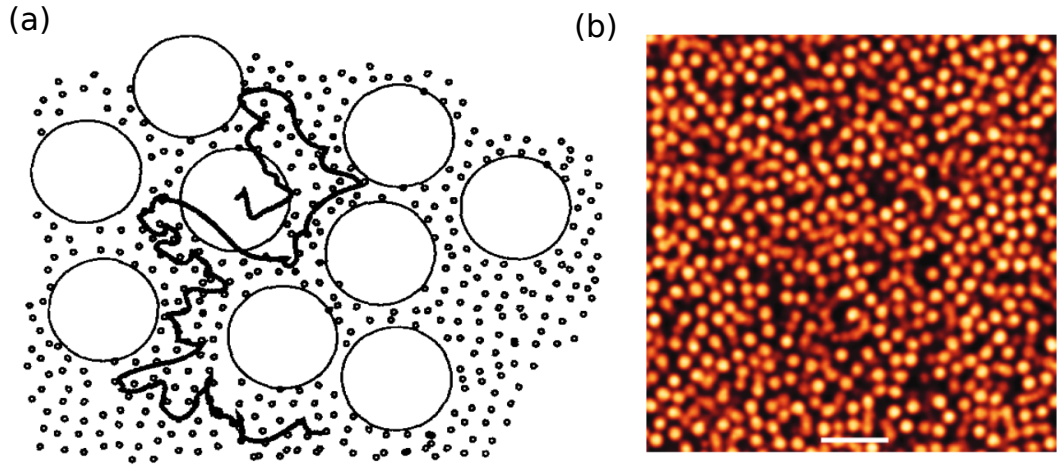

Figure 1.3 (a) Illustration of a colloidal suspension. The colloids (big spheres) experience frequent random kicks by the solvent molecules (small spheres) leading to stochastic trajectories. From H. Löwen, Phys. Rep. **237**, 249 (1994). (b) Image of hard-sphere like colloids taken via confocal microscopy. The scale bar is 10 μm. From C. P. Royall *et al.*, Nat. Mater. **7**, 556 (2008).

new perspectives. While the structure of colloidal fluids in momentum space can be explored with scattering techniques that employ visible light (static- and dynamic light scattering) instead of X-rays, colloids particularly are sufficiently large to be visualized in real space using optical imaging techniques, most notably via confocal microscopy. The latter allows one to track single-particle trajectories and draw conclusions on particle configurations even in large three-dimensional samples [21–23]. A typical snapshot of a colloidal liquid obtained from confocal microscopy is provided in Fig. 1.3 (b) (taken from Ref. 24). Moreover, the significantly larger time scales on which the colloidal dynamics take place allow for real-time resolutions of gas-liquid phase separation [25, 26] or crystal growth [27] in experiments. These examples manifest the great advantage of colloids over atomic fluids: they provide the ability to probe predictions from statistical mechanics via a vast diversity of methods, ranging from analyzing single-particle trajectories to simply observing macroscopic phase behavior by eye.

Attractive interactions between colloids can e.g. be controlled by employing the depletion effect. The addition of non-adsorbing polymers to a solution of hard-sphere like colloids induces a purely entropic effective attraction between the colloids. Theoretically, this phenomenon was first described by Asakura and Oosawa in 1954 [28] and later by Vrij [29]. The range of the attraction is set by the size of the polymers, and its strength is dictated by the polymer concentration. If the polymer size ratio $q = \sigma_p/\sigma_c$ is $q \sim 1$, where σ_p denotes the effective polymer radius and σ_c that of the colloids, then the phase diagram mimics that of a simple fluid i.e. is of the form shown in Fig. 1.2 (a). For small polymers, $q \lesssim 0.3$, the colloid-colloid depletion attraction can become very short-ranged (a few per cent of σ_c). In such systems, the liquid-liquid coexistence region (i.e., the coexistence of a colloid-poor and colloid-rich phases) often becomes suppressed with respect to the solid phase [30, 31], and so coexistence of a

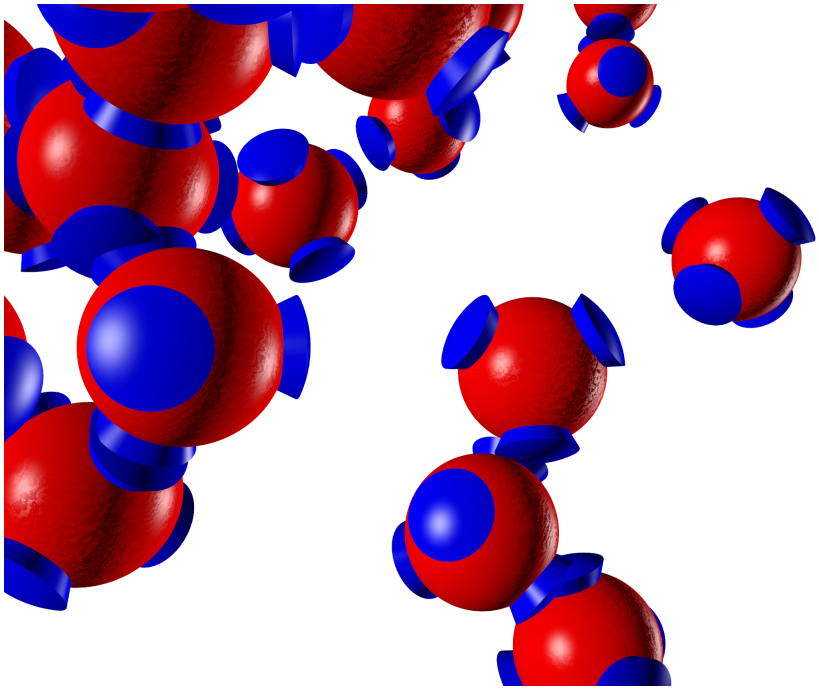

Figure 1.4 Sketch of patchy particles with four patches (blue cones). A bond between a pair of particles is formed if their patches overlap.

colloidal gas and solid is the only thermodynamic stable phase. A generic equilibrium phase diagram is sketched in Fig. 1.2 (b). At this point it is important to point out that colloidal suspensions can also show both exciting equilibrium and non-equilibrium behavior, that is not seen in simple atomic fluids. For instance, if a colloidal hard-sphere fluid is compressed rapidly beyond its equilibrium freezing point, so-called glass states can occur in which the particles are highly jammed with a lacking long-ranged order [32]. Liquid-crystal phases are observed in colloidal fluids where the particles are of ellipsoidal shape, including nematic, smectic, or twisted phases. In experiments with colloid-polymer mixtures at a small size ratio q, the equilibrium phase behavior as shown in Fig. 1.2 (b) is often not reached due the occurrence of highly stable non-equilibrium states, such as colloidal aggregation or dynamically arrested gel phases [33].

1.3 Patchy colloids

In this thesis we will mostly be concerned with the statistical physics of so-called patchy colloids [34, 35], where the particles interact via highly anisotropic (attractive) forces. These forms of interactions can give rise to a equilibrium phase behavior and microscopic structure that both differ substantially from that of colloidal fluids with isotropic pair interactions [36]. More generally, the framework of *patchy particles* allows one to model directional interactions for a far more wide class of systems. This ranges from simple atomic models for water [37–40], over explicit realizations in colloidal [41] and biology-inspired systems [42] to the modeling of effective interactions between

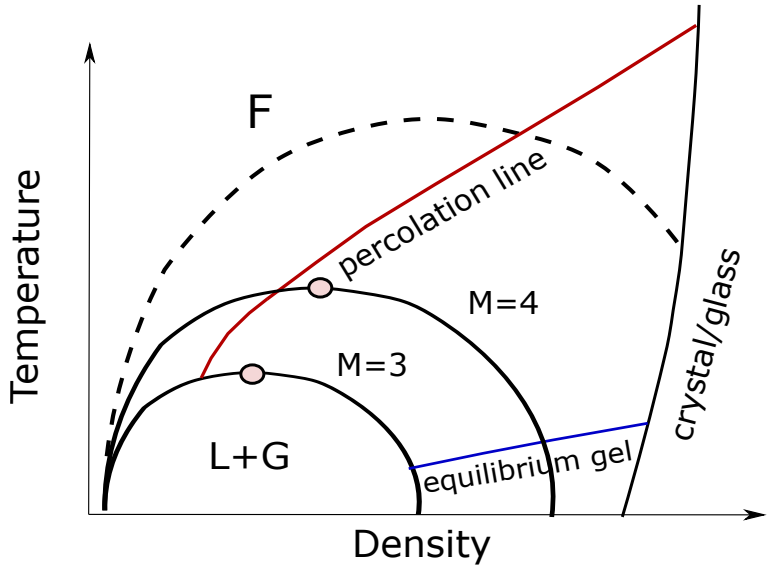

Figure 1.5 Schematic phase diagram of the patchy fluid with $M = 3$ or $M = 4$ interaction sites where the gas-liquid coexistence region is not metastable with respect to the solid phase. The binodals (black solid lines) shrink significantly compared to fluids with isotropic interactions with the same interaction strength and range (dashed line). The percolation threshold, defined as the line where system-wide networks of bonded particles can exist, is marked by the red line. Note that bond lifetimes in the vicinity to the percolation line are typically much smaller than macroscopic observation times, i.e. the network is flexible. This changes with decreasing temperature, where equilibrium gel phases may exist (below the blue line). In this region the system remains in a disordered state, but is kinetically arrested due to macroscopically long bond lifetimes. Such states are not found in fluids with isotropic interactions.

globular proteins [43–46]. In this theses, the term 'patchy particle' means the following: consider a hard sphere of diameter σ, decorated with M interaction sites. If two (or more) of these interaction sites of distinct particles overlap, they form a bond. We call the sites also 'patches'. An illustration for the case of $M = 4$ patches arranged in tetrahedral symmetry is shown in Fig. 1.4, where the hard spheres are displayed in red and the patches are the blue cones.

Patchy colloids with two sites can form chains and rings; with three sites, chain branching and extended network formation becomes possible. A tetrahedrally arrangement of four patches may serve as a crude model of e.g. a water molecule. Patchy colloids with such small numbers of interaction sites have been at the focus of liquid-state physics for the past decade as their phase behavior shows several exciting features:

- Gas-liquid coexistence regions can occur at particular low densities and temperatures [47] compared to isotropic pair potentials. For a chain-forming fluid with two attractive sites, the gas-liquid coexistence even ceases to exist. Curiously, mixture of two- and three-patch particles yield the possibility to continuously move the location of critical points towards zero density and temperature with appropriate mixtures of two- and three-patch particles [47, 48]. As a result, it is possible to realize 'empty liquid' states where packing fractions of the coexisting liquid well below ten percent are possible. Experimentally, such behavior was

found in colloidal clays [41] and DNA-nanostars [42], both of which examples for soft-matter systems where highly directional particle interactions occur.

- Another curiosity is the fact that although the patch-patch interaction range typically is of the order of 10% of the hard-core diameter σ, the gas-liquid coexistence region in patchy colloidal fluids is not necessarily metastable with respect to the solid phase [49] as is the usual case for fluids interacting via isotropic pair potentials with a short-ranged attraction; this is controlled by the geometry and interaction range of the patches. In particular, computer simulations have suggested that for certain patch geometries the disordered fluid phase can be retained as the most stable phase even down to zero temperature [50]. In Fig. 1.5 we show a schematic phase diagram for $M = 3$ and 4, where the liquid is not metastable with respect to the solid phase. The binodals are the black solid lines, and the dashed line indicates the respective isotropic case (with the same range of the attraction as the patches). The red line is the so-called percolation line defining the locus in the phase diagram below which system-wide networks of bonded particles can occur. Below the percolation line, the probability of finding a patch bonded to another, denoted by p_b, is high, $\gtrsim 90\%$. However, the bond lifetimes between two particles in vicinity to the percolation line are typically still much smaller than macroscopic observation times [51], i.e. bonds are frequently formed and broken and the network is flexible.

- This changes at lower temperatures. The fact that the disordered phase can be more stable than the solid even at temperatures well below the critical value provides the remarkable possibility of so-called equilibrium gels. Such states are characterized by bond lifetimes that can become macroscopically large, likely resulting in slow dynamics and eventually kinetic arrest at extremely low temperatures. In Fig. 1.5 these regions occur below the blue line. Equilibrium gel phases were for instance observed in colloidal clays [41]. Recall that arrested gel phases that are observed in experiments with colloids interacting via short-ranged isotropic forces are typically metastable and are not predicted by equilibrium theories or simulations (cf. discussion at the end of Sec. 1.2) or Ref. 33.

1.4 Applications of patchy models

1.4.1 Water

Many atomic or molecular fluids that arise in nature interact via highly anisotropic forces. The probably most prominent representatives are directional hydrogen bonds in water [52–56, 40]. It is the particular geometry of the water molecule and its anisotropic interactions with other water molecules giving rise to both thermodynamic and structural features that are not seen in fluids such as argon. The macroscopic properties of water exhibit several anomalies – the probably widest known example is the fact that the density of water (at atmospheric pressure) has a maximum at 4° C

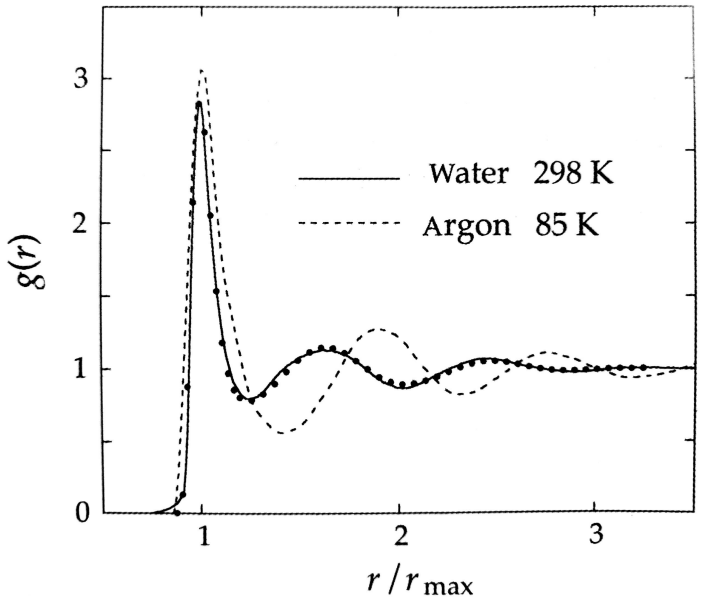

Figure 1.6 Experimental results for the radial distribution function $g(r)$ for oxygen atoms in water at room temperature (sold line) and for liquid argon near its triple point (dashed line). The points are results from computer simulations for a water model with four interaction sites [55]. Image taken from J.-P. Hansen and I. McDonald, *Theory of Simple Liquids with Applications to Soft Matter*, Academic Press, 4th Edition, London, 2013.

and hence the solid phase (ice) is less dense. In order to reproduce these phenomena in simulations, it turned out to be crucial to incorporate directional interactions mimicking hydrogen-bonds between water molecules [55, 56].

In Fig. 1.6 we show experimental results for the radial distribution function $g(r)$ for liquid argon near its triple point (dashed line) in comparison to that of the oxygen atoms of liquid water at room temperature (solid line), which is also rather close to its triple point. The data was obtained from X-ray scattering experiments and is replotted from Ref. 57. The radial distribution function provides information about the microscopic structure in a fluid; it is proportional to the probability of finding a particle at distance r given that there is a particle located at the origin $r = 0$. A more detailed definition will be provided in Ch. 2. It is clear from Fig. 1.6 that the microscopic structure is very different in the two liquids. The nearest neighbor coordination number, which is the volume integral over $g(r)$ until the first minimum after the main peak, and does provide information on the average number of direct neighbors around a reference particle, is significantly smaller for water than is for argon. The latter has a coordination number of ≈ 12, whereas for water one finds approximately four nearest neighbors. Second, the oscillations in the two curves are out of phase, where the second peak of water is shifted towards the nearest neighbor peak. Both the reduced coordination number, and the shift of the oscillations, comply with the molecules forming (strained) tetrahedral networks of hydrogen-bonds in the liquid phase; these structures are in particular apparent in hexagonal ice [58].

1.4.2 Proteins in solution

Aqueous solutions of proteins (e.g. lysozyme) are an important example of soft matter where anisotropic interactions play an essential role [36, 59]. Proteins are crucial to many processes of life, where they for instance are responsible for metabolism, defining the structure of cells, or the transport of molecules such as oxygen. Moreover, degenerated protein interactions are known to play a key role in many diseases such as Alzheimer or eye cataract [60, 61].

From a physical perspective, proteins are difficult to describe with all their details as each particle consists of thousands of atoms or molecules resulting in considerable more complex interactions between two proteins than that between two spherical colloids. Surprisingly, it turns out that colloid physics can at least qualitatively explain [62, 63] the fluid phase behavior of many solutions of globular proteins, where the latter are modeled as hard spheres with an isotropic very short-ranged attraction. Similar to colloidal suspensions, proteins in solution undergo liquid-solid and liquid-liquid transitions, where the former is typically found to be metastable with respect to the latter [64], i.e. the equilibrium phase diagrams are similar to the one shown in Fig. 1.2 (b). In contrast to colloid-polymer mixtures, where phase separation experimentally is often preempted by kinetically-arrested gels, coexistence of protein-poor and protein-rich phases is readily observed; phenomena such as gelation typically set in at lower temperatures.

However, the assumption of pure isotropic interactions between proteins is certainly not justified. Generally, anisotropy in protein-protein interactions may be the result of non-uniformly distributed surface charges, the presence of hydrophobic and hydrophilic zones on the protein surface, or the formation of hydrogen bonds. In particular, the shape and location of liquid-liquid binodals in protein solution points towards the influence of patchy attractions [65, 45]. Furthermore, the variety of lattice types observed in protein crystals, and their relatively low densities, provides further evidence that anisotropic attraction plays a dominant role [43, 66]. In addition, for many protein solutions experimentally determined values of the second virial coefficient can be only understood with the assumption of orientation-dependent interactions [67].

A system which shall be of deeper interest in this thesis, are protein solutions in presence of multivalent salt [68, 69, 46]. In these systems protein aggregates and liquid-liquid phase separation are the result of multivalent salt ions binding to the surface of proteins inducing highly directional bonds between the latter. For sufficient salt concentrations, the anisotropic attraction drives formation of protein aggregates and metastable liquid-liquid phase separation. We will return to this system in detail in Ch. 7.

1.5 Thesis outline

The purpose of this thesis generally is to gain a deeper theoretical understanding of complex fluids in which highly anisotropic interparticle forces play a dominant role.

We choose to employ the framework of patchy particles, which allows to address a vast number of systems being characterized by directional particle interactions in soft-matter physics and also molecular liquid-state theory. Our focus shall be on the augmentation of existing, and development of novel theoretical approaches relevant for but not bounded to (colloidal) fluids of patchy particles. We will outline the thesis in what follows.

Chapter 2: Concepts in liquid-state theory. We will start this thesis with a brief recapitulation of the key concepts in modern classical liquid-state theory that are important for this work. We shall also discuss a novel approach to the fundamental question: 'How do we measure the balance between attractive and repulsive forces in classical fluids?' – see Sec. 2.4. Note, however, that it is beyond the scope of this work to provide an extensive review of liquid-state theory; for this purpose we refer to excellent text books such as Hansen's and McDonald's *Theory of Simple Liquids with Applications to Soft Matter*, Academic Press 4th Edition, London, 2013.

Computer simulations. Particle-based computer simulations of the patchy fluid will play an important, but not the key role in this thesis. The reasons for this are as follows. Simulations are accurate and reliable tools to investigate e.g. the structure and dynamics of a fluid as their results are formally exact and only subject to statistical noise. As such, they pose important cornerstones in liquid-state physics. However, extracting thermodynamic properties can be a demanding task, and typically requires sophisticated algorithms and sufficient computational resources. In particular for patchy fluids the interaction energies can be of several orders of magnitudes larger than that in simple fluids, which can drive determination of any fluid property to an extraordinary delicate task. The main drawback of simulations is, however, that it is not easy to surmise what physical mechanisms govern the behavior of a certain observable – a simulation doesn't provide one formulas (though one still might fit a parameterized theory to simulation results but this requires already some idea of the ongoing physics). Questions of the form: 'How does parameter A depend on another parameter B, and how does A change if B is changed?' are difficult to answer from simulations.

Density functional theory. This is one of the reasons why in this thesis we will focus on classical density functional theory (DFT) [16] formulations for the patchy fluid rather than to only rely on simulations. DFT is one of the most powerful and successful theoretical frameworks in liquid-state theory, as it treats the structure of *inhomogeneous* fluids and its thermodynamics on equal footing. The key quantity in DFT is the particle-density field $\rho(\mathbf{r})$. In most cases, DFT calculations are computationally much more efficient than a particle-based simulation and expressions for thermodynamic properties, such as the pressure or compressibility, often can be written down analytically. However, there is a trade-off: while the framework of DFT itself is mathematically exact, in

practice one has to rely on approximations to the description of particle interactions. In fact, the key task in DFT is to construct robust and self-consistent approximations, that, on the one hand, can reproduce known behavior and properties of a fluid, but, on the other hand, do also yield reliable predictions in novel situations. To provide a successful example, the thermodynamics and structure of the fluid phase of hard spheres are captured by DFT to an extraordinary degree of accuracy [17, 70]. The basics and framework of DFT will be introduced in Sec. 2.2 of Ch. 2.

Chapters 3 and 4: Thermodynamics and structure of the patchy fluid. DFT formulations for the inhomogeneous patchy fluid [71, 72] are based on seminal theoretical work by Wertheim [73–77] that has paved the way to theoretically understand the rich thermodynamic phase behavior of homogeneous patchy fluids (see Ch. 3). We shall see that existing DFT approaches do not, and cannot, provide reliable and accurate results in any situation. In Ch. 4 we provide an extensive investigation of structural properties of the patchy fluid as given by DFT, and compare to results from particle-based computer simulations. This includes questions such as: 'What is the form of density correlations in a homogeneous patchy fluid that is not subject to an external potential and how do they decay?' or 'What is the density distribution of a patchy fluid in vicinity to a planar, hard wall?'. We will also see that a simple modification of a widely-applied DFT formulation for the patchy fluid yields reliable results in many situations, but it should be applied with care when orientations of the particles become distinguished (as e.g. may be the case in certain external potentials).

Chapter 5: Dynamic properties of the patchy fluid. As outlined in Sec. 1.3 of this chapter, the dynamics of patchy fluids will be highly affected by bond formation at sufficiently low temperatures. At such state points, patchy particles can even form equilibrium gel-like structures, due to macroscopically long bond lifetimes. In Sec. 5.1 we will be presenting results for the bulk dynamics in systems with three and four patches obtained from dynamic Monte-Carlo simulations (Appendix B). This includes the mean-squared displacement and the van Hove function, both of which provide information about diffusion and structural relaxation processes in a fluid. The results that we present in Sec. 5.1 are mostly known and are in accordance with recent publications, see e.g. Refs. 78, 51, 79 and references therein.

Dynamic quantities such as the mean-squared displacement in principle are also accessible via a time-dependent version of DFT [80, 81] and it has been shown that dynamic DFT provides a satisfactory description of the bulk dynamics of hard spheres [82] and hard disks [83]. However, in Ch. 5 it is demonstrated that the DFT formulations that exist for the patchy fluid fail to describe fundamental dynamic properties seen in computer simulations.

Chapter 6: Fluids with competing interactions. Although the title of this thesis is 'Structure and Thermodynamics of Fluids with Anisotropic Interactions' in

Chapter 6 we will focus on fluids with so-called competing interactions. What is meant by this terminology is is the presence of a longer-ranged repulsive force in addition to some form of a short-ranged interparticle attraction in the fluid pair potential. Competing interactions can give rise to a rich and exciting phase behavior, including equilibrium cluster phases [84–87] and microphase-separated states [88–90].

We introduce the general framework and outline the most recent state of research for these kinds of fluids in Sec. 6.2 and in Sec. 6.3 we proceed with analyzing the physics of fluids with anisotropic competing interactions, where the attractive part of the pair potential is patchy-like. This particular form of a particle interaction is of interest for models of protein solutions in presence of multivalent salts (see Ch. 7).

Chapter 7: Patchy models for protein solutions. In the final chapter of this thesis, we will focus on an experimental system in which patchy interactions are believed to play a crucial role: protein solutions in the presence of multivalent salts [68, 91, 69]. In these systems, salt ions can bind to the protein surface and thereby act as mediator of a highly-directional attraction between individual proteins. This yields a very rich experimental phase behavior, including reentrant protein aggregation and liquid-liquid phase separation. We summarize the experimental findings in Sec. 7.2.

Some aspects of the experimental bulk phase behavior are captured by a simple coarse-grained patchy colloidal model, where individual interaction sites can be activated by salt ions. As a result, the strength of the protein-protein attraction is controlled by the salt concentration [46]. The model, which is formulated within Wertheim's theory for patchy particles [73–77] omits any longer-ranged electrostatic forces. It is introduced in Sec. 7.3, where we discuss its thermodynamic predictions in comparison to experiments. Subsequently, in Sec. 7.4 we incorporate the model within DFT in order to describe inhomogeneous protein phases. It is demonstrated that the DFT model adequately accounts for protein adsorption at attractive substrates as measured in experiments, which, in turn, provides evidence that protein solutions, despite their inherent complexity, do not only follow the predictions of the statistical physics of 'simple fluids' in terms of bulk thermodynamics, but also in terms of more complex surface and adsorption phenomena.

Finally, in Sec. 7.5 we introduce a simple extension of the protein model to include effects of an additional longer-ranged electrostatic repulsion. This poses a realization of anisotropic competing interactions and we discuss the possibility of equilibrium protein cluster phases in light of recent experimental results.

1.6 Publications

This thesis is in parts based on the following publications.

1. *Massively parallel GPU-accelerated minimization of classical density functional theory.* D. Stopper and R. Roth, J. Chem. Phys. **147**, 064508 (2017).

2. *Phase behavior and bulk structural properties of a microphase former with anisotropic competing interactions: A density functional theory study.* D. Stopper and R. Roth, Phys. Rev. E **96**, 042607 (2017).

3. *Multivalent ion-activated protein adsorption reflecting bulk reentrant behavior.* M. Fries, D. Stopper, M. W. A. Skoda, A. Hinderhofer, F. Zhang, R. M. J. Jacobs, R. Roth, and F. Schreiber, Phys. Rev. Lett. **119**, 228001 (2017).

4. *Non-equilibrium phase transitions of sheared colloidal microphases: Results from dynamical density functional theory.* D. Stopper and R. Roth, Phys. Rev. E **97**, 062602 (2018).

5. *Bulk structural information from density functionals for patchy particles.* D. Stopper, F. Hirschmann, M. Oettel, and R. Roth J. Chem. Phys. **149**, 224503 (2018).

6. *On the decay of the pair correlation function and the line of vanishing excess isothermal compressibility in simple fluids.* D. Stopper, H. Hansen-Goos, R. Roth, and R. Evans, J. Chem. Phys. **151**, 014501 (2019).

7. *Enhanced protein adsorption upon approaching liquid-liquid phase separation as wetting by patchy particles.* M. Fries, D. Stopper, M. W. A. Skoda, M. Blum, C. Kertzscher, A. Hinderhofer, F. Zhang, R. M. J. Jacobs, R. Roth, and F. Schreiber, In final preparation to be submitted to Proceedings of the National Academy of Sciences of the U. S. A. (2019).

8. *The remarkable remnants of the disappeared critical point in chain-forming patchy fluids.* D. Stopper, H. Hansen-Goos, R. Roth, and R. Evans, in preparation (2019).

Chapter 2

Concepts in Liquid-State Theory

2.1 Thermodynamics and structure of fluids

2.1.1 Reminder: Statistical Mechanics

Let $\Gamma = (\mathbf{r}_1, ..., \mathbf{r}_N,\ \mathbf{p}_1, ..., \mathbf{p}_N\ ;\ N)$ denote a point in the $6N$-dimensional phase space spanned by the locations $\mathbf{r}_i$ and momenta $\mathbf{p}_i$ of all particles, $i = 1, ..., N$, of a classical fluid. We also call Γ a 'configuration' or 'microstate' of the system. The corresponding Hamiltonian H is given by Eq. (1.2). In classical statistical mechanics the mean or average value $\langle \mathcal{A} \rangle$ of an observable $\mathcal{A}(\Gamma)$ (e.g., the mean energy $E = \langle H \rangle$) is calculated from

$$\langle \mathcal{A} \rangle = \sum_{\Gamma} \mathcal{A}(\Gamma) f(\Gamma) \equiv \mathrm{tr}_{\mathrm{cl}}\, \mathcal{A}(\Gamma) f(\Gamma)\,, \tag{2.1}$$

where $f(\Gamma)$ is the phase-space probability, i.e. it gives the probability that a particular configuration Γ is realized. In Eq. (2.1) we have furthermore introduced the 'classical' trace as the summation over all possible configurations Γ inspired by the notation commonly used in quantum mechanics. For a classical system, the positions and momenta of the particles are continuous variables, and thus the 'summation' over microstates in Eq. (2.1) generally involves integrations over particle positions and momenta.

In equilibrium, explicit expressions for the phase-space probability f_{eq} can be obtained from Gibbs principle of maximal entropy where one maximizes the statistical entropy S demanding specific side conditions (in the canonical ensemble one e.g. demands a constant mean energy E and constant particle number N). The entropy S of the system is defined as

$$S = -k_B \left\langle \ln(f_{\mathrm{eq}}) \right\rangle = -k_B\, \mathrm{tr}_{\mathrm{cl}} f_{\mathrm{eq}}\, \ln(f_{\mathrm{eq}})\,. \tag{2.2}$$

The latter definition stays meaningful even for non-equilibrium configurations, but in such situations expressions for f are in general unknown.

Canonical ensemble. In the canonical (c) ensemble one consider a system at constant temperature T, particle number N and volume $\mathcal{V}$ that can exchange energy with its environment. In equilibrium, the mean energy E will be a constant, i.e. $E = \langle H \rangle = \text{const}$. The phase-space probability distribution f_c is given by

$$f_c = \frac{\exp\left[-\beta H\right]}{Z(N, \mathcal{V}, T)}\,, \tag{2.3}$$

where $Z(N, \mathcal{V}, T)$ is a normalization constant ensuring that $\mathrm{tr}_{\mathrm{cl}}\, f_c = 1$. It is termed the (canonical) partition sum and defined as

$$\begin{aligned} Z(N, \mathcal{V}, T) &= \mathrm{tr}_{\mathrm{cl}}\, \exp[-\beta H] && (2.4)\\ &= \frac{1}{h^{3N}\, N!} \int_{\mathcal{V}} \mathrm{d}\mathbf{r}_1 \cdots \int_{\mathcal{V}} \mathrm{d}\mathbf{r}_N \int \mathrm{d}\mathbf{p}_1 \cdots \int \mathrm{d}\mathbf{p}_N\, \exp[-\beta H] && (2.5)\\ &= \frac{1}{\lambda_{\mathrm{th}}^{3N}\, N!} \int_{\mathcal{V}} \mathrm{d}\mathbf{r}_1 \cdots \int_{\mathcal{V}} \mathrm{d}\mathbf{r}_N \exp[-\beta(U+V)]\,, && (2.6) \end{aligned}$$

where the factor $1/(h^{3N})$ ensures that the partition sum is dimensionless (h has the dimension of an action) and incorporates Heisenberg's uncertainty relation between particle positions and momenta. Furthermore, $1/N!$ ensures overcounting of physically equivalent configurations. Clearly, the (trivial) kinetic degrees of freedoms T_{kin} in the Hamiltonian can be integrated out resulting in Eq. (2.6), containing solely contributions from the interparticle interactions U and external field V. We also see that the classical trace in the canonical ensemble is given by

$$\mathrm{tr}_{\mathrm{cl}} \equiv \frac{1}{h^{3N}\, N!} \int_{\mathcal{V}} \mathrm{d}\mathbf{r}_1 \cdots \int_{\mathcal{V}} \mathrm{d}\mathbf{r}_N \int \mathrm{d}\mathbf{p}_1 \cdots \int \mathrm{d}\mathbf{p}_N\,. \tag{2.7}$$

The free energy F provides the link between the microscopic fluid configurations and its thermodynamic properties. It is defined as the Legendre transform of the mean energy E with respect to the entropy S:

$$\begin{aligned} F &= E - TS\,, && (2.8)\\ &= \mathrm{tr}_{\mathrm{cl}}\, f_c \left[H + k_B T \ln(f_c)\right]. && (2.9) \end{aligned}$$

If we make use of Eq. (2.3) we obtain from (2.9) the familiar relation

$$F = -k_B T \ln(Z)\,, \tag{2.10}$$

between the free energy and the canonical partition sum.

Grand-canonical ensemble. The grand-canonical (gc) description is the most natural ensemble to describe a fluid. Here, the chemical potential μ, temperature T, and volume $\mathcal{V}$ of the system are prescribed and in addition to the energy, the particle number N fluctuates around a mean value $\langle N \rangle$. The equilibrium grand-canonical

phase-space probability f_{gc} for finding N particles in a particular configuration Γ reads:

$$f_{gc} = \frac{\exp\left[\beta N\mu - \beta H\right]}{\Xi(\mu, \mathcal{V}, T)}\,, \tag{2.11}$$

where $\Xi(\mu, \mathcal{V}, T)$ denotes the grand-canonical partition sum

$$\begin{aligned}
\Xi(\mu, \mathcal{V}, T) &= \mathrm{tr}_{\mathrm{cl}}\, \exp\left[\beta N\mu - \beta H\right] && (2.12)\\
&= \sum_{N=0}^{\infty} \frac{1}{\lambda_{\mathrm{th}}^{3N}\, N!} \int_{\mathcal{V}} \mathrm{d}\mathbf{r}_1 \cdots \int_{\mathcal{V}} \mathrm{d}\mathbf{r}_N \exp\left[\beta N\mu - \beta(U+V)\right] && (2.13)\\
&= \sum_{N=0}^{\infty} e^{\beta\mu N} Z(N,\, \mathcal{V},\, T)\,, && (2.14)
\end{aligned}$$

where the classical trace now reads

$$\mathrm{tr}_{\mathrm{cl}} \equiv \sum_{N=0}^{\infty} \frac{1}{h^{3N}\, N!} \int_{\mathcal{V}} \mathrm{d}\mathbf{r}_1 \cdots \int_{\mathcal{V}} \mathrm{d}\mathbf{r}_N \int \mathrm{d}\mathbf{p}_1 \cdots \int \mathrm{d}\mathbf{p}_N\,. \tag{2.15}$$

In the grand-canonical ensemble, the grand potential Ω provides the link with the thermodynamics. It is defined as the Legendre transform of the free energy F with respect to the (mean) particle number $\langle N\rangle$:

$$\begin{aligned}
\Omega &= F - \mu\langle N\rangle && (2.16)\\
&= E - TS - \mu\langle N\rangle && (2.17)\\
&= \mathrm{tr}_{\mathrm{cl}}\, f_{gc}[H - \mu N + k_B T \ln(f_{gc})]\,, && (2.18)
\end{aligned}$$

which, if we take into account Eq. (2.11), reduces to the well-known result:

$$\Omega = -k_B T \ln(\Xi)\,. \tag{2.19}$$

Note that, in the thermodynamic limit $N \to \infty$, $\mathcal{V} \to \infty$, $N/\mathcal{V} = \text{const.}$, the free energy obtained in the canonical ensemble from Eq. (2.9) with $N = \langle N\rangle$ is quasi-equivalent to that arising in Eqs. (2.16), (2.17) and (2.18) in the grand-canonical ensemble. This is due to the fact that particle fluctuations around $\langle N\rangle$ vanish with $\sim 1/\sqrt{N}$ and thus are negligible in a macroscopic system.

Assume now that the system is homogeneous and isotropic which implies $V_{\mathrm{ext}}(\mathbf{r}) = 0$. Then the mean energy E consists only of intrinsic contributions: $E = \langle T_{\mathrm{kin}}\rangle + \langle U\rangle$ and hence does the free energy. Generally, the internal energy is for uniform fluids given by the fundamental relation $E = TS - p\mathcal{V} + \mu N$. Thus for uniform systems the grand potential Ω reduces to

$$\Omega = -p\mathcal{V}\,, \tag{2.20}$$

where p is the pressure in the fluid. Recall that the latter and the chemical potential μ can be obtained from Ω or F via differentiation with respect to their conjugate

variables:

$$\mu = \left(\frac{\partial F}{\partial N}\right)_{\mathcal{V},T} = \left(\frac{\partial f}{\partial \rho_b}\right)_{\mathcal{V},T} , \tag{2.21}$$

$$p = -\left(\frac{\partial F}{\partial \mathcal{V}}\right)_{N,T} = -\left(\frac{\partial \Omega}{\partial \mathcal{V}}\right)_{\mu,T} . \tag{2.22}$$

where we have introduced $f \equiv F/\mathcal{V}$ the free energy density. Combining Eqs. (2.20) and (2.21) we find for the pressure the useful relation:

$$p = \mu\rho_b - f . \tag{2.23}$$

Another quantity that will be of relevance in this work is the isothermal compressibility χ_T, which measures the relative change of the fluids' volume $\mathcal{V}$ due to pressure gradients, i.e.

$$\chi_T = -\frac{1}{\mathcal{V}}\left(\frac{\partial \mathcal{V}}{\partial p}\right)_{\mu,T} = -\frac{1}{\mathcal{V}}\left(\frac{\partial p}{\partial \mathcal{V}}\right)^{-1}_{\mu,T} . \tag{2.24}$$

2.1.2 Density distribution functions

One-body density profile $\rho(\mathbf{r})$. We now consider the one-body density distribution (or density profile) $\rho(\mathbf{r})$ of a fluid in equilibrium described by the grand-canonical ensemble. Multiplied with an infinitesimal volume element $\mathrm{d}\mathbf{r}$, $\rho(\mathbf{r})$ gives the probability of finding a particle within $\mathrm{d}\mathbf{r}$ at position $\mathbf{r}$. If the external potential vanishes, $V_{\mathrm{ext}}(\mathbf{r}) = 0$, and if the fluid is in a stable one-phase region, i.e. in a gaseous, liquid or supercritical phase, then $\rho(\mathbf{r})$ will be constant and equal the bulk density: $\rho(\mathbf{r}) = \rho_b$.

In general, however, $\rho(\mathbf{r})$ will spatially vary, i.e. $\rho(\mathbf{r}) \neq$ const. and its the precise form is determined by the particle interactions and external field. If we integrate $\rho(\mathbf{r})$ over the volume $\mathcal{V}$, we obtain the average particle number in the system:

$$\langle N \rangle = \int_{\mathcal{V}} \mathrm{d}\mathbf{r}\, \rho(\mathbf{r}) . \tag{2.25}$$

The density profile $\rho(\mathbf{r})$ can be written as a statistical average of a microscopic density field operator $\hat{\rho}(\mathbf{r})$ counting particles at location $\mathbf{r}$:

$$\rho(\mathbf{r}) = \langle \hat{\rho}(\mathbf{r}) \rangle = \left\langle \sum_{i=0}^{N} \delta(\mathbf{r} - \mathbf{r}_i) \right\rangle , \tag{2.26}$$

where averages $\langle \cdot \rangle$ are taken according to Eqs. (2.1) and (2.11) and $\delta(\cdot)$ denotes the three-dimensional Dirac-delta function.

The density profile $\rho_{\mathrm{id}}(\mathbf{r})$ of non-interacting ideal particles subject an external potential can be calculated explicitly from Eqs. (2.26), (2.11), and (2.1):

$$\rho_{\mathrm{id}}(\mathbf{r}) = \frac{e^{\beta\mu_{\mathrm{id}}}}{\lambda_{\mathrm{th}}^3} e^{-\beta V_{\mathrm{ext}}(\mathbf{r})} , \tag{2.27}$$

If there is no external potential, it follows from Eq. (2.27) that

$$\rho_b = \frac{\langle N \rangle}{\mathcal{V}} = \frac{e^{\beta\mu_{\rm id}}}{\lambda_{\rm th}^3} \,. \tag{2.28}$$

Since the chemical potential $\beta\mu_{\rm id}$ of an ideal gas has to satisfy $\mu_{\rm id} = \partial f_{\rm id}/\partial\rho_b$, one can integrate to obtain the ideal-gas free energy density:

$$\beta f_{\rm id} = \rho_b[\ln(\rho_b\lambda_{\rm th}^3) - 1] \,. \tag{2.29}$$

Radial distribution function $g(r)$. Let us now consider the conditional probability of finding a particle at position $\mathbf{r}$, given that there is already another particle at $\mathbf{r}'$. This provides a quantity termed the two-body density distribution $\rho^{(2)}(\mathbf{r}, \mathbf{r}')$ and yields information about density correlations in the fluid between two positions $\mathbf{r}$ and $\mathbf{r}'$. Similar to the one-body density $\rho(\mathbf{r})$, the two-body density can be defined in terms of an ensemble average [57]:

$$\rho^{(2)}(\mathbf{r}, \mathbf{r}') = \left\langle \sum_{i\neq j} \delta(\mathbf{r} - \mathbf{r}_i)\delta(\mathbf{r}' - \mathbf{r}_j) \right\rangle \,. \tag{2.30}$$

For non-interacting particles one finds the simple result $\rho^{(2)}(\mathbf{r},\, \mathbf{r}') = \rho(\mathbf{r})\rho(\mathbf{r}')$ which expresses that there are no spatial correlations between the particles. For the uniform ideal gas it follows $\rho^{(2)}(\mathbf{r},\, \mathbf{r}') = \rho_b^2$.

Consider now an uniform fluid of interacting particles. Isotropy then demands $\rho^{(2)}(\mathbf{r}, \mathbf{r}') = \rho^{(2)}(|\mathbf{r} - \mathbf{r}'|) = \rho^{(2)}(r) \neq$ const, i.e. correlations between $\mathbf{r}$ and $\mathbf{r}'$ will depend only on their relative distance $r \equiv |\mathbf{r} - \mathbf{r}'|$ to each other. The radial distribution function $g(r)$ is defined as

$$g(r) = \frac{\rho^{(2)}(r)}{\rho_b^2} \,, \tag{2.31}$$

and provides information about the density-density correlations of a homogeneous bulk fluid relative to an uniform ideal gas. Clearly, we can also introduce a more general definition $g(\mathbf{r}, \mathbf{r}') = \rho^{(2)}(\mathbf{r},\, \mathbf{r}')/\rho(\mathbf{r})\rho(\mathbf{r}')$.

There is another more helpful and intuitive definition for $g(r)$ which goes back to Percus [92] and holds for fluids with pairwise additive interactions: consider an arbitrary chosen test (or reference) particle, and choose the origin of the laboratory coordinate system to be at the center-of-mass of that test particle. Then the latter imposes an effective external field to surrounding fluid which is *equivalent* to the pair potential, i.e. $V_{\rm ext}(r) = \phi(r)$, and the one-body density distribution $\rho(\mathbf{r})$ satisfies $\rho(\mathbf{r}) = \rho(r) = \rho_b g(r)$. This definition provides considerable insight into what is meant by the structure of a fluid: it implies that the average number of particles within the range r and $r + {\rm d}r$ around the reference (test) particle is $4\pi r^2\rho_b g(r){\rm d}r$ and peaks in $g(r)$ correspond to 'shells' of neighbors. A typical plot of $g(r)$ for the hard-sphere fluid at low ($\eta = 0.05$, black curve) and high packing fraction ($\eta = 0.4$, red curve) is displayed in Fig. 2.1. The red curve nicely shows the typical short-ranged order characteristic for

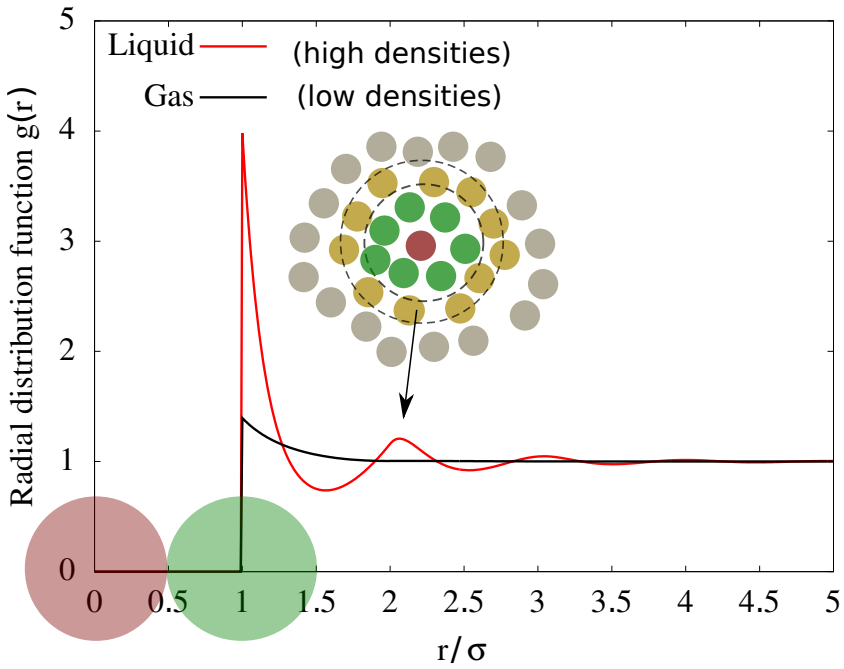

Figure 2.1 Radial distribution function $g(r)$ of the hard-sphere fluid at a packing fraction of $\eta = 0.4$ (red) and 0.05 (black). The figure also illustrates the interpretation of $g(r)$ in Percus' test particle picture as the one-body density profile $\rho(r) = \rho_b g(r)$ around an arbitrary test particle (colored in red).

dense fluids, which is generated by the shells of nearest (green particles) and second (yellow particles) neighbors, and gives rise to the prominent structural correlation peaks in $g(r)$. Since the fluid is disordered this information is successively lost at larger separations, and hence $g(r) \to 1$ as $r \to \infty$. The decay rate to unity defines the true correlation length ξ.

At this point we also introduce the total pair correlation function $h(r)$, which is defined as the deviation of $g(r)$ from the ideal gas result, i.e. $h(r) = g(r) - 1$. Its 3d Fourier transform

$$\widehat{h}(k) = \int \mathrm{d}\mathbf{r}\, e^{-i\mathbf{k}\cdot\mathbf{r}}\, h(r) = 4\pi \int_0^\infty \mathrm{d}r\, r^2 h(r) \frac{\sin(kr)}{kr}\,, \tag{2.32}$$

is accessible in diffraction experiments (typically neutron or x-ray scattering for atomic fluids or light scattering in the case of larger colloidal particles), where the static structure factor $S(k)$ can be measured:

$$S(k) = 1 + \rho_b \widehat{h}(k)\,. \tag{2.33}$$

In colloidal suspensions, experimental advances allows one also to measure $g(r)$ directly via individual particle tracking techniques, see, e.g., Ref. 18.

2.1.3 The role of computer simulations in liquid-state theory

The general dilemma in statistical physics for a given Hamiltonian is that partition sums and ensemble averages cannot be evaluated exactly for a given thermodynamic

state point (i.e. given temperature T, volume $\mathcal{V}$, et cetera). Only in limited cases such as for the ideal gas or one-dimensional hard-rods are exact expressions available [93, 94]. However, thermodynamic and structural properties can be extracted numerically from particle-based computer simulations. A simulation treats the locations (and momenta) of N particles and their interactions explicitly within a finite simulation volume $\mathcal{V}$. Challenges arising in real experiments, including the precise control of particle interactions or of environmental conditions, typically are not present in a simulation.

But other pitfalls can arise. First, even with nowadays computing power, the number of particles N in a simulation is significantly restricted by practicality as the time taken for a double loop scales with N^2 (for instance to evaluate the total instantaneous intrinsic energy from the pair potential). One therefore studies systems typically consisting of a few hundred up to several thousands of particles. This gives rise to a second point one has to care about. In order to avoid surface effects in a relatively small system, periodic boundary conditions are introduced i.e. when a particle leaves the simulation box, it reenters on the opposite side. For sufficiently short-ranged (i.e. quickly decaying) particle interactions, it is possible to obtain reliable results using a cubic box with side length $L \approx 6\sigma$ [95] (which applies to hard-sphere or Lennard-Jones fluids). However, longer-ranged pair interactions may require significantly larger simulation volumes, and if the pair potential decays as a power law, $\phi(r) \sim r^{-l}$, where l is smaller than the dimensionality of the system, sophisticated techniques are required [95]. Moreover, one also has to stay sufficiently far away from critical points, where density fluctuations can become macroscopic, which implies that critical phenomena are difficult to assess in a simulation. Nevertheless, the common experience is that structural and thermodynamic quantities of simple fluids with quickly decaying pair potentials, and away from the critical point, are only slightly affected by applying periodic boundary conditions. As such are simulations a very important cornerstones in liquid-state physics and soft-matter science.

The main drawback of a simulation is, however, that explicit expressions (i.e. formula) for structural or thermodynamic properties, and their mutual dependencies, are difficult to assess from simulations. But this clearly is necessary to gain broad insight into *what* physics drives the behavior of a fluid. Here, approximative and perturbation theories are indispensable.

Molecular and Brownian dynamics simulations. In a *molecular dynamics* simulation, one explicitly solves Newton's equations for an atomic system, whereas in a *Brownian dynamics simulation* Langevin's equation are solved for particles that are subject to Brownian motion. Observable means can then be obtained by computing time-averages:

$$\langle \mathcal{A} \rangle = \langle \mathcal{A}(\Gamma(t)) \rangle_{\text{time}} = \lim_{t\to\infty} \frac{1}{t} \int_0^t \mathrm{d}t' \; \mathcal{A}(\Gamma(t')) \approx \frac{1}{\nu_t} \sum_{i=0}^{\nu_t} \mathcal{A}(\Gamma(i\,\Delta t)) \,, \tag{2.34}$$

where $t = \nu_t \Delta t$ and $\nu_t \in \mathbb{N}$. In this thesis, we will not make use of molecular or Brownian dynamics simulations.

Monte-Carlo simulations. Consider for simplicity a canonical ensemble, where the particle number N is fixed. It follows from Eqs. (2.1) and (2.3), that averages of momentum-independent observables can be obtained from

$$\langle \mathcal{A} \rangle = \frac{\int_{\mathcal{V}} \mathrm{d}\mathbf{r}_1 \cdots \int_{\mathcal{V}} \mathrm{d}\mathbf{r}_N \, \mathcal{A}(\mathbf{r}_1, ..., \mathbf{r}_N) \, \exp[-\beta(U+V)]}{\int_{\mathcal{V}} \mathrm{d}\mathbf{r}_1 \cdots \int_{\mathcal{V}} \mathrm{d}\mathbf{r}_N \exp[-\beta(U+V)]} \tag{2.35}$$

$$\equiv \int_{\mathcal{V}} \mathrm{d}\mathbf{r}_1 \cdots \int_{\mathcal{V}} \mathrm{d}\mathbf{r}_N \, A(\mathbf{r}_1, ..., \mathbf{r}_N) P(\mathbf{r}_1, ..., \mathbf{r}_N) \tag{2.36}$$

where the reduced phase-space probability density $P(\mathbf{r}_1, ..., \mathbf{r}_N)$ is defined as

$$P(\mathbf{r}_1, ..., \mathbf{r}_N) = \frac{\exp[-\beta(U+V)]}{\int_{\mathcal{V}} \mathrm{d}\mathbf{r}_1 \cdots \int_{\mathcal{V}} \mathrm{d}\mathbf{r}_N \, \exp[-\beta(U+V)]} \, . \tag{2.37}$$

The remaining integrals may be approximated by employing stochastic (Monte-Carlo) integration schemes along with a technique called 'importance sampling', introduced by Metropolis in 1953: If we were able to generate a random sequence of positional configurations $\left\{ \{\mathbf{r}_1^1, ..., \mathbf{r}_N^1\}, ..., \{\mathbf{r}_1^K, ..., \mathbf{r}_N^K\} \right\}$ distributed *according* to the reduced probability distribution $P(\mathbf{r}_1, ..., \mathbf{r}_N)$, then Eq. (2.35) might be approximated by

$$\langle \mathcal{A} \rangle \approx \frac{1}{K} \sum_{j=1}^{K} \mathcal{A}_j \, , \tag{2.38}$$

where $\mathcal{A}_j \equiv \mathcal{A}(\mathbf{r}_1^j, ..., \mathbf{r}_N^j)$, which would become exact for $K \to \infty$. But how to generate such a set of configurations? This is the key challenge in a *Monte-Carlo (MC) simulation*. The most common scheme is the Metropolis algorithm [96], which, among other schemes employed in this thesis, is described in Appendix B, where we also give details regarding e.g. the calculation of the radial distribution function $g(r)$. A great benefit of MC techniques is that hard-core interactions can be treated exactly, whereas they have to be approximated in MD simulations (in order to ensure that the particle accelerations and velocities are smooth quantities).

2.1.4 Approximate theories for bulk properties of simple fluids

The total correlation function $h(r)$ of an uniform bulk fluids which was introduced at the end of Sec. 2.1.2 may be split into a part which stems from direct interactions between any two particles, and the rest. This is encoded within the Ornstein-Zernike (OZ) relation [57]

$$h(r) = c(r) + \rho_b \int \mathrm{d}\mathbf{r}' \, h(r') c(|\mathbf{r} - \mathbf{r}'|) \, , \tag{2.39}$$

where $c(r)$ is the so-called bulk pair direct correlation function. The latter is less structured than $h(r)$ and its range is similar to that of the pair potential. Note also

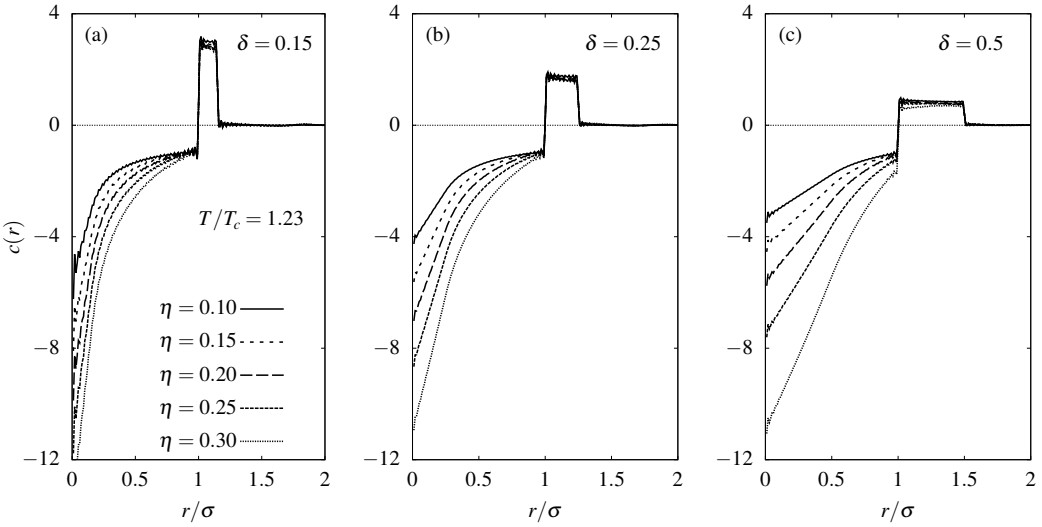

Figure 2.2 The bulk pair direct correlation function $c(r)$ of the square-well fluid with well-widths $\delta = 0.15$, 0.25 and 0.5, from left to right (in units of σ). The data was obtained from simulation results for $g(r)$ and the Ornstein-Zernike relation (2.39) for several packing fractions $\eta = 0.1 - 0.3$. For all cases the temperature is set to $T/T_c = 1.23$ where T_c is the critical temperature.

that the OZ relation is an exact one; it shifts the focus from $h(r)$ towards $c(r)$, so without further information it is not too helpful for gaining theoretical insights into the structure and correlations of an uniform fluid.

Away from critical points, $c(r)$ decays as the pair potential [57]:

$$c(r) = -\beta\phi(r) \ , \quad r \to \infty \, . \tag{2.40}$$

Furthermore, it can be shown [57] that $c(r)$ obeys the exact low-density expansion

$$c(r) = f(r) + \rho_b f(r) \int \mathrm{d}\mathbf{r}' \, f(|\mathbf{r} - \mathbf{r}'|) f(|\mathbf{r}'|) + \ldots \, . \tag{2.41}$$

where $f(r) = e^{-\beta\phi(r)} - 1$ is the Mayer-f function. Note that the asymptotic result (2.40) is included in Eq. (2.41) as for $r \to \infty$ the pair potential is weak, so that we can expand: $f(r) \approx -\beta\phi(r)$.

For simple fluids with a harshly repulsive core and a quickly decaying attractive tail in the pair potential, $c(r)$ is [57] negative for $r < \sigma$ arising from repulsive packing effects, and has a positive contribution for $r > \sigma$ where the pair potential is attractive. In Fig. 2.2 the typical behavior of $c(r)$ is shown[1] for the square-well fluid for different well-widths (in units of σ; see Eq. (1.8)) $\delta = 0.15$ (a), 0.25 (b) and 0.5 (c) of the attraction and several packing fractions $\eta = 0.1$ – 0.3 at fixed supercritical temperatures $T/T_c = 1.23$ where T_c is the critical temperature. We observe that the negative contribution for

[1]The curves in Fig. 2.2 were obtained from MC simulations. In order to extract $c(r)$ from the latter, the OZ equation was solved numerically in Fourier space using the simulated $h(r)$ as an input. We simulated 10 000 particles for each shown state point with the standard Metropolis algorithm (see App. B) in order to obtain an accurate $h(r)$ out to separations of $r \approx 15\sigma$ in order to minimize the cut-off error during the subsequent numerical Fourier transformation.

$r < \sigma$ associated with repulsive packing effects becomes more negative with increasing density, while the attractive tail is not very sensitive to the packing fraction suggesting that the asymptotic result (2.40) remains rather accurate down to the hard core $r = \sigma$.

Quantitative knowledge of a closure relation between $h(r)$ and $c(r)$, or a second independent access to one of the latter, would provide us the possibility to calculate the one from the other via the OZ relation (2.39). In particular, knowledge of $h(r)$ or $c(r)$ would provide one insight into thermodynamic properties of the fluid, which is precisely why these are key quantities in equilibrium liquid-state theory. For example, the isothermal compressibility χ_T is related exactly [57] to the volume integral over $h(r)$:

$$\rho_b k_B T \chi_T = 1 + 4\pi\rho_b \int_0^\infty \mathrm{d}r\, r^2 h(r) = 1 + \rho_b \widehat{h}(0) = S(0)\,, \tag{2.42}$$

or, alternatively, using the OZ relation (2.39) in Fourier space, we find

$$\rho_b k_B T \chi_T = \frac{1}{1 - \rho_b \widehat{c}(0)}\,. \tag{2.43}$$

The results for χ_T could then be integrated via Eq. (2.24) to find the fluid pressure p, which may eventually be integrated to yield the free energy F (recall that $p = \partial F/\partial \mathcal{V}$). For the sake of completeness, in what follows we provide a brief overview on the most important approximations to $c(r)$ and the corresponding free energies. However, we shall see in Sec. 2.2 that DFT provides a more general and powerful access to approximative expressions for $c(r)$.

van der Waals fluid. Consider the lowest order of the density expansion (2.41) for the pair direct correlation function, i.e. $c(r) = f(r)$. This is the simplest approximation to $c(r)$. Integrating twice yields the equation of state

$$\frac{\beta p}{\rho_b} = 1 + B_2 \rho_b\,, \tag{2.44}$$

where $B_2 = -2\pi \int_0^\infty \mathrm{d}r\, r^2 f(r)$ is the so-called second virial coefficient. If the pair potential can be decomposed in to a hard-sphere reference plus an attractive tail, $\phi = \phi_{\mathrm{HS}} + \phi_{\mathrm{att}}$, we obtain in the limit of high temperatures (i.e., $|\phi_{\mathrm{att}}(r)| \ll k_B T$) the van der Waals equation of state

$$\frac{\beta p_{\mathrm{vdW}}}{\rho_b} = 1 + 4\eta + 2\pi\rho_b \int_\sigma^\infty \mathrm{d}r\, r^2 \beta\phi_{\mathrm{att}}(r)\,. \tag{2.45}$$

This is the crudest model for a fluid that exhibits phase-separation into gaseous and liquid phases.

Percus-Yevick approximation. The Percus-Yevick (PY) approximation [97] provides an additional more complex relation between $c(r)$ and $g(r)$ in terms of the pair

potential $\phi(r)$ and reads:

$$c(r) \approx (1 - \exp[\beta\phi(r)])\ g(r)\,. \tag{2.46}$$

Equation (2.46) is in particular consistent with the asymptotic behavior of $c(r)$ (2.40) as $g(r) \approx 1$ and $e^{\beta\phi(r)} \approx 1 + \beta\phi(r)$ for $r \to \infty$. It is also consistent with the leading order of the low density expansion (2.41) since $g(r) \approx e^{-\beta\phi(r)}$ for $\rho_b \to 0$. Importantly, the PY approximation has an exact analytical solution for hard spheres [98]. It is given by ($c_{\mathrm{HS,PY}}(r) = 0$ for $r \geq \sigma$):

$$c_{\mathrm{HS,PY}}(r) = -\lambda_1 - 6\eta\lambda_2 \left(\frac{r}{\sigma}\right) - \frac{1}{2}\eta\lambda_1 \left(\frac{r}{\sigma}\right)^3 \quad , \quad r < \sigma\,, \tag{2.47}$$

where

$$\lambda_1 = \frac{(1+2\eta)^2}{(1-\eta)^4}\,, \qquad \lambda_2 = -\frac{(2+\eta)^2}{4(1-\eta)^4}\,. \tag{2.48}$$

The pressure is given by the expression

$$\frac{\beta p_{\mathrm{HS,PY}}}{\rho_b} = \frac{1+\eta+\eta^2}{(1-\eta)^3}\,, \tag{2.49}$$

and is in good accordance with computer simulations up to the fluid-solid transition. The corresponding excess (over ideal) free energy density reads

$$\beta f_{\mathrm{ex}}^{\mathrm{HS,PY}} = \beta f - \beta f_{\mathrm{id}} = \rho_b \left[\frac{3\eta(2-\eta)}{2(1-\eta)^2} - \ln(1-\eta)\right]\,. \tag{2.50}$$

Random phase approximation. In general, the PY approximation can be solved only numerically and so analytic expressions for e.g. the isothermal compressibility or the pressure cannot be obtained via this route. But we can obtain a simple analytic form for $c(r)$ for arbitrary attractive interactions since we know the asymptotic behavior of $c(r)$ for $r \to \infty$, see Eq. (2.40). For $\phi = \phi_{\mathrm{HS}} + \phi_{\mathrm{att}}$ it follows

$$c(r) \sim -\beta\phi_{\mathrm{att}}(r)\,. \tag{2.51}$$

Hence, we may simply assume that

$$c(r) = c_{\mathrm{HS}}(r) - \beta\phi_{\mathrm{att}}(r)\,, \tag{2.52}$$

where $c_{\mathrm{HS}}(r)$ may be given by the PY solution (2.47) for hard spheres, but any other approximate expression might be used. Equation (2.52) is known as random-phase approximation (RPA) and is fairly accurate for longer-ranged attractions (cf., e.g., Fig. 2.4). The resulting excess free energy density has the form of a generalized van der Waals model

$$\beta f_{\mathrm{ex}} = \beta f_{\mathrm{ex}}^{\mathrm{HS}} + \frac{4\pi}{2}\rho_b^2 \int_\sigma^\infty \mathrm{d}r\, r^2 \beta\phi_{\mathrm{att}}(r)\,. \tag{2.53}$$

There is another way to derive Eq. (2.52). The Mayer-f function of the full pair

potential can be decomposed into

$$f(r) = f_{\mathrm{HS}}(r) + e^{-\beta\phi_{\mathrm{HS}}(r)} f_{\mathrm{att}}(r)\,, \tag{2.54}$$

where $f_{\mathrm{HS}}(r)$ and $f_{\mathrm{att}}(r)$ are the Mayer-f functions of the hard-sphere and attractive part of the pair potential, respectively. We now may neglect all terms in the expansion (2.41) for $c(r)$ of order ρ_b or higher that contain $f_{\mathrm{att}}(r)$, but keep higher-order terms that include $f_{\mathrm{HS}}(r)$. If $\phi_{\mathrm{att}}(r)$ is sufficiently weak so that $e^{-\beta\phi_{\mathrm{att}}(r)} \approx 1 - \beta\phi_{\mathrm{att}}(r)$ we arrive at Eq. (2.52). As such, the RPA can also be interpreted as the leading-order correction of a perturbation expansion for simple fluids where the hard-sphere fluid acts as a reference.

Corrected RPA. The RPA is in qualitative accordance with simulations regarding the phase behavior for e.g. square-well fluids. However, it significantly underestimates for instance critical temperatures in comparison to simulations. This can empirically be corrected by extending the attractive portion of the pair potential $\beta\phi_{\mathrm{att}}(r)$ down to the core. The free energy in the corrected version of RPA is then given by

$$\beta f_{\mathrm{ex}} = \beta f_{\mathrm{ex}}^{\mathrm{HS}} + \frac{4\pi}{2}\rho_b^2 \int_0^\infty \mathrm{d}r\, r^2 \beta\phi_{\mathrm{att}}(r)\,, \tag{2.55}$$

where a common choice for $r < \sigma$ is $\phi_{\mathrm{att}}(r) = \phi_{\mathrm{att}}(\sigma)$.

Carnahan-Starling equation of state. In the latter examples, thermodynamic quantities are determined based on approximations for microscopic correlation functions of the uniform bulk fluid. There are also ways to determine macroscopic properties directly. Of course, having only a thermodynamic relation at hand we cannot deduce a corresponding microscopic quantity such as $c(r)$ or $h(r)$. The Carnahan and Starling (CS) equation of state for hard spheres is a well-known example. It is given by [99]

$$\frac{\beta p_{\mathrm{HS,CS}}}{\rho_b} = \frac{1 + \eta + \eta^2 - \eta^3}{(1-\eta)^3}\,. \tag{2.56}$$

Equation (2.56) is more accurate (in comparison to results from computer simulations) than the PY compressibility equation of state (2.49). The corresponding excess free energy density reads

$$\beta f_{\mathrm{ex}}^{\mathrm{HS,CS}} = \rho_b \frac{\eta(4-3\eta)}{(1-\eta)^2}\,. \tag{2.57}$$

2.2 Classical density functional theory (DFT)

So far we have not introduced theoretical methods (apart from simulations) that tell us how e.g. the equilibrium density profile $\rho(\mathbf{r})$ depends on a given external potential $V_{\mathrm{ext}}(\mathbf{r})$. All that we know is that $\rho(\mathbf{r})$ will not be a constant, since external forces will break the translational invariance of the system. However, spatially varying density profiles can also occur in systems that are not subject to any external forces – think of

a coexisting gas-liquid interface at state points located on the binodal, or of fluid-solid interfaces where the solid phase may be viewed as a strongly spatially localized liquid. The most appropriate theoretical framework for these kinds of questions is classical density functional theory (DFT) [16] introduced by R. Evans in 1979. Its key strength is that it accounts for the structure and thermodynamics of an inhomogeneous fluid, subject to an arbitrary external potential $V_{\text{ext}}(\mathbf{r})$, on equal footing.

We consider the intrinsic free energy $\mathcal{F}$ of the fluid, defined by[2]

$$\begin{aligned}\mathcal{F}[f_{gc}] &= \text{tr}_{\text{cl}}\, f_{gc}\,[T_{\text{kin}} + U + k_B T \ln(f_{gc})] && (2.58)\\ &= \text{tr}_{\text{cl}}\, f_{gc}\,[T_{\text{kin}} + k_B T \ln(f_{gc})] + \text{tr}_{\text{cl}}\, f_{gc}\,[U] && (2.59)\\ &\equiv \mathcal{F}_{\text{id}}[f_{gc}] + \mathcal{F}_{\text{ex}}[f_{gc}]\,, && (2.60)\end{aligned}$$

which we have split into the ideal-gas free energy $\mathcal{F}_{\text{id}}$ and the excess (over ideal) contribution $\mathcal{F}_{\text{ex}}$. The key idea of DFT is that $\mathcal{F}[f_{gc}]$, which is a *functional* of the equilibrium phase-space probability density f_{gc}, is also an unique functional of the equilibrium density profile $\rho(\mathbf{r})$: $\mathcal{F} = \mathcal{F}[\rho(\mathbf{r})]$. This follows from the fact [16] that the external potential $V_{\text{ext}}(\mathbf{r})$ is uniquely determined by a given one-body density $\rho(\mathbf{r})$, i.e. two distinct external fields $V'_{\text{ext}} \neq V_{\text{ext}}$ cannot give rise to the same equilibrium density profile $\rho(\mathbf{r})$. Note that the opposite is not necessarily true – there might exist different density profiles subject to the same external field e.g. at phase coexistence. As a result we have that the external potential can be written as a unique functional of the density: $V_{\text{ext}} = V_{\text{ext}}[\rho(\mathbf{r})]$.

It directly follows from the definition of f_{gc}, Eq. (2.11), that we can view f_{gc} as a functional of $V_{\text{ext}}(\mathbf{r})$, i.e. $f_{gc} = f_{gc}[V_{\text{ext}}(\mathbf{r})]$. In turn, this implies $f_{gc} = f_{gc}[\rho(\mathbf{r})]$ and hence it follows from Eq. (2.60) that $\mathcal{F} = \mathcal{F}[\rho(\mathbf{r})]$. With the same arguments one can show that the grand potential Ω is a unique functional of the density $\rho(\mathbf{r})$:

$$\begin{aligned}\Omega[f_{gc}] &= \text{tr}_{\text{cl}}\, f_{gc}[H - \mu N + k_B T \ln(f_{gc})]\\ &= \mathcal{F}[\rho(\mathbf{r})] + \text{tr}_{\text{cl}}\, f_{gc}[V - \mu N]\\ &= \mathcal{F}[\rho(\mathbf{r})] + \int \mathrm{d}\mathbf{r}\, \rho(\mathbf{r})(V_{\text{ext}}(\mathbf{r}) - \mu) && (2.61)\\ &\equiv \Omega[\rho(\mathbf{r})]\,, && (2.62)\end{aligned}$$

In particular, the equilibrium density $\rho(\mathbf{r})$ minimizes the grand-potential functional, i.e. any other density distribution $\widetilde{\rho}(\mathbf{r})$ which is not the equilibrium one, $\widetilde{\rho}(\mathbf{r}) \neq \rho(\mathbf{r})$, leads to a number that is larger than the grand potential: $\widetilde{\Omega} = \Omega[\widetilde{\rho}] > \Omega[\rho] = \Omega$. This may be summarized in the important result:

$$0 = \left.\frac{\delta\Omega[\widetilde{\rho}]}{\delta\widetilde{\rho}(\mathbf{r})}\right|_{\widetilde{\rho}=\rho} = \left.\frac{\delta\mathcal{F}[\widetilde{\rho}]}{\delta\widetilde{\rho}(\mathbf{r})}\right|_{\widetilde{\rho}=\rho} + V_{\text{ext}}(\mathbf{r}) - \mu\,. \qquad (2.63)$$

[2]Recall that the Hamiltonian is written as $H = T_{\text{kin}} + U + V$, where $T_{\text{kin}} = 1/(2m)\sum_i |\mathbf{p}_i|^2$, $U = \sum_{i<j} \phi(\mathbf{r}_i, \mathbf{r}_j)$ and $V = \sum_i V_{\text{ext}}(\mathbf{r}_i)$

The splitting of the intrinsic Helmholtz free-energy in Eq. (2.60) into ideal and excess contributions naturally translates to $\mathcal{F}[\rho] = \mathcal{F}_{\mathrm{id}}[\rho] + \mathcal{F}_{\mathrm{ex}}[\rho]$, where the ideal-gas free energy functional is known exactly:

$$\beta\mathcal{F}_{\mathrm{id}}[\rho] = \int \mathrm{d}\mathbf{r}\, \rho(\mathbf{r}) \left[\ln\left(\rho(\mathbf{r})\lambda_{\mathrm{th}}^3\right) - 1\right] . \tag{2.64}$$

The excess free energy functional $\mathcal{F}_{\mathrm{ex}}[\rho]$ contains all information about the particle interactions. The total free energy F of the system is given by

$$F = \mathcal{F}[\rho(\mathbf{r})] + \int \mathrm{d}\mathbf{r}\, \rho(\mathbf{r}) V_{\mathrm{ext}}(\mathbf{r}) . \tag{2.65}$$

Equation (2.63) yields an implicit equation for the density profile $\rho(\mathbf{r})$

$$\rho(\mathbf{r}) = \rho_b \exp\left(-\beta V_{\mathrm{ext}}(\mathbf{r}) + c^{(1)}(\mathbf{r}) + \beta\mu_{\mathrm{ex}}\right) , \tag{2.66}$$

where the chemical potential $\mu = \mu_{\mathrm{id}} + \mu_{\mathrm{ex}}$ was also split into ideal-gas and excess contributions. The quantity $c^{(1)}(\mathbf{r})$ is the so-called one-body direct correlation function and defined as

$$c^{(1)}(\mathbf{r}) := -\frac{\delta\beta\mathcal{F}_{\mathrm{ex}}[\rho]}{\delta\rho(\mathbf{r})} , \tag{2.67}$$

and therefore is the (negative) excess part of the local chemical potential

$$\beta\mu(\mathbf{r}) = \frac{\delta\beta\mathcal{F}[\rho]}{\delta\rho(\mathbf{r})} = \ln\left[\lambda_{\mathrm{th}}^3\rho(\mathbf{r})\right] - c^{(1)}(\mathbf{r}) . \tag{2.68}$$

More generally, the n-body direct correlation functions are defined as

$$c^{(n)}(\mathbf{r}_1, ..., \mathbf{r}_n) := -\frac{\delta^n\beta\mathcal{F}_{\mathrm{ex}}[\rho]}{\delta\rho(\mathbf{r}_1)\cdots\delta\rho(\mathbf{r}_n)} . \tag{2.69}$$

In particular, it can be shown [16] that the second member of the hierarchy, $c^{(2)}(\mathbf{r}_1, \mathbf{r}_2)$, in uniform systems equals the bulk pair direct correlation function $c(r)$ introduced previously in Eq. (2.39):

$$c(r) = c^{(2)}(|\mathbf{r} - \mathbf{r}'|) = -\left.\frac{\delta^2\mathcal{F}_{\mathrm{ex}}[\rho]}{\delta(\mathbf{r})\delta(\mathbf{r}')}\right|_{\rho_b} . \tag{2.70}$$

However, in general, the excess free energy functional $\mathcal{F}_{\mathrm{ex}}[\rho]$ is not known exactly, as this would be equivalent to having access to the exact partition sum of the system. Knowledge of (an exact or approximate) excess free energy functional $\mathcal{F}_{\mathrm{ex}}[\rho]$ would map the equilibrium statistical mechanics of inhomogeneous fluids to a problem of functional minimization rather than a cumbersome numerical evaluation of the grand partition sum Ξ or sampling configurations according to a phase-space probability distribution. The key task in DFT is therefore to construct reliable approximations for $\mathcal{F}_{\mathrm{ex}}[\rho]$ for a given model Hamiltonian, which poses a non-trivial challenge. The typical route for determining $\mathcal{F}_{\mathrm{ex}}[\rho]$ for fluids that interact via a harshly repulsive core and a

longer-ranged tail is as follows: the two-body density $\rho^{(2)}(\mathbf{r}, \mathbf{r}')$ can be obtained [16] from taking the functional derivatives of the excess free energy functional w.r.t. the pair potential $\phi(\mathbf{r}, \mathbf{r}')$, i.e.

$$\rho^{(2)}(\mathbf{r}, \mathbf{r}') = 2\,\frac{\delta\beta\mathcal{F}_{\rm ex}[\rho]}{\delta\phi(\mathbf{r}, \mathbf{r}')}\,. \tag{2.71}$$

If we now split the pair potential into a reference part $\phi_0(\mathbf{r}, \mathbf{r}')$ and a perturbation $\phi_{\rm per}(\mathbf{r}, \mathbf{r}')$ we may define a family of intermediate pair potentials:

$$\phi_\alpha(\mathbf{r}, \mathbf{r}') = \phi_0(\mathbf{r}, \mathbf{r}') + \alpha\phi_{\rm per}(\mathbf{r}, \mathbf{r}')\,, \quad 0 \le \alpha \le 1\,. \tag{2.72}$$

Increasing the parameter α smoothly from 0 to 1 would correspond to turning on the perturbation. Functional integration of (2.71) at constant density profile $\rho(\mathbf{r})$ then yields [16]

$$\begin{aligned}\mathcal{F}_{\rm ex}[\rho] - \mathcal{F}^0_{\rm ex}[\rho] &= \frac{1}{2}\int_0^1 {\rm d}\alpha \iint {\rm d}\mathbf{r}\,{\rm d}\mathbf{r}'\,\rho^{(2)}(\mathbf{r}, \mathbf{r}'\,;\,\alpha)\phi_{\rm per}(\mathbf{r}, \mathbf{r}') \\ &= \frac{1}{2}\int_0^1 {\rm d}\alpha \iint {\rm d}\mathbf{r}\,{\rm d}\mathbf{r}'\,\rho(\mathbf{r})g^{(2)}(\mathbf{r}, \mathbf{r}'\,;\,\alpha)\rho(\mathbf{r}')\phi_{\rm per}(\mathbf{r}, \mathbf{r}')\,,\end{aligned} \tag{2.73}$$

where $\mathcal{F}^0_{\rm ex}[\rho]$ is the free energy functional of the reference fluid, and in the second equation we used the general form of the pair correlation function $g^{(2)}(\mathbf{r}, \mathbf{r}') = \rho^{(2)}(\mathbf{r}, \mathbf{r}')/(\rho(\mathbf{r})\rho(\mathbf{r}'))$. In order to make progress one may expand $g^{(2)}(\mathbf{r}, \mathbf{r}',\,\alpha)$ about $\alpha = 0$:

$$g^{(2)}(\mathbf{r}, \mathbf{r}'\,\alpha\,) = g^{(2)}_0(\mathbf{r}, \mathbf{r}') + \alpha\,\left.\frac{\partial g^{(2)}(\mathbf{r}, \mathbf{r}'\,\alpha\,)}{\partial\alpha}\right|_{\alpha=0} + ... \tag{2.74}$$

Truncation at lowest order gives rise to

$$\mathcal{F}_{\rm ex}[\rho] = \mathcal{F}^0_{\rm ex}[\rho] + \frac{1}{2}\iint {\rm d}\mathbf{r}\,{\rm d}\mathbf{r}'\,\rho(\mathbf{r})g^{(2)}_0(\mathbf{r}, \mathbf{r}')\rho(\mathbf{r}')\phi_{\rm per}(\mathbf{r}, \mathbf{r}')\,. \tag{2.75}$$

For spherically-symmetric pair interactions, this result reduces to

$$\mathcal{F}_{\rm ex}[\rho] = \mathcal{F}^0_{\rm ex}[\rho] + \frac{1}{2}\iint {\rm d}\mathbf{r}\,{\rm d}\mathbf{r}'\,\rho(\mathbf{r})\rho(\mathbf{r}')g_0(|\mathbf{r} - \mathbf{r}'|)\phi_{\rm per}(|\mathbf{r} - \mathbf{r}'|)\,, \tag{2.76}$$

where $g_0(r)$ is the radial distribution function of the reference fluid. The crudest approximation is to assume $g_0(r) \approx 1$ in the range where the perturbation acts. We then obtain the generalization of Eq. (2.53) towards inhomogeneous fluids:

$$\mathcal{F}_{\rm ex}[\rho] - \mathcal{F}^0_{\rm ex}[\rho] = \frac{1}{2}\iint {\rm d}\mathbf{r}\,{\rm d}\mathbf{r}'\,\rho(\mathbf{r})\rho(\mathbf{r}')\phi_{\rm per}(|\mathbf{r} - \mathbf{r}'|)\,. \tag{2.77}$$

By taking two functional derivatives and evaluating the result at constant bulk density, we obtain the random phase approximation (2.52) for $c(r)$.

If $\phi_{\rm per}(r)$ describes an attractive tail, $\phi_{\rm per}(r) = \phi_{\rm att}(r)$, one may correct the right-hand side of Eq. (2.76) by means of extending $\phi_{\rm att}(r)$ down to the core, where are common choice for $r \le \sigma$ is $\phi_{\rm att}(r) = \phi_{\rm att}(\sigma)$. This empirically compensates an

underestimation of correlations due to omitting $g_0(r)$ of the reference fluid, and leads to the corrected RPA discussed in Sec. 2.1.4. Moreover, Eq. (2.77) constitutes a mean-field (MF) approximation for the non-hard-core interactions, as we can easily rewrite

$$\mathcal{F}_{\rm ex}[\rho] - \mathcal{F}^0_{\rm ex}[\rho] = \frac{1}{2}\iint \mathrm{d}\mathbf{r}\,\mathrm{d}\mathbf{r}'\,\rho(\mathbf{r})\rho(\mathbf{r}')\phi_{\rm per}(|\mathbf{r}-\mathbf{r}'|) \tag{2.78}$$

$$= \int \mathrm{d}\mathbf{r}\,\rho(\mathbf{r})\zeta(\mathbf{r})\,, \tag{2.79}$$

where $\zeta(\mathbf{r})$ may be viewed as a background field generated by all other particles

$$\zeta(\mathbf{r}) = \frac{1}{2}\int \mathrm{d}\mathbf{r}'\,\rho(\mathbf{r}')\phi_{\rm per}(|\mathbf{r}-\mathbf{r}'|)\,. \tag{2.80}$$

However, Eq. (2.77) is not very helpful without knowledge of approximations for the free-energy functional $\mathcal{F}^0_{\rm ex}[\rho]$ of the reference system. The latter is often assumed to be the hard-sphere fluid, and hence deriving accurate excess free energy functionals for the latter is crucial.

2.3 Density functionals for the hard-sphere fluid

A crude way of constructing an excess free energy functional is to assume that bulk equations for the free energy hold also in inhomogeneous situations. This is referred to as local density approximation (LDA). In fact, the second term of Eq. (2.77) may e.g. be viewed as a local density approximation for the non-hard-sphere part in Eq. (2.55). For hard spheres, one may assume that the Carnahan-Starling free energy, Eq. (2.57), holds also for the inhomogeneous fluid, i.e.

$$\beta\mathcal{F}^{\rm HS}_{\rm ex}[\rho] = \int \mathrm{d}\mathbf{r}\;\rho(\mathbf{r})\frac{\eta(\mathbf{r})(4-3\eta(\mathbf{r}))}{(1-\eta(\mathbf{r}))^2}\;, \tag{2.81}$$

with $\eta(\mathbf{r}) = \pi\rho(\mathbf{r})\sigma^3/6$. However, it turns out that Eq. (2.81) is reliable only for slowly varying density profiles and furthermore is not consistent with the exact low-density expansion of $c(r)$ (2.41).

A possible alternative is to expand $\mathcal{F}_{\rm ex}[\rho]$ about the homogeneous state $\rho(\mathbf{r}) = \rho_b$:

$$\mathcal{F}_{\rm ex}[\rho] = \mathcal{F}_{\rm ex}[\rho_b] + \int \mathrm{d}\mathbf{r}\;\left.\frac{\delta\mathcal{F}_{\rm ex}[\rho]}{\delta\rho(\mathbf{r})}\right|_{\rho_b}\Delta\rho(\mathbf{r}) + \frac{1}{2}\iint \mathrm{d}\mathbf{r}\,\mathrm{d}\mathbf{r}'\;\left.\frac{\delta^2\mathcal{F}_{\rm ex}[\rho]}{\delta(\mathbf{r})\delta(\mathbf{r}')}\right|_{\rho_b}\Delta\rho(\mathbf{r})\Delta\rho(\mathbf{r}') + ..., \tag{2.82}$$

where $\Delta\rho(\mathbf{r}) = \rho(\mathbf{r}) - \rho_b$. Taking together Eqs. (2.70) and (2.82) we obtain

$$\mathcal{F}_{\rm ex}[\rho] \approx \mathcal{F}_{\rm ex}[\rho_b] + \mu_{\rm ex}\int \mathrm{d}\mathbf{r}\,\Delta\rho(\mathbf{r}) - \frac{1}{2}\iint \mathrm{d}\mathbf{r}\,\mathrm{d}\mathbf{r}'\,c(|\mathbf{r}-\mathbf{r}'|)\Delta\rho(\mathbf{r})\Delta\rho(\mathbf{r}')\,, \tag{2.83}$$

where $\mu_{\rm ex} = \partial\mathcal{F}_{\rm ex}[\rho_b]/\partial N$. Equation (2.83) is known as the Ramakrishnan-Yussouff

approximation [100]. Making use of e.g. the PY solution to $c(r)$ for hard spheres as an input to Eq. (2.82) yields a functional that provides a decent description of structural properties of the hard-sphere fluid over a wide range of densities as compared to simulations [100, 101]. Remarkably, it is also capable of predicting the freezing transition.

However, to date, the most reliable density functionals for hard spheres are based on so-called weighted density approximations (WDA). We will discuss two types in the subsequent Secs. 2.3.1 and 2.3.2: first, the formalism of Tarazona, typically just termed 'WDA functionals' and then Rosenfeld's successful fundamental measure theory.

2.3.1 Tarazona's weighted density approach

From Eqs. (2.41) and (2.70) it follows an *exact* expansion of the excess free energy functional in terms of Mayer-f functions:

$$\begin{aligned}\beta\mathcal{F}_{\mathrm{ex}}[\rho] = &-\frac{1}{2}\iint \mathrm{d}\mathbf{r}_1\,\mathrm{d}\mathbf{r}_2\;\rho(\mathbf{r}_1)\rho(\mathbf{r}_2)f(r_{12}) \\ &-\frac{1}{6}\iiint \mathrm{d}\mathbf{r}_1\,\mathrm{d}\mathbf{r}_2\,\mathrm{d}\mathbf{r}_3\,\rho(\mathbf{r}_1)\rho(\mathbf{r}_2)\rho(\mathbf{r}_3)f(r_{12})f(r_{23})f(r_{31}) + \dots\,,\end{aligned} \tag{2.84}$$

which is a very useful starting point to construct functionals that are valid at higher particle densities. As mentioned above, the LDA functional for hard spheres, Eq. (2.81), does not satisfy this low-density limit (2.84). In a first paper [102], Tarazona showed that a functional can be constructed which satisfies the leading term of the expansion (2.84) by introducing the following weighted density $\bar{\rho}(\mathbf{r})$:

$$\bar{\rho}(\mathbf{r}) = -\frac{1}{8}\int \mathrm{d}\mathbf{r}'\;\rho(\mathbf{r}')f(r)\,, \tag{2.85}$$

which replaces $\eta(\mathbf{r})$ in Eq. (2.81). However, the resulting density profiles at e.g. a planar hard wall were still rather poor at high fluid densities in comparison to computer simulations [103].

In a following work [104] Tarazona augmented the above idea to construct a functional for hard spheres which satisfies Eq. (2.84) up to second order and proposed a generic form for the excess free energy functional:

$$\beta\mathcal{F}_{\mathrm{ex}}[\rho] = \int \mathrm{d}\mathbf{r}\,\rho(\mathbf{r})\beta\Psi(\bar{\rho}(\mathbf{r}))\,, \tag{2.86}$$

where $\Psi(\bar{\rho}(\mathbf{r}))$ is the bulk excess free energy per particle evaluated[3] at $\bar{\rho}(\mathbf{r})$. The weighted density $\bar{\rho}(\mathbf{r})$ is written more generally as a convolution of the bare density $\rho(\mathbf{r})$ with a (density-dependent) weight function ω:

$$\bar{\rho}(\mathbf{r}) = \int \mathrm{d}\mathbf{r}'\rho(\mathbf{r}')\omega(|\mathbf{r}-\mathbf{r}'|\,,\,\widetilde{\rho}(\mathbf{r}))\,. \tag{2.87}$$

[3] For the Carnahan-Starling expression (2.57) this for instance means $\beta\Psi(\bar{\rho}(\mathbf{r})) = \bar{\eta}(\mathbf{r})(4-3\bar{\eta}(\mathbf{r}))/(1-\bar{\eta}(\mathbf{r}))^2$ with $\bar{\eta}(\mathbf{r}) = \pi\sigma^3\bar{\rho}(\mathbf{r})/6$.

In bulk one has the constraint that $\bar{\rho}(\mathbf{r}) = \widetilde{\rho}(\mathbf{r}) = \rho(\mathbf{r}) = \rho_b$ and hence $\omega(r,\, \rho)$ has to satisfy

$$\int \mathrm{d}\mathbf{r}\, \omega(r,\, \rho) = 1\,. \tag{2.88}$$

The resulting bulk pair direct correlation $c(r)$ has then the generic form [104]

$$\begin{aligned} c(r) = &- 2\beta\Psi'(\rho_b)\omega(r,\, \rho_b) - \rho_b\beta\Psi''(\rho_b)\,(\omega * \omega)(r,\, \rho_b) \\ &- 2\beta\rho_b\Psi'(\rho_b)\,(\omega * \omega')(r,\, \rho_b)\,, \end{aligned} \tag{2.89}$$

where primes in Eq. (2.89) denote differentiation with respect to the density and $*$ denotes a three-dimensional convolution of the weight functions. In order to specify the yet unknown weight function ω, Tarazona expanded in powers of the density:

$$\omega(r,\, \rho) = \omega_0(r) + \rho\omega_1(r) + \rho^2\omega_2(r) \,+\, \ldots\,, \tag{2.90}$$

leading to the relation

$$\bar{\rho}(\mathbf{r}) = \rho_0(\mathbf{r}) + \widetilde{\rho}(\mathbf{r})\rho_1(\mathbf{r}) + [\widetilde{\rho}(\mathbf{r})]^2\rho_2(\mathbf{r}) \,+\, \ldots\,, \tag{2.91}$$

where

$$\rho_i(\mathbf{r}) \equiv \int \mathrm{d}\mathbf{r}'\, \rho(\mathbf{r}')\omega_i(|\mathbf{r} - \mathbf{r}'|)\,,\ \text{with}\ i \,=\, 0\,,1\,,2\,,\ldots\,. \tag{2.92}$$

This expansion may be plugged into Eq. (2.89) and a comparison of coefficients with the low-density expansion Eq. (2.41) of $c(r)$ yields exact relations for $\omega_0(r)$ and $\omega_1(r)$. For example $\omega_0(r)$ is given by

$$\omega_0(r) = \frac{3}{4\pi\sigma^3}\Theta(\sigma - r)\,. \tag{2.93}$$

In order to obtain a density functional which is valid at higher particle densities, Tarazona truncated the expansion (2.90) at second order and determined $\omega_2(r)$ by fitting the generated $c(r)$ to the PY solution (2.47).

Note that in Tarazona's original work $\widetilde{\rho}(\mathbf{r}) = \bar{\rho}(\mathbf{r})$ and thus Eq. (2.91) yields a quadratic equation for $\bar{\rho}(\mathbf{r})$ when truncated at second order in the density. Kim *et al.* [105] alternatively suggested that the weighted densities $\widetilde{\rho}(\mathbf{r})$ may be obtained by the global average

$$\widetilde{\rho}(\mathbf{r}) = \int \mathrm{d}\mathbf{r}'\rho(\mathbf{r}')\omega(|\mathbf{r} - \mathbf{r}'|, \rho_b)\,, \tag{2.94}$$

which guarantees that the resulting bulk pair direct correlation function The form of Kim *et al.* produces nearly indistinguishable results [105] compared to the original WDA by Tarazona, but is computationally less intensive as it only requires the calculation of additional convolutions. Both theories produce density profiles that are in very good agreement with results from computer simulations up to high particle densities [103, 105] (see also Fig. 2.3).

2.3.2 Fundamental measure theory (FMT)

While Tarazona's WDA for hard spheres has proven to yield reliable predictions even at high fluid densities, the most accurate density functionals for hard spheres are based on Rosenfeld's fundamental measure theory (FMT) [17, 70]. Besides the gratifying observation that it performs even better at very high fluid packing fractions compared to simulations, a cornerstone is posed by the fact that it generates the PY bulk pair direct correlation function as an output without using it as an input. Moreover, the theory is constructed for hard-sphere mixtures. In what follows we will outline the basics of FMT, but we will not discuss every detail; we refer the further interested reader to the excellent review of Roth [70].

At the center of FMT is the observation that the Mayer-f function $f_{ij}(r) = -\Theta(R_i + R_j - r)$ for a pair of spheres with radii R_i and R_j, where $\Theta(\cdot)$ is the Heaviside step function, can be decomposed into convolutions of weight functions $\omega_\nu^i(\mathbf{r})$ characterizing the geometry of the particles. As a result, the exact low-density free energy functional, generalized to a ℓ-component mixture, can be written as

$$\begin{aligned}\beta\mathcal{F}_{\text{ex}}^{\text{HS}}[\rho] &= \frac{1}{2}\sum_{i,\,j=1}^{\ell}\iint \mathrm{d}\mathbf{r}\,\mathrm{d}\mathbf{r}'\,\rho_i(\mathbf{r})\rho_j(\mathbf{r}')\Theta(R_i + R_j - |\mathbf{r}-\mathbf{r}'|)\\ &= \int \mathrm{d}\mathbf{r}\,\{n_0(\mathbf{r})n_3(\mathbf{r}) + n_1(\mathbf{r})n_2(\mathbf{r}) - \mathbf{n}_1(\mathbf{r})\cdot\mathbf{n}_2(\mathbf{r})\}\,, \end{aligned} \tag{2.95}$$

where the $n_\nu(\mathbf{r})$ are weighted densities defined as

$$n_\nu(\mathbf{r}) = \sum_{i=1}^{\ell}\int \mathrm{d}\mathbf{r}'\,\rho_i(\mathbf{r}')\omega_\nu^i(\mathbf{r}-\mathbf{r}')\,. \tag{2.96}$$

For instance, $n_3(\mathbf{r})$ is the total local packing fraction given by

$$n_3(\mathbf{r}) = \sum_{i=1}^{\ell}\int \mathrm{d}\mathbf{r}'\,\rho_i(\mathbf{r}')\Theta(R_i - |\mathbf{r}-\mathbf{r}'|)\,, \tag{2.97}$$

which reduces to the total packing fraction $\eta = \pi/6\sum_{i=1}^{\ell}\rho_{b,i}\,R_i^3$ in the uniform fluid. All together, the weight functions of species i are:

$$\omega_3^i(\mathbf{r}) = \Theta(R_i - |\mathbf{r}|)\,, \qquad \omega_2^i(\mathbf{r}) = \delta(R_i - |\mathbf{r}|)\,, \tag{2.98}$$

$$\omega_1^i(\mathbf{r}) = \frac{\omega_2^i(\mathbf{r})}{4\pi R_i}\,, \qquad \omega_0^i(\mathbf{r}) = \frac{\omega_2^i(\mathbf{r})}{4\pi R_i^2}\,, \tag{2.99}$$

$$\vec{\omega}_2^i(\mathbf{r}) = \frac{\mathbf{r}}{r}\omega_2^i(\mathbf{r})\,, \qquad \vec{\omega}_1^i(\mathbf{r}) = \frac{\vec{\omega}_2^i(\mathbf{r})}{4\pi R_i}\,. \tag{2.100}$$

In order to derive an excess free energy functional at larger densities, Rosenfeld employed the ansatz:

$$\beta\mathcal{F}_{\text{ex}}^{\text{HS}}[\{\rho_i\}] = \int \mathrm{d}\mathbf{r}\;\Phi(\{n_\nu(\mathbf{r})\})\,, \tag{2.101}$$

which is motivated by the exact result for one-dimensional hard-rod mixtures [94]. Equation (2.101) yields the following form for the direct correlation function $c_i^{(1)}(\mathbf{r})$ of species i:

$$c_i^{(1)}(\mathbf{r}) = -\sum_\nu \int \mathrm{d}\mathbf{r}' \, \frac{\partial\Phi(\{n_\gamma(\mathbf{r}')\})}{\partial n_\nu} \frac{\delta n_\nu(\mathbf{r}')}{\delta\rho_i(\mathbf{r})} \tag{2.102}$$

$$= -\sum_\nu \int \mathrm{d}\mathbf{r}' \, \frac{\partial\Phi(\{n_\gamma(\mathbf{r}')\})}{\partial n_\nu} \omega_\nu^i(\mathbf{r}' - \mathbf{r}) \,. \tag{2.103}$$

Rosenfeld FMT. In order to determine the function Φ, Rosenfeld used dimensional analysis, the condition that Eq. (2.101) has to recover the low-density expansion Eq. (2.84), and an exact relation from scaled-particle theory, which reads

$$\lim_{R_i\to\infty} \frac{\beta\mu_{\mathrm{ex}}^i}{\frac{4\pi}{3}R_i^3} = \beta p \;, \tag{2.104}$$

relating the work of reversibly introducing a large sphere into the fluid (i.e. the excess chemical potential μ_{ex}^i of species i) to the bulk pressure p. The final result obtained by Rosenfeld reads

$$\Phi^{\mathrm{RF}}(\{n_\nu^i\}) = -n_0 \ln(1-n_3) + \frac{n_1 n_2 - \mathbf{n}_1\cdot\mathbf{n}_2}{1-n_3} + \frac{n_2^3 - 3n_2\mathbf{n}_2\cdot\mathbf{n}_2}{24\pi(1-n_3)^2} \tag{2.105}$$

$$\equiv \Phi_1 + \Phi_2 + \Phi_3 \,. \tag{2.106}$$

Remarkably, the bulk pair correlation function generated by this functional is identical to the exact solution of the Percus-Yevick approximation for hard-sphere mixtures [106], i.e.

$$c_{ij}^{\mathrm{FMT,RF}}(r) = -\sum_{\nu,\nu'} \left.\frac{\partial^2\Phi(\{n_\gamma\})}{\partial n_\nu \, \partial n_{\nu'}}\right|_{\rho_b} (\pm\omega_\nu^i * \omega_{\nu'}^j)(r) \tag{2.107}$$

$$= c_{ij}^{\mathrm{HS,PY}}(r) \,, \tag{2.108}$$

where the negative sign in Eq. (2.108) holds for the vector-type weight functions.
While being very successful in describing many aspects of the inhomogeneous hard-sphere fluid, it turned out that Rosenfeld's free energy density in its original form is not able to describe a hard-sphere crystal [17, 107]. A negative divergence occurs in the final term Φ_3 for strongly peaked density profiles. In order to regularize Φ_3, Rosenfeld *et al.* suggested to modify the term Φ_3 as follows [108, 109]:

$$\tilde{\Phi}_3 = \frac{1}{24\pi(1-n_3)^2}\left(n_2 - \frac{\mathbf{n}_2\cdot\mathbf{n}_2}{n_2}\right)^3 \;, \tag{2.109}$$

which is referred to as the 'q_3 correction'. An alternative approach that regularizes Φ_3 was given by Tarazona who introduced an additional tensorial (t) weight function, and

thus a tensorial weighted density [110]. These are given by

$$\omega_t^i(\mathbf{r}) = \left(\frac{\mathbf{r} \otimes \mathbf{r}}{r^2} - \frac{1}{3} \mathbb{1} \right) \omega_2^i(\mathbf{r}) \ , \tag{2.110}$$

and

$$n_t(\mathbf{r}) = \sum_{i=1}^{\ell} \int \mathrm{d}\mathbf{r}' \ \rho_i(\mathbf{r}') \omega_t^i(\mathbf{r} - \mathbf{r}'). \tag{2.111}$$

Here $\mathbb{1}$ denotes the 3×3 unity matrix and $\mathbf{r} \otimes \mathbf{r}$ represents the dyadic product of two vectors. Φ_3 is replaced by a new term Φ_3^t containing n_t:

$$\Phi_3^t = \Phi_3 + \frac{\frac{9}{2} \left(\mathbf{n}_2 n_t \mathbf{n}_2 - \mathrm{Tr} \left(n_t^3 \right) \right)}{24\pi(1 - n_3)^2} \ , \tag{2.112}$$

where $\mathrm{Tr}(\cdot)$ denotes the trace of a matrix. Both the q_3 correction and the tensorial modification lead to functionals that give decent descriptions of the hard-sphere crystal, while leaving the already excellent properties of the functional regarding the descriptions of the fluid phase virtually unaffected.

White-Bear versions of FMT. It is possible to use the more accurate Mansoori-Carnahan-Starling-Leland (MCSL) equation of state [111], which is a ℓ-component generalization of the CS equation of state (cf. last paragraph of Sec. 2.1.4), as an input to derive a new excess free energy density Φ^{WB} - the White Bear (WB) version of FMT [112]. The WB functional performs better in describing density profiles of hard sphere mixtures, especially at high bulk densities close to freezing transition. However, it is found that the WB functional does not recover Eq. (2.104), meaning that the partial derivative of Φ^{WB} with respect to n_3 does not give rise to the equation of state originally used for the derivation of Φ^{WB}. Obviously, this inconsistency with scaled-particle theory has to be expected because, as discussed above, using Eq. (2.104) in order to determine Φ precisely leads one to the less accurate PY equation of state. In order to minimize this inconsistency, a new generalization of the Carnahan-Starling equation of state has been put forward [113]. Based on this new equation of state it is possible to derive the following functional [114]:

$$\begin{aligned} \Phi^{\mathrm{WB2}} = & -n_0 \ln(1 - n_3) + (n_1 n_2 - \mathbf{n}_1 \cdot \mathbf{n}_2) \frac{1 + \frac{1}{3}\phi_2(n_3)}{1 - n_3} \\ & + \left(n_2^3 - 3 n_2 \mathbf{n}_2 \cdot \mathbf{n}_2 \right) \frac{1 - \frac{1}{3}\phi_3(n_3)}{24\pi(1 - n_3)^2} \ , \end{aligned} \tag{2.113}$$

in which the functions ϕ_2 and ϕ_3 are given by

$$\begin{aligned} \phi_2(n_3) &= \frac{1}{n_3} \left(2n_3 - n_3^2 + 2(1 - n_3) \ln(1 - n_3) \right) \ , \\ \phi_3(n_3) &= \frac{1}{n_3^2} \left(2n_3 - 3n_3^2 + 2n_3^3 + 2(1 - n_3)^2 \ln(1 - n_3) \right) . \end{aligned} \tag{2.114}$$

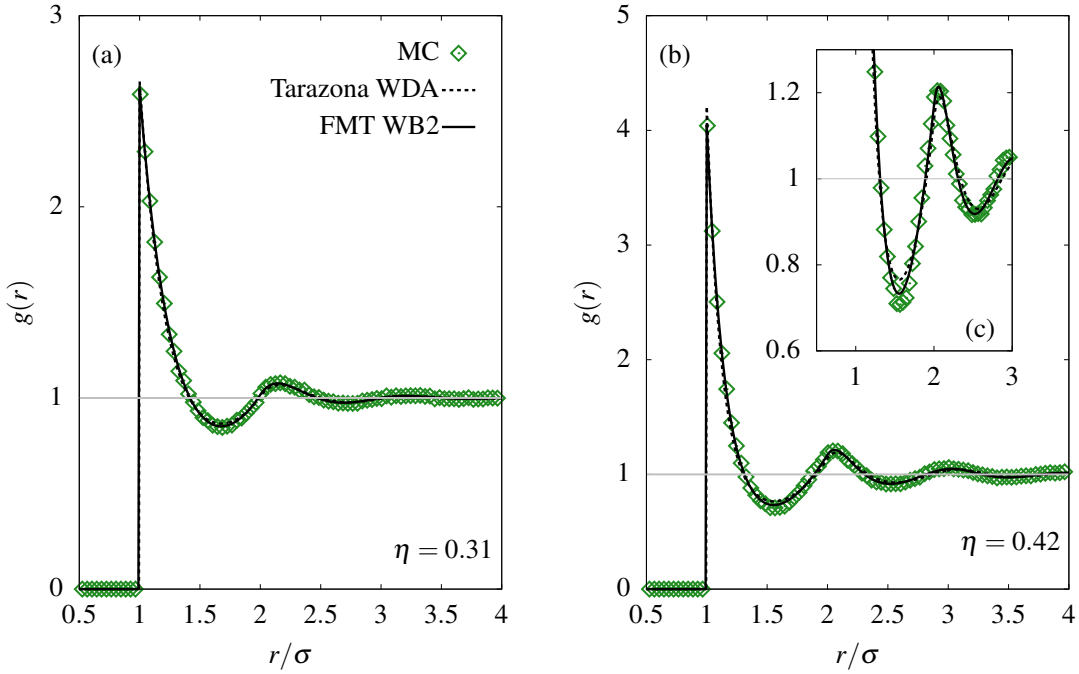

Figure 2.3 Radial distribution function $g(r) = \rho(r)/\rho_b$ of the hard-sphere fluid as obtained from minimizing the grand-potential functional $\Omega[\rho]$ in presence of a test particle: WDA functional (dashed line); FMT WB2 functional (solid line); MC simulations (symbols). The packing fractions are $\eta = 0.31$ (a) and 0.42 (b). The inset (c) shows a magnification of (b) highlighting slight differences between WDA and FMT.

This functional, the White Bear version Mark 2 (WB2), is consistent with the scaled-particle relation, i.e. $\beta p_{\mathrm{CS}} = \partial\Phi/\partial n_3$ in the case of the one-component fluid. Since the derivations of the White Bear versions of FMT start from the same ansatz as Rosenfeld's FMT (mainly they differ in the choice of the equation of state) it is obvious that they face the same problems when describing a hard sphere crystal. However, one can also apply the empirical q_3 correction or the tensorial approach due to Tarazona to Φ_3. In particular the tensorial WBII functional has been demonstrated to provide an excellent description of hard sphere crystals [115].

Finally, it is worth mentioning that there exists also a very accurate version of FMT to describe hard-disk mixtures [116] which has proven to be in excellent agreement with experiments for both structural and thermodynamic properties [18, 20] and Lin and Oettel used this functional to study properties of the two-dimensional fluid-solid interface [117].

2.3.3 Calculation of density profiles

In Fig. 2.3 we show results for the radial distribution function $g(r) = \rho(r)/\rho_b$ of hard spheres obtained from minimizing the grand-potential functional $\Omega[\rho]$ in presence of a test particle (Percus' idea of defining $g(r)$). This situation corresponds to setting the external potential equal to the pair interaction, i.e. $V_{\mathrm{ext}}(r) = \phi_{\mathrm{HS}}(r)$. The equilibrium density profile $\rho(r)$ can then be calculated numerically from solving Eq. (2.66) with

iterative schemes. The packings are $\eta = 0.31$ (a) and 0.42 (b); recall that the fluid-solid transition appears at roughly $\eta \approx 0.49$. The dashed line corresponds to Tarazona's WDA functional with modification according to Kim [105] (cf. Sec. 2.3.1), and the solid lines are results from the FMT WB2 functional. The theoretical data predicted by both DFT versions fit very well to results obtained from MC simulations (green symbols). The WB2 functional performs slightly better at higher particle densities, see inset of Fig. 2.3 (c).

Classical DFT in particular allows us to also calculate density profiles in complex external potentials such as fluids confined to three-dimensional capillaries [118], where in such cases the density profile will depend on all three spatial coordinates x, y and z and the numerical solution of Eq. (2.66) can computationally be inefficient using solely iterative procedures. In Appendix A we outline the possibility to calculate the density profile $\rho(\mathbf{r})$ massively in parallel on graphics cards, which in two- and three dimensions can speed up the minimization procedure by nearly two orders of magnitude.

The density functionals for hard disks in two, and hard spheres in three dimensions, based on FMT are state of the art and their accuracy compared to simulations and experiments is striking. In particular, this allows us to shift the focus towards the study of fluids with more complex pair interactions. An example for this is provided in the next Sec. 2.4, where we will focus on the behavior of the radial distribution function $g(r)$ and its role in determining thermodynamic properties for fluids where the particles interact via a hard core and an additional attractive tail.

2.4 On the decay of pair correlations and related topics[4]

The statistical physics of fluids is frequently concerned with the role of repulsive and attractive interparticle potentials, and their competition, in determining the thermodynamic and structural properties. At the most basic level, the virial expansion of the pressure $p = k_B T(\rho_b + B_2(T)\rho_b^2 + \cdots)$ provides a measure of the competition at low number densities ρ_b. T is the temperature and k_B is Boltzmann's constant. If repulsion dominates the second virial coefficient is positive, $B_2(T) > 0$, so that the pressure p is larger than the ideal-gas value, $p > p^{\mathrm{id}} = k_B T \rho_b$, whereas if attraction is dominant then $B_2(T) < 0$ and $p < p^{\mathrm{id}}$. The Boyle temperature T_B, defined by $B_2(T_B) = 0$, is that for which repulsive and attractive interactions cancel in a dilute gas. For a Lennard-Jones fluid $k_B T_B/\varepsilon \approx 3.418$ where ε is the Lennard-Jones well-depth [119]. In colloid science and in the physics of proteins the sign and magnitude of the second virial coefficient B_2 plays an important role in quantifying the effective interactions between these mesoscopic particles suspended in a solvent [120–122]. The value of B_2 is also believed to play an important role in determining the onset of phase coexistence in *dense* fluids. The empirical criterion [123, 124] for the critical value, i.e. $B_2^{\mathrm{crit}}/B_2^{\mathrm{HS}} \lesssim -1.5$ is often used to estimate the gas-liquid critical temperature.

[4]This section is reproduced from: D. Stopper, H. Hansen-Goos, R. Roth, and R. Evans, J. Chem. Phys. **151** 014501 (2019), with the permission of AIP Publishing

Here $B_2^{\rm HS} = 2\pi\sigma^3/3$ is the second virial coefficient for hard spheres (HS) of diameter σ. For very short-ranged attractive potentials the adhesive hard-sphere criterion $B_2^{\rm crit}/B_2^{\rm HS} \lesssim -1.2$ is preferred [125]. These criteria are based on the idea: provided there is sufficient net attraction, as measured by a sufficiently negative $B_2(T)$, phase coexistence can occur.

The competition between repulsive and attractive interatomic forces also governs the form of the pair and higher order correlation functions, i.e. the structure of the fluid. Seminal work [6, 7] explained the importance of repulsive forces and their softness in determining the short-ranged behavior of the total correlation function $h(r) \equiv g(r) - 1$, where $g(r)$ is the radial distribution function. Here we focus primarily on the long-ranged behavior of $h(r)$. For a dilute gas at low T, or in the vicinity of the gas-liquid critical point, $rh(r)$ should decay to zero exponentially, as $r \to \infty$; the decay length defines the true correlation length ξ. On the other hand, in the liquid state or in a supercritical high density fluid state we expect $rh(r)$ to decay in an exponentially damped oscillatory fashion, similar to the decay found for one-component HS fluids at all state points. The former mode of asymptotic decay requires sufficient interparticle attraction, whereas the latter is a signature that repulsion is dominating. The crossover between pure exponential and exponentially damped oscillatory decay of $rh(r)$ defines a line in the phase diagram, first identified by Fisher and Widom (FW) [126] in their analysis of one-dimensional models. They conjectured that similar crossover would occur in three dimensional fluids. Determining the FW line requires knowledge of the poles of the Fourier transform $\widehat{h}(k)$ of the total pair correlation function $h(r)$. In turn, this requires calculating the pair direct correlation function $c(r)$ at many thermodynamic state points [57, 127–129]. One learns that the form of $c(r)$ is crucial in determining whether the ultimate decay of $rh(r)$ is damped oscillatory or monotonic.

In this section, we revisit how the competition between repulsive and attractive interparticle potentials influences the structure of fluids. In particular, we enquire whether there is a simple physical criterion that indicates where in the phase diagram the FW structural crossover should occur. By considering the repulsive and attractive contributions to $c(r)$ we propose a simple approximate criterion: FW crossover should occur close to the line where the isothermal compressibility χ_T takes its ideal gas value $\chi_T^{\rm id}$. We also investigate the so-called Widom (W) line, which we define as the line of a local maximum of the true correlation length ξ. In recent literature, the term 'Widom line' is often associated with lines of extrema of thermodynamic response functions, which appears to have its origin in papers from H. E. Stanley and co-workers, see e.g. Ref. [130], dealing with a liquid-liquid transition. In Ref. [131] several lines of maximal response functions are plotted for the square-well fluid. The title of the paper: 'True Widom line for a square-well system' is unfortunate as the authors consider the Ornstein-Zernike (OZ) correlation length ξ_{OZ}, which appears in the celebrated expansion of the static structure factor $S(k) = S(0)/(1 + \xi_{\rm OZ}^2 k^2)$ at low wavenumbers $k \to 0$, *not* the true correlation length ξ which is determined by the asymptotic decay of $rh(r)$.

2.4.1 The Fisher-Widom line and decay of pair correlations

In addition to determining macroscopic phase behavior, i.e. the existence of gaseous, liquid and solid phases, the competition between interparticle attraction and repulsion is also reflected in the microscopic structure of fluids. As earlier, Fisher and Widom [126] conjectured that in three-dimensional systems in the fluid phase, the total correlation function $h(r) \equiv g(r) - 1$ should decay to zero in damped oscillatory fashion as $r \to \infty$ at state points for which repulsion dominates over attraction; typically at sufficiently high volume fractions η and/or temperatures T. In contrast, at state points where attraction dominates, e.g. in proximity to the critical point or in the gaseous phase, $h(r)$ should decay monotonically to zero, from above, as $r \to \infty$.

The asymptotic behavior of $h(r)$ can be extracted from its Fourier representation along with the Ornstein-Zernike relation [57]. In $d = 3$

$$\begin{aligned} rh(r) &= \frac{1}{2\pi^2} \int_0^\infty \mathrm{d}k\, k \sin(kr)\, \widehat{h}(k) \\ &= \frac{1}{4\pi^2 i} \int_{-\infty}^\infty \mathrm{d}k\, k\, e^{ikr} \frac{\widehat{c}(k)}{1 - \rho_b \widehat{c}(k)}\,, \end{aligned} \tag{2.115}$$

where $\rho_b = N/V$ is the number density of the fluid and $\widehat{c}(k)$ is the Fourier transform of the bulk pair direct correlation function $c(r)$. Note that the second equation holds only if $\widehat{c}(k)$ is an even function; this is the case for exponentially or faster decaying pair potentials or pair potentials of finite range. If the pair potential decays as a power law, as is the case for dispersion interactions, there are complications [127]. In this paper, we restrict consideration to short-ranged interactions.

The right-hand side of Eq. (2.115) can be evaluated by performing a contour integration in the upper half-plane and applying the residue theorem. Provided that all poles of $\widehat{h}(k)$ in the complex plane are simple, it follows that

$$rh(r) = \sum_n e^{ik_n r} A_n\,, \tag{2.116}$$

where k_n is the n-th pole satisfying $1 - \rho_b \widehat{c}(k_n) = 0$, and $2\pi A_n$ is the residue of $k\widehat{c}(k)/(1 - \rho_b \widehat{c}(k))$ at $k = k_n$. Clearly, the pole with the smallest imaginary part determines the asymptotic decay. We term this the leading pole. If this pole is complex it will occur as a conjugate pair: $k_n = \pm\alpha_1 + i\alpha_0^{\mathrm{osc}}$ and the ultimate decay takes the form

$$rh(r) \sim \exp(-\alpha_0^{\mathrm{osc}}\, r) \cos(\alpha_1\, r - \theta)\,, \quad r \to \infty\,, \tag{2.117}$$

where θ is a phase [128, 129]. On the other hand, the leading pole may be purely imaginary: $k = i\alpha_0^{\mathrm{mon}}$ and $\alpha_1 = 0$. Then $rh(r)$ vanishes purely exponentially for $r \to \infty$, i.e.

$$rh(r) \sim \exp(-\alpha_0^{\mathrm{mon}} r)\,, \quad r \to \infty\,. \tag{2.118}$$

In some (approximate) theories one finds leading poles with $\alpha_0^{\mathrm{osc}} = 0$ and $\alpha_1 > 0$, corresponding to pure oscillatory decay of $r\,h(r)$. These point to an instability of

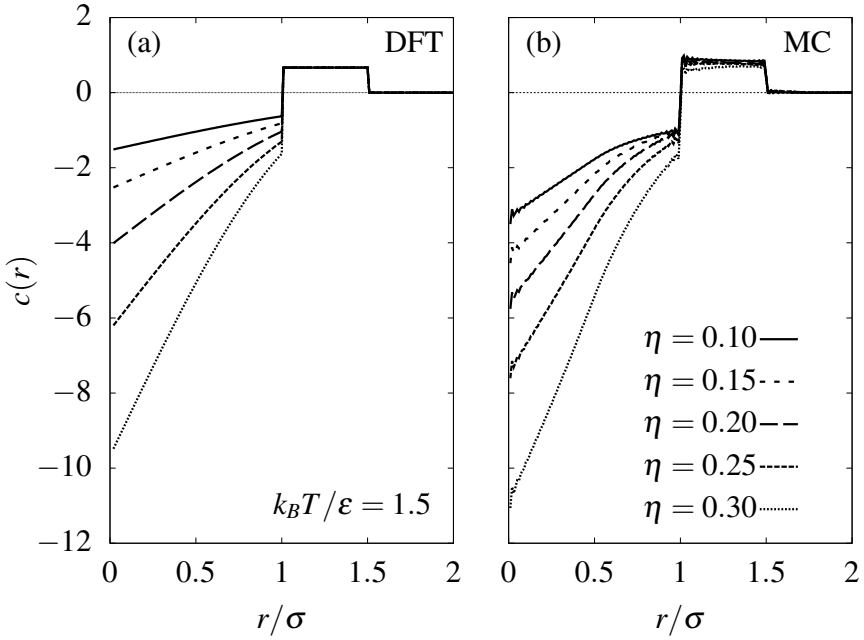

Figure 2.4 The bulk pair direct correlation function $c(r)$ of the square-well fluid with diameter σ and well-width 0.5σ ($\lambda = 1.5$ or $\delta = 0.5$) obtained from (a) mean-field density functional theory and (b) Monte-Carlo simulations for fixed reduced temperature $k_BT/\varepsilon = 1.5$ and packing fractions $\eta = 0.1 - 0.3$. Note that mean-field DFT gives rise to the random phase approximation (RPA) (2.52).

the uniform fluid with respect to density modulations [132, 133]. The FW line is the boundary in the phase diagram where pure exponential ($\alpha_1 \equiv 0$) and damped oscillatory solutions have the same imaginary part, i.e. $\alpha_0^{\rm mon} = \alpha_0^{\rm osc}$.

For several models and theories $\widehat{c}(k)$ is known analytically so poles of $\widehat{h}(k)$ can be calculated directly. However, in many cases $c(r)$ is only available numerically. Poles can be found by equating real and imaginary parts in the solution to $1 - \rho_b\widehat{c}(k) = 0$. One obtains the following coupled equations [128, 129]

$$1 = 4\pi\rho_b \int_0^\infty {\rm d}r\, r^2 c(r) \frac{\sinh(\alpha_0 r)}{\alpha_0 r} \cos(\alpha_1 r)\,, \tag{2.119}$$

$$1 = 4\pi\rho_b \int_0^\infty {\rm d}r\, r^2 c(r) \cosh(\alpha_0 r) \frac{\sin(\alpha_1 r)}{\alpha_1 r}\,. \tag{2.120}$$

These equations can be solved numerically to find α_0 and α_1 for the leading pole at a given state point, provided that the inputted $c(r)$ decays sufficiently quickly to zero so that the integrals converge – this is typically the case for interparticle potentials decaying faster than a power law. The leading pure imaginary pole can be found from Eq. (2.119) alone with $\alpha_1 = 0$. From Eqs. (2.117) and (2.118) we see that $(\alpha_0^{\rm mon})^{-1}$ is precisely the (true) correlation length ξ of the fluid. The liquid-gas spinodal corresponds to solutions of Eqs. (2.119) and (2.120) with $\alpha_1 = \alpha_0 = 0$ and the FW line is bounded by the liquid spinodal [128].

It is evident from Eqs. (2.119) and (2.120) that the location of imaginary poles relative to the complex ones is controlled by the form of the bulk direct correlation

function $c(r)$. Typically, in simple fluids, $c(r)$ exhibits a negative repulsive core region for $r < \sigma$, the atomic diameter, arising from repulsive packing effects, and a positive contribution for $r > \sigma$, where the pair potential $\phi(r)$ is attractive [57]. It follows that the asymptotic decay of correlations in a fluid is determined by the competition between repulsive and attractive interactions. For illustration, in Fig. 2.4 we plot $c(r)$ for a square-well fluid as obtained from (a) standard mean-field density functional theory [16, 57, 134] description (more details will be given in Sec. 2.4.3) and (b) MC simulations. In order to extract $c(r)$ from simulation we followed the method described in Ref. 135. The reduced temperature $T^* = k_B T/\varepsilon = 1.5$ is fixed well above the critical temperature T_c^*, and the packing fraction is η is varied. There is good qualitative agreement between theory and simulations: As observed in Ref. 135 for a truncated and shifted Lennard-Jones fluid, the attractive tail of $c(r)$ is not very sensitive to the packing fraction but the core contribution becomes more negative with increasing particle density. Recall [57] that, away from the critical point, $c(r) = -\beta\phi(r)$, $r \to \infty$. The simulation results in Fig. 2.4 (b) show that this asymptotic result remains rather accurate[5] down to the core diameter σ. In Fig. 2.5 we show the asymptotic decay of $h(r)$ from MC for the same state points as in Fig. 2.4. For $\eta = 0.10$ and 0.15 $rh(r)$ decays monotonically at large r/σ, consistent with a leading pure imaginary pole. For $\eta = 0.25$ the decay is exponentially damped oscillatory, consistent with a leading conjugate pair of complex poles. The results for $\eta = 0.20$ also point to oscillatory asymptotic decay but this state point lies close to the FW crossover from pure exponential to damped oscillatory decay – see Sec. 2.4.3. Which pole is leading is governed by competition between interparticle attraction and repulsion. However, it is not easy to glean from Eqs. (2.119) and (2.120) what *physical* criterion determines the location of the FW line. In the next section we seek such a criterion for the crossover.

2.4.2 Interparticle forces and isothermal compressibility

An insightful paper by Widom [6] noted that the isothermal compressibility χ_T can provide a qualitative measure for the overall balance of repulsive and attractive particle interactions in a fluid. We augment his arguments. Recall that χ_T is related directly [57] to $h(r)$ via the relation

$$\rho_b k_B T \chi_T = \left(\frac{\partial \beta p}{\partial \rho_b}\right)_T^{-1} = 1 + 4\pi\rho_b \int_0^\infty \mathrm{d}r\, r^2 h(r)\,, \tag{2.121}$$

where $\beta = 1/(k_B T)$ denotes the inverse temperature. Suppose that we are close to the critical point so that pressure gradients $(\partial p/\partial \rho_b)_T$ become very small. Then χ_T is very large, i.e. $\chi_T/\chi_T^{\mathrm{id}} \gg 1$, where $\chi_T^{\mathrm{id}} = (\rho_b k_B T)^{-1}$ is the compressibility of the ideal gas. Such behavior can occur only if $h(r)$ decays monotonically, from above, at large r with a long decay length. Asymptotic decay described by Eq. (2.118) with a positive amplitude, meets this requirement when the correlation length $\xi \equiv (\alpha_0^{\mathrm{mon}})^{-1}$ is large.

[5] We found similar good agreement with the asymptotic result in MC simulations for smaller values of the width of the square-well, i.e. $c(r)$ retains the shape and variation with η as displayed in Fig. 2.4.

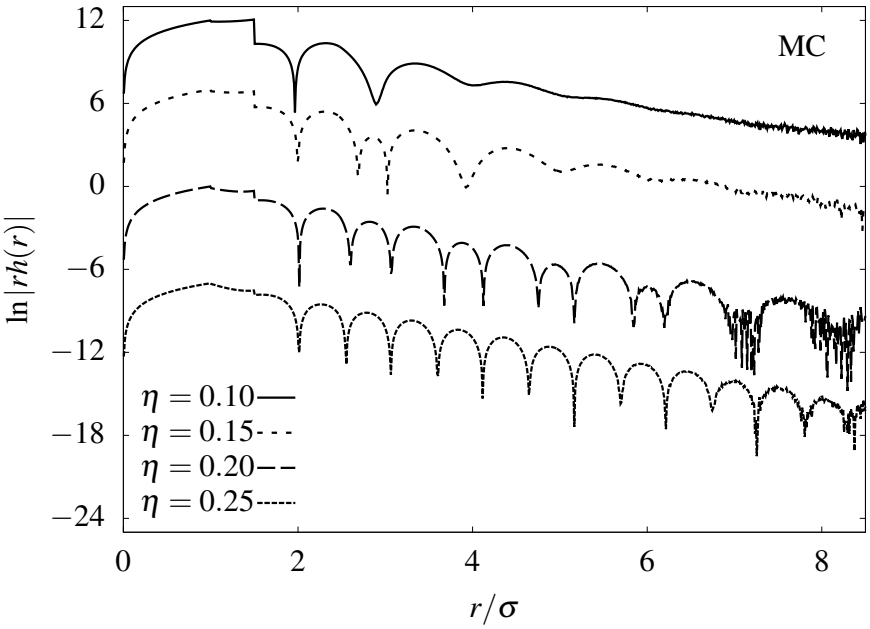

Figure 2.5 Asymptotic decay of the total correlation function $h(r)$ for the square-well fluid with $\lambda = 1.5$, and fixed $k_BT/\varepsilon = 1.5$ as obtained from MC simulations for the same state points as in Fig. 2.4 apart from $\eta = 0.30$. Fisher-Widom (FW) crossover from monotonic to damped oscillatory decay occurs at roughly $\eta \approx 0.2$. The curves have been shifted vertically for clarity.

The divergence of χ_T at the critical point, driven by a diverging correlation length $\xi \to \infty$, requires sufficiently strong attractive interactions so that Eq. (2.118) is valid, i.e. the critical point must lie on the monotonic side of the FW line.

At higher densities or temperatures, where repulsive interactions dominate, χ_T may fall well below $\chi_T^{\rm id}$. Such behavior can occur if $h(r)$ is oscillatory, as in Eq. (2.117), so that the integral in Eq. (2.121) is negative. For mechanical stability, χ_T must always be positive. Such observations suggest a crossover from monotonic to damped oscillatory decay of $h(r)$ might be reflected in the behavior of the thermodynamic quantity $\chi_T/\chi_T^{\rm id}$ across the phase diagram.

We explore this possibility, focusing on the excess, over ideal, compressibility defined by

$$\chi_T \equiv \chi_T^{\rm id} + \chi_T^{\rm ex}\,, \tag{2.122}$$

and argue that the line in the phase diagram where $\chi_T^{\rm ex} = 0$ should lie near the FW line for simple liquids. Recall that the relative location of the poles is controlled by the form of $c(r)$ (see discussion in Sec. 2.4.1). A pure imaginary pole, $q = i\alpha_0^{\rm mon}$, is determined by Eq. (2.119) with $\alpha_1 = 0$:

$$1 = 4\pi\rho_b \int_0^\infty {\rm d}r\, r^2 c(r) \frac{\sinh(\alpha_0^{\rm mon} r)}{\alpha_0^{\rm mon} r}\,. \tag{2.123}$$

Suppose first we are at a state point where repulsion dominates so that $c(r)$ is dominated by its negative core contribution $r < \sigma$. Then it is likely that the smallest solution $\alpha_0^{\rm mon}$ will be greater than the imaginary parts $\alpha_0^{\rm osc}$ of the complex poles obtained

from solving Eqs. (2.119) and (2.120) and therefore the ultimate decay of $h(r)$ will be damped oscillatory. This follows since the right-hand side of Eq. (2.123) must be equal to one and thus the integral is positive definite. But this can be achieved only for large values of $\alpha_0^{\rm mon}$ if $c(r)$ has only small positive contributions arising from weak attraction. In order to obtain a leading imaginary pole, the interparticle attraction must be sufficiently strong to counterbalance the negative core contributions in $c(r)$.

In this context it is useful to consider a near-critical state point where $\alpha_0^{\rm mon}$ is small. Expanding $\sinh(\alpha_0^{\rm mon} r)$ in Eq. (2.123) to second order one finds

$$(\alpha_0^{\rm mon})^2 \, \frac{2\pi}{3} \rho_b \int_0^\infty {\rm d}r \, r^4 \, c(r) = 1 - C \,, \tag{2.124}$$

with

$$C = 4\pi\rho_b \int_0^\infty {\rm d}r \, r^2 c(r) = \rho_b \widehat{c}(0) \,. \tag{2.125}$$

Recalling that the static structure factor $S(k)$ is given by [57]

$$S(k) = \frac{1}{1 - \rho_b \widehat{c}(k)} \,, \tag{2.126}$$

it follows that $1 - C = S(0)^{-1}$, which must be positive for the fluid to be stable. Thus, Eq. (2.124) has real solutions, which we denote α_{OZ}, provided the second moment of $c(r)$ is positive. This requires $c(r)$ to be sufficiently positive at large r, i.e. there must be sufficient attraction. Note that the solution of Eq. (2.124) then yields the second moment or Ornstein-Zernike (OZ) correlation length:

$$\xi_{OZ}^2 \equiv \alpha_{OZ}^{-2} = R^2 S(0) \,, \tag{2.127}$$

where $R^2 = \frac{2\pi}{3} \rho_b \int_0^\infty {\rm d}r \, r^4 c(r)$ defines the short-ranged correlation length or Debye persistence length [57] and expanding $\widehat{c}(k)$ to $\mathcal{O}(k^2)$ in Eq. (2.126) yields the celebrated OZ formula for the structure factor: $S(k) = S(0)/(1 + \xi_{OZ}^2 k^2)$, $k \to 0$. By considering the Taylor expansion of $x \sinh(x)$ it is easy to show $\alpha_0^{\rm mon} < \alpha_{OZ}$, i.e. the true correlation length ξ, obtained from Eq. (2.123), is larger than the OZ one, obtained from Eq. (2.124): $\xi > \xi_{OZ}$.

These considerations point to the importance of having a positive second moment of $c(r)$ in order to obtain monotonic decay of $h(r)$ with a long correlation length. By contrast, for a model fluid that exhibits purely repulsive interactions, such as hard-spheres, $c(r)$ is negative apart from a very weak, rapidly decaying tail outside the hard core, so that both the second and first moments of $c(r)$ are negative. Then the only poles are complex, $\alpha_1 > 0$, and are determined by solving Eqs. (2.119) and (2.120).

For a model fluid that exhibits, both repulsive and attractive interactions, it is clear that the first moment Eq. (2.125) at a given state point provides a measure of the competition between repulsive and attractive contributions to $c(r)$. C will be positive when attraction dominates but negative when repulsion dominates. From plots such as

those in Fig. 2.4 for $c(r)$ in the SW fluid one can surmise that C changes from positive values at low packing fractions η to negative values at large η. And we know from Fig. 2.5 that FW crossover occurs at an intermediate η. We conjecture that generally the change of sign of C should reflect the change from monotonic to damped oscillatory decay of $h(r)$. Since the criterion $C = 0$ corresponds to $S(0) = 1$, see Eq. (2.126), this implies FW crossover should occur when the $k = 0$ limit of the structure factor is near the ideal gas value. Using the compressibility sum rule [57] $S(0) = \rho_b k_B T \chi_T$, identical to (2.121), it follows that the line defined by $C = 0$ corresponds to the line of vanishing excess compressibility: $\chi_T^{\rm ex} = 0$. From the arguments above it is clear that this line cannot be identical to the FW line, defined by equality of asymptotic decay lengths, i.e. $(\alpha_0^{\rm osc})^{-1} = (\alpha_0^{\rm mon})^{-1}$ but we conjecture the lines will be close.

In the next section, we examine how close these two lines are for the square-well fluid. To this end, we employ classical density functional theory, which is a powerful framework to describe structure and thermodynamics on equal footing. In Ref. 136 we furthermore investigate the hard-core Yukawa fluid, the sticky hard-sphere fluid, and the Asakura-Oosawa model [28, 137].

2.4.3 Results for the square-well fluid

We consider the square-well (SW) fluid which is the crudest model system for describing simple fluids such as argon. The pair interaction potential $\phi(r)$ is given by

$$\phi(r) = \begin{cases} \infty & ;\ r < \sigma \\ -\varepsilon & ;\ \sigma < r < \lambda\sigma \\ 0 & ;\ r > \lambda\sigma\,, \end{cases} \tag{2.128}$$

where ε is the strength of the attraction which acts in the range $\sigma < r < \lambda\sigma$. We describe the model fluid via the standard mean-field (MF) approach [57, 134], i.e.

$$\mathcal{F}_{\rm ex}[\rho] = \mathcal{F}_{\rm ex}^{\rm HS}[\rho] + \frac{1}{2}\iint {\rm d}\mathbf{r}\,{\rm d}\mathbf{r}'\rho(\mathbf{r})\rho(\mathbf{r}')\phi_{\rm att}^{\rm SW}(|\mathbf{r}-\mathbf{r}'|)\,, \tag{2.129}$$

where $\phi_{\rm att}^{\rm SW}(r)$ denotes the attractive portion of the SW pair potential. Of course, there is flexibility in defining this. Here we split the total pair potential $\phi(r) = \phi_{\rm HS}(r) + \phi_{\rm att}^{\rm SW}(r)$ into the hard-sphere contribution and an attractive tail given by:

$$\phi_{\rm HS}(r) = \begin{cases} \infty & ;\ r < \sigma \\ 0 & ;\ r > \sigma\,, \end{cases} \qquad ; \qquad \phi_{\rm att}^{\rm SW}(r) = \begin{cases} -\varepsilon & ;\ r < \lambda\sigma \\ 0 & ;\ r > \lambda\sigma\,. \end{cases} \tag{2.130}$$

Extending the attraction to inside the core compensates underestimation of correlations. For the hard-sphere part of the excess free-energy functional, $\mathcal{F}_{\rm ex}^{\rm HS}[\rho]$, we employ the accurate White-Bear Mark 2 functional [114]. For illustration, in Fig. 2.6 we show $g(r)$ for several packing fractions $\eta = 0.10$ (a), 0.20 (b), 0.30 (c) and 0.40 (d) and compare to results from MC simulations (green symbols). Within the range of attraction, the

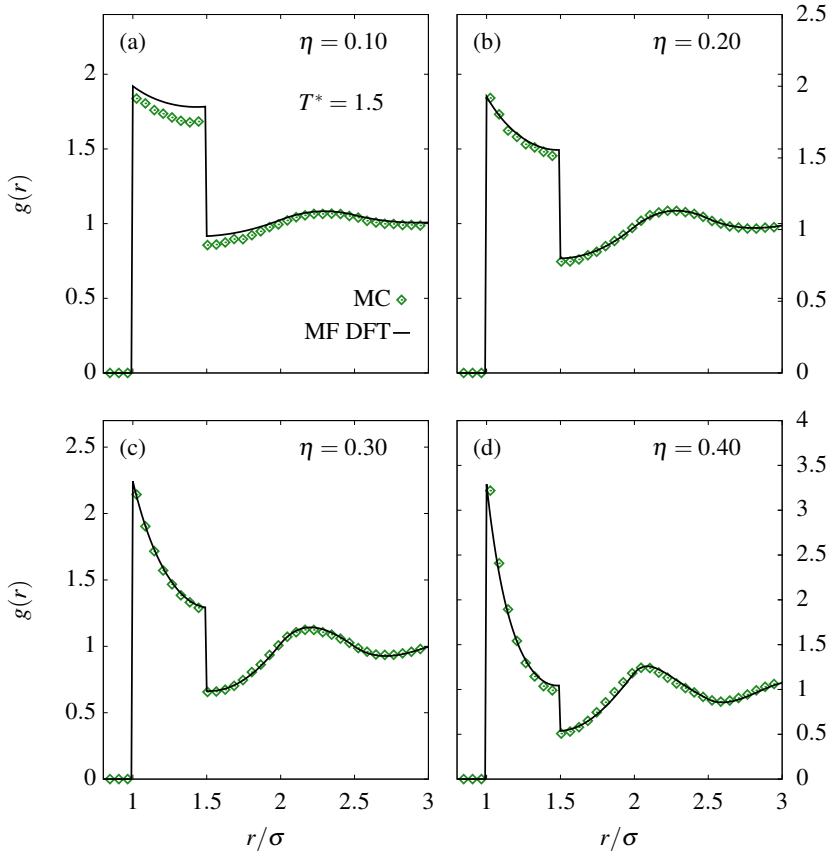

Figure 2.6 Radial distribution function $g(r)$ of the square-well fluid with $\lambda = 1.5$ for $\eta = 0.10$ (a), 0.20 (b), 0.30 (c) and 0.40 (d) as obtained from mean-field DFT (black solid lines) and simulation (green symbols). The reduced temperature is $T^* = 1.5$.

density profiles exhibit a correlation peak in which the probability of finding a particle is increased. For a low density $\eta = 0.10$ some clear differences between DFT and simulation can be seen, which at first glance might seem surprising. However considering that the critical point and phase diagrams predicted by DFT differ from the respective quantities obtained from MC simulations [138], we may conclude that these deviations are likely to be expect. They are observed to vanish in denser fluids. Especially for $\eta = 0.30$ the overall agreement between simulation and DFT is remarkably well given the simplicity of the MF description.

For bulk (uniform) fluids, with a constant bulk density ρ_b, Eq. (2.129) yields to the excess free energy density

$$\beta f_{\text{ex}} = \frac{\beta \mathcal{F}_{\text{ex}}[\rho_b]}{V} = \rho_b \frac{4\eta - 3\eta^2}{(1-\eta)^2} + \frac{1}{2}\rho_b^2 \, \beta \widehat{\phi}_{\text{sw}}(0) \,, \tag{2.131}$$

where $\eta = \pi\sigma^3\rho_b/6$ is the fluid packing fraction, and $\widehat{\phi}^{\text{sw}}_{\text{att}}(0) = 4\pi \int_0^\infty \mathrm{d}r \, r^2 \phi^{\text{sw}}_{\text{att}}(r)$ is the $k = 0$ limit of

$$\widehat{\phi}^{\text{sw}}_{\text{att}}(k) = -\frac{4\pi\varepsilon}{k^3} \left[\sin(\lambda\sigma k) - \lambda\sigma k \, \cos(\lambda\sigma k)\right] \,, \tag{2.132}$$

the three-dimensional Fourier transform of the pair potential $\phi_{\rm att}^{\rm sw}(r)$. The pressure of the SW fluid is then given by the generalized van der Waals form

$$\beta p = \rho_b \frac{1+\eta+\eta^2-\eta^3}{(1-\eta)^3} - 4\beta\varepsilon\rho_b\eta\lambda^3\,, \tag{2.133}$$

where the first term is the accurate Carnahan-Starling (CS) reduced pressure of hard-spheres. The isothermal compressibility χ_T is easily calculated using Eq. (2.121). The condition $\chi_T^{\rm ex}=0$ is equivalent to $\rho_b k_B T\chi_T = 1$, which is identical to

$$\frac{\partial\beta p}{\partial\rho_b} = 1 \quad \Leftrightarrow \quad \beta\varepsilon\lambda^3 = \frac{1-\frac{\eta}{4}}{(1-\eta)^4}\,. \tag{2.134}$$

Thus, for the SW model treated in mean-field DFT, the line where the isothermal compressibility takes its ideal gas value is described by a simple formula. The form of Eq. (2.134) is a direct result of the simple generalized van der Waals equation of state (2.133), where the attractive contribution to the pressure is proportional to ρ_b^2. If we consider a general form $\phi_{\rm att}(r)$ for the attractive potential in Eq. (2.129) the condition $\chi_T^{\rm ex}=0$ reduces to

$$-\beta\widehat{\phi}_{\rm att}(0)\sigma^{-3} = \frac{4\pi}{3}\frac{1-\frac{\eta}{4}}{(1-\eta)^4}\,, \tag{2.135}$$

with $\widehat{\phi}_{\rm att}(0) = 4\pi\int_0^\infty {\rm d}r\, r^2\phi_{\rm att}(r)$.

It is clear that determining this line is much simpler than calculating the FW line where the leading poles of $\widehat{h}(k)$ must be determined. The former is determined by a thermodynamic criterion, i.e. only the bulk free energy density is required. By contrast, and as discussed in Sec. 2.4.1, the FW line is determined by the bulk correlation function $c(r)$ that must be provided by the underlying microscopic theory. Within the framework of DFT, $c(r)$ can be obtained by functional differentiation of the (approximate) excess free-energy functional $\mathcal{F}_{\rm ex}[\rho]$:

$$c(\eta\,;\,r) = -\left.\frac{\delta^2\beta\mathcal{F}_{\rm ex}[\rho]}{\delta\rho(\mathbf{r})\delta\rho(\mathbf{r}')}\right|_{\rho_b}\,. \tag{2.136}$$

For the MF DFT (2.129), $c(r)$ reduces to the (corrected) RPA (cf. Sec. 2.1.4):

$$c(\eta\,;\,r) = c_{\rm HS}(\eta\,;\,r) - \beta\phi_{\rm att}^{\rm sw}(r)\,, \tag{2.137}$$

where $c_{\rm HS}(r)$, obtained from White-Bear Mark II, is a third-order polynomial of r with range σ, depending on the packing fraction η and the hard-sphere diameter σ. Results for $c(r)$ from this mean-field DFT are shown in Fig. 2.4 (a).

In Fig. 2.7 we plot the phase diagram for the SW fluid with $\lambda = 1.5$ in the $T^*-\eta$ plane where $T^* = k_BT/\varepsilon$, also recently considered by Roth in Ref. [139]. The critical point is located at $(\eta_c, T_c^*) = (0.13, 1.27)$. The solid line shows the binodal, where the gas and liquid coexist. The fine dotted line below the binodal is the spinodal, which is most easily determined by searching for solutions where the isothermal compressibility

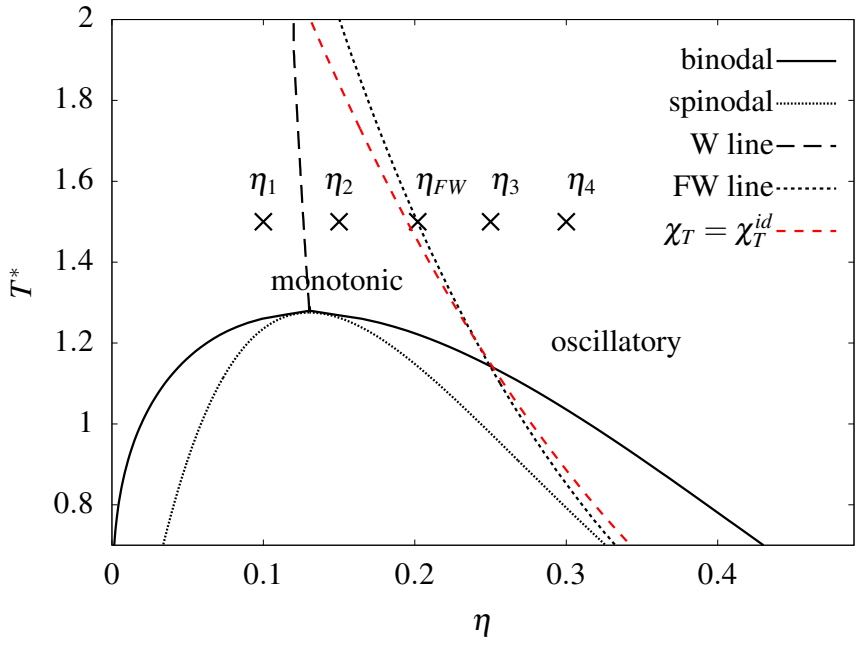

Figure 2.7 The phase diagram of the square-well fluid with $\lambda = 1.5$ treated within mean-field DFT fashion in the $T^* - \eta$ plane. The solid line shows the binodal, and the fine dotted line below the binodal is the spinodal. The long-dashed line terminating at the critical point black square $(\eta_c, T_c^*) = (0.13, 1.27)$ is the Widom line, i.e. the line of local maximal correlation length $\xi = \alpha_0^{-1}$. The short dashed-line is the Fisher-Widom line separating regions of monotonic and oscillatory decay, and the medium-dashed line is where $\chi_T = \chi_T^{\mathrm{id}}$. The crosses labeled η_1, η_2, η_3, η_4, and η_{FW} denote state points considered in this work.

diverges. The Fisher-Widom line is the short-dashed line, which is bounded by the spinodal at low T^*. This follows since the spinodal can also be defined as the solutions of Eq. (2.119) with $\alpha_0 = 0$, corresponding to $1 - \rho_b \widehat{c}(0) = 0$. On the low density side of the FW line, correlations decay purely monotonically (where $\alpha_1 = 0$), whereas on the high density side the decay is damped oscillatory. The FW line is determined numerically by searching for solutions of $1 - \rho_b \widehat{c}(k) = 0$ where complex poles and imaginary poles have the same (smallest) imaginary part, $\alpha_0^{\mathrm{mon}} = \alpha_0^{\mathrm{osc}}$. The long-dashed line in Fig. 2.7 emanating almost vertically from the critical point is the Widom (W) line, which we defined as the line of a local maximum of the true correlation length ξ, corresponding to a minimum of α_0. At higher temperatures, the W line approaches the FW line.

Strikingly, the line where χ_T^{ex} vanishes (medium dashed-line) is rather close to the FW line. At higher temperatures the deviations become larger, but in the important region approaching coexistence these are fairly small. In particular, there is no systematic offset between the FW line and the line where $\chi_T^{\mathrm{ex}} = 0$. This means that at state points where $c(r)$ has sufficient positive (attractive) contributions such that the integral in Eq. (2.125) vanishes, we are likely to find FW crossover in close proximity to the $\chi_T^{\mathrm{ex}} = 0$ criterion. Fig. 2.7 indicates nicely how the FW line is bounded by the liquid spinodal [128]. It is obvious from Sec. 2.4.2 that the line $\chi_T = \chi_T^{\mathrm{id}}$ must lie

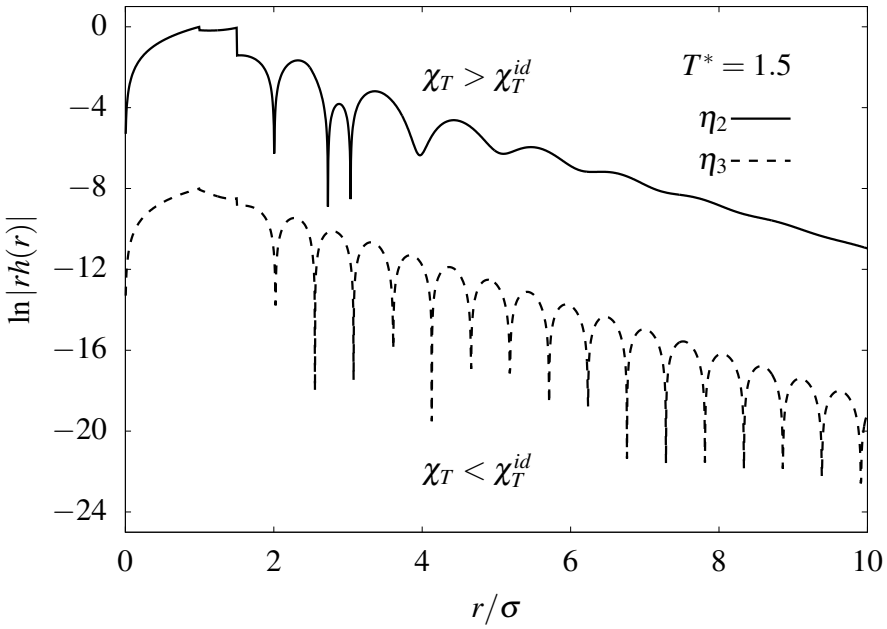

Figure 2.8 Asymptotic decay of $h(r)$ for the SW fluid, as obtained from MF DFT by minimizing the grand-potential functional in the presence of a test particle. The curves are shifted vertically for clarity. The state points, both at temperature $T^* = 1.5$, are located on the monotonic side of the FW line ($\eta_2 = 0.15$; upper curve), and the oscillatory side of the FW line ($\eta_3 = 0.25$; bottom curve).

outside the spinodal, i.e. at larger η, and we observe it also lies outside the FW line at low T^*.

In Fig. 2.8 we plot the asymptotic decay of $h(r)$ as obtained from numerically minimizing the grand-potential functional in presence of a test particle – the Percus' test-particle procedure [57]. This corresponds to fixing a particle at the origin so that it exerts an external potential $V_{\text{ext}}(r) = \phi(r)$, the pair interaction potential, on other particles. Then the one-body density profile satisfies $\rho(\mathbf{r}) = \rho(r) = \rho_b g(r)$, with $g(r) = h(r) + 1$. It is important to recognize that the inverse decay length and the wavelength that can be extracted from the decay of (test particle) plots such as Fig. 2.8 correspond precisely to α_0 and $2\pi/\alpha_1$ determined by calculating the poles of $\widehat{h}(k)$ or zeros of $1 - \rho_b \widehat{c}(k)$ with $\widehat{c}(k)$ from Eq. (2.137), usually termed the OZ route. The equivalence between the test particle and OZ routes for asymptotic decay is discussed in a recent paper [140], and is based on linear response arguments [141]. We consider two state points, marked as crosses in Fig. 2.7, at constant temperature $T^* = 1.5$: One is located on the monotonic side of the FW line at volume fraction $\eta_1 = 0.15$, and the other on the oscillatory side of the FW line at $\eta_2 = 0.25$. As found in the simulations (cf. Fig. 2.5), we observe a crossover from monotonic to damped oscillatory decay as η is increased. Calculating $h(r)$ precisely at the point where FW crossover occurs, i.e. where both types of poles (complex and imaginary) contribute to the decay for $r \to \infty$, we find that $h(r)$ decays overall in a damped oscillatory fashion. At FW crossover

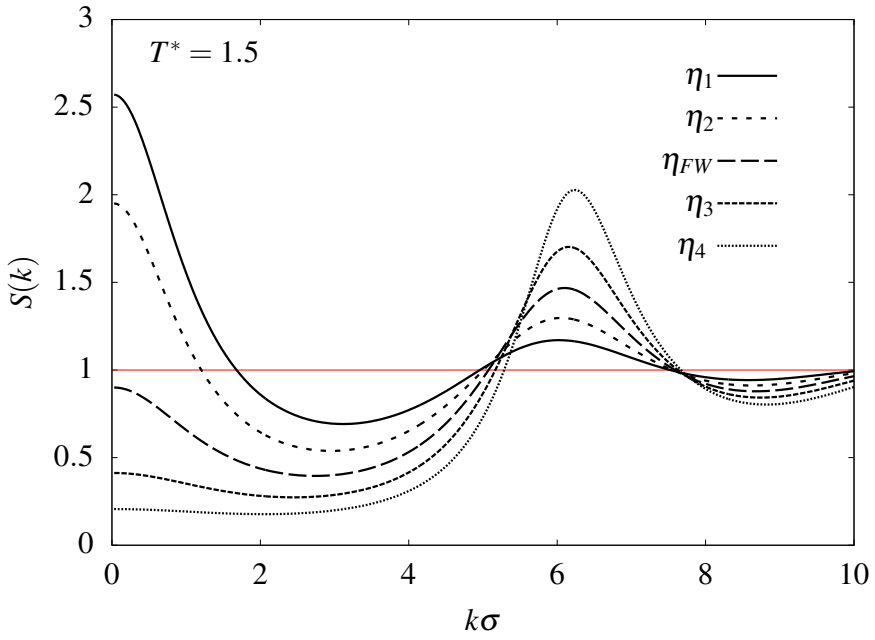

Figure 2.9 Static structure factor $S(k) = [1 - \rho_b \widehat{c}(k)]^{-1}$ of the SW fluid within MF DFT for the state points (crosses) shown in Fig. 2.7 with fixed temperature $T^* = 1.5$.

$r\,h(r)$ decays as

$$\begin{aligned} rh(r) \sim\; & A_{\text{mon}} \exp(-\alpha_0^{\text{mon}}\, r) \\ & + A_{\text{osc}} \exp(-\alpha_0^{\text{osc}}\, r) \cos(\alpha_1\, r - \theta)\,, \quad r \to \infty\,, \end{aligned} \tag{2.138}$$

where $\alpha_0^{\text{mon}} = \alpha_0^{\text{osc}}$, and A_{mon} and A_{osc} are amplitudes. Note that on the FW line one still finds damped oscillatory (non-monotonic) decay of $rh(r)$ as $r \to \infty$, regardless of the (non-zero) values of A_{mon} and A_{osc}. If $A_{\text{osc}} > A_{\text{mon}}$ then $rh(r)$ has zeros, which is not the case if $A_{\text{osc}} < A_{\text{mon}}$. At this state point, the isothermal compressibility is close to its ideal-gas value; see Fig. 2.7. This is also demonstrated in Fig. 2.9 where the static structure factor $S(k)$ is plotted for the five state points shown in Fig. 2.7. We use the OZ route, i.e. $S(k)$ is given by Eq. (2.126). Within this framework, $S(k)$ can be computed analytically. On the monotonic side of the FW line (packings η_1 and η_2) the value of $S(k=0) = \chi_T/\chi_T^{\text{id}}$ is substantially greater than unity. At high packing fractions (η_3 and η_4), $S(k=0) < 1$, and decreases rapidly with increasing η, reflecting the rapid decrease of χ_T. For $\eta = \eta_{FW}$ we find $S(k=0)$ is close to unity. Note that the position and the height of the maximum of $S(k)$ increases smoothly with increasing η.

Chapter 3

Bulk Theory for Patchy Particles

3.1 The Kern-Frenkel model

Consider a system consisting of hard spheres with diameter σ, supplemented with a specific number M of identical attractive sites on their surfaces. A sketch of patchy particles with three and four interaction sites is shown in Figs. 3.1 (a) and (b). The pair potential between two patchy particles, 1 and 2, may be described by the Kern-Frenkel (KF) model [44, 142]. It is composed of two contributions

$$\phi(\mathbf{r}_{12},\, \varpi_1,\, \varpi_2) = \phi_{\mathrm{HS}}(|\mathbf{r}_{12}|) + \phi_{\mathrm{bond}}(\mathbf{r}_{12},\, \varpi_1,\, \varpi_2)\,, \tag{3.1}$$

the usual hard-sphere interaction (1.6) and a bonding potential $\phi_{\mathrm{bond}}(\mathbf{r}_{12},\, \varpi_1,\, \varpi_2)$, where ϖ_i denotes an individual orientation vector of particle with label i. The total interaction energy of the system is given by

$$U = \Phi(\mathbf{r}_1, ..., \mathbf{r}_N, \varpi_1, ..., \varpi_N) = \frac{1}{2}\sum_{i=1}^{N}\sum_{j\neq i}^{N} \phi(\mathbf{r}_{ij},\, \varpi_i,\, \varpi_j)\,. \tag{3.2}$$

The bonding potential $\phi_{\mathrm{bond}}(\mathbf{r}_{12},\, \varpi_1,\, \varpi_2)$ between particles 1 and 2 can be written as

$$\phi_{\mathrm{bond}}(\mathbf{r}_{12},\, \varpi_1,\, \varpi_2) = \sum_{\alpha=1}^{M}\sum_{\beta=1}^{M} \phi_{\mathrm{patch}}\left(\mathbf{r}_{12},\, \hat{\mathbf{r}}_1^{\alpha}(\varpi_1),\, \hat{\mathbf{r}}_2^{\beta}(\varpi_2)\right)\,, \tag{3.3}$$

where ϕ_{patch} describes the interaction between a patch α on particle 1 and some patch β on particle 2. In the KF model, the patch-patch interaction is decomposed into a product of a spherically-symmetric attractive potential $\phi_{\mathrm{att}}(r)$ and a function $G(\hat{\mathbf{r}}_{12},\, \hat{\mathbf{r}}_1^{\alpha}(\varpi_1),\, \hat{\mathbf{r}}_2^{\beta}(\varpi_2))$ containing the orientational character of the interaction. If the attraction is described by a square-well potential we have

$$\phi_{\mathrm{att}}^{\mathrm{SW}}(r) = \begin{cases} -\varepsilon & \text{if } \ \sigma < r < \sigma(1+\delta) \\ 0 & \text{otherwise}\,, \end{cases} \tag{3.4}$$

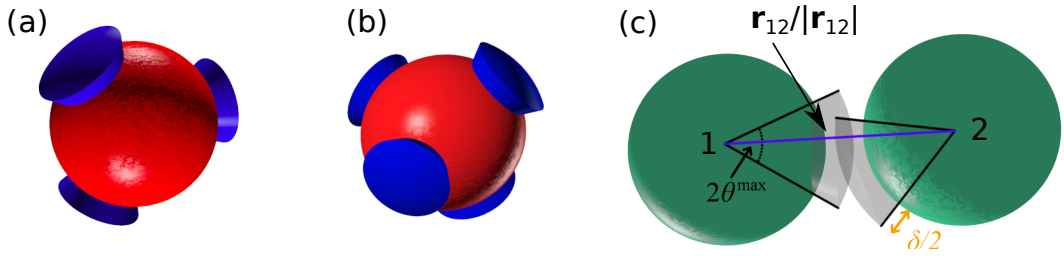

Figure 3.1 Sketch of a patchy particle with three (a) and four (b) patches (blue cones). (c) Illustration of the Kern-Frenkel pair potential (3.1) with a square-well attraction between the patches of range δ. A bond is formed between particles 1 and 2 if two patches with opening angle $2\Theta_{\max}$ overlap. The blue line indicates the center-to-center unit vector between particles 1 and 2. Right image adapted and modified from Rovigatti *et al.* Eur. Phys. J. E **41**, 59 (2018).

where the parameter δ controls the range of the attraction, and ε is the potential depth, as in Eq. (1.8). Throughout this thesis we assume both quantities to be identical for all patches. The orientational character of the patch-patch interaction is given by [44]

$$G(\hat{\mathbf{r}}_{12},\, \hat{\mathbf{r}}_1^{\alpha}(\varpi_1),\, \hat{\mathbf{r}}_2^{\beta}(\varpi_2)) = \begin{cases} 1 & \text{if } \begin{cases} \hat{\mathbf{r}}\cdot\hat{\mathbf{r}}_1^{\alpha} > \cos(\theta^{\max})\,, \\ -\hat{\mathbf{r}}\cdot\hat{\mathbf{r}}_2^{\beta} > \cos(\theta^{\max})\,, \end{cases} \\ 0 & \text{else}\quad , \end{cases} \tag{3.5}$$

where $\hat{\mathbf{r}}_{12} = \mathbf{r}_{12}/|\mathbf{r}_{12}|$ denotes the center-to-center unit vector between particles 1 and 2, and $\hat{\mathbf{r}}_i^{\alpha}$ is a unit vector from the center of particle i to a patch α on its surface depending on the individual orientation ϖ_i. Hence, the product of ϕ_{SW} and G defines interactions between particles such that it is attractive only if two patches are within a small distance and are orientated to each other properly, depending on the patch opening angle $\theta^{\max}$. This is illustrated in Fig. 3.1 (c).

Note that the KF pair potential can readily be generalized to describe distinct types of patches. Of course, there is more than one possibility to define a pair potential describing patchy-type interaction; see e.g. the work 'How to simulate patchy particles' by Rovigatti *et al.* [142] for a general discussion. We also mention the floating-bond model [143, 144] which generates patchy-type interactions via a non-additive binary mixture of particles, where the individual pair potentials are spherically-symmetric.

3.2 Wertheim's theory for associating particles

In Sec. 2.1.4 of Ch. 2 we have outlined conventional schemes for deriving approximate theories describing bulk structural and thermodynamic properties of simple fluids (i.e. particles that interact via a hard core and an additional isotropic attraction). The non-hard core interaction is thereby commonly treated in mean-field fashion, i.e. the excess part of the free energy of the uniform fluid is given by Eq. (2.53) or by Eq. (2.55), which empirically corrects a potential underestimation of correlations in the reference fluid. For inhomogeneous fluids, the excess free-energy functional (2.77) is

the natural analogue. These concepts are general and in principle may also be applied to non-isotropic pair interaction potentials.

The corresponding mean-field excess free energy of patchy particles interacting via the Kern-Frenkel potential (3.1) might be written as:

$$\begin{aligned}\beta f_{\mathrm{ex}} - \beta f_{\mathrm{ex}}^{\mathrm{HS}} &= \frac{1}{2}\rho_b^2 \int \mathrm{d}\mathbf{r}\ \langle \beta\phi_{\mathrm{bond}}(\mathbf{r},\varpi_1,\varpi_2)\rangle_{\varpi_1,\varpi_2} \\ &= \frac{M^2\,\rho_b^2}{2} \int \mathrm{d}\mathbf{r}\,\beta\phi_{\mathrm{att}}^{\mathrm{SW}}(r)\,\langle G(\mathbf{r},\varpi_1,\varpi_2)\rangle_{\varpi_1,\varpi_2} \\ &= -v_b \frac{M^2\,\rho_b^2}{2}\,\beta\varepsilon\,, \end{aligned} \tag{3.6}$$

where v_b is the 'bonding volume' between two patches

$$v_b = \frac{4\pi\sigma^3}{3}\sin^4\left(\frac{\theta^{\max}}{2}\right)\left[(1+\delta)^3 - 1\right]\,, \tag{3.7}$$

and $\langle\cdots\rangle_{\varpi_1,\varpi_2}$ denotes an unbiased orientational average:

$$\langle\cdots\rangle_{\varpi_1,\varpi_2} \equiv \frac{1}{(4\pi)^2}\int \mathrm{d}\varpi_1 \int \mathrm{d}\varpi_2\ \cdots\,. \tag{3.8}$$

However, it is important to recall the genesis of mean-field type theories: in essence they embody a generalized form of van der Waal's theory where the particle attraction is incorporated making use of simple perturbation arguments about the hard-sphere (or some other reference) fluid. As such, these approaches are expected to be reliable for sufficiently weak and long-ranged perturbations or at sufficiently low particle densities (see also discussions in Secs. 2.1.4 and the last paragraph of Sec. 2.2). In particular the former is in general not satisfied in patchy fluids as the range of the interaction between the patches is typically short ($\sim 10\%$ of the hard-core diameter σ) and the interaction energy needs to be rather strong in order to promote e.g. system-spanning association and polymerization. Moreover, the fluid state differs considerable from that of fluids with isotropic pair potentials, especially at low particle densities and at low temperatures. For such state points the directionality of the site-site interaction dictates the microscopic structure and thus the phase behavior of the fluid. As a result, we would expect a reasonable theory for the patchy fluid to depend on quantities that describe a certain degree of association such as the probability to find a pair of bonded patches, or the fraction of particles engaged in a cluster (i.e., the degree of polymerization). If we consider Eq. (3.6) one readily realizes that contributions of directionality treated within standard mean-field fashion enter only in form of an additional multiplicative factor relative to the isotropic square-well case. But this merely changes the temperature or energy scale on which interactions and hence the phase behavior take place. As a result we cannot expect a crude perturbation argument, sufficient for the qualitative description of simple fluids, to succeed for fluids with highly directional interactions.

The most successful and widest applied theory for associating fluids is that of

Wertheim [73–76], which is derived within cluster graph expansions; we will not discuss the details in this thesis – the interested reader is referred to, e.g., Refs. 145, 146. The key point is that Wertheim treats different associating aggregates (monomers, dimers, in general a 's-mer') as distinct species, each with a separate number density, which is termed 'multi-density formalism'. There are several fundamental assumptions underlying Wertheim's approach: first, Wertheim considers hard-spheres decorated with attractive sites (or patches), so he chooses to employ the hard-sphere fluid as a reference system. Second, it is assumed that the site-site interaction potential allows every site to be engaged in at most one bond with another site (the *singly-bonded condition*). This can be achieved by choosing the patch-patch interaction sufficiently short-ranged an narrow (for the KF potential this is controlled by $\theta^{\max}$). A third assumption is the so-called *single-chain approximation* where monomer-monomer correlations in the associated fluid are considered to be the same as those in the reference hard-sphere system. Within the cluster graph formalism, this means that contributions where more than one ($s \geq 2$)-mer is present are neglected. The remaining graphs then contain a single ($s \geq 2$)-mer surrounded by an arbitrary number of monomers. Interestingly, Wertheim's theory is valid for inhomogeneous situations, and in fact the final expressions can be written in a density functional formalism [145, 146] as we shall see in Secs. 3.2.1 and 3.2.2.

3.2.1 Dimerizing spheres

The simplest case of an associating fluid that one may consider are dimerizing particles, i.e. particles carrying only one single interaction site. As a result, only attractive two-body interactions are possible. In this case, no more approximations then those mentioned above are needed. The final contribution due to association to the excess free energy functional is

$$\beta\mathcal{F}_{\text{ex}}[\rho] - \beta\mathcal{F}_{\text{ex}}^{\text{HS}}[\rho] = \frac{1}{4\pi}\int \mathrm{d}\mathbf{r}\,\mathrm{d}\varpi\,\rho(\mathbf{r},\varpi)\left[\ln X_0(\mathbf{r},\,\varpi) - \frac{X_0(\mathbf{r},\,\varpi)}{2} + \frac{1}{2}\right], \tag{3.9}$$

where $X_0(\mathbf{r},\varpi) = \rho_0(\mathbf{r},\varpi)/\rho(\mathbf{r},\varpi)$ is the monomer-fraction, i.e. the fraction of particles at position $\mathbf{r}$ with orientation ϖ that are *not* bonded $\rho_0(\mathbf{r},\varpi)$ relative to all particles $\rho(\mathbf{r},\varpi)$. The central result of Wertheim's theory is that X_0 is determined by the equation

$$\frac{\rho(\mathbf{r}_1,\,\varpi_1)}{\rho_0(\mathbf{r}_1,\,\varpi_1)} - 1 = \frac{1}{4\pi}\int \mathrm{d}\mathbf{r}_2\,\mathrm{d}\varpi_2\,\rho_0(\mathbf{r}_2,\varpi_2)g_{\text{HS}}(r_{12})f_{\text{patch}}(\mathbf{r}_{12},\varpi_1,\varpi_2)\,, \tag{3.10}$$

with the patch Mayer-f function $f_{\text{patch}} = e^{-\beta\phi_{\text{patch}}} - 1$. For uniform fluids, ρ and ρ_0, and thus X_0, become orientation and position independent quantities. We can then average Eq. (3.10) over orientations and after reordering we arrive at

$$X_0^2\rho_b\Delta + X_0 - 1 = 0\,, \tag{3.11}$$

where Δ is defined as [77]

$$\Delta = \int \mathrm{d}\mathbf{r}\, g_{\mathrm{HS}}(r)\, \langle \exp(-\beta\phi_{\mathrm{patch}}(\mathbf{r}, \varpi_1, \varpi_2)) - 1 \rangle_{\varpi_1,\varpi_2} \tag{3.12}$$

$$\approx v_b\, g_{\mathrm{HS}}(\sigma^+)(e^{\beta\varepsilon} - 1)\,. \tag{3.13}$$

The quantity Δ thus connects all geometrical and physical properties of the patches. The radial distribution function $g_{\mathrm{HS}}(r)$ of the hard-sphere reference system is approximated by its contact value $g_{\mathrm{HS}}(\sigma^+)$, since we consider only rather short ranged site-site interactions. We note that one may also use a more accurate linear approximation to $g(r)$ [39]. The contact value can approximated by the Carnahan-Starling expression

$$g_{\mathrm{HS}}(\sigma^+) = \frac{1 - \frac{\eta}{2}}{(1-\eta)^3}\,. \tag{3.14}$$

Equation (3.11) can be solved explicitly to give the monomer fraction

$$X_0 = \frac{-1 + \sqrt{1 + 4\rho_b\Delta}}{2\rho_b\Delta}\,. \tag{3.15}$$

This expression satisfies the limit $\lim_{\rho_b \to 0} X_0 = 1$ which is obviously correct. The bulk excess free energy density is finally given by

$$\beta f_{\mathrm{bond}} \equiv \beta f_{\mathrm{ex}} - \beta f_{\mathrm{ex}}^{\mathrm{HS}} = \rho_b \left[\ln(X_0) - \frac{X_0}{2} + \frac{1}{2} \right]\,. \tag{3.16}$$

Wertheim's theory turned out to be much more efficient than other approaches, for example the one by Anderson [52, 147]. For dimerizing fluids, Anderson's approach had led to the same expression (3.15) for the monomer fraction X_0 as Wertheim's theory a decade later, but it requires the solution of a series of complex integral equations [145]. But with his multiple-density formalism, Wertheim managed to employ to advantage in an intriguing way what had been made other theories for fluids with anisotropic interactions insufficient and cumbersome.

3.2.2 Multiple association sites

Further approximations have to be introduced for the more general case of multiple patches per particle. Clearly, for more than one site, complex structures and binding situations can occur. In addition to the singly-bonded condition and the single-chain approximation, Wertheim neglected ring-forming structures (e.g. loops), multiply bonded association sites (e.g. one site of one particle simultaneously bonded to two sites of another particle) and multiple bonds between particles. As a result, only chain and tree like clusters are considered. However, in ($s > 2$)-mers also many-body correlations between patches can play a role. The first-order contribution of Wertheim's theory (TPT1) contains all contributions describing the association between a pair of molecules, i.e. it describes two-body effects. Higher-order correlations, such as

information about the simultaneous association of three molecules, are not taken into account. It follows that TPT1 assumes bonding to occur independently at each site. Nevertheless, note that it is still possible to describe elongated networks of associated particles with these restrictions.

For M identical patches, the TPT1 contribution to the excess free energy functional due to association is

$$\beta\mathcal{F}_{\mathrm{ex}}[\rho] - \beta\mathcal{F}_{\mathrm{ex}}^{\mathrm{HS}}[\rho] = \frac{M}{4\pi}\int \mathrm{d}\mathbf{r}\,\mathrm{d}\varpi\,\rho(\mathbf{r},\varpi)\left[\ln X(\mathbf{r},\,\varpi) - \frac{X(\mathbf{r},\,\varpi)}{2} + \frac{1}{2}\right], \tag{3.17}$$

where now X is the probability that an arbitrary chosen patch on a particle at position $\mathbf{r}$ with orientation ϖ is *not* bonded (which is equivalent to the monomer fraction X_0 for $M = 1$). It is given by the self-consistent relation [145, 146]

$$X(\mathbf{r}_1,\,\varpi_1) = \left[1 + \frac{M}{4\pi}\int \mathrm{d}\mathbf{r}_2\,\mathrm{d}\varpi_2\,\rho(\mathbf{r}_2,\,\varpi_2)X(\mathbf{r}_2,\,\varpi_2)f_{\mathrm{patch}}(\mathbf{r}_{12},\varpi_1,\varpi_2)g_{\mathrm{HS}}(r_{12})\right]^{-1}. \tag{3.18}$$

The latter is equivalent to Eq. (3.10) apart from the factor M. It is important to note that Eq. (3.18) is valid only under the assumption of two-body interactions i.e. for independent bonding processes. This is why the expressions within TPT1 are independent of the geometrical locations of the patches on the particle surface. For bulk fluids, we obtain

$$X = \frac{-1 + \sqrt{1 + 4\rho_b M\Delta}}{2\rho_b M\Delta} = \frac{2}{1 + \sqrt{1 + 4M\rho_b\Delta}}, \tag{3.19}$$

where the previous definition of Δ (Eq. (3.12)) remains unchanged. X is the fraction of unbonded sites, or, equivalently, the probability that an arbitrary chosen patch is not bonded. We can therefore also introduce the bonding probability of a site as $p_b = 1 - X$. The bulk excess free energy density reads:

$$\beta f_{\mathrm{ex}} - \beta f_{\mathrm{ex}}^{\mathrm{HS}} = \rho_b M\left[\ln(X) - \frac{X}{2} + \frac{1}{2}\right] \tag{3.20}$$

$$= \rho_b M\left[\ln(1 - p_b) + \frac{p_b}{2}\right]. \tag{3.21}$$

If we describe the hard-sphere excess free energy by the accurate Carnahan-Starling expression (2.57), the total bulk free energy density of the patchy fluid may be written as

$$\beta f = \rho_b\left(\ln(\eta) - 1\right) + \rho_b\frac{\eta(4 - 3\eta)}{(1 - \eta)^2} + \rho_b M\left[\ln(X) - \frac{X}{2} + \frac{1}{2}\right]. \tag{3.22}$$

For small densities and finite temperatures, the right-hand side of Eq. (3.20) can be expanded up to the leading order in the density resulting in

$$\lim_{\rho_b\to 0}\beta f_{\mathrm{bond}} = -\frac{M^2}{2}(e^{\beta\varepsilon} - 1)v_b\rho_b^2, \tag{3.23}$$

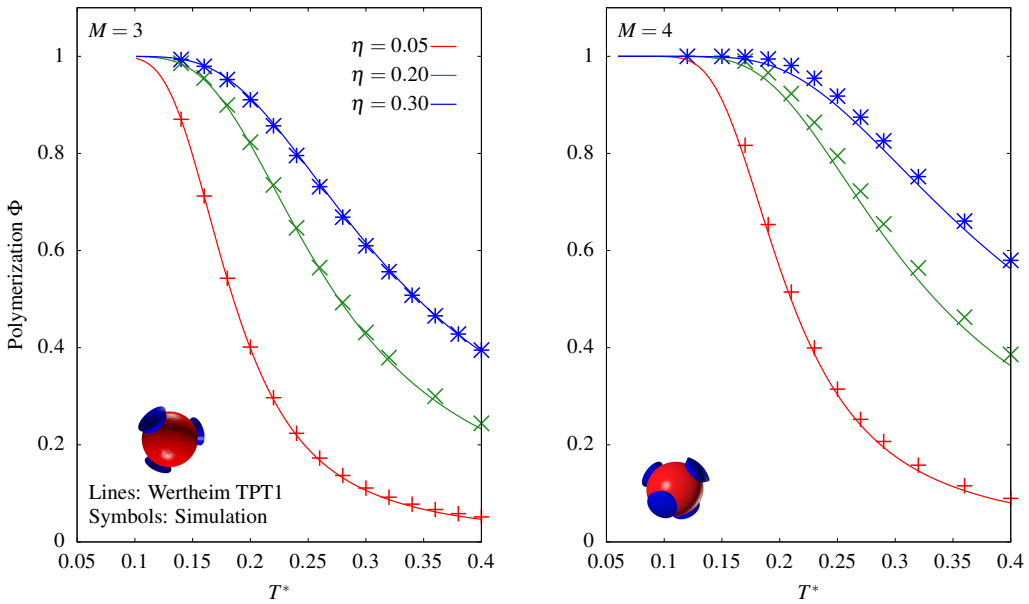

Figure 3.2 Polymerization Φ as a function of the reduced temperature $T^* = k_B T/\varepsilon$ for packing fractions $\eta = 0.05$ (red), 0.2 (green), and 0.3 (blue). Individual symbols show results from MC simulations and solid lines are predictions by TPT1. Left: three-site particles, right: four-site particles. The range of the patch-patch potential is set to $\delta = 0.119\sigma$ and the half-opening angle is fixed by $\cos(\theta^{\max}) = 0.895$.

which, at high temperatures, where $e^{\beta\varepsilon} - 1 \approx \beta\varepsilon$, is equivalent to the mean-field expression (3.6).

3.3 Cluster distributions and percolation

Wertheim's TPT1 naturally provides a framework for studying clusters and polymerization, as the underlying assumptions of the theory are equivalent [148] to those of the Flory-Stockmeyer theory [149]. In particular, the latter provides expressions for the number density ρ_n of n-particle clusters as a function of the number of patches and the bonding probability p_b. For M identical sites we have

$$\rho_n = \rho_b (1-p_b)^M \left[p_b (1-p_b)^{M-2}\right]^{n-1} \omega_n \,, \tag{3.24}$$

$$\omega_n = \frac{M(Mn-n)!}{(Mn-2n+2)!n!} \,. \tag{3.25}$$

The total bulk density satisfies $\rho_b = \sum_{n=0}^{\infty} n\rho_n$. The Flory-Stockmeyer theory provides also a measure for percolation. Recall that the latter is defined as the locus in the phase diagram where system-wide association can occur (i.e. presence of system-spanning clusters). This is related to a high probability of finding a patch engaged in a bond. However, percolation does typically not mean that the bonds forming the clusters have a long lifetime, i.e. the networks are flexible, with bonds forming and breaking frequently. If bond lifetimes become macroscopically long, i.e. on the timescale of experiments, the system forms a percolated gel state (see also discussion in Sec. 1.3). However,

Flory-Stockmeyer theory yields only a static measure for the bonding probability p_b^p at percolation (i.e. it does not include information regarding the lifetimes of bonds). It is given by:

$$p_b^p = \frac{1}{M-1}\,. \tag{3.26}$$

We can also define the degree of polymerization Φ, i.e. the probability that a particle is part of a cluster via [149, 148]

$$\Phi = 1 - (1-p_b)^M\,. \tag{3.27}$$

In Fig. 3.2 we show theoretical results for Φ as obtained from TPT1 (lines) compared to simulations (symbols) as a function of T^* for trivalent particles ($M = 3$, left) and tetravalent particles ($M = 4$, right). The packing fractions are $\eta = 0.05$ (red), 0.2 (green), and 0.3 (blue). The agreement between theory and simulation is striking given the number of underlying approximations entering TPT1. For the case of two patches, $M = 2$, the theory becomes even more accurate – see Ref. 150.

In simulations, the fractions of particles engaged in at least one bond have been accumulated for each state point. In the KF potential (3.1) we set $\delta = 0.119$ and $\cos(\theta^{\max}) = 0.895$ ensuring that the potential meets the single-bond assumption of the Wertheim theory. The simulations were performed based on open-source code [142].

3.4 Bulk phase behavior

We now focus on the bulk phase behavior of patchy fluids described within TPT1. In order to calculate binodals and spinodals, we need to determine the chemical potential $\beta\mu = \partial\beta f/\partial\rho_b$, with βf given by Eq. (3.22), as well as the pressure $p = \rho_b\mu - f$. Using Eq. (3.20) we find for the contribution to the chemical potential due to bonding μ_{bond}:

$$\beta\mu_{\text{bond}} = \frac{\partial\beta f_{\text{bond}}}{\partial\rho_b} = M\left(\ln(X) - \frac{X}{2} + \frac{1}{2}\right) + M\rho_b\left[\frac{1}{X} - \frac{1}{2}\right]\frac{\partial X}{\partial\rho_b}\,. \tag{3.28}$$

and for the pressure contribution due to bonding:

$$\beta p_{\text{bond}} = M\rho_b^2\left[\frac{1}{X} - \frac{1}{2}\right]\frac{\partial X}{\partial\rho_b}\,. \tag{3.29}$$

The change of X with respect to the density ρ_b is given by

$$\frac{\partial X}{\partial\rho_b} = \left(\Delta + \rho_b\frac{\partial\Delta}{\partial\rho_b}\right)\left[\frac{1}{\rho_b\Delta\sqrt{1+4M\rho_b\Delta}} - \frac{X}{\rho_b\Delta}\right]\,, \tag{3.30}$$

where $\partial\Delta/\partial\rho_b = v_b(e^{\beta\varepsilon}-1)g'_{\text{HS}}(\sigma^+)$ and the prime means differentiation w.r.t. the density. We find for the total pressure

$$\beta p = \rho_b\frac{1+\eta+\eta^2-\eta^3}{(1-\eta)^3} + M\rho_b^2\left[\frac{1}{X} - \frac{1}{2}\right]\frac{\partial X}{\partial\rho_b}\,, \tag{3.31}$$

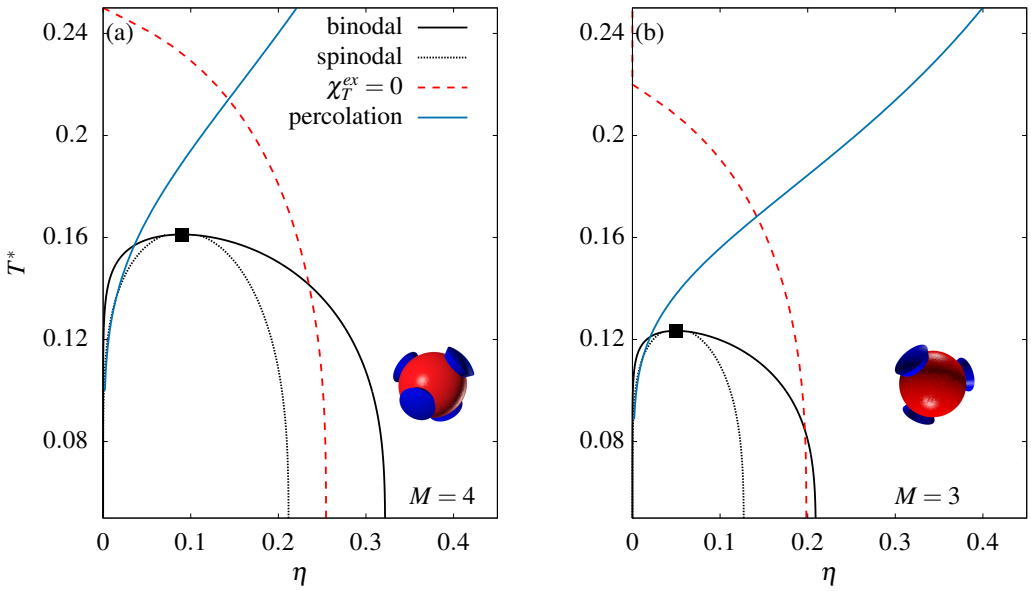

Figure 3.3 Phase diagram in the T^*–η plane of the patchy fluid with four (a) and three sites (b), treated within Wertheim's first-order perturbation theory. The black solid lines show the coexistence curves, the fine-dotted line below the latter is the spinodal, and the black squares denote the critical points. The red dashed line shows the line of vanishing excess isothermal compressibility $\chi_T^{\text{ex}} = 0$, i.e. where $\overline{\chi}_T = 1$. The blue line is the percolation line, below which system-spanning association can occur.

from which one can obtain the reduced isothermal compressibility $\overline{\chi}_T \equiv \chi_T/\chi_T^{\text{id}} = (\partial\, \beta p/\partial \rho_b)^{-1}$ where $\chi_T^{\text{id}} = 1/(k_B T \rho_b)$ is the compressibility of the ideal gas. Recall also that $\overline{\chi}_T$ is equivalent to $\overline{\chi}_T = S(0)$, where $S(0)$ is the static structure factor evaluated at zero wavenumber. The line where the isothermal compressibility takes its ideal-gas value, $\overline{\chi}_T = 1$, cf. Sec. 2.4.2, is then determined by the relation:

$$-\frac{\partial \beta p_{\text{bond}}}{\partial \rho_b} = \frac{8\eta\left(1-\frac{\eta}{4}\right)}{(1-\eta)^4}\,. \tag{3.32}$$

In Fig. 3.3 we show the bulk phase diagrams for patchy particles with four (a) and three patches (b) as obtained from TPT1. The potential parameters are as in Fig. 3.2. The black lines are the gas-liquid coexistence curves (binodals), and the filled squares denote critical points. Note that the critical temperatures for fluids that interact with spherically-symmetric pair potentials are roughly order of magnitude higher than those in patchy fluids (cf. Fig. 2.7). The fine-dashed line below the binodal is the spinodal, determined as the locus where $\overline{\chi}_T$ diverges, or, equivalently, where $1/\overline{\chi}_T$ approaches zero. The red dashed line is the line of vanishing excess isothermal compressibility $\chi_T^{\text{ex}} = 0$, i.e. where $\overline{\chi}_T = 1$. Furthermore, the blue solid line intersecting the binodal on the low-density branch is the percolation line where $p_b = 1/(M-1)$. Curiously, the present binodals and spinodals, as well as the $\chi_T^{\text{ex}} = 0$ lines exhibit an infinite slope at low temperatures $T^* \to 0$; this also seen in simulations [148, 50] – we will return to this in Sec. 4.3 of Ch. 4.

As outlined in Sec. 1.3, critical points in patchy fluids move towards lower densities and temperatures [47] as the number of sites is lowered. For a chain-forming fluid, with only two interaction sites, the coexistence of gaseous and liquid phases ceases to exist. In particular, mixtures of two- and three-site patchy fluids provide the possibility to move the location of the critical point continuously towards the origin; recall that this is also found in simulations [47, 151]. This is consistent with what we observe in Fig. 3.3; for three patches per particle, the critical point predicted by TPT1 is located at $(\eta_c, T_c^*) = (0.05, 0.123)$, whereas for tetravalent particles we find $(\eta_c, T_c^*) = (0.09, 0.161)$. Relatedly, the $\chi_T^{ex} = 0$ line terminates at the density-axis at $T^* = 0$ at lower packing fractions. A low density and low temperature expansion of $1/\overline{\chi}_T$ provides further physical and mathematical insight into this behavior [152]:

$$\frac{1}{\overline{\chi}_T} = \frac{\partial \beta p}{\partial \rho_b} = c_0(\eta) + c_1(\eta)\, e^{-\beta\varepsilon/2} + \mathcal{O}(e^{-\beta\varepsilon})\,, \tag{3.33}$$

where

$$c_0(\eta) = \left(1 - \frac{M}{2}\right) + \left(8 - \frac{5M}{2}\right)\eta + \mathcal{O}(\eta^2)\,, \tag{3.34}$$

$$c_1(\eta) = \frac{\sqrt{M}}{\sqrt{\eta\, v_b/v_s}} + \frac{15}{16}\frac{\sqrt{M\,\eta}}{\sqrt{v_b/v_s}} + \mathcal{O}(\eta^{3/2})\,, \tag{3.35}$$

where $v_s = \pi\sigma^3/6$ is the hard-sphere volume. It follows from Eq. (3.34) that $1/\overline{\chi}_T$ can become negative at small densities and temperatures for $M > 2$, as the first two leading terms in $c_0(\eta)$ become negative, and $c_1(\eta) > 0$ is exponentially damped for low T^*. However, the case $1/\overline{\chi}_T < 0$ implies mechanical instability, and hence there will always be a spinodal for $M > 2$. We clearly see that $c_0(\eta)$ becomes more negative with an increasing number of patches, and thus the regions of mechanical instability will become larger. Note that the higher-order terms of $c_0(\eta)$ in Eq. (3.34) are positive and will counter-balance the negative contributions at higher densities.

In Sec. 3.3 we have seen that thermodynamic cluster properties, such as the degree of polymerization, are described accurately by TPT1, for tri- and tetravalent patchy particles and in Ref. 150 excellent agreement is found for chain-forming fluids. However, the gas-liquid binodals are not in such well agreement with simulations; here Wertheim's theory particularly underestimates the densities of the coexisting liquid branch for $M \geq 4$ [148]. The critical points found in simulations [153] for the present model parameters are $(\eta_c,\, T_c^*) = (0.14,\, 0.168)$ for $M = 4$, and $(\eta_c, T_c^*) = (0.07,\, 0.125)$ for $M = 3$. The latter is rather close to the predictions of TPT1.

We may conclude that Wertheim's first-order perturbation theory provides a valuable approach to account for the phase behavior of associating fluids with highly anisotropic interactions. Thereby it naturally yields to a theory for clustering and polymerization. On passing, we finally note that TPT1 has also proven to be reliable in more complex situations. An example are so-called $2AnB$ patchy colloids. There one places two sites of type A at the poles of each particles and n patches of type B

are placed along the equator. The particles interact via AA or via AB bonds only (with distinct interaction energies ε_{AA} and ε_{AB}), while BB bonds are forbidden. Here one for instance finds [154, 155] reentrant binodals, i.e. coexistence curves that vanish asymptotically for temperatures sufficiently below the critical temperature T_c^*. We will find a similar behavior in systems with anisotropic competing interactions. This is discussed Sec. 6.3 of Ch. 6.

Chapter 4

Static Structure of Patchy Fluids

4.1 Density functionals for the patchy fluid

For the uniform associating fluid, Wertheim developed a successful thermodynamic perturbation theory. In its first order formulation (TPT1), correlations between bonding sites are neglected, and loop-forming structures are not considered. Moreover, it is assumed that each site is engaged in not more than one bond, and each pair of particles can be connected by at most one bond. Finally, the theory includes no information about the geometrical arrangement of the patches on the particles surface. As we have seen in the previous chapter 3, Wertheim's approach produces reliable and robust results as regards the phase behavior and bonding statistics – see also Refs. 77, 148, 156, 157.

The theoretical description of the inhomogeneous patchy fluid appears to be more challenging. Wertheim's theory is, in principle, valid for inhomogeneous fluids [145, 146] and can be written in a density functional language – see Eq. (3.17). In particular, in its inhomogeneous form the theory respects particle orientations. However, from a practical point of view, this makes functional minimization a challenging and complex numerical task. In the literature, it is therefore quite common to neglect the orientational dependency, which amounts to averaging out the latter under the assumption that both the density profile $\rho(\mathbf{r})$ and the fraction of unbonded sites $X(\mathbf{r})$ do not depend on the particle orientation ϖ. However, the orientational averaged inhomogeneous form of TPT1 yields relatively poor density profiles compared to simulations [71].

Up to the present date, the perhaps most common method used in the literature is to employ the bulk form of TPT1 as a starting point: there is the DFT version of Segura *et al.* [71, 158], which makes use of the WDA formalism of Tarazona [104] (see also Sec. 2.3.1) for both the hard sphere and association contribution. Another version is a density functional suggested by Yu and Wu [72] which is constructed within the framework of Rosenfeld's FMT for hard-sphere mixtures in combination with TPT1. In particular, it phenomenologically incorporates the vector-type weighted densities of FMT. Both functionals were initially tested close to a hard, planar wall for particles carrying four patches. Here, good agreement was observed over a wide range of densities

and not too low temperatures (i.e. well above from the critical point) in comparison with computer simulations. The FMT-based functional appeared to perform slightly better at higher particle densities and being less computationally intensive for mixtures. Deviations between WDA and FMT were fairly small. To date the approach by Yu and Wu seems to have become 'state-of-the-art' and is commonly applied, e.g., to investigate properties of associating fluids at planar [159–161] or spherical interfaces [162–164]. However, in situations in which the particle orientations become important, such as at a hard wall and sufficiently low temperatures, both density functional models break down [159]. This breakdown is most likely a consequence of the fact that the theories for inhomogeneous patchy fluids do not respect particle orientations as they are based on an orientation-independent bulk theory. The latter in addition does not provide explicit information on the geometric arrangement of bonding sites.

Weighted-density functional (WDA). We first outline the WDA approach by Segura *et al.* [71]. Recall that in Tarazona's WDA formalism the density functionals have the form

$$\beta\mathcal{F}_{\mathrm{ex}}[\rho] = \int \mathrm{d}\mathbf{r}\, \rho(\mathbf{r})\beta\Psi(\bar{\rho}(\mathbf{r}))\,, \tag{4.1}$$

where $\Psi(\rho)$ is the *bulk* excess free energy density per particle evaluated at a weighted density $\bar{\rho}(\mathbf{r}) = \int \mathrm{d}\mathbf{r}'\, \rho(\mathbf{r}')\omega(|\mathbf{r}-\mathbf{r}'|\,;\,\widetilde{\rho})$ – see Sec. 2.3.1 for details. For hard-spheres, the very accurate CS expression may be employed:

$$\beta\Psi_{\mathrm{CS}}(\bar{\rho}(\mathbf{r})) = \frac{4\bar{\eta}(\mathbf{r}) - 3\bar{\eta}(\mathbf{r})^2}{(1-\bar{\eta}(\mathbf{r}))^2}\,, \tag{4.2}$$

where $\bar{\eta}(\mathbf{r}) = \pi\sigma^3\bar{\rho}(\mathbf{r})/6$. Although the above approach has been derived for the pure hard-sphere fluid, Segura *et al.* were the first who used this WDA formalism to obtain a density functional for associating fluids, where [71, 158, 159]

$$\beta\Psi(\bar{\rho}(\mathbf{r})) = \beta\Psi_{\mathrm{CS}}(\bar{\rho}(\mathbf{r})) + M\left[\ln(X(\bar{\rho}(\mathbf{r}))) - \frac{X(\bar{\rho}(\mathbf{r}))}{2} + \frac{1}{2}\right].$$

As can be seen, the bonding contribution in the inhomogeneous case is assumed to be of Wertheim's form, Eq. (3.20), where the bulk density dependence of the bonding probability has been replaced by a dependence on the weighted density $\bar{\rho}(\mathbf{r})$. Note that the weight function $\omega(r,\,\rho)$, determined by Tarazona to match the PY solution of $c(r)$ for hard-spheres, remains unchanged.

Fundamental-measure functional (FMT). Yu and Wu extended the bonding contribution to the inhomogeneous fluid via an empirical weighted-density approximation of Eqs. (3.20), (3.19), and (3.12) incorporating the weighted densities $n_\nu(\mathbf{r})$ of Rosenfeld's FMT. The idea is to replace all bulk quantities by corresponding weighted densities – e.g. ρ_b with n_0, which is exact for the homogeneous fluid, and assume that these relations hold also for the non-uniform case. The excess free-energy functional

reads then [72]

$$\beta\mathcal{F}_{\text{ex}}[\rho] = \int \mathrm{d}\mathbf{r}\, \left[\Phi_{\text{HS}}(\{n_\nu(\mathbf{r})\}) + \Phi_{\text{bond}}(\{n_\nu(\mathbf{r})\})\right] , \tag{4.3}$$

where

$$\Phi_{\text{bond}}(\{n_\nu\}) = M\, n_0(\mathbf{r})\, [\xi(\mathbf{r})]^q \left[\ln\left(X(\mathbf{r})\right) - \frac{X(\mathbf{r})}{2} + \frac{1}{2}\right] , \tag{4.4}$$

with $X(\mathbf{r})$ being now a position-dependent function via the weighted densities $n_\nu(\mathbf{r})$ given by

$$\frac{1 - X(\mathbf{r})}{[X(\mathbf{r})]^2} = n_0(\mathbf{r})\, [\xi(\mathbf{r})]^q\, M\, \Delta(\{n_\alpha(\mathbf{r})\}) . \tag{4.5}$$

The quantity $\Delta = v_b(e^{\beta\varepsilon} - 1) g_{\text{hs}}(\{n_\nu(\mathbf{r})\})$ depends on weighted densities through the generalized contact value of hard-sphere mixtures:

$$g_{\text{HS}}(\{n_\nu\}) = \frac{1}{1 - n_3} + \frac{\sigma n_2 \xi^q}{4(1 - n_3)^2} + \frac{\sigma^2 n_2^2 \xi^q}{72(1 - n_3)^3} . \tag{4.6}$$

Importantly, the factor $\xi = 1 - \mathbf{n}_2 \cdot \mathbf{n}_2 / n_2^2$ has been incorporated purely phenomenologically by Yu and Wu, probably to obtain better results in comparison to computer simulations. Note that in this work we allow for a slightly more general form for ξ in powers of q. This, of course, does not affect the bulk form of Wertheim's theory, since in uniform systems $\xi^q = 1$ for all values of q due to the fact that the volume integral over the vector-type weight functions vanishes. Yu and Wu assumed $q = 1$; however, as we will see later, results significantly can be improved when employing $q = 3$. To the latter we will refer to as the mFMT (modified FMT) functional, whereas the original approach with $q = 1$ is referred to as the FMT functional.

4.2 Bulk structure of tetravalent patchy particles[1]

Surprisingly, systematic studies addressing the bulk structural behavior of density functionals describing patchy particles based on TPT1 seem to be lacking. This is probably due to the fact that it is a priori not clear how to proper model the directional interactions between a test particle and its surrounding fluid within Percus' test particle approach to obtain the (orientationally averaged) radial distribution function $g(r)$ of the fluid. We will demonstrate in this chapter, that density profiles obtained from DFT around a test particle, interacting via a short-ranged spherically-symmetric SW potential with its patchy neighbors, can match simulation results of $g(r)$ and the corresponding static structure factor $S(k)$ nicely. We argue that it is precisely the orientational independence of the theory that leads to a good agreement with simulations. We consider three different density functionals: (i) the WDA-based approach of Segura *et al.* [71], (ii) the original FMT-functional by Yu and Wu [72],

[1] This section is reproduced from: D. Stopper, F. Hirschmann, M. Oettel, and R. Roth, J. Chem. Phys. **149**, 224503 (2018), with permission of AIP Publishing

and (iii) a slightly modified version (which we will refer to as mFMT) of the latter incorporating the vector-type weighted densities in a different manner.

4.2.1 Test particle approach

In the present context of particles with directional interactions the Percus' test particle approach for determining $g(r)$ poses a challenging task. Any density functional which employs the bulk Wertheim theory and makes use of purely spherical weight functions cannot depend on particle orientations. This makes it very hard to realize an *exact* realization of Percus' test particle theory as this would require a proper coupling of the orientational character of the pair potential and an orientationally independent ensemble-averaged density profile of the particles.

We propose a method to obtain approximate radial distribution functions from DFT as follows. We calculate the density profiles around a particle that interacts with the fluid via a short-ranged spherical SW potential, where the interaction range is set equal to the range of the pair potential δ. More precisely, the external potential acting on the fluid is given by

$$V_{\text{ext}}(r) = \begin{cases} \infty & ; \quad r < \sigma \\ -\varepsilon_{\text{sw}} & ; \ \sigma \leq \quad r < \sigma + \delta \\ 0 & ; \quad r \geq \sigma + \delta \,, \end{cases} \tag{4.7}$$

where ε_{sw} sets the interaction energy between test particle and the surrounding particles.

In simulations, such a spherical tracer(in view of Percus' test particle approach this means that the tracer does not know about the orientational character of the interaction between the surrounding particles, and interacts with the latter via a spherically-symmetric SW pair potential) will influence the local ordering of the particles within the first few coordination shells. The density around the tracer will not result in the radial distribution function $g(r)$. Indeed, in order to minimize configurational energy, we expect that the particles surrounding the test particle prefer such orientations in which their patches are not face-to-face with the latter since this would result in a decrease of bonding possibilities. This is demonstrated in Fig. 4.1, where a simulated $g(r)$ (blue symbols) at packing fraction $\eta = 0.3$ and temperature $T^* = 0.2$ is compared to the simulated density profile around a spherical attractive test particle (black dashed line). The potential depth ε_{sw} is chosen such that the height of the first peak matches the peak height found in the $g(r)$. The second peak in $g(r)$ at $r \approx 1.75\sigma$, which is typical for directional fluids exhibiting tetrahedral networks, is not found in the correlations around the tracer, but occurs at $r \approx 2\sigma$ indicating a local distortion of the bulk structure. However, such a distortion of the local structure driven mainly by distinguished particle orientations cannot be captured by the present density functionals, since, as mentioned in the first paragraph of this subsection, they do not consider preferred orientations explicitly. In particular, this may be interpreted as if the theory assumes that the average (bulk) particle orientations are unaffected by a given

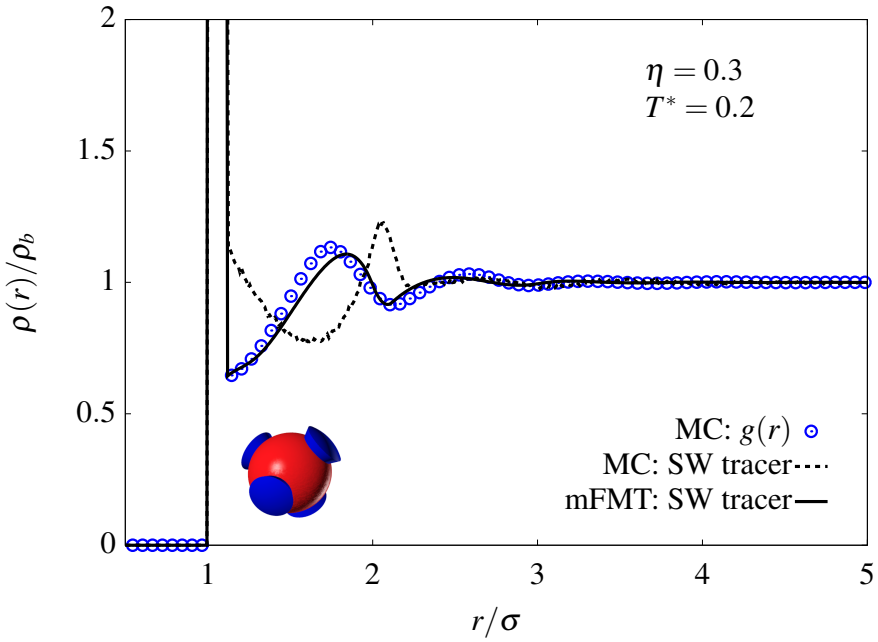

Figure 4.1 Radial distribution function $g(r)$ obtained from MC simulations of tetravalent patchy particles (individual symbols) at packing fraction $\eta = 0.3$ and temperature $T^* = 0.2$. The dashed line shows the MC result for the density around an isotropic square-well test particle. The solid line plots a DFT result using the mFMT functional around an external potential according to Eq. (4.7) with $\varepsilon_{\rm sw}$ chosen to match the first peak in the simulated $g(r)$ (not visible on the scale of the graph).

external potential. In general this, of course, physically cannot be correct. However, for the present situation describing the bulk structure of a tetravalent patchy fluid one may benefit from the orientational independence of the theory. For suitably chosen values of the potential depth $\varepsilon_{\rm sw}$ Eq. (4.7) may mimic an *effective* (orientationally averaged) patch-patch interaction potential. Note that if $\varepsilon_{\rm sw}$ is chosen such to fit the first peak of $g(r)$, the first shell around the tracer particle contains as many particles as a true test particle, and according to the argument given before, in DFT the first shell corresponds to particles properly oriented with their patches towards the tracer particle. This situation can also be modeled explicitly in simulations: If the spherical interaction introduced by the tracer acts only on the patches of the surrounding particles, then $\varepsilon_{\rm sw}$ can be chosen such that the resulting density profiles deviate only marginally from the real $g(r)$. For illustration, when calculating the density profiles around an external potential according to Eq. (4.7) making use of the mFMT functional, we find excellent agreement between the mFMT functional (black solid line in Fig. 4.1) and the radial distribution function $g(r)$ from simulations.

We note that the above approach should be most reliable in case of isotropically distributed patches on the particle surfaces which is in best accordance with the assumption of orientationally independent density functionals. For example, we have verified that the $g(r)$ of the chain-forming fluid (with two sites per particle located at the north- and southpole) is not adequately described by the present approach: the correlation peaks, which in this case occur roughly at integer values of σ in simulations,

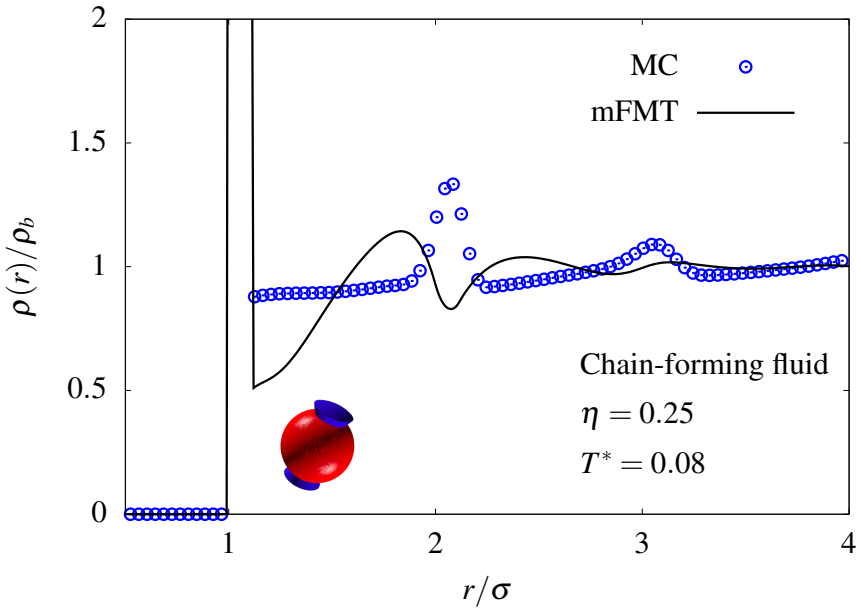

Figure 4.2 Radial distribution function of the chain-forming fluid with two patches per particle located at the north- and south pole. The packing fraction is $\eta = 0.25$ and the temperature $T^* = 0.08$. The symbols show simulation results, and the solid line is the prediction of DFT along with the mFMT functional.

are still located at non-integer values in the corresponding DFT results (using the mFMT functional). This is illustrated in Fig. 4.2 for a packing fraction of $\eta = 0.25$ and temperature $T^* = 0.08$.

4.2.2 Density around hard spherical tracer

We now compare results from the WDA, FMT and the mFMT functionals to that from simulations for the structure of tetravalent patchy particles around a hard spherical tracer of diameter σ (i.e., $\varepsilon_{\text{sw}} = 0$ in Eq. (4.7)). The results are summarized in Fig. 4.3, for temperatures $T^* = 10.0$ (a), 0.2 (b), 0.16 (c), and 0.14 (d). The packing fraction is $\eta = 0.3$, which yields a degree of polymerization Φ ranging from nearly zero at $T^* = 10.0$ where particles behave as hard spheres, to nearly fully bonded states with $\Phi \approx 1$ at low temperatures, cf. also Fig. 3.2. Lines in Fig. 4.3 correspond to results from mFMT (solid), FMT (short-dashed), and WDA (long-dashed), whereas individual symbols show simulation results. It was verified that all DFT implementations fulfilled the Gibbs adsorption theorem providing a proof of internal consistency [70].

While in the hard-sphere limit all three curves are nearly indistinguishable, qualitative differences between (i) the functionals and (ii) with the simulations emerge when association between the particles increases. The WDA predicts a continuous decrease of the contact density $\rho(\sigma^+)$ while simultaneously a broad correlation peak at $r \lesssim 1.6\sigma$ emerges, whose intensity does not further increase for $T^* < 0.16$. This behavior bears resemblance to the results reported in Ref. [159], where density profiles at a planar hard wall have been considered for trivalent patchy particles.

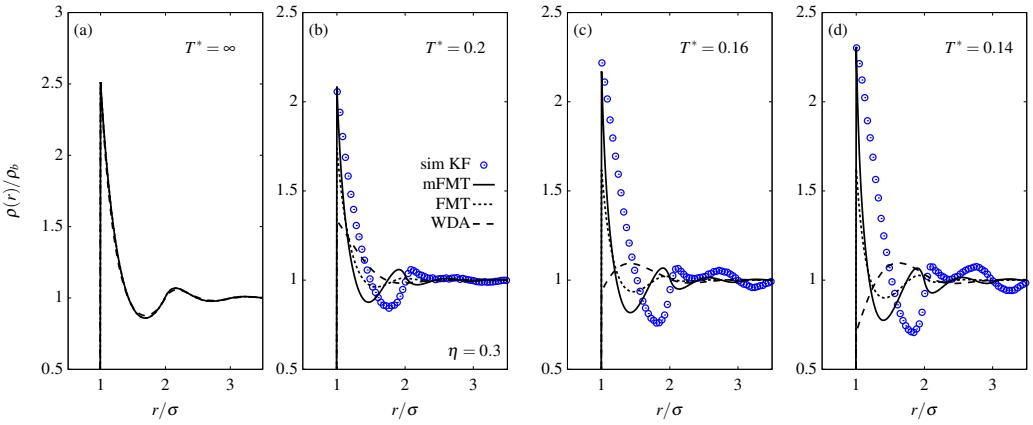

Figure 4.3 Normalized density profile $\rho(r)/\rho_b$ of tetravalent patchy particles around a hard spherical tracer particle ($\varepsilon_{\mathrm{sw}} = 0$) with same hard-core diameter σ as the fluid particles. The packing fraction is $\eta = 0.3$. The temperatures are $T^* = \infty$ (a, hard-sphere limit), 0.2 (b), 0.16 (c), and 0.14 (d). The solid lines are the results borne out by the mFMT functional, the short-dashed curves are the FMT results, and the long-dashed lines correspond to the predictions of the WDA functional. The individual symbols in (b) – (d) show results from MC simulations.

In contrast, the contact values given by the mFMT and the FMT functional, respectively, increase slightly upon cooling. Importantly, only the mFMT approach provides an accurate representation of the contact density and the structural intensity in comparison to simulation results. However, the density peaks are out of phase with the latter. Facing the discussion in the previous Sec. 4.2.1, this may be traced back to the fact that the theory cannot account for orientational inhomogeneities as necessarily are introduced by a spherical hard test particle. The particles directly surrounding the tracer will prefer to orient themselves such that the number of possible bonds is maximized, i.e. it is unlikely that a patch is oriented face-to-face with the test particle; this gives rise to that the second peak in $\rho(r)$ is located at $r \approx 2\sigma$ instead of $r \approx 1.75\sigma$ as would be the case within a perfect bulk situation. The third peak located at $r \approx 2.7\sigma$ [most prominent visible for the lowest T considered here, cf. Figs. 4.3 (c) and (d)] is then associated with the structural information of a tetrahedral network starting in the third coordination shell around the hard tracer. The (m)FMT predicts that the bulk order is not significantly distorted by the presence of the hard tracer particle, and thus the second peak arises at $r < 2\sigma$.

4.2.3 Radial distribution functions

In this section, we examine whether the test-particle approach described previously can be applied to *effectively* describe radial distribution functions $g(r)$ and compare to simulation results. We start with comparison between DFT and MC simulations of Kern-Frenkel-type patchy particles. In Fig. 4.4 we plot radial distribution functions obtained from simulations (individual symbols) compared to DFT results employing the effective test-particle method for $\eta = 0.2$ (upper panel) and 0.3 (lower panel) at temperatures $T^* = 0.22$ [(a), (e)], 0.2 [(b), (f)], 0.18 [(c), (g)], 0.17 (d) and 0.16 (h).

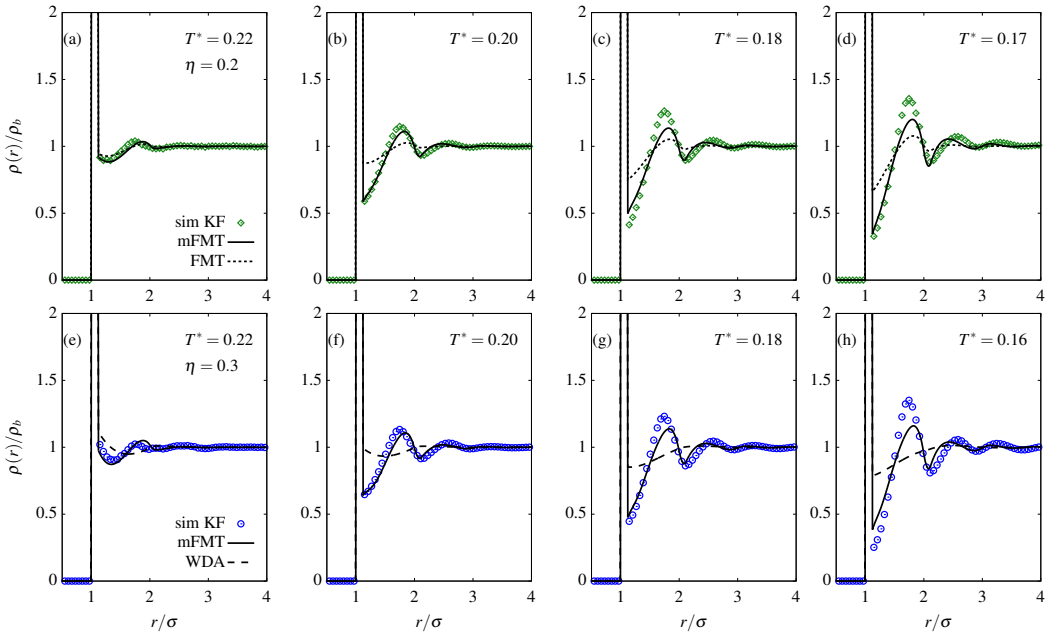

Figure 4.4 Density profiles of the tetravalent patchy fluid around an effective test particle as obtained from the mFMT functional (black solid lines). The height of the first peak was fitted to simulations (individual symbols). The packing fractions are $\eta = 0.2$ (upper panel) and 0.3 (lower panel) at temperatures $T^* = 0.22$ [(a), (e)], 0.2 [(b), (f)], 0.18 [(c), (g)], 0.17 (d), and 0.16 (h). The short-dashed lines in the upper panel correspond to the original FMT, while the long-dashed lines in the bottom panel show results from the WDA functional.

Recall that the critical temperature is $T_c^* = 0.168$. At such temperatures and densities the overall degree of polymerization Φ is always larger than 90% (see Fig. 3.2). The lines correspond to the same three functionals as shown in Fig. 4.3. The quantity ε_{sw} is chosen such that the peak height of $\rho(r)/\rho_b$ given by DFT for $\sigma < r < \sigma + \delta$ fits to simulations with a tolerance of a few per cent. Note that we do not provide ε_{sw} for each case, as it slightly varies for distinct density functionals and state points. Typically, we find $\varepsilon_{\text{sw}}/\varepsilon \approx 0.25 - 0.35$.

Already at intermediate temperatures [(a), (b), and (e), (f)] where association between particles is not too strong, the mFMT performs clearly better than FMT in comparison to simulations. A correlation peak grows being located at $r \approx 1.75\sigma$, indicating an increasing tetrahedral ordering of the particles [165, 143, 166]. In contrast, the WDA functional (dashed lines in lower panel) completely fails to describe such a peak. For lower temperatures [(c), (d) and (g), (h)] the oscillations in simulations significantly become more pronounced; here, only the mFMT functional yields density profiles which are in adequate agreement with the simulations, although the correlations, and in particular the intensity of the second peak, are underestimated and slightly out of phase with simulations.

The overall good agreement between the latter and the theory is also reflected in momentum space when considering the static structure factor $S(k) = 1 + \rho_b \widehat{h}(k)$, where $\widehat{h}(k)$ is the three-dimensional Fourier transform of $g(r) - 1$. In Fig. 4.5 we compare $S(k)$ extracted from simulations (symbols) and mFMT (solid lines) by numerically

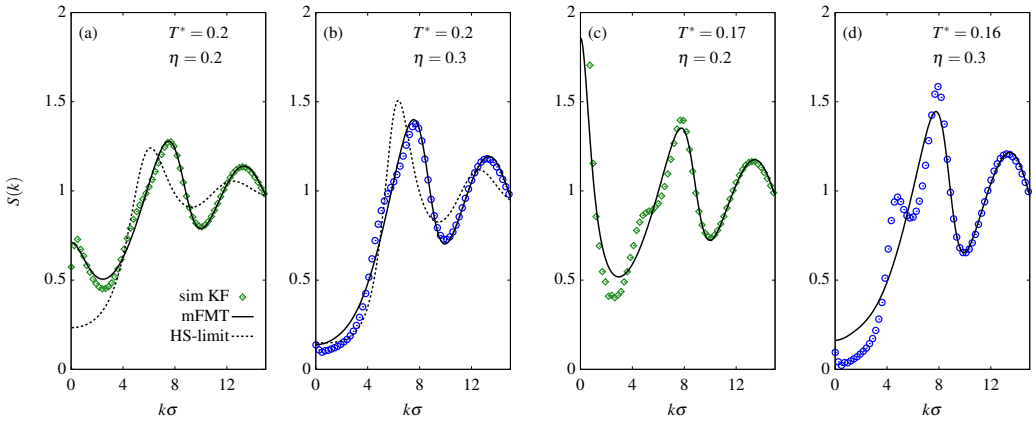

Figure 4.5 Static structure factor $S(k)$ as obtained by numerically Fourier transforming some of the theoretical density profiles shown in Fig. 4.4 (solid lines) in comparison to simulation results (symbols). The dashed lines in (a) and (b) display the hard-sphere structure factor.

Fourier transforming the real-space data shown in Fig. 4.4. For higher temperatures $T^* = 0.2$ and packing fractions $\eta = 0.2$ (a) and 0.3 (b), we find excellent agreement between simulation and DFT, even in the low-k region related to bulk thermodynamic properties of the system such as the isothermal compressibility. The dashed lines in (a) and (b) show the corresponding Percus-Yevick solution for the structure factor $S_{\mathrm{hs}}(k)$ of hard spheres. For lower temperatures $T^* = 0.17$ (c) and 0.16 (d), however, deviations between DFT and simulations in the region $0 < k\sigma < 8$ become visible. In particular, for $\eta = 0.3$ the static structure factors from simulations feature an additional peak at $k\sigma \approx 4.5$, which is absent in the theoretical calculations. Indeed, the presence of two peaks in $S(k)$ at $k\sigma \approx 4.5$ and $k\sigma \approx 8$ is a prominent signal of a system-spanning amorphous tetrahedral network [165, 143, 166]. While the shift of the monomer-monomer correlation peak from initially $k\sigma \approx 2\pi$ at high temperatures towards $k\sigma \approx 8$ at lower temperatures is also captured by the mFMT functional, we never observe a second peak at lower k, even for lower temperatures $T^* < 0.16$ than discussed here. These discrepancies are most likely due to approximations introduced by Wertheim's perturbation theory related to the absence of geometrical informations regarding the arrangement of bonding sites. This presumably makes it impossible to obtain an even better agreement in terms of bulk structural properties between a theory making use of TPT1 and simulations of patchy particles.

The present results impressively demonstrate that density functional theory making use of Wertheim's perturbation theory is capable of describing fundamental structural aspects prominent for fluids with directional interactions via an effective test-particle route. However, our findings also show that the quality of the results obtained from density functionals based on the bulk form of TPT1 seem rather sensitive on how precisely the generalization to the inhomogeneous fluid is achieved. In particular, for the FMT-based approaches this sensitivity can be traced back to the incorporation of the factor $\xi = 1 - \mathbf{n}_2 \cdot \mathbf{n}_2 / n_2^2$: When setting $\xi \equiv 1$, the FMT exhibits a very poor behavior, similar to the performance of the WDA functional. On the other hand, we

have seen that replacing $\xi \to \xi^3$ yields accurate results in comparison to simulations over a wide range of densities and temperatures (we should also note that in planar geometries, such as introduced by a hard wall, the mFMT differs only marginally from the original FMT approach by Yu and Wu). Furthermore, the remarkable performance obtained by minimization of the mFMT functional is rather interesting, as it turns out that the approach (as the WDA functional) does not respect the leading-order term of the exact virial expansion

$$\lim_{\rho\to 0} \beta\mathcal{F}_{\mathrm{ex}}[\rho] = -\frac{1}{2}\iint \mathrm{d}\mathbf{r}\,\mathrm{d}\mathbf{r}'\,\rho(\mathbf{r})\rho(\mathbf{r}')\langle f(|\mathbf{r}-\mathbf{r}'|)\rangle\,, \tag{4.8}$$

where the angular averaged Mayer-f function is given by

$$\begin{aligned}\langle f(r)\rangle &= -\Theta(\sigma - r) + \mathcal{A}\left[\Theta(\sigma+\delta-r) - \Theta(r-\sigma)\right] \\ &\equiv f_{\mathrm{hs}}(r) + \langle f_{\mathrm{bond}}(r)\rangle\,,\end{aligned} \tag{4.9}$$

with $\mathcal{A} = M^2(e^{\beta\varepsilon}-1)\sin^4(\theta_c/2)$. The latter features a prominent peak for $\sigma < r < \sigma+\delta$ arising from nearest neighbor patch-patch interactions. By means of performing a functional Taylor expansion about $\rho = 0$ up to second order in density, one obtains the following low-density behavior of the FMT-type functionals (we consider only the bonding contribution, as the hard-sphere parts do respect Eq. (4.8))

$$\lim_{\rho\to 0} \beta\mathcal{F}_{\mathrm{bond}}[\rho] = -\frac{\mathcal{B}}{2}\int \mathrm{d}\mathbf{r}\left([n_0(\mathbf{r})]^2 - q\frac{\mathbf{n}_2(\mathbf{r})\cdot\mathbf{n}_2(\mathbf{r})}{\pi^2\sigma^4}\right)\,. \tag{4.10}$$

The factor $\mathcal{B}$ is given by $\mathcal{B} = M^2(e^{\beta\varepsilon}-1)v_b$, where the bonding volume v_b is defined in Eq. (3.7). For completeness we also provide the low-density limit of the WDA functional:

$$\lim_{\rho\to 0} \beta\mathcal{F}_{\mathrm{bond}}[\rho] = -\frac{\mathcal{B}}{2}\int \mathrm{d}\mathbf{r}\,\rho(\mathbf{r})\rho_0(\mathbf{r})\,. \tag{4.11}$$

Taking two functional derivatives one readily recognizes that Eqs. (4.10) and (4.11) do not yield $\langle f_{\mathrm{bond}}(r)\rangle$ as given in Eq. (4.9). In the uniform fluid, however, both expressions are consistent with Eq. (4.8) and are equivalent to the Wertheim free energy (Eq. (3.20)) expanded up to second order in ρ_b,

$$\lim_{\rho_b\to 0} \beta f_{\mathrm{bond}} = -\frac{\mathcal{B}}{2}\rho_b^2\,. \tag{4.12}$$

The above shortcoming of the mFMT functional is also reflected when considering the full bulk pair direct correlation function $c(r)$ compared to simulations. Recall that it is defined as the negative second functional derivative of $F_{\mathrm{ex}}[\rho]$ evaluated for the uniform fluid (cf. Eq. (2.70)). From simulations and integral equation theories it is known that $c(r)$ typically is negative inside the hard core due to repulsive interactions, and has positive contributions outside due to the presence of attractive forces [135, 136] (see also Fig. 2.2). Extracting a bulk pair direct correlation function $c_{\mathrm{sim}}(r)$ from our simulations of patchy particles via the OZ relation, Eq. (2.39), we observe a

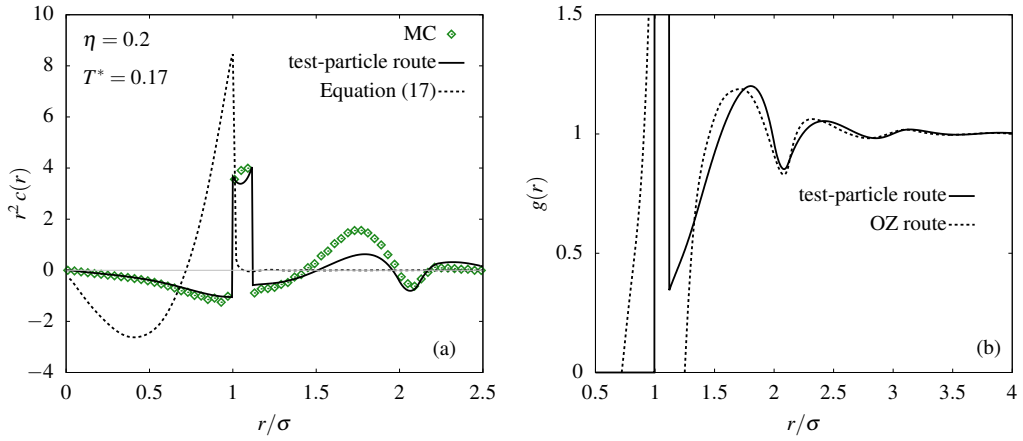

Figure 4.6 (a) Bulk pair direct correlation function $r^2\,c(r)$ obtained from simulations (symbols), functional differentiation according to Eq. (2.70) (dashed line), and the test-particle route (solid line). Both lines show results from the mFMT functional. (b) Comparison of a $g(r)$ obtained via the test-particle route (solid line) and from solving the Ornstein-Zernike equation (2.39) along with $c(r)$ from Eq. (2.70) (dashed line). The state point in (a) and (b) is the same as in Fig. 4.4 (d).

significant peak for $\sigma < r < \sigma + \delta$ in accordance with the Mayer-f function (in the low-density limit it follows from Eq. (4.8) that $c(r) = f(r)$) – see Fig. 4.6 (a), where the symbols show $c_{\rm sim}(r)$ for the same state point as in Fig. 4.4 (d). In contrast, the $c(r)$ obtained from taking two functional derivatives of the mFMT functional exhibits a fundamentally distinct behavior (dashed line): it is zero for $r > \sigma$, but becomes positive inside the core. This can readily be understood since the FMT-type weight functions $\omega_\nu(r)$ (see Eqs. (2.98)) are of range $\sigma/2$ and thus $c(r)$ is of range σ. As a result, the patchy attraction is completely mapped into the hard-core region. Note that there is no significant qualitative difference between the FMT and mFMT, albeit the former produces a less pronounced curve which goes in hand with the less structured density profiles in Fig. 4.4. On the other hand, when extracting an effective $c_{\rm eff}(r)$ from density profiles obtained via the test-particle route and the mFMT approach, it shows a similar level of good agreement with simulations as do the effective radial distribution functions which is impressively demonstrated by the solid curve in Fig. 4.6 (a). Remarkably, the $g(r)$ obtained from the OZ relation (2.39) using the $c(r)$ as generated by Eq. (2.70) does not deviate too strongly from the $g(r)$ obtained via the test-particle route for $r \gtrsim 1.5\sigma$, see Fig. 4.6 (b). However, it does not exhibit the first-neighbor correlation peak for $\sigma < r < \sigma + \delta$ nor does it satisfy the core-condition $g(r) = 0$ for $r < \sigma$, which trivially is fulfilled in the test-particle situation.

The disagreement between the $c(r)$ obtained from directly differentiating the mFMT functional and that via the test-particle route is striking; but following Archer and Evans [134] one should not judge a density functional solely based on its performance on the level of the (bulk) pair direct correlation function: for mean-field type DFTs, which are commonly employed for treating longer-ranged attractive spherically-symmetric pair interactions, it is well known that functional minimization according to Eq. (2.66) may lead to much more reliable results than taking two functional derivatives of $F_{\rm ex}[\rho]$. We

thus emphasize that the (m)FMT functional for patchy particles is not necessarily bound to yield unreliable results for the one-body density $\rho(\mathbf{r})$ in inhomogeneous situations. We also note that the (m)FMT functional is consistent with the compressibility sum rule

$$\rho_b \, k_B T \, \chi_T = \left(\frac{\partial \beta p}{\partial \rho_b} \right)^{-1} = S(0) \, , \tag{4.13}$$

i.e., where the pressure is calculated from Eq. (3.29) employing the bulk free energy (3.22), and $S(0) = 1/(1 - \rho_b \widehat{c}(0))$ is obtained from the $k \to 0$ limit of the Fourier transform of the bulk pair correlation function $c(r)$, where the latter is in turn obtained from Eq. (2.70).

4.3 Asymptotic decay of correlations

In Sec. 2.4 we discussed in detail the asymptotic behavior of the pair correlation function $h(r)$ for model fluids with short-ranged isotropic pair potentials; it is straightforward to show that two distinct types of decay of $h(r)$ exist as $r \to \infty$: damped oscillatory (Eq. (2.117)) or purely exponential monotonic decay (Eq. (2.118)). Which sort of decay dominates depends on the thermodynamic state point and is controlled by the competition between attraction and repulsion, which, in turn, controls the form of the bulk pair direct correlation function $c(r)$. As a result, there exists a line in the phase diagram at which crossover from one type of decay to the other occurs, first conjectured by Fisher and Widom [126], and hence this line is referred to as Fisher-Widom (FW) line. In the following Secs. 4.3.1 and 4.3.2 we investigate FW lines for the patchy fluid with four, three and two patches per particle. Moreover, we also consider Widom (W) lines of local extrema of the true correlation length ξ (i.e. the decay rate of $h(r)$ to zero) as well as lines of extrema of thermodynamic response functions.

4.3.1 Fisher-Widom and Widom lines

In Figs. 4.7 (a) and (b) we display the bulk phase diagrams of four- and three-site patchy particles, including the FW (black dotted) and W (green solid) lines, as obtained from the mFMT functional and Eqs. (2.70), (2.119) and (2.120). Note that the deviation of the FW line obtained from the original FMT functional proposed by Yu and Wu compared to the mFMT functional is not significant, and therefore we do not show results borne out by the former. Furthermore we show as the purple line where the reduced isothermal compressibility $\overline{\chi}_T = \chi_T / \chi_T^{\mathrm{id}} = S(0)$ has local maximums, where $\chi_T^{\mathrm{id}} = 1/(k_B T \rho_b)$ is the ideal gas compressibility. In what follows, we call this the $\overline{\chi}_T^{\mathrm{max}}$ line. This line, similar to the W line, emanates from the critical point (black square), at which $\overline{\chi}_T \to \infty$. We also show the lines at which $\overline{\chi}_T = 1$ (red dashed), i.e. where $\chi_T = \chi_T^{\mathrm{id}}$, as well as the spinodals (black solid) and the corresponding critical points (black squares). In Fig. 4.7 (c) we also display the bulk phase behavior of a chain-forming fluid ($M = 2$). For this system there is no gas-liquid coexistence region

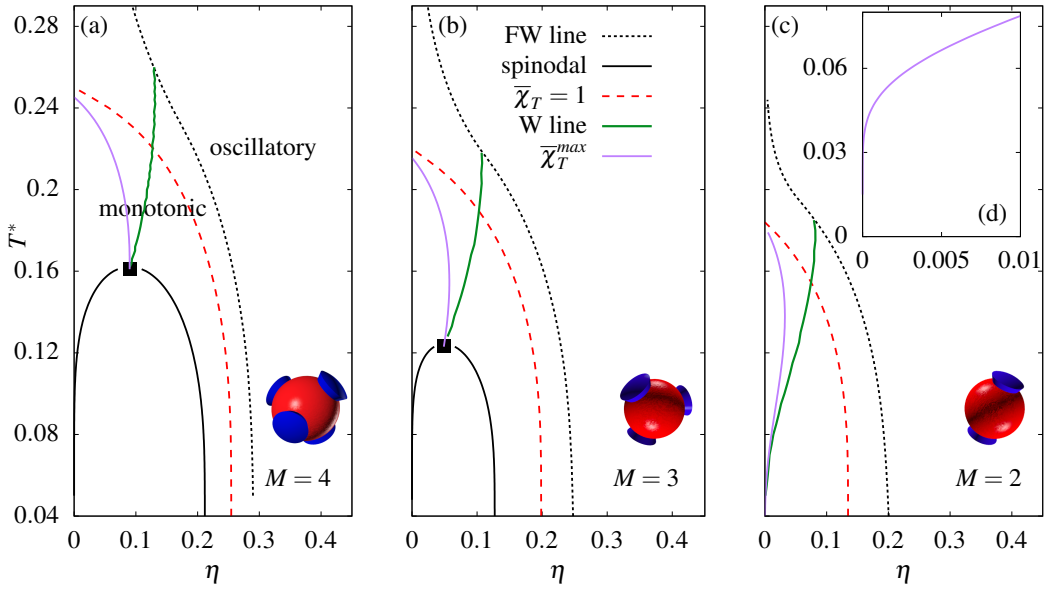

Figure 4.7 Bulk phase diagrams of the patchy fluid with $M = 4$ (a), $M = 3$ (b) and $M = 2$ (c) interaction sites, including the Fisher-Widom (black dotted) and Widom line (green solid), both obtained from the mFMT functional via Eqs. (2.70), (2.119) and (2.120). The purple line displays the $\overline{\chi}_T^{\max}$ line, emanating from the critical point, and the red dashed line shows where $\overline{\chi}_T = 1$ (see Sec. 2.4). The black solid lines in (a) and (b) additionally show the spinodals as well as the corresponding critical points (black squares). The binodals are for the sake of clarity not plotted. In (c) we show the phase diagram for the chain-forming fluid with two patches per particles, i.e. $M = 2$, which is separately discussed in Sec. 4.3.2. The inset (d) shows a magnification of the $\overline{\chi}_T^{\max}$ line at lower densities and temperatures.

and hence no (true) critical point, but we find both FW and W lines. These results are curious and interesting – we will come back to this in the subsequent Sec. 4.3.2.

We observe that the locations of the FW lines in the $T^* - \eta$ plane behave similar to other (thermodynamic) quantities: if the number of patches per particle is reduced, the crossover from monotonic to damped oscillatory decay moves to lower densities and temperatures. And there is another curiosity: the FW lines seem to not be bounded by the spinodals as for instance is the case for the square-well fluid (cf. Fig. 2.7), and generally for simple fluids with spherically-symmetric pair potentials [136]. This means that outside of gas-liquid instability regions the correlation length ξ remains finite for all temperatures, which, interestingly, complies with the fact that disordered states can exist in low-valence patchy fluids down to very low temperatures [50, 51].

How accurate and reliable are the FW (and W) lines for the present mFMT functional given the deviations between the $c(r)$ obtained from the test-particle and OZ routes? (see Fig. 4.6). We first recall what we found in Sec. 2.4.3 for the SW fluid: the line at which the isothermal compressibility takes its ideal gas value, $\chi_T - \chi_T^{\text{id}} = \chi_T^{\text{ex}} = 0$, or, equivalently, where $\overline{\chi}_T = 1$, is a simple and reliable approximate criterion for where in the phase diagram FW crossover is expected to occur. In the paper [136] we demonstrated that this criterion remains also valid for other model fluids. From Figs. 4.7 (a)–(c) we see that the $\overline{\chi}_T = 1$ lines (red-dashed) follow well the actual FW

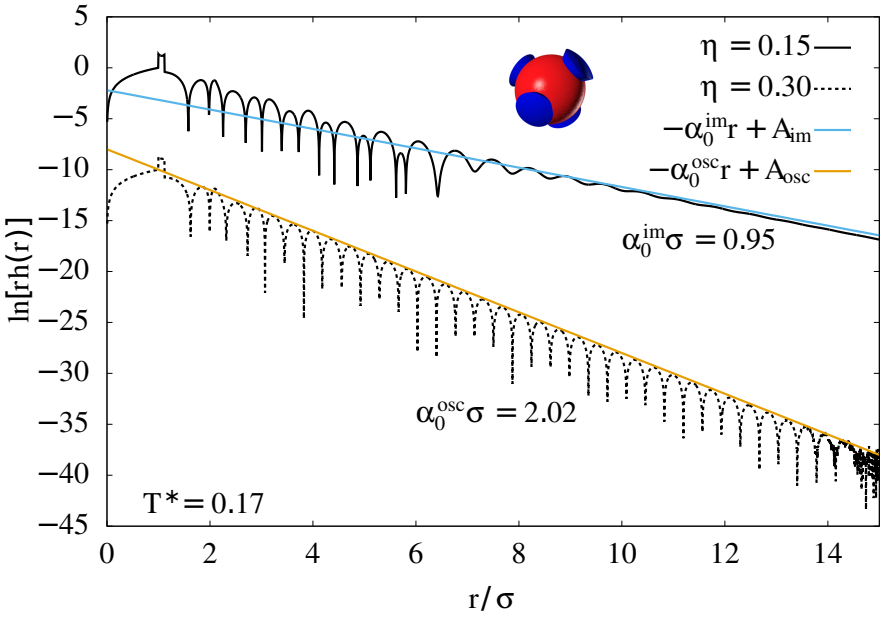

Figure 4.8 Asymptotic decay of $rh(r)$ to zero for the tetravalent patchy fluid, as obtained from the mFMT functional and the effective test-particle route discussed in Sec. 4.2. The temperature is $T^* = 0.17$ and the packing fractions are $\eta = 0.15$ (black solid) and 0.30 (black dotted). The blue and orange straight lines show the expected asymptotic decay rates of $rh(r)$ according to Eqs. (2.119) and (2.120) at these state points (see main text).

lines; in particular, the former decrease with a infinite slope as $T^* \to 0$ evidencing that the correlation length ξ (outside of regions of mechanical instability) does not diverge upon approaching zero temperature (since a divergence of ξ would result in a divergence of $\overline{\chi}_T$ – cf. Eq. (2.121)) and hence the qualitative behavior of the FW lines for $T^* \to 0$ should be reliable.

Furthermore, in Fig. 4.8 we display the asymptotic decay of $rh(r)$ at a temperature $T^* = 0.17$ and packing fractions $\eta = 0.15$ (top solid) and 0.3 (bottom dashed). The curves were obtained using the mFMT functional and the Percus test particle procedure as described in Sec. 4.2.1. The state point where $\eta = 0.3$ is located on the oscillatory side of the FW line, while the state point at lower density is on the monotonic side. The decay rates of $rh(r)$ to zero predicted by Eqs. (2.119) and (2.120) along with Eq. (2.70) is *identical* to those emerging in the asymptotic decay of the density profiles. To a first instance this might seem remarkable given the deviations between the $c(r)$ as obtained from functional differentiation and from the test-particle route (cf. Fig. 4.6). However, it can be shown that these two routes (for any density functional) must yield equivalent results for the real- and imaginary parts of the poles of $\widehat{c}(k)/(1 - \rho_b \widehat{c}(k))$ (but not necessarily for amplitudes), which goes back to linear response arguments [141]. From a mathematical point of view, this is expressed by the fact that the real- and imaginary parts of the poles are determined by an volume integral over $c(r)$, Eqs. (2.119) and (2.120), and thus depend primarily on the integrated strength rather than the precise form of $c(r)$. In Fig. 4.8 the agreement between the two routes is demonstrated by the two lines $-\alpha_0^{\text{im}} r + A_{\text{im}}$ (top blue) and $-\alpha_0^{\text{osc}} r + A_{\text{osc}}$ (bottom orange), where α_0^{im}

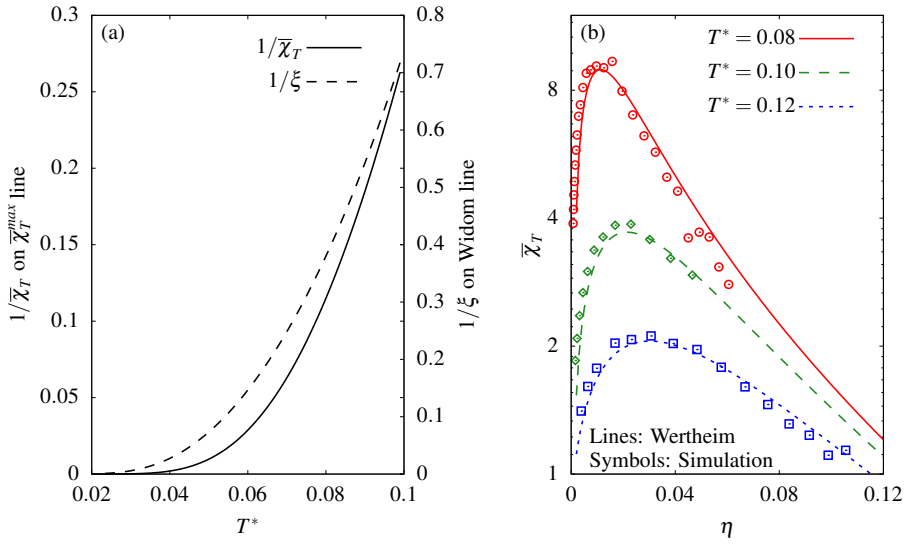

Figure 4.9 (a) Asymptotic behavior of $1/\overline{\chi}_T$ (solid) on the $\overline{\chi}_T^{\max}$ line and $1/\xi$ (dashed) on the Widom line as a function of the temperature T^* obtained from Wertheim's theory and the mFMT functional. (b) $\overline{\chi}_T$ as a function of the packing fraction η at temperatures $T^* = 0.08$ (red solid), 0.10 (green dashed) and 0.12 (blue dotted). The symbols are results from grand-canonical MC simulations.

and α_0^{osc} are the imaginary parts of the solutions to Eqs. (2.119) and (2.120) for pure exponential and damped oscillatory decay. A_{osc} and A_{im} denote offsets chosen so that the lines lie on the top of the density profiles for $r \to \infty$. Note in particular that for the case of patchy particles with four interaction sites, the equivalence between the test-particle and OZ route for determining the asymptotic decay rates of $h(r)$ provides evidence that the FW line shown in Fig. 4.7 (a) should lie close to where FW crossover occurs in simulations.

4.3.2 Chain-forming fluid

In Fig. 4.7 (c) we have shown that the (m)FMT functional based on Wertheim's theory predicts both FW and W lines for the chain-forming fluid, and we also find lines of local extrema of thermodynamic response functions, all of which emanating from the origin. Even more striking, in Fig. 4.9 (a) we observe a divergence of the correlation length ξ (dashed) following the Widom, and of $\overline{\chi}_T$ (solid) following the $\overline{\chi}_T^{\max}$ line, upon approaching zero temperature $T^* \to 0$ and packing fraction $\eta \to 0$. This is curious given the fact that for the case of two patches there is no phase separation into gaseous and liquid phases. In models of three-dimensional simple fluids the occurrence of FW and W lines and lines of extrema of thermodynamic response functions, is always accompanied by the presence of a critical point (located at finite temperatures). We thus conjecture that these surprising results for the chain-forming patchy fluid might be understood as the remains of a pseudo-critical point suppressed to the origin at zero density and temperature; we emphasize that both, the values of ξ and $\overline{\chi}_T$ do not diverge as $T \to 0$ for all finite packing fractions $\eta > 0$, which can be seen nicely from Eqs. (3.33) – (3.35) for $M = 2$.

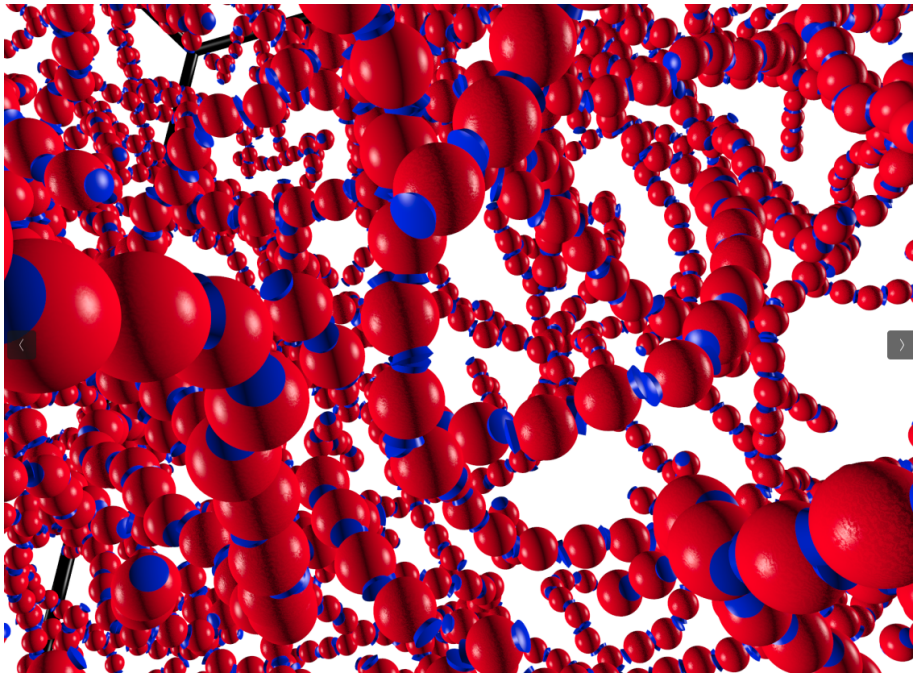

Figure 4.10 Simulation snapshot of a configuration with 30 000 particles at a packing fraction of $\eta = 0.02$ and temperature $T^* = 0.08$. At such densities and temperatures the particles form elongated chains.

In order to test the theoretical predictions, we performed grand-canonical MC simulations based on the open-source code *PatchyParticles* [142], that allows us to directly measure particle fluctuations. As a result, it is possible to calculate the the isothermal compressibility since we have the exact relation [57]

$$\overline{\chi}_T = \frac{\langle N^2 \rangle - \langle N \rangle^2}{\langle N \rangle} \,. \tag{4.14}$$

We considered three fixed temperatures $T^* = 0.08$, 0.10 and 0.12, and measured $S(0)$ as a function of the packing fraction η. In a grand-canonical MC simulation the chemical potential μ, or, equivalently, the activity $z = e^{\beta\mu}$ is prescribed which controls the average number $\langle N \rangle$ of particles present in the system. The precise values of z were chosen by hand, depending on the temperature so that average number of simulated particles ranged roughly between $\langle N \rangle \approx 150 - 2000$. Before taking measurements, we equilibrated the systems for 5×10^6 MC steps, which turned out to be sufficient in order to guarantee that initial shifts in the internal energy and the particle number had disappeared. The aggregation-volume-bias MC move (cf. Appendix B) was applied in order to speed up the phase-space sampling.

In Fig. 4.9 (b) we compare the theoretical predictions for $\overline{\chi}_T$ according to TPT1 (solid lines) to the simulation results (individual symbols). The agreement between theory and the latter is excellent, even at $T^* = 0.08$. The shift of the maximum in $\overline{\chi}_T$ towards lower densities with decreasing temperature nicely resembles the behavior of the purple curve in Fig. 4.7 (c). These results provide clear evidence that Wertheim's

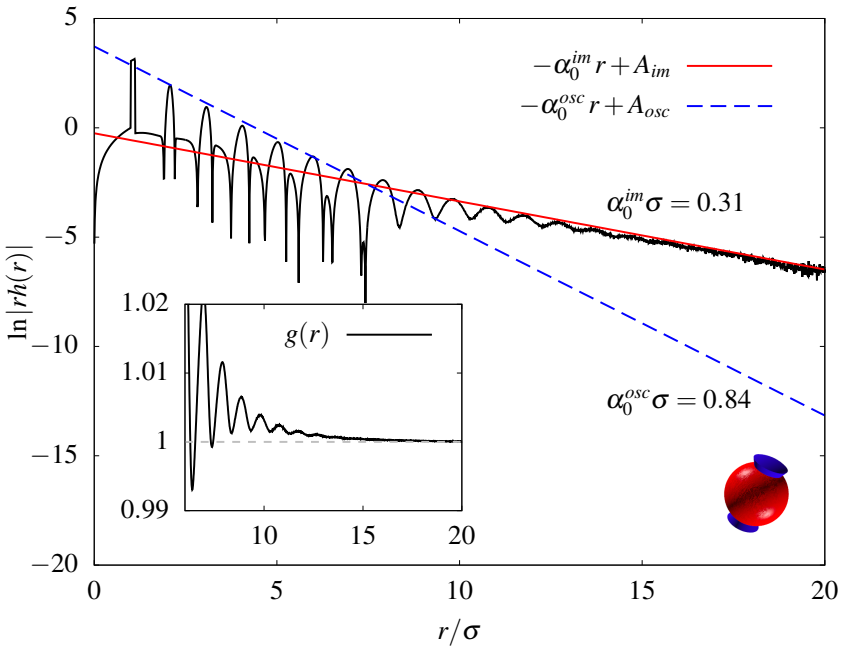

Figure 4.11 Asymptotic decay of $rh(r)$ of the chain-forming fluid as obtained from simulations at the same state point as in Fig. 4.10. We can clearly identify two distinct decay rates: on short distances, the lowest-lying complex pole dominates (blue dashed line), but for $r \to \infty$ the decay becomes monotonic (decay rate indicated by red solid line) evidencing a leading purely imaginary pole. The inset shows a magnification of $g(r)$ demonstrating its decay to unity from above.

theory stays reliable even at very low temperatures. This in particular is in line with the findings of Ref. 150, where other thermodynamic properties of chain-forming fluids (including the degree of polymerization, average chain-lengths et cetera) described by TPT1 were excessively tested against MC simulations.

We also tested the theoretical prediction of the presence of a FW line. To our knowledge, there exist no three-dimensional (simple) fluids that show FW crossover but do not exhibit gas-liquid phase separation. However, it is important to note that the existence of a FW line without the presence of a critical point does not contradict the original results of Fisher and Widom [126]: in their work they considered a one-dimensional lattice gas as well as a one-dimensional continuum model fluid, and both systems do not phase separate. We simulated a system consisting of $N = 30\,000$ particles at temperature $T^* = 0.08$ and a packing fraction of $\eta = 0.02$ which roughly corresponds to a state point where $\overline{\chi}_T$ has a maximum – see red curve in Fig. 4.9 (b). At this temperature and density the system is populated with elongated chains; a configuration snapshot is shown in Fig. 4.10. The side length of the simulation box is $L = 84\sigma$, which allows us to calculate $g(r)$ up to $r = 42\sigma$. We equilibrated ten independent systems for 5×10^6 MC steps, where a step consists of N individual attempts of performing an AVB-move. The production runs for calculating $g(r)$ last for $N_p = 5 \times 10^7$ steps, where a histogram recording was performed every 10^3-th step in order to ensure that the samples were sufficiently decorrelated, which we concluded by

considering the autocorrelation function of the internal energy. Since sampling of $g(r)$ scales with $\sim N^2$, we employed graphics cards to speed up the histogram calculations, although the overall sampling still took two months of computation time.

The final result for the total correlation function $h(r)$ is shown in Fig. 4.11. As in Fig. 4.8, we plot $\ln|r\,h(r)|$ so that pure exponential decay according to Eq. (2.118) occurs as a straight decreasing line, and this is what we observe. The initial oscillations in $rh(r)$, arising from strong particle association, start to decay at $r \approx 10\sigma$ and vanish beyond $r \approx 15\sigma$. Note that for $r \gtrsim 25\sigma$ the curve reaches a plateau at $\ln|r\,h(r)| \approx -10$ due to statistical fluctuations. It would require significant effort to further suppress fluctuations at such long distances. The inset in Fig. 4.11 shows a magnification of $g(r)$, where its decay to unity from above nicely is visible, as was conjectured by Fisher and Widom [126] if attraction dominates over repulsion. When extracting $c(r)$ from $h(r)$ via the OZ relation, and searching for solutions to Eqs. (2.119) and (2.120), we find a purely imaginary leading pole; the corresponding asymptotic behavior of $h(r)$, according to Eq. (2.118), is shown as the solid straight line in Fig. 4.11. When searching for the lowest-lying complex pole, we find that the decay rate α_0^{osc} matches exactly the decay of $h(r)$ over the first coordination shells up to $r \approx 6\sigma$. This is indicated by the blue dashed line. We emphasize that the presence of only one state point, where $h(r)$ decays monotonically, is sufficient to prove the existence of FW crossover: we know that at high temperatures and densities the decay must be oscillatory as the fluid behaves hard-sphere like in those regions of the phase diagram.

4.4 Density profiles at a hard wall

In the final section of this chapter we consider density profiles of patchy particles at a hard wall. Similar to Sec. 4.2, we compare results from DFT to simulations. To this end, systems with $N = 1000$ particles carrying two, three, and four patches were simulated where walls placed at $z = \sigma$ and $z = L - \sigma$. In Ref. [159] Gnan and de las Heras have studied in detail the performance of the WDA and FMT functional for particles with three patches. Here, we focus on tetravalent particles. In Fig. 4.12 we show results for $\rho(z)\sigma^3$ from mFMT (solid line), FMT (dashed line) and MC simulations (symbols). The packing fractions are $\eta = 0.1$, 0.2, and 0.3, from top to bottom. We consider temperatures $T^* = 0.25$, 0.22, 0.20, and 0.18 (from left to right). For $\eta = 0.1$ and 0.2, we observe a desorption of the density from the wall as the temperature is lowered, reflected in a contact density smaller than that of the bulk value, i.e. $\rho(\sigma^+) < \rho_b$. This is consistent with the exact thermodynamic sum rule [57]

$$\beta p = \rho(\sigma^+)\,, \tag{4.15}$$

which follows from that the fluid pressure βp, exerted from the fluid on the wall, equals the negative pressure exerted from the wall on the fluid.

Recall that the critical temperature in both TPT1 and simulations occurs at roughly

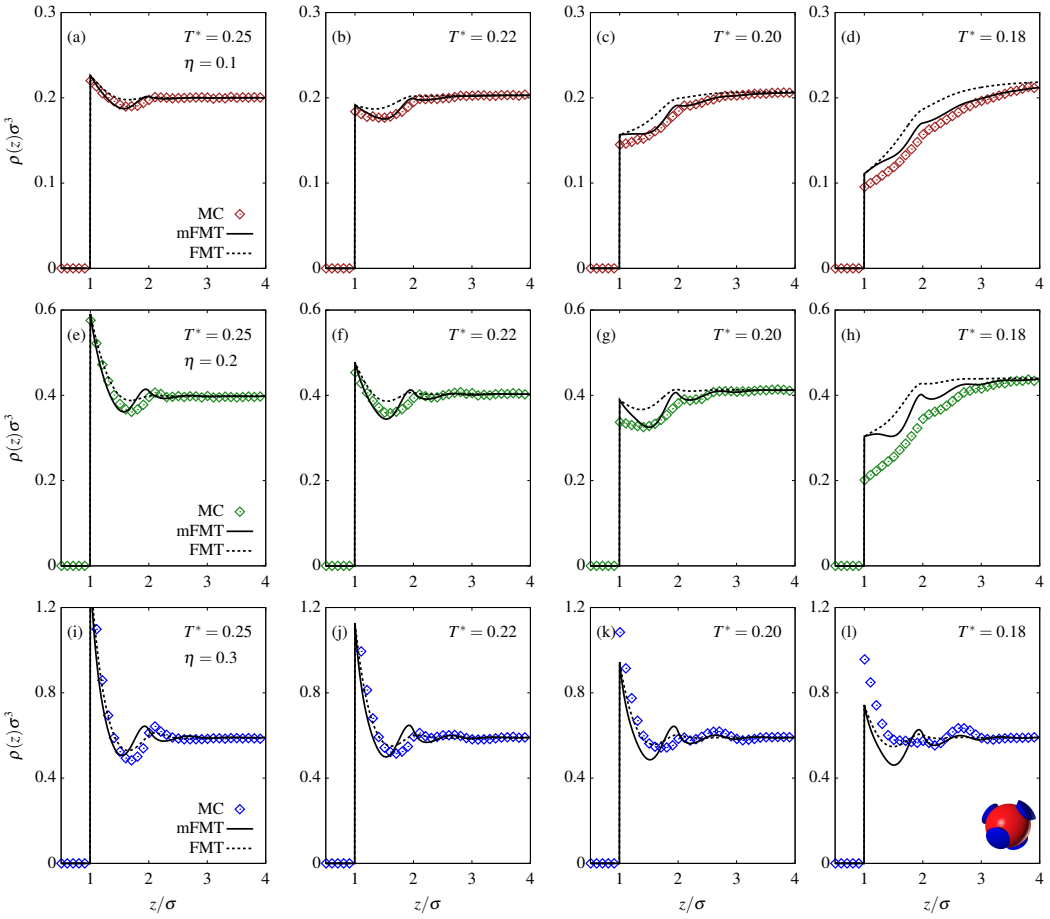

Figure 4.12 Density profiles of tetravalent patchy particles at a hard wall located at $z/\sigma = 0.5$. The individual symbols show results from MC simulations and the lines DFT calculations making use of the mFMT (solid line) and FMT functional (dashed line). The packing fractions are, from top to bottom, $\eta = 0.1$, 0.2, and 0.3. The temperatures, from left to right, are $T^* = 0.25$, 0.22, 0.20, and 0.18. Note that the differences between the contact densities $\rho(\sigma^+)$ arise from deviations between the bulk pressure predicted by TPT1 and simulations.

$T_c^* \approx 0.16$. At the binodal, the pressure of the liquid phase equals the pressure in the gaseous phase, i.e. it is low. As a result, when approaching the binodal from above the critical point, according to Eq. (4.15), we expect a decrease and desorption of the density from the wall. However, performing simulations very close to the binodal is a challenging task as this would require large simulation boxes due to a significant depletion of the density close to the walls. We therefore restrict consideration to temperatures $T^* \geq 0.18$.

For the lowest packing fraction, $\eta = 0.1$, we see that the mFMT approach provides an overall better description than the FMT which overestimates the amount of density close to the wall, particularly at $T^* = 0.18$. At $\eta = 0.2$, however, deviations between the equation of states of theory and simulation are already significant leading to different contact densities and thus a systematic bias. The latter impedes a quantitative comparison. Nevertheless, the qualitative behavior is reasonable and the structural properties seen in simulations are captured by the theoretical curves, even though the mFMT slightly overestimates the degree of structural intensity. No desorption

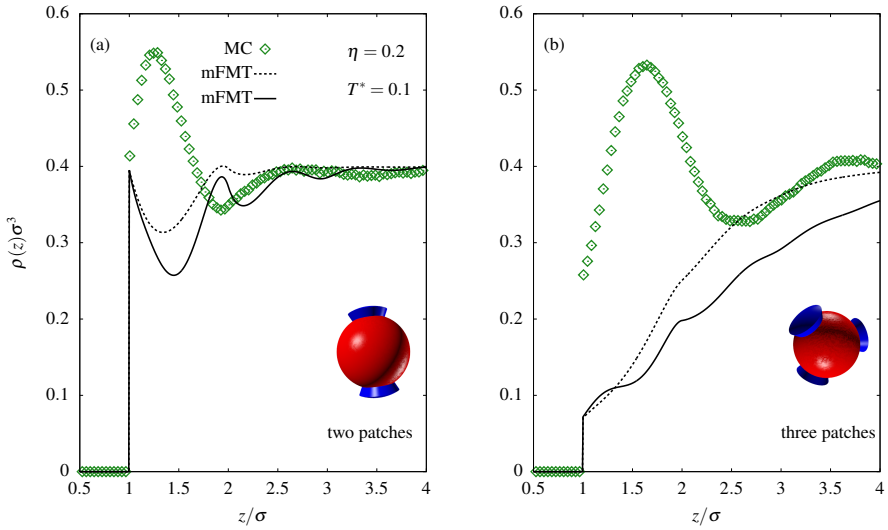

Figure 4.13 Density profiles as obtained from the mFMT functional for the two-site (a) and three-site (b) patchy fluid at a hard wall in comparison to MC results (individual symbols). In both cases the packing fraction is $\eta = 0.2$ and the temperature $T^* = 0.1$.

occurs at a packing fraction of $\eta = 0.3$ when lowering the temperature, and both DFT versions underestimate the contact density. For temperatures $T^* \lesssim 0.20$, the density profiles from simulations exhibit a clear peak in the third layer from the wall at $z \approx 2.5\sigma$ which we can associate with a tetrahedral network signal, similar to what we have observed in the density profile around a hard tracer particle (cf. Sec. 4.2.2). This peak is hardly visible in the DFT results; it may be surmised from the mFMT curves. The latter predicts a significant peak at $r \approx 1.8\sigma$, not seen in the simulations. In light of our discussion in Sec. 4.2, this disagreement may also be a consequence of density functionals failing to capture orientational inhomogeneities as necessarily being introduced by a hard wall.

In particular, the present density functionals have shown to fail dramatically in cases where the patch arrangement is no longer isotropic and the temperature is low [159]. This is demonstrated in Fig. 4.13 where for $\eta = 0.2$ and $T^* = 0.1$ the density profiles of a fluid of chains are displayed in (a) and for trivalent patchy particles in (b). In both cases we observe that simulations predict a significant correlation peak located close to the wall. In contrast, the DFT completely fails to predict these properties. This breakdown of the theory can be traced back to the independence of orientational degrees of freedom [159]: in both cases, at sufficiently low temperatures, the particles close to the hard wall orient and locate themselves such that the plane containing the patches is parallel to the wall resulting in the strong correlation signal at $z \approx 1.5\sigma$.

Chapter 5

Bulk Dynamics and van Hove Function

In the previous Ch. 4, we focused on static properties of patchy fluids including the bulk structure and the asymptotic decay of correlations, or density profiles at a planar hard wall. In thermal equilibrium, these quantities are not time-dependent as external and internal forces are balanced. In this chapter, we will shift consideration to dynamic bulk properties, i.e. diffusive and structural relaxation processes. The questions of interest will involve: How is the mobility of a single particle influenced by bond formation? How is the collective dynamic behavior affected if a system-spanning network occurs?

In order to investigate these questions, we first recall the colloidal picture, where the (patchy) particles are considered as big spheres immersed within a solvent of much smaller molecular particles. We assume the so-called high-friction limit, i.e. any initial momenta of the colloids relax quasi-instantaneously relative to the Brownian time scale $\tau_B = \sigma^2/D_0$, where $D_0 = k_B T/(3\pi\eta_s\sigma)$ is the Stokes-Einstein diffusion coefficient and η_s the viscosity of the solvent. The Brownian time τ_B is a measure for the time that it takes a particle to travel a distance comparable to its own diameter. Typical values for τ_B are $\approx 10^{-3}$ – 10^{-4} s, whereas initial momenta in the large-friction limit relax on time scales of $\approx 10^{-9}$ s [57].

Let us now assume that the interactions among colloidal particles are weak so that the ideal-gas approximation is justified. Then the mean-squared displacement (MSD) $\delta r^2(t) \equiv \langle[\mathbf{r}(t) - \mathbf{r}(0)]^2\rangle$, measuring the average volume that a reference particle has explored at time t relative to some time origin, behaves as $\delta r^2(t) = 6D_0 t$ for all times $t > 0$. In contrast, in a dense colloidal fluid, the single-particle long-time diffusion will be reduced significantly [21, 101] w.r.t. the ideal gas case, i.e. $\delta r^2(t) = 6Dt$ where $D < D_0$ for $t \to \infty$. This is due to many collisions that the reference particle has experienced with other colloidal particles at long times giving rise to a stochastic motion with a reduced diffusion constant. For short-times, $t \ll \tau_B$, the particle diffuses free as $\delta r^2(t) \approx 6D_0 t$ since it has not yet experienced many collisions other colloidal particles. As a result there is an intermediate time regime $t \approx \tau_B$ where the MSD behaves nonlinearly, and decreases to approach its asymptotic long-time value.

As we have discussed in Sec. 1.3, low-valence patchy colloids can give rise to states of matter called 'equilibrium gels' (see Fig. 1.5) at sufficiently low temperatures. These states are characterized by bond lifetimes that are macroscopically large, i.e. on experimental time scales. In general, we expect that bond lifetimes will increase continuously with decreasing temperature. For short times and temperatures T well below the critical value, $T \ll T_c$, we expect that the particles can 'vibrate' in their initial local environment, i.e. small orientational and translational changes may be possible if they comply with the geometric restrictions of the anisotropic pair potential. However, for a sufficiently strong attraction it is unlikely that many particles will frequently break existing bonds and we expect this to be reflected in ensemble averaged dynamic quantities such as the MSD as compared to a weakly bonded network fluid.

In this chapter, we shall study the bulk dynamics of tetravalent patchy particles by means of dynamic Monte-Carlo simulations [167, 168] (see Appendix B for details). In particular, we seek for signals indicating changes in the dynamics due to association and network formation, where our studies go closely along the lines of earlier work [78, 51, 79]. We will also explore the possibility to account for the dynamics of patchy fluids by means of dynamical density functional theory (DDFT) [169, 80], the dynamic counterpart of equilibrium DFT. We build on a recent framework which has been proposed by Stopper, Hansen-Goos and Roth, based on foundational work of Hopkins and Schmidt [81, 101] extending Percus' test particle approach beyond the equilibrium case, allowing to investigate the bulk dynamics of hard spheres [82], hard disks [83] or model colloid-polymer mixtures [170].

5.1 Results from dynamic Monte-Carlo simulations

5.1.1 Mean-squared displacement

We simulated systems consisting of $N = 7500$ tetravalent ($M = 4$) at packing fraction $\eta = 0.3$, and trivalent ($M = 3$) patchy particles at packing fraction $\eta = 0.25$ up to times $t = 50\tau_B$. In both cases, the considered densities are on the right-hand side of the liquid branch of the gas-liquid coexistenc curves [148]. The investigated temperatures range from $T^* = 0.5$ down to 0.06 for trivalent particles [critical point: $(\eta_c, T_c^*) = (0.07, 0.125)$] and from $T^* = 0.5$ down to 0.12 for tetravalent particles [critical point: $(\eta_c, T_c^*) = (0.14, 0.168)$]. For comparison, we also simulated bare hard spheres at a packing fraction $\eta = 0.3$. We waited for 5×10^6 MC prior to all measurements, where we employed the aggregation-volume bias moves to boost equilibration [142]. The number of chosen equilibration steps appeared to be sufficient to ensure that the internal energies, as a function of MC steps, had reached plateaus. The MSD was calculated directly from its statistical definition $\langle[\mathbf{r}(t) - \mathbf{r}(0)]^2\rangle$, where $\mathbf{r}(t)$ is the position of a tagged particle at time t, and $\langle\cdot\rangle$ denotes an average over configurations and all particles (see Sec. B.3 in Appendix B).

In Fig. 5.1 we display the simulated MSDs as a function of t/τ_B normalized w.r.t. to the ideal gas law $\delta r_{\mathrm{id}}^2(t) = 6\sigma^2\, t/\tau_B$. Fig. 5.1 (a) shows results for tetravalent and (b)

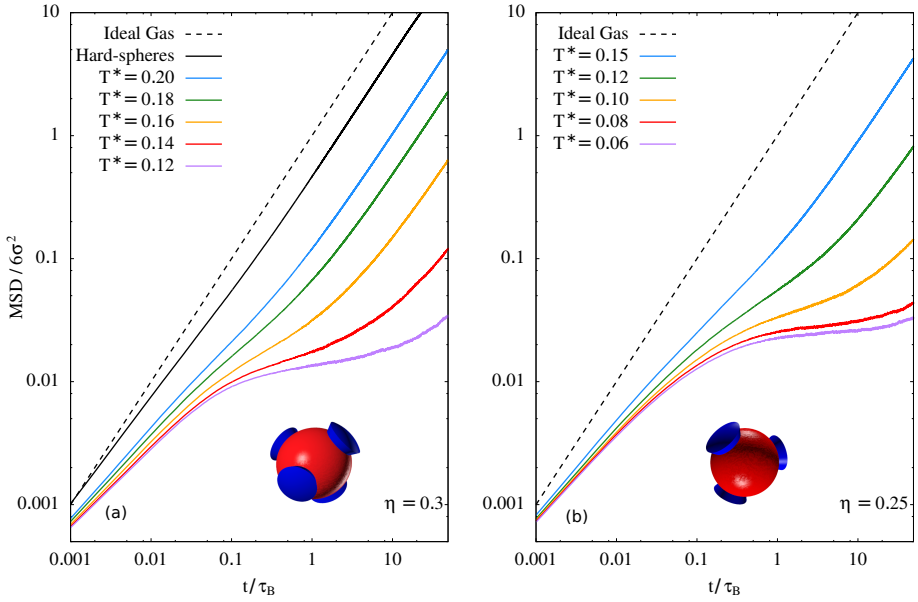

Figure 5.1 Mean-squared displacement normalized relative to its ideal-gas value for tetravalent (a) and trivalent (b) patchy particles as obtained from dynamic MC simulations for several temperatures (see key). The packing fraction is $\eta = 0.3$ in (a) and 0.25 in (b). All state points lie outside of the gas-liquid coexistence region.

for trivalent patchy particles, where the dashed line shows the idel gas result. The data is displayed on a double logarithmic scale in order to highlight the crossover from the short-time diffusion regime for $t \ll \tau_B$ to the long-time diffusion regime for $t \to \infty$. In the hard-sphere limit (i.e. at high temperatures), the MSD exhibits the usual behavior: for short times, the particles diffuse with the Stokes-Einstein ideal-gas diffusivity D_0, as here the particles on average have not experienced many collisions with other particles. For longer times, the MSD behaves nonlinearly and rather quickly approaches its long-time limit with a reduced diffusivity $D_{\mathrm{HS}} < D_0$ (which can be extracted from the asymptotic slope of the MSD, however the difference between D_{HS} and D_0 is hardly visible on the scale of the graph).

For the two state points marked by the blue lines [$T^* = 0.2$ in (a) and $T^* = 0.15$ in (b)], which are located well below the percolation line (here the degree of polymerization is $\gtrsim 97\%$ – see Fig. 3.2), the long-time diffusivity D is clearly reduced although the overall behavior of the MSD is similar to that in the hard-sphere fluid. This indicates that at these temperatures the diffusive motion of the particles is not affected dramatically by bond and cluster formation.

However, the behavior of the MSD changes considerably upon on approaching the lowest considered temperatures ($T^* = 0.12$ in (a) and 0.06 in (b)). Here, the MSDs become very flat at intermediate times, indicating particle caging: as written earlier, for short times we expect that particles can move and rotate in their local environment rather undisturbed and indeed, for $t/\tau_B \to 0$ all MSDs are rather close to each other. For longer times it is unlikely that bonds are broken, which impedes particles from diffusing quickly over distances greater than the range of the site-site interaction resulting in plateaus that spans over roughly two order magnitudes in time. For

even lower temperatures this trend is expected to become more pronounced [78, 79], eventually reaching the equilibrium gel state with macroscopically long bond lifetimes.

In the long-time limit the MSDs will increase again with a linear slope but with dramatically reduced diffusion constants. This is related to the fact that the probability of forming or breaking bonds is very low but, of course, non-zero as long as $T > 0$. Thus, in the long-time limit, $t \to \infty$, particles eventually loose memory about their initial bonding state. In the subsequent Sec. 5.1.2, we will focus on the dynamic behavior of spatial correlations.

5.1.2 The van Hove function of tetravalent patchy particles

The van Hove function $G(\mathbf{r},\, t)$ [171] is a key quantity in order to investigate the temporal behavior of density correlations in a fluid. It in particular allows one to study single particle (or self) dynamics as well as the collective behavior caused by all particles on equal footing. As such, $G(\mathbf{r},\, t)$ for instance has proven to be of great value for characterizing phenomena such as glass- [21] or gel-transitions [172]. The van Hove function is defined as [57]

$$\begin{aligned} G(\mathbf{r}, t) &= \frac{1}{N} \left\langle \sum_{i=1}^{N} \sum_{j=1}^{N} \delta(\mathbf{r} + \mathbf{r}_j(0) - \mathbf{r}_i(t)) \right\rangle \\ &\equiv G_s(\mathbf{r}, t) + G_d(\mathbf{r}, t)\,, \end{aligned} \tag{5.1}$$

where $\langle\cdot\rangle$ denotes an configurational average, and $\delta(\cdot)$ is the Dirac delta function. Physically, $G(\mathbf{r},\, t)$ describes the probability that a particle i is located at position $\mathbf{r}$ at time t, given that there has been another particle j at the origin $\mathbf{r} = 0$ at time $t = 0$. Furthermore, by discriminating between the cases $i = j$ and $i \neq j$, it naturally splits into the self part $G_s(\mathbf{r},\, t)$, describing the motion of the (test) particle initially located at the origin, and the distinct part $G_d(\mathbf{r},\, t)$ accounting for the behavior of the surrounding particles. For a uniform bulk system, Eq. (5.1) depends only on the distance $r = |\mathbf{r}|$ to the origin. Technically, $G(r,\, t)$ is a correlation function on the two-particle level, similar to the radial distribution function $g(r)$. In fact, for $t = 0$, the distinct part is exactly given by $G_d(r,\, 0) = \rho_b g(r)$. The self part satisfies $G_s(r,\, 0) = \delta(\mathbf{r})$. In the long-time limit we have $G_d(r,\, t \to \infty) = \rho_b$ and $G_s(r,\, t \to \infty) = 0$. The MSD, alternatively to its statistical definition, is the second moment of $G_s(r,\, t)$, i.e.

$$\delta r^2(t) = 4\pi \int_0^\infty \mathrm{d}r\, r^4\, G_s(r,\, t)\,. \tag{5.2}$$

Note that from Eq. (5.2) it follows that only a pure Gaussian form of $G_s(r,\, t)$ gives rise to a strictly linear MSD as a function of time. For $t \to \infty$ we thus have

$$G_s(r,\, t) = \frac{1}{(4\pi D t)^{3/2}} \exp\left[-r^2/(4Dt)\right]\,, \tag{5.3}$$

which, when plugged into Eq. (5.2), gives rise to $\delta r^2(t) = 6Dt$.

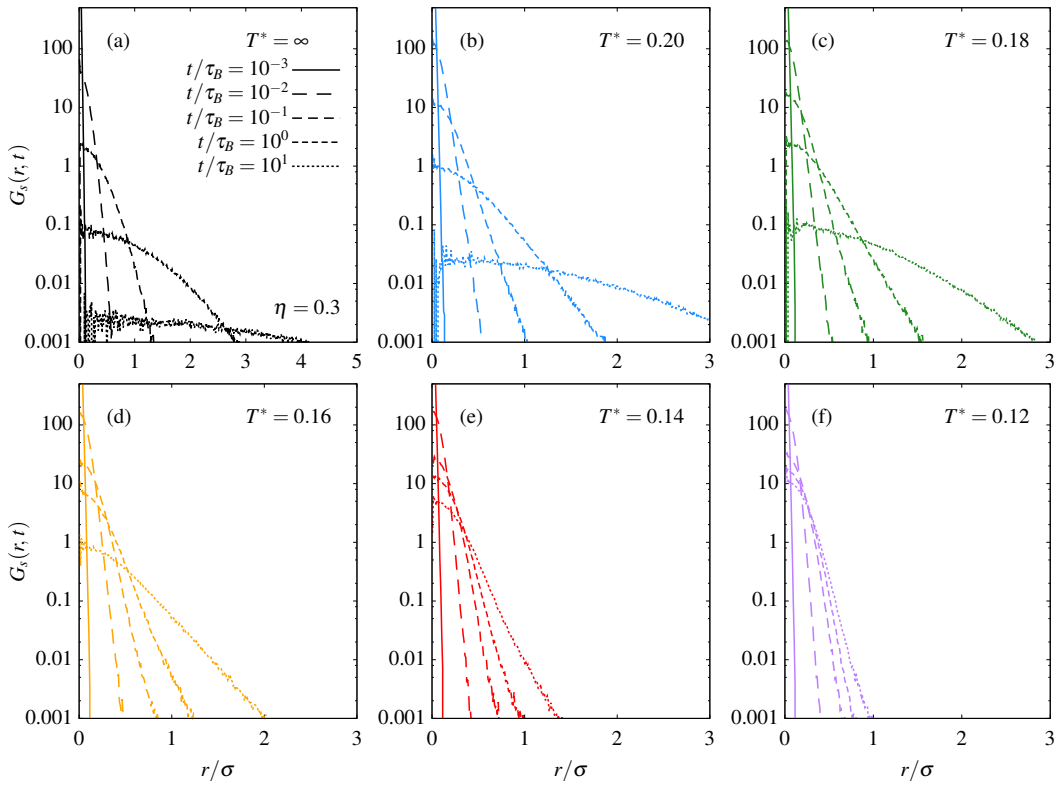

Figure 5.2 Simulation results for the self part $G_s(r, t)$ of the van Hove function of tetravalent patchy particles for the same temperatures, packing fraction and color code as in Fig. 5.1 (a). The times are shown in logarithmic steps, i.e. $t/\tau_B = 10^{-3}$ (solid lines), 10^{-2} (long dashed), 10^{-1} (medium dashed), 10^0 (short dashed) and 10^1 (dotted).

Behavior of $G_s(r, t)$. We first focus on the behavior of the self part $G_s(r, t)$ for tetravalent patchy particles (the results of the three-patch case do not provide much new insight, and, therefore, are not discussed). This is displayed in Figs. 5.2 (a) – (f) for the same temperatures T^* and packing fraction as in Fig. 5.1 (a); for clarity, the same color coding is used. In each figure, we show results at times $t/\tau_B = 10^{-3}$ (solid), 10^{-2} (long-dashed), 10^{-1} (medium-dashed), 10^0 (short-dashed) and 10^1 (dotted). The magnitude of $G_s(r, t)$ is shown on a logarithmic scale. Even for rather dense hard-sphere systems it is known that $G_s(r, t)$ to a good approximation has the form of a Gaussian distribution [101, 173], which is the exact result for the ideal gas and the long-time limit, cf. Eq. (5.3). This complies with what we observe in Fig. 5.2 (a), where $G_s(r, t)$ appears also to be of Gaussian form for all times. However, the behavior and shape of $G_s(r, t)$ changes if directional interactions start to play a role. While for $T^* = 0.2$ and 0.18 the self part seems to be of Gaussian shape at short and long times, at intermediate times $t/\tau_B \approx 10^{-2}$ – 10^0 we observe a clear deviation from a Gaussian distribution, where $G_s(r, t)$ exhibits an exponential tail, i.e. $G_s(r, t) \sim e^{-r/\lambda(t)}$, where $\lambda(t)$ is a characteristic length scale increasing with time. The deviation of the self part from Gaussian shape becomes more pronounced as the temperature is lowered. In particular, in Figs. 5.2 (d) – (f) we observe that $G_s(r, t)$ exhibits an exponential tail up to 10 Brownian times. Moreover, for the lowest temperatures [Figs. 5.2 (e) and (f)],

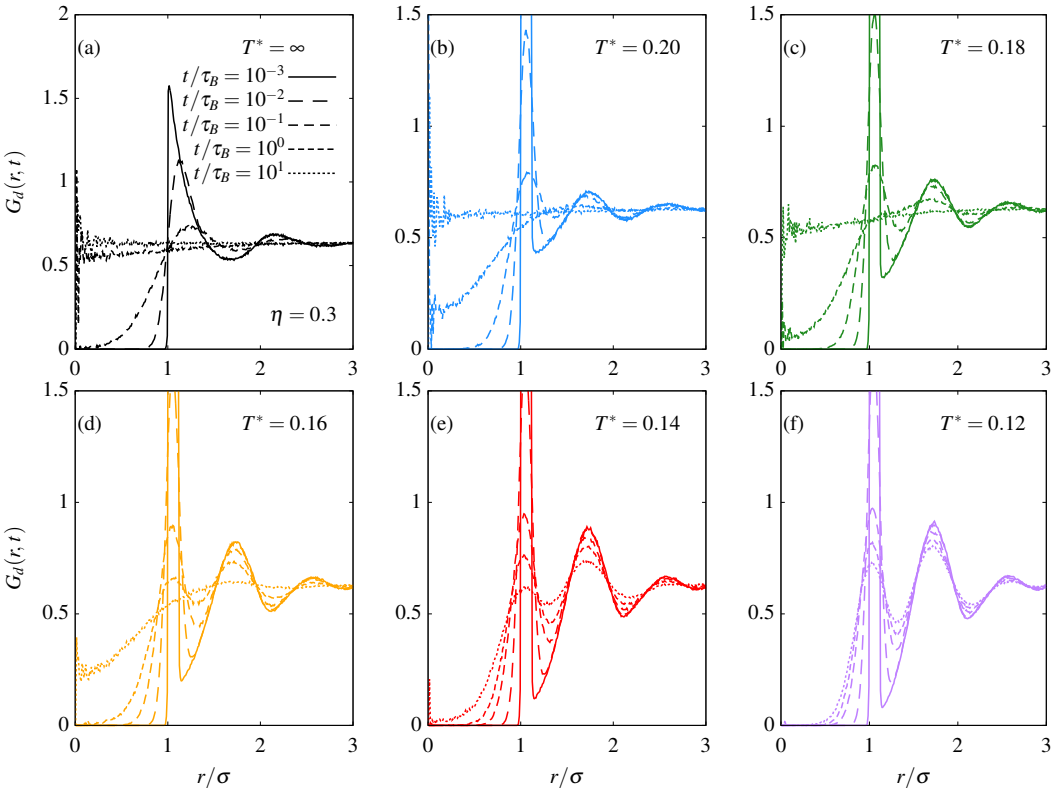

Figure 5.3 Simulation results for the distinct part $G_d(r, t)$ of the van Hove function of tetravalent patchy particles for the same state points as in Fig. 5.2.

$G_s(r, t)$ is still significantly peaked at the origin, suggesting that most of the particles have not yet diffused over distances larger than their diameter. This complies with the behavior of the corresponding MSDs at these temperatures, which do not have entered the Gaussian diffusion regime with a linearly increasing MSD at $t = 50\tau_B$ (cf. red and purple curves in Fig. 5.1).

Behavior of $G_d(r, t)$. The distinct part $G_d(r, t)$ of the van Hove function contains all information about the correlations between a particle i located at the origin at time $t = 0$ and particles j located at distance r to the origin at time t, where $i \neq j$. As mentioned above, $G_d(r, 0) = \rho_b g(r)$. In Figs. 5.3 (a) – (f) we show the distinct part for the same packing fraction, temperatures and times as in Figs. 5.2 (a)–(f). In the upper panel, $G_d(r, t)$ has relaxed nearly to the asymptotic result $G_d(r, \infty) = \rho_b$ for $t \approx 10\tau_B$. For hard spheres, this state is already reached after roughly one Brownian time. Interestingly, we observe that the first correlation peak, corresponding to the shell of bonded nearest neighbors, decays significantly faster than the second peak. This becomes more pronounced at lower temperatures, see bottom panel. For $T^* = 0.14$ (e) and 0.12 (f), a significant correlation structure is retained even for very long times $t \approx 50\tau_B$, in accordance with the behavior of the MSD and self part $G_s(r, t)$. Note that the corresponding static correlation functions at $t = 0$, where $G_d(r, 0) = \rho_b g(r)$, do not exhibit such a strong temperature dependence. Indeed, once the bond probability

p_b has reached 100% and the network has formed, no significant changes in static correlations are expected upon on further decreasing the temperature. We conclude that it is both worth and necessary to also investigate dynamic quantities in addition to static and thermodynamic properties in order to fully determine phenomena arising in fluids with anisotropic interactions.

5.2 Dynamic DFT approach

Wertheim's theory for bulk patchy fluids cannot describe dynamic properties, nor can equilibrium DFT. However, an dynamic version of the latter, dynamic density functional theory (DDFT), allows us to also investigate non-equilibrium phenomena within the framework set by equilibrium DFT. The latter is, from a mathematical point of view rigorous, and approximations are typically introduced when seeking for explicit expressions of excess free energy functionals. By contrast, dynamic DFT already introduces approximations on a more fundamental level. It assumes that exact relations on the two-body (and higher-order) level, valid in equilibrium, hold also out-of-equilibrium [169, 80]; this means that DDFT assumes that higher-order correlations equilibrate much faster, quasi-instantaneously, compared to the respective one-body quantities. Nevertheless, DDFT has been applied successfully to spinodal decomposition [80], colloidal sedimentation [174], quasi-crystal formation [175], or cell growth in tissues and tumors [176].

DDFT along with Rosenfeld's FMT has been employed to approximate the van Hove function of hard spheres [101, 82] hard disks [83] and model colloid-polymer mixtures [170] within a dynamic extension of Percus' test particle theory [81]. It treats a one-component system as a binary mixture of species s (self) consisting of only the test particle, and species d (distinct) which consists of the remaining $N-1$ particles. Hence, in thermal equilibrium at time $t=0$, the one-body density distribution $\rho_d(r,t=0)$ around species s is given by $\rho_d(r,t=0)=\rho_b g(r)$, and $\rho_s(r,t=0)=\delta(\mathbf{r})$. Now assume that the coordinate system is fixed in space at the original position of the tagged particle. Thus for times $t>0$, we can follow the time evolution of the densities $\rho_s(r,t)$ and $\rho_d(r,t)$. Considering the definition of $G(r,t)$, we can identify $\rho_s(r,t)\equiv G_s(r,t)$ and $\rho_d(r,t)\equiv G_d(r,t)$. In previous studies [101, 177, 82] it turned out that the quality of the results compared to those from simulations depends crucially on the precise treatment of the self component s, which represents one single particle – the free-energy functionals of equilibrium DFT are constructed within the grand-canonical ensemble, and particle fluctuations are known to yield unphysical contributions in systems where particles are treated explicitly [178, 179]. Importantly, in Ref. 82 a method was derived which removes possible self-interactions within the FMT-based functionals by considering the zero-dimensional crossover and a proper modeling of the grand potential in that situation.

In this section, we explore the possibility to determine the van Hove function of associating fluid via DDFT and the dynamic test particle approach. In the next section

5.2.1, we shall therefore outline briefly the basics of DDFT; in the subsequent Sec. 5.2.2 we give more details on the dynamic test particle theory for hard spheres. We then attempt to augment the ideas to the patchy fluid in Sec. 5.2.3.

5.2.1 Dynamic density functional theory

The dynamical behavior of a system of N classical (identical) colloids with positions $\mathbf{r}_i,\ i = 1, .., N$ in the overdamped (high-friction) limit can be described by the following set of Langevin equations [12]:

$$\Gamma^{-1} \frac{\mathrm{d}\mathbf{r}_i}{\mathrm{d}t} = \mathbf{F}_i + \eta_i(t) \ , \tag{5.4}$$

where Γ^{-1} is a friction constant due to the motion of the Brownian particles through the solvent, $\eta_i(t)$ is a stochastic force caused by random collisions of the solvent molecules with the colloids, fulfilling the condition $\langle \eta_i(t) \rangle = 0$. Note that Γ is related to ideal-gas diffusivity via $D_0 = k_B T \Gamma$. Furthermore, in this section, $\langle \cdot \rangle$ denotes an average over initial conditions of the solvent and $\mathbf{F}_i$ denotes the external force acting on particle i, which can be decomposed into the gradient of the inter-particle potential $\Phi(\mathbf{r}_1, .., \mathbf{r}_N)$ and an arbitrary external potential V_{ext}. Assuming $\Phi(\mathbf{r}_1, .., \mathbf{r}_N)$ to be a sum over a pair interaction potential, which depends only on the distance between two colloids k and j, yields an expression for $\mathbf{F}_i$:

$$\mathbf{F}_i = -\nabla_i \left(\frac{1}{2} \sum_{k=1}^{N} \sum_{j \neq k}^{N} \phi(|\mathbf{r}_k - \mathbf{r}_j|) + \sum_{k=1}^{N} V_{\mathrm{ext}}(\mathbf{r}_k) \right) \tag{5.5}$$

Following Marconi and Tarazona [169] the set of equations in Eq. (5.4) can be rewritten as

$$\begin{aligned} \frac{\partial \rho(\mathbf{r}, t)}{\partial t} &= \nabla \left[k_B T \nabla \rho(\mathbf{r}, t) + \rho(\mathbf{r}, t) \nabla V_{\mathrm{ext}}(\mathbf{r}) \right] \\ &\quad + \nabla \left[\int \mathrm{d}\mathbf{r}' \ \rho^{(2)}(\mathbf{r}, \mathbf{r}', t) \nabla \phi(|\mathbf{r} - \mathbf{r}'|) \right] \ , \end{aligned} \tag{5.6}$$

where $\rho(\mathbf{r}, t)$ is the ensemble-averaged one-body density distribution

$$\rho(\mathbf{r}, t) = \langle \hat{\rho}(\mathbf{r}, t) \rangle = \left\langle \sum_{i=1}^{N} \delta(\mathbf{r}_i(t) - \mathbf{r}) \right\rangle \ , \tag{5.7}$$

and $\rho^{(2)}(\mathbf{r}, \mathbf{r}', t) = \langle \hat{\rho}(\mathbf{r}, t) \hat{\rho}(\mathbf{r}', t) \rangle$ is the time-dependent two-body distribution function. Unfortunately, in general $\rho^{(2)}(\mathbf{r}, \mathbf{r}', t)$ is not known exactly. Therefore some approximations have to be made. One possibility is to make the assumption that the relation

$$k_B T \rho_{\mathrm{eq}}(\mathbf{r}) \nabla c^{(1)}(\mathbf{r}) = - \int \mathrm{d}\mathbf{r}' \ \rho^{(2)}_{\mathrm{eq}}(\mathbf{r}, \mathbf{r}') \nabla \phi(|\mathbf{r} - \mathbf{r}'|) \ , \tag{5.8}$$

where

$$c^{(1)}(\mathbf{r}) = -\beta \left. \frac{\delta \mathcal{F}_{\rm ex}[\rho(\mathbf{r})]}{\delta \rho(\mathbf{r})} \right|_{\rho=\rho_{\rm eq}} , \tag{5.9}$$

which holds for $\rho^{(2)}_{\rm eq}(\mathbf{r}, \mathbf{r}')$ in thermodynamic equilibrium, can be used as an approximation also for non-equilibrium systems [169, 80]. Substituting Eqs. (5.8) and (5.9) into Eq. (5.6) yields to the key equation of dynamical density functional theory:

$$\frac{\partial \rho(\mathbf{r},t)}{\partial t} = \Gamma \nabla \cdot \left[\rho(\mathbf{r},t) \nabla \frac{\delta F[\rho(\mathbf{r},t)]}{\delta \rho(\mathbf{r},t)} \right] , \tag{5.10}$$

where $F_{\rm ex}[\rho]$ denotes the *full* free energy functional, i.e.

$$\begin{aligned} F[\rho(\mathbf{r},t)] = k_B T \int {\rm d}\mathbf{r}\ \rho(\mathbf{r},t) \left(\ln \left(\lambda_{\rm th}^3 \rho(\mathbf{r},t) \right) - 1 \right) \\ + \mathcal{F}_{\rm ex}[\rho(\mathbf{r},t)] + \int {\rm d}\mathbf{r}\ \rho(\mathbf{r},t) V_{\rm ext}(\mathbf{r},t) \, . \end{aligned} \tag{5.11}$$

Note that in this derivation of DDFT the mobility Γ is assumed to be a constant in space and time; Eq. (5.10) can be generalized to include a time- and space-dependent mobility (or, diffusivity):

$$\frac{\partial \rho(\mathbf{r},t)}{\partial t} = \nabla \cdot \left(\Gamma(\mathbf{r},t) \left[\rho(\mathbf{r},t) \nabla \frac{\delta F[\rho(\mathbf{r},t)]}{\delta \rho(\mathbf{r},t)} \right] \right) . \tag{5.12}$$

The multi-component generalization of Eq. (5.12) to a system consisting of ℓ species of colloids with radii $R_i\,,\ i = 1, ..., \ell$ is given by [180]

$$\frac{\partial \rho_i(\mathbf{r},t)}{\partial t} = \nabla \cdot \left(\Gamma_i(\mathbf{r},t) \left[\rho_i(\mathbf{r},t) \nabla \frac{\delta F[\{\rho_j\}]}{\delta \rho_i(\mathbf{r},t)} \right] \right) , \tag{5.13}$$

where the Helmholtz free energy functional now takes the form

$$\begin{aligned} F[\{\rho_i\}] = k_B T \sum_{i=1}^{\ell} \int {\rm d}\mathbf{r}\ \rho_i(\mathbf{r},t) \left[\ln \left(\lambda_{\rm th}^3 \rho_i(\mathbf{r},t) \right) - 1 \right] \\ + \mathcal{F}_{\rm ex}[\{\rho_i\}] + \sum_{i=1}^{\ell} \int {\rm d}\mathbf{r}\ \rho_i(\mathbf{r},t) V^i_{\rm ext}(\mathbf{r}). \end{aligned} \tag{5.14}$$

5.2.2 Dynamic test particle theory for hard spheres

As outlined earlier, it is possible to employ DDFT within the framework of dynamic test particle theory to calculate the van Hove function of hard spheres or hard disks. In this section, we will review the key elements. The adoption to the associating fluid is then (to some extent) straight forward.

For a binary mixture consisting only of self (s) and distinct particles (d), the key equation of DDFT, written in the form of a continuity equation, can be written as (we

use the notation of Ref. 82)

$$\frac{\partial \rho_{s/d}(\mathbf{r},t)}{\partial t} = -\nabla \cdot \mathbf{j}_{s/d}(\mathbf{r},t)\,, \tag{5.15}$$

where the particle currents $\mathbf{j}_{s/d}(\mathbf{r},t)$ read

$$\mathbf{j}_{s/d}(\mathbf{r},t) = -D_{s/d}(\mathbf{r},t)\rho_{s/d}(\mathbf{r},t)\nabla\beta\mu_{s/d}(\mathbf{r},t)\,, \tag{5.16}$$

with the local chemical potentials $\mu_{s/d}(\mathbf{r},t)$ obtained from the functional-derivative of the intrinsic Helmholtz free-energy functional (as there is no external field):

$$\mu_{s/d}(\mathbf{r},t) = \frac{\delta\mathcal{F}[\rho_s,\rho_d]}{\delta\rho_{s/d}(\mathbf{r},t)}\,. \tag{5.17}$$

Note that the DDFT equations have to be integrated forward in time numerically. Prior to this step it is useful to carry out functional derivatives and apply gradients by hand to reduce the complexity of the equations. The resulting expressions may then be integrated via e.g. a simple Euler-forward algorithm if the associated time step Δt is chosen sufficiently small. A good choice is e.g. $\Delta t = 10^{-5}\tau_B$.

In Ref. 82 we derived a method to remove unphysical self-self interactions occurring within the FMT functionals for hard spheres. It is based on the idea that in the zero-dimensional limit, i.e. a cavity that can hold at most one particle, the free energy takes a specific form that can be constructed explicitly from the associated partition sum. The final result for the binary-mixture FMT functional reads (either Rosenfeld's original version or more accurate versions such as White-Bear Mark 2 may be used):

$$\mathcal{F}^q_{\mathrm{ex}}[\rho_s,\rho_d] = \mathcal{F}^{\mathrm{HS}}_{\mathrm{ex}}[\rho_s,\rho_d] - \mathcal{F}^{\mathrm{HS}}_{\mathrm{ex}}[\rho_s]\,, \tag{5.18}$$

so the unphysical self-self interactions are simply subtracted from the full mixture FMT functional, which is referred to as 'quenched' approach (hence the superscript 'q'). Note that in Eq. (5.16) a space- and time-dependent particle self-diffusivity $D(\mathbf{r},t)$ is assumed, in oder to capture effects of high particle densities on the self-diffusion. In contrast, standard DDFT is not capable of adequately describing the crossover from free diffusion at very short times to the slowed down long-time self-diffusivity $D_{\mathrm{HS}} < D_0$ at long times [101, 177]: The MSD given by standard DDFT typically shows the onset of a decrease at intermediate times, but subsequently speeds up to ideal-gas diffusion in the long-time limit. Hereby the theory predicts a behavior of the MSD which is akin to superdiffusivity, but is clearly unphysical in the context of overdamped equilibrium dynamics. This failure is due to the fact that the decay of $G_s(r,t)$ in standard DDFT can be affected only by structural information that is encoded within the respective distinct part of the van Hove function. However, for long times, when the correlations in $G_d(r,t)$ have decayed sufficiently to a flat bulk profile, and thus structural information is lost, DDFT is bound to yield the (incorrect) ideal-gas diffusivity. In order to fix this shortcoming, a result obtained by Leegwater

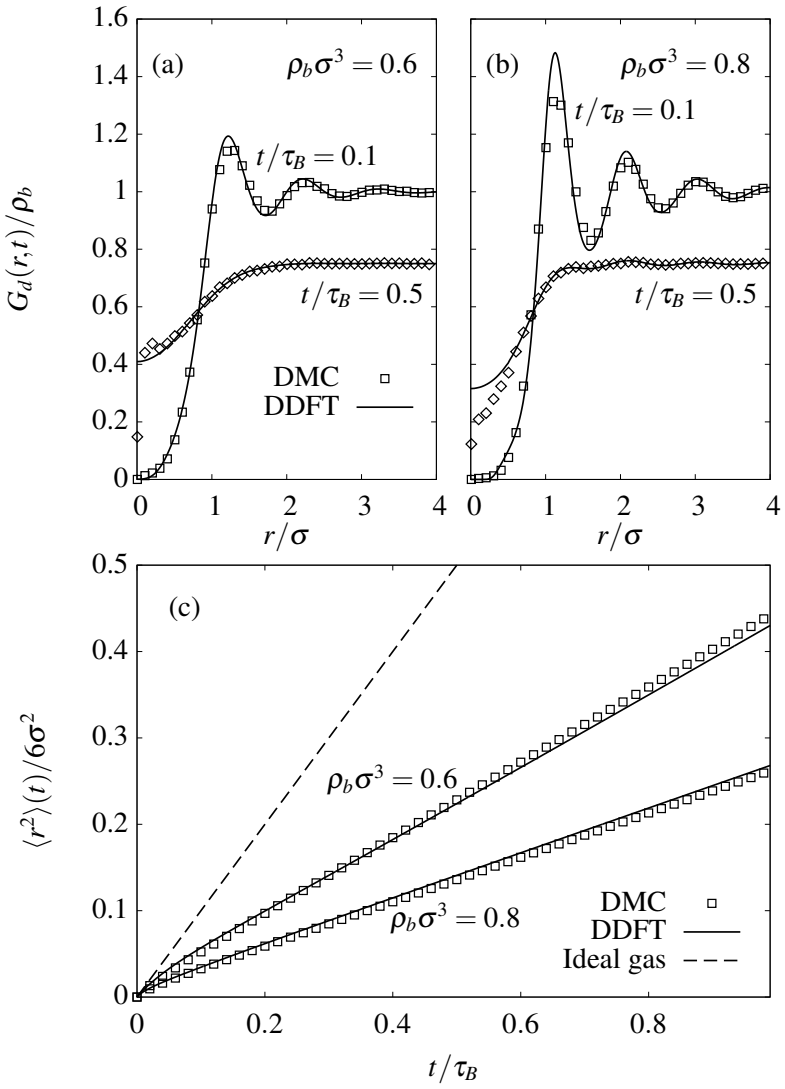

Figure 5.4 Top: DDFT results (solid lines) for the distinct part of the van Hove function of hard spheres using the FMT functional (5.18) and the diffusivity given in Eq. (5.20) compared to DMC results (symbols). Bottom: the mean-squared displacement obtained from the self part of the van Hove function via Eq. (5.2). The graphic is reproduced from D. Stopper, H. Hansen-Goos and R. Roth, J. Phys.: Condens. Matter **28**, 455101 (2016).

and Szamel [181] for the long-time diffusivity $D_{\mathrm{HS}}(\eta)$ of the hard-sphere fluid at packing fraction η can be employed [82]. Leegwater and Szamel obtained the expression

$$D_{\mathrm{HS}}(\eta) = \frac{D_0}{1 + 2\eta g(\sigma^+)}\,, \tag{5.19}$$

where D_0 is the mobility of the spheres in the dilute limit and $g(\sigma^+)$ is the radial distribution function at contact, itself a function of η (see Eq. (3.14)). As Yu and Wu have done in their construction of the (m)FMT functional for the patchy fluid, we may generalize to the inhomogeneous fluid by employing the local packing fraction based on the weighted density n_3, which integrates the fluid density over the volume of a sphere.

Hence in the bulk fluid $n_3 = \eta$ while in the inhomogeneous fluid we have $0 \leq n_3 \leq 1$. More specifically we set

$$D_s(\mathbf{r},t) \equiv D_{\text{HS}}(n_3^d(\mathbf{r},t))\,,\;\; D_d(\mathbf{r},t) \equiv D_{\text{HS}}(n_3^s(\mathbf{r},t) + n_3^d(\mathbf{r},t))\,. \tag{5.20}$$

These definitions take into account that there are no interactions within the self-component, consequently the respective mobility depends only on $n_3^d(\mathbf{r})$. Obviously, in the long-time limit where $n_3^s \to 0$ and $n_3^d \to \eta$ the correct values for the mobility are obtained. The definition further ensures that for short times, $t \to 0$, the self particle can diffuse freely. For illustration, in Figs. 5.4 (a) and (b), replotted from Ref. 170, we show results (solid lines) for the distinct part $G_d(r,\, t)$ obtained from DDFT along with Eqs. (5.18) and (5.20) and compare these to DMC simulation results (symbols). The (reduced) densities are $\rho_b\sigma^3 = 0.6$ in (a) and 0.8 in (b). The agreement between simulation and DDFT is very good; also, the accompanying MSD, obtained from the self part of the van Have function via Eq. (5.2), displayed in Fig. 5.4 (c), is very close to the simulation results.

5.2.3 Hard-sphere tracer immersed in the patchy fluid

We will now discuss results from DDFT for the dynamics of a single hard spherical test particle, diffusing in a surrounding fluid of tetravalent patchy particles. The consideration of hard-sphere like test particle poses a simplification as regards the theoretical modeling: we do not have to take care of how to treat a patchy test particle at times $t > 0$. The 'distinct part' $\rho_d(r,t)$, i.e. the density around the hard tracer at time t, is then, of course, not equivalent to the bulk counterpart $G_d(r,\, t)$ discussed earlier in Sec. 5.1.2. Nevertheless, $\rho_d(r,\, t)$ should capture essential physics: The influence of increasing bond lifetimes on the distinct dynamics as the temperature is lowered. The associated excess free-energy functional, to be employed along with the DDFT equations (5.15), (5.16), and (5.17) for times $t^* > 0$, is given by:

$$\mathcal{F}_{\text{ex}}[\rho_s,\rho_d] = \mathcal{F}_{\text{ex}}^{\text{HS}}[\rho_s,\rho_d] + \mathcal{F}_{\text{ex}}^{\text{bond}}[\rho_d] - \mathcal{F}_{\text{ex}}^{\text{HS}}[\rho_s]\,, \tag{5.21}$$

where the mFMT version for the bonding free-energy functional $\mathcal{F}_{\text{ex}}^{\text{bond}}[\rho]$ is employed.

We solved the respective DDFT equations up to times of $t^* = 0.5$ for the same state points as shown in Fig. 4.3, where we used the displayed density profiles as an initialization for $\rho_d(r,0)$. The self part $\rho_s(r,t)$ is initialized as a normalized, sharply peaked, Gaussian distribution: $\rho_s(r,0) = (\beta/\pi)^{3/2}\exp(-\beta r^2/\sigma^2)$ with $\beta = 10^3$. Further implementation details can be found e.g. in Refs. [177, 170]. The diffusivity $D_{s/d}(\mathbf{r},\, t)$ is that of hard-spheres, i.e. Eq. (5.20). We also performed accompanying DMC simulations in order to check the DDFT results. The methodology does in principle not differ from the usual DMC method (cf. Appendix B); however, now the test particle is distinguished from the other particles. This means that histogram recordings, in contrast to calculating e.g. the bulk van Hove function, cannot be averaged over all

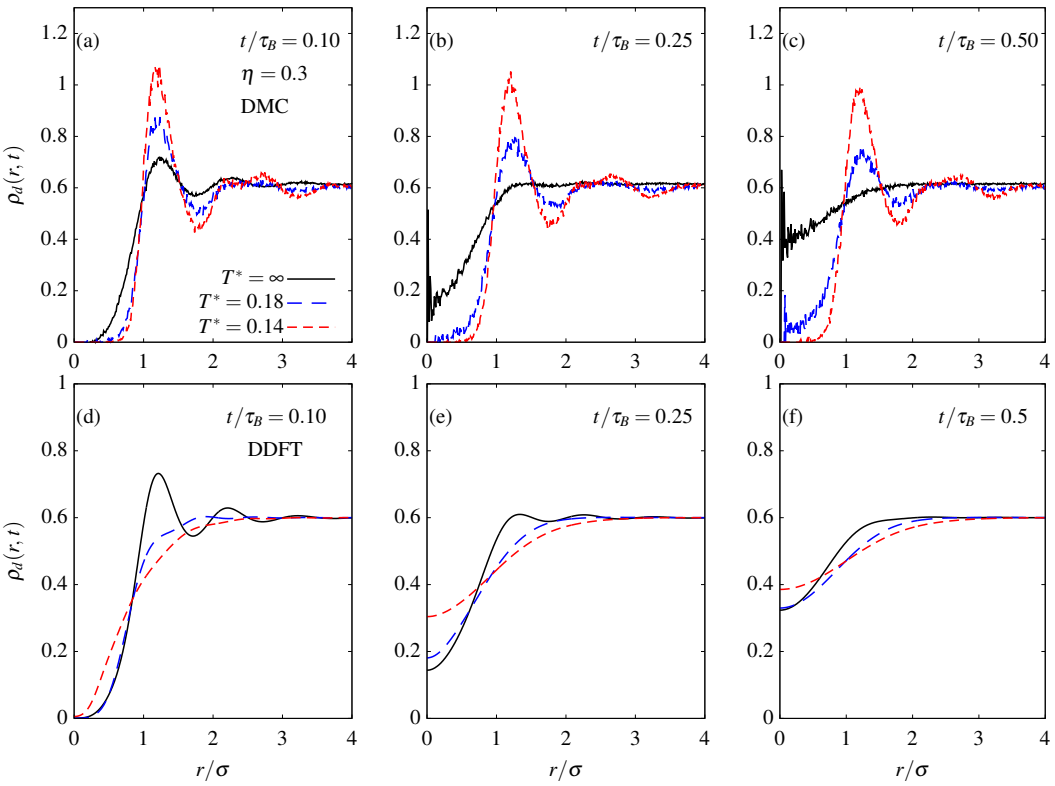

Figure 5.5 Top: DMC results for the density $\rho_d(r, t)$ around a hard-sphere test particle. The temperatures are $T^* = \infty$ (hard-sphere limit, black solid), 0.18 (blue dashed), and 0.14 (red short-dashed). The times are, from left to right, $t/\tau_B = 0.1$, 0.25, and 0.5. Bottom: the respective DDFT predictions.

particles, resulting in poorer statistics, which accordingly has to be compensated by increasing the number of samples.

In Fig. 5.5 we display results for $\rho_d(r, t)$ at temperatures $T^* = \infty$ (the hard-sphere limit, black solid), 0.18 (blue dashed) and 0.14 (red short-dashed). The times are, from left to right, $t/\tau_B = 0.1$, 0.25, and 0.5. The packing fraction is $\eta = 0.3$. The top panel shows results from DMC simulations, and the bottom panel from DDFT. We observe a drastic failure of the latter. The simulation results show a clear slowdown of the distinct dynamics, relative to the hard-sphere limit, as the temperature decreases, which is what we expect. In contrast, the DDFT predicts an *increase* of the relaxation of $\rho_d(r, t)$ towards the flat bulk profile. In the asymptotic long-time limit, $t \to \infty$, the present DDFT is indeed doomed to predict a diffusivity that will be too fast compared to simulations, due to the fact that we prescribe the long-time dynamics as that of hard-spheres by employing Eq. (5.20). However, we find that the theory significantly overestimates the dynamics, right after relatively short times; here it is even much faster than the corresponding hard-sphere limit (cf. Figs. 5.5 (a) and (d)).

The complete overestimation of the relaxation speed predicted by DDFT may be traced back to the several shortcomings. One important deficit is that, in DDFT, the extent of dynamic relaxation is affected only by instantaneous (i.e. at the present point in time) structural correlations. This is precisely related to the necessity to

empirically correct the long-time diffusivity in order to capture the correct long-time dynamics in case of hard-spheres – see discussion in the previous Sec. 5.2.2. Secondly, as the Wertheim theory itself is an equilibrium, time-independent bulk theory, it cannot provide information on bond lifetimes, and so cannot the associated free-energy functionals. We note that recent simulation results [79] suggest that the single-particle diffusivity, which is directly controlled by bond lifetimes, can be related to the probability $p_b = 1 - X$ of finding a patch engaged within a bond (i.e. a static bulk variable), but no precise dependency is yet known. However, we have seen in previous sections that long bond lifetimes dramatically affect the dynamics of the system. But why are the dynamics even faster than in bare hard-sphere fluids ? This may be related to the form of the density profiles at time $t = 0$: if we solve only the ideal diffusion equation, i.e. $\partial\rho/\partial t = \nabla^2\rho$, where no information regarding the particle interaction enters, and using the same initial density profiles for $\rho_d(r, 0)$, we observe that the correlations in $\rho_d(r, t)$ at e.g. $T^* = 0.14$ also relax faster than in the hard-sphere limit, i.e. for $T^* \to \infty$. In conclusion, we have seen that DDFT is a both qualitatively and quantitatively inadequate tool to describe the dynamics of patchy fluids, and for this purpose one has to rely on alternative approaches such as simulations.

Chapter 6

Competing Interactions

6.1 Introduction

In addition to a hard core, fluids with competing interactions are characterized by the presence of a short-ranged attraction that competes with a longer-ranged repulsion in the pair potential. A frequently considered model is the hard-core two-Yukawa fluid, for which the pair potential is sketched in Fig. 6.1. In such systems, depending on the amplitude ratio between the attraction and repulsion, stable spherical-like clusters can form [182, 183] at low packing fractions $\eta \lesssim 0.1$ that coexist with a gaseous phase consisting of few monomers, and the radial distribution function $g(r)$ can exhibit prominent long-ranged oscillations out to very large separations from the origin. Cluster formation may occur if the attraction is sufficiently strong and the repulsion sufficiently weak, so that it is likely that few particles can overcome the repulsive barrier in the pair potential to form an aggregate. The entropy loss necessarily associated with the formation of clusters is (over-) compensated by a gain in configurational energy and hence the free energy is lowered. The size of such clusters is, however, limited by the strength and range of the repulsion, as the effective repulsive barrier that e.g. a monomer has to overcome in order to attach to an existing cluster is proportional to size of the latter. As a result, if the cluster size exceeds a certain threshold no further particles can attach, and thereby the repulsion stabilizes aggregates of a certain size. The formation of equilibrium clusters was for instance observed in experiments with colloid-polymer mixtures, where an attraction between the colloids was induced via the depletion effect, and a surface charge of the colloids resulted in a (long-ranged) screened Coulomb repulsion [84]. A confocal-microscopy image from Ref. 84 is shown in Fig. 6.2; note that the fluid is still ergodic and disordered, i.e. the clusters are mobile and break and reform frequently.

At intermediate packing fractions, $0.1 \lesssim \eta \lesssim 0.25$ the clusters may become [182, 183] more elongated and eventually percolate at high densities, i.e. they form system-spanning structures. In experiments, similar behavior was observed though here the systems showed the tendency towards dynamic arrest and the formation of (non-equilibrium) percolated gels [184]. At high densities, $\eta \gtrsim 0.25$ 'inverse-cluster' phases

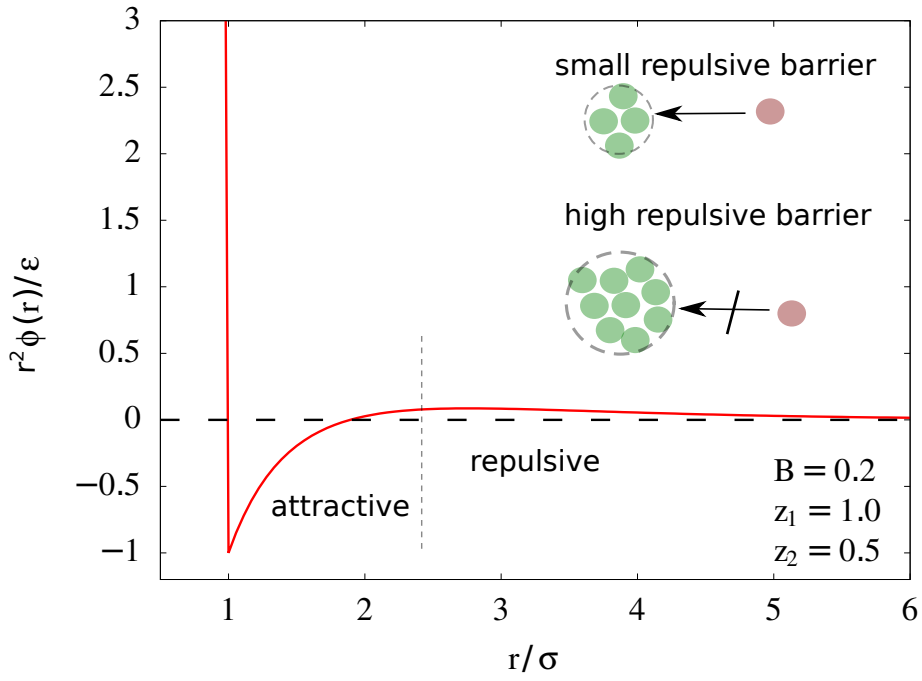

Figure 6.1 Illustration of the hard-core two-Yukawa pair potential defined in Eq. (6.2) where the amplitude ratio B between the attraction and repulsion and their individual range (controlled by $z_1 > z_2$ in Eq. (6.2)) favor the formation of stable equilibrium clusters. Note that the graph shows $r^2\phi(r)$ in order to highlight the repulsive barrier.

may occur, where e.g. spherical voids coexist with a dense liquid-like percolated fluid [182].

In addition to (unordered) low-density cluster and high-density percolated states, various recent theoretical [88, 89, 185] and simulation studies [90, 183] have predicted that colloidal fluids interacting via competing interactions may self-organize into periodically-ordered structures, consisting of low- and high-density fluid domains (also referred to as microphases or mesophases), that are thermodynamically more stable than the homogeneous bulk fluid. A line in the temperature-density phase diagram akin to a spinodal (the so-called 'λ line') separates the disordered fluid state, potentially populated with clusters, from microphase-separated regions. The structure of these mesophases can be 'simple', e.g., a lamellar phase where high- and low-density domains interchange along one spatial direction, but also more complex morphologies such as spherical micelles arranged on a bace-centered-cubic (BCC) lattice or gyroid structures are possible. Intriguingly, gyroids can be found in the wings of some butterfly or bird species, where they scatter visible light resulting in brilliant structural colors [186, 187].

However, the predictions of simulations and theory are at odds with the reality found in colloidal experiments. While unordered equilibrium cluster phases, as mentioned above, were observed in experiments [84, 184], microphase-separated states have yet to be obtained. In Ref. 188 Royall argues that it turns out to be difficult to experimentally control the required balance between attraction and repulsion suggested by theory and simulations to be necessary in order to trigger microphase formation.

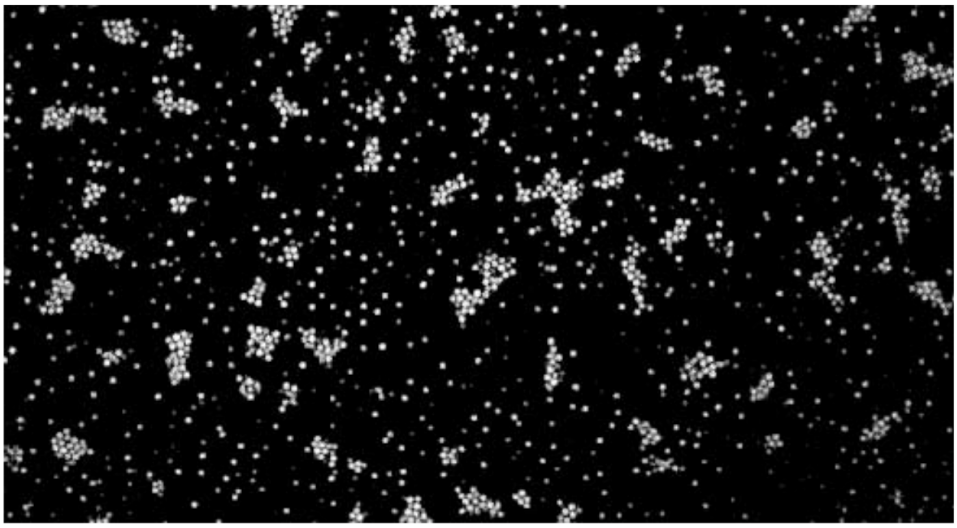

Figure 6.2 Confocal microscopy image of equilibrium clusters in a colloid-polymer mixture, where the colloids are charged resulting in a longer-ranged screened Coulomb repulsion. The packing fraction of the colloids is $\eta \approx 0.05$. Image replotted from A. Stradner *et al.*, Nature **432**, 492 (2004).

Furthermore, dynamic slowdown and gel formation may impede self-assembly into complex microphases [189].

Note that there are other soft-matter systems for which self-assembly into microphases including lamellae and gyorid structures are well-known phenomena, where the most prominent representatives are diblock copolymer melts [190, 191]. In these systems, two immiscible polymer components, say A and B, are linked together via a chemical bond which impedes a phase separation into macroscopic A- and B-rich regions (similar to e.g. water and oil). As a result, the distinct polymer components can form complex microphase-separated states on the microscopic scale, i.e. on the scale of their chainlength. The equilibrium phase behavior of block copolymers shows an intriguing quantitative similarity with that theoretically predicted for colloidal suspensions with competing interactions [88–90], and also non-equilibrium properties such as the behavior under shear flow reveals analogies [192]. The current scientific consensus is that the formation of ordered patterns seems to be the general result of complex physical mechanisms leading to a competition between attraction and repulsion on different lengthscales, irrespective of its precise microscopic origin [193].

In Sec. 6.2 we will provide an overview on the rich physics found in fluids with competing interactions, where we focus on the hard-core two-Yukawa fluid described with a simple mean-field DFT. The results presented there mainly go back to early work carried out by Sear in 1999 [194], Imperio and Reatto in 2004 [195] and continued work by Pini and Archer [85, 182, 196] as well as recent results by Edelmann and Roth [89].

While all the aforecited studies considered spherically-symmetric pair potentials, there are systems in which anisotropic competing interactions occur. This particularly is the case for many protein solutions [45] (see also Sec. 7.5 of Ch. 7), where a longer-

ranged repulsion is the result of screened Coulomb interactions. In Sec. 6.3 of this chapter, we will investigate the phase behavior and equilibrium structure of a simple model of anisotropic competing interactions based on the framework of patchy particles.

6.2 The hard-core two-Yukawa fluid

We consider the following interaction potential

$$\phi(r) = \phi_{\text{HS}}(r) + \phi_{\text{2Y}}(r)\,, \tag{6.1}$$

where $\phi_{\text{HS}}(r)$ denotes the hard-sphere potential (1.6). The two-Yukawa (2Y) contribution $\phi_{\text{2Y}}(r)$ is given by

$$\phi_{\text{2Y}}(r) = \begin{cases} -\varepsilon\left(e^{-z_1} - Be^{-z_2}\right) & ; \quad r < \sigma \\ -\varepsilon\left(\frac{\sigma}{r}e^{-z_1 r/\sigma} - B\frac{\sigma}{r}e^{-z_2 r/\sigma}\right) & ; \quad r \geq \sigma\,, \end{cases} \tag{6.2}$$

where ε sets the overall energy scale, and B fixes the amplitude ratio between attraction and repulsion. The parameters z_1 and z_2 (with $z_1 > z_2$) control the interaction range of the latter. The excess free energy functional is given by

$$\beta\mathcal{F}_{\text{ex}}[\rho] = \beta\mathcal{F}_{\text{ex}}^{\text{HS}}[\rho] + \frac{1}{2}\iint \mathrm{d}\mathbf{r}\,\mathrm{d}\mathbf{r}'\,\rho(\mathbf{r})\rho(\mathbf{r}')\beta\phi_{\text{2Y}}(|\mathbf{r}-\mathbf{r}'|)\,, \tag{6.3}$$

where we employ the original version of Rosenfeld's FMT [17] to describe the hard-sphere correlations. Similar to the study of the square-well fluid in Sec. 2.4.3, the non-hard-core bit $\phi_{\text{2Y}}(r)$ is extended down to the core as we employ the standard mean-field approach to treat the non-hard-core interactions which systematically underestimates correlations.

In Fig. 6.3 (a) we show the radial distribution functions $g(r)$ at a low packing fraction $\eta = 0.05$ for temperatures $k_BT/\varepsilon = 0.28$ (blue) and 0.25 (red), where we observe that $g(r)$ exhibits long-ranged, slowly decaying oscillations with a wavelength of $\approx 12\sigma$ as the temperature is lowered. Furthermore, the probability of finding a particle in vicinity to the origin at $r = 0$ is very high out to separations of $r \approx 5\sigma$. Such behavior is a signal of the formation of clusters that coexist with a gas of monomers [182], where the long-ranged oscillations correspond to cluster-cluster correlations and the sharp 'bumps' in the region $r < 5\sigma$ correspond to hard-sphere-like particle-particle correlations within a cluster. Moving to higher temperatures, we find that the cluster-cluster correlations become quickly damped (cf. green curve in the inset where $k_BT/\varepsilon = 0.29$).

The long-ranged oscillations in $g(r)$ are also reflected in Fourier space by a maximum in the static structure factor $S(k)$ at a wave number k_{pre} that is smaller than that associated with the monomer-monomer correlations, $k_{\text{pre}} < k_{\text{mono}}$. Recall that $S(k)$ is

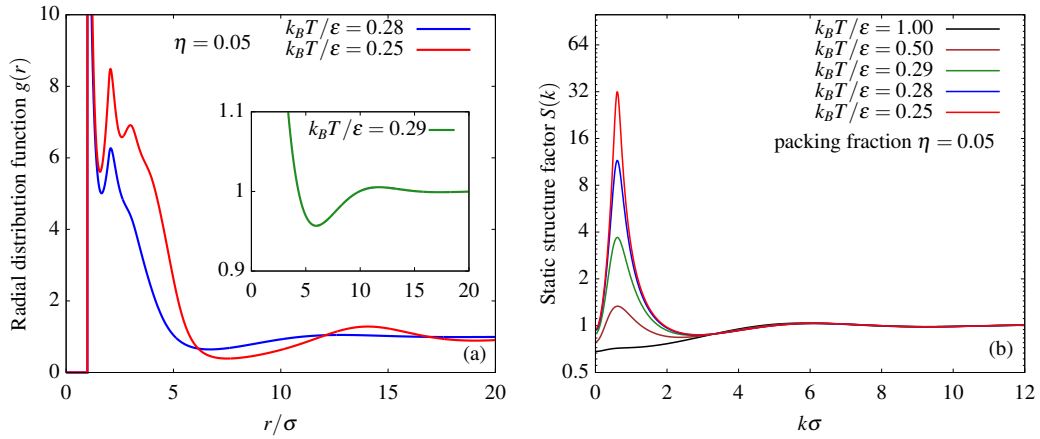

Figure 6.3 (a) Typical behavior of $g(r)$ for the hard-core two-Yukawa fluid treated in mean-field DFT at packing fraction $\eta = 0.05$ and temperatures $k_BT/\varepsilon = 0.28$ (blue) and 0.25 (red). These are fluid states at which spherical clusters coexist with few monomers. At higher temperatures ($k_BT/\varepsilon = 0.29$) the long-ranged cluster-cluster correlations become quickly damped (see inset). (b) Behavior of the static structure factor $S(k)$ at packing fraction $\eta = 0.05$ and several temperatures. A prominent pre-peak occurs at low wavenumbers $k_{\rm pre} \ll 2\pi/\sigma$ as the temperature is lowered, and can emerge long before cluster correlations dominate the intermediate shape of $g(r)$. The parameters of the two-Yukawa potential are $z_1 = 1$, $z_2 = 0.5$ and $B = 0.2$.

related to the Fourier transform $\widehat{c}(k)$ bulk pair direct correlation function $c(r)$ via

$$S(k) = \frac{1}{1 - \rho_b \widehat{c}(k)} \,. \tag{6.4}$$

Recall also that in mean-field DFT $\widehat{c}(k)$ is given by the simple result

$$\widehat{c}(k) = \widehat{c}_{\rm HS}(k) - \beta\widehat{\phi}_{\rm 2Y}(k) \,, \tag{6.5}$$

where $\widehat{c}_{\rm HS}(k)$ is the Fourier transform of the hard-sphere pair direct correlation function, which can be calculated from Eq. (2.70); for the original Rosenfeld functional (see Eqs. (2.105) and (2.108)) $\widehat{c}_{\rm HS}(k)$ is given by the 3d Fourier transform of the Percus-Yevick solution (2.47). It can be written in the form [197]

$$\begin{aligned}\widehat{c}_{\rm HS}(k) = &- 4\pi\sigma^3 \left[\left(\frac{\alpha + 2\beta + 4\gamma}{q^3} \right) \sin(q) + \left(-\frac{\alpha + \beta + \gamma}{q^2} + \frac{2\beta + 12\gamma}{q^4} \right) \cos(q) \right. \\ &\left. + \frac{24\gamma}{q^6} \left(1 - \cos(q)\right) - \frac{2\beta}{q^4} \right] \,,\end{aligned} \tag{6.6}$$

whith $q = k\sigma$ and density-dependent coefficients

$$\alpha = \frac{(1+2\eta)^2}{(1-\eta)^4} \quad ; \quad \beta = \frac{-6\eta(1+\frac{\eta}{2})^2}{(1-\eta)^4} \quad ; \quad \gamma = \frac{\eta(1+2\eta)^2}{2(1-\eta)^4} \quad . \tag{6.7}$$

The Fourier transform of the two-Yukawa part (6.2) is easily calculated:

$$\beta\widehat{\phi}_{\rm 2Y}(k) = 4\pi\beta\varepsilon\sigma^3 \left[\frac{-e^{-z_1} + Be^{-z_2}}{q^3} \left(\sin(q) - q\cos(q) \right) \right.$$

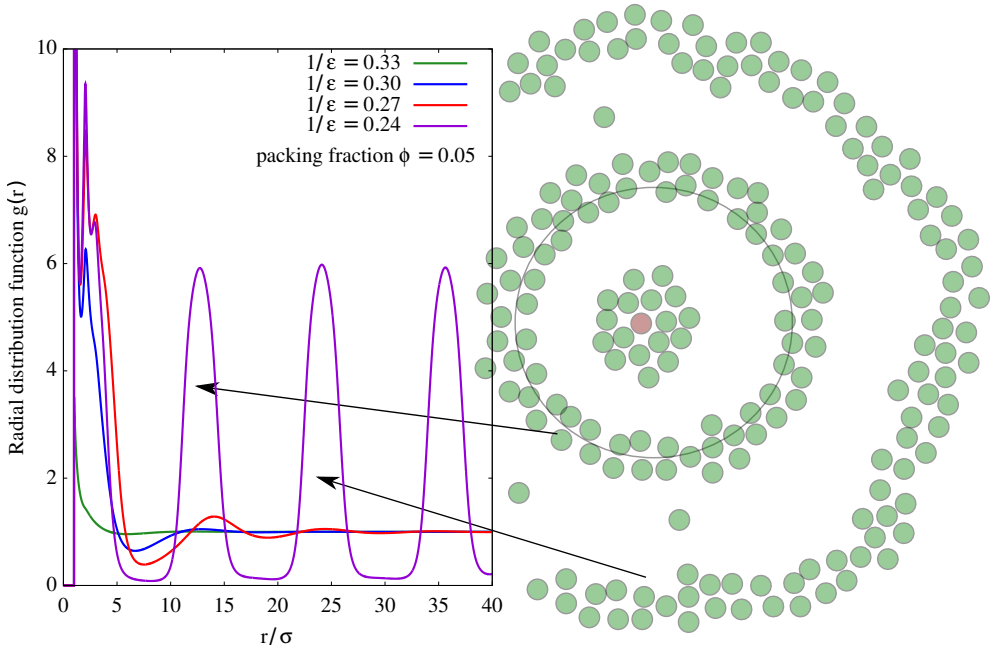

Figure 6.4 Microphase-separation manifests itself in non-decaying peaks in the radial distribution function $g(r)$ (purple curve). At these state points the uniform bulk fluid is an unstable phase. The peaks in $g(r)$ correspond to spherical shells of particles periodically ordered around the reference particle (colored in red in the sketch). Note that this particular form is the result of an artificially imposed spherical symmetry to the density profile $\rho(r)$ during the minimization procedure of the grand-potential functional.

$$- \frac{e^{-z_1}}{z_1^2+q^2}\left(\cos(q)+\frac{z_1}{q}\sin(q)\right) + \frac{Be^{-z_2}}{z_2^2+q^2}\left(\cos(q)+\frac{z_2}{q}\sin(q)\right)\Bigg] . \tag{6.8}$$

In Fig. 6.3 (b) we show $S(k)$ for several values of the reduced temperature k_BT/ε and the same packing fraction $\eta = 0.05$ as in Fig. 6.3 (a). We observe a quickly growing so-called pre-peak in $S(k)$ at wavenumbers $0 < k_{\text{pre}} \ll k_{\text{mono}}$, where $k_{\text{mono}}\sigma \approx 2\pi$, as the temperature is lowered. Note that the inverse $2\pi/k_{\text{pre}}$ roughly corresponds to the wavelength of the long-ranged density modulations in $g(r)$. Note also that computer simulations have find a very similar behavior for $g(r)$ and $S(k)$ [182].

Interestingly, we can conclude from Figs. 6.3 (a) and (b) that a prominent peak in $S(k)$ at low wavenumbers can be retained despite that the long-ranged cluster oscillations in $g(r)$ become significantly damped upon increasing temperature. Indeed, for several years there has been an extensive scientific debate [198, 199, 86, 87, 200, 201] to which extent the pre-peak in $S(k)$ provides information about the significance of cluster formation in the fluid at low densities. The debate was triggered by contradicting statements regarding the interpretation of an experimentally observed (small) pre-peak in $S(k)$ in solutions of proteins [84, 202]. Subsequent insights from theoretical and simulation studies [198, 199, 86] suggested that a small pre-peak in $S(k)$ is the general result of pair potentials that exhibit a competition on different lengthscales, and does not necessarily imply the presence equilibrium cluster phases. Based on a

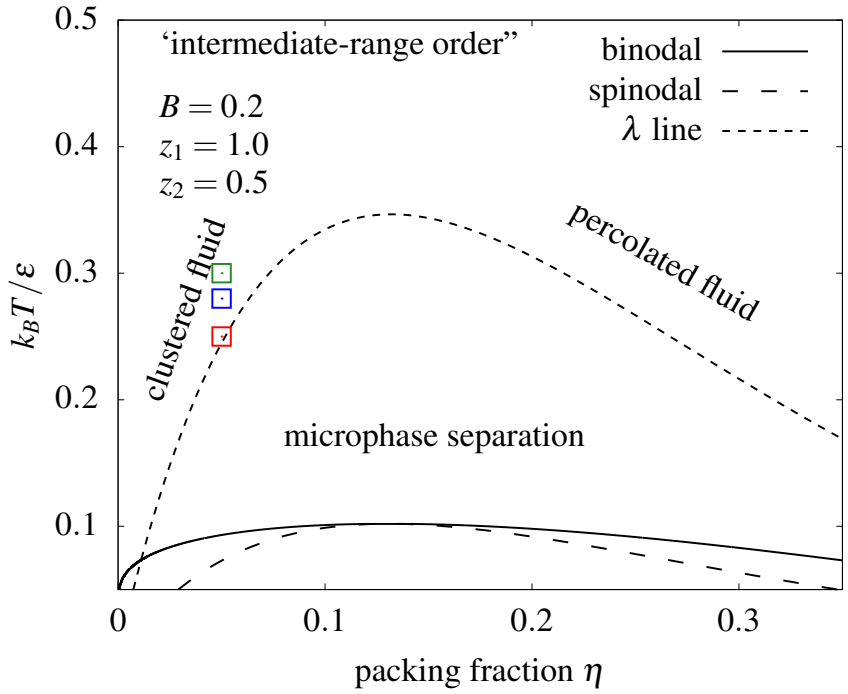

Figure 6.5 Bulk phase diagram of the hard-core two-Yukawa fluid treated within mean-field DFT for $B = 0.2$, $z_1 = 1.0$ and $z_2 = 0.5$. In a broad region enclosed by the λ line the homogeneous bulk state is unstable with respect to density fluctuations, and microphases (or inhomogeneous bulk phases) are always the thermodynamic stable state. On and below the λ line, the structure factor diverges at wavenumber $0 < k_{\text{pre}} \ll 2\pi/\sigma$, i.e. $S(k_{\text{pre}}) \to \infty$. At low density and in the vicinity to the λ line clustering occurs, manifested by a prominent (but finite) peak in $S(k = k_{\text{pre}})$ and long-ranged oscillations in $g(r)$. At higher temperatures, these long-ranged oscillations become quickly suppressed, though a small pre-peak in $S(k = k_{\text{pre}})$ is retained (see Fig. 6.3). In recent literature [86, 201], this region is termed 'intermediate range-order' fluid, a state which is dominantly populated by monomers and small transient clusters consisting of few particles. At higher densities, outside the λ line, clusters can percolate and form system-spanning unordered structures [183].

careful analysis of microscopic particle configurations, the authors of Ref. 199 identified an empirical threshold based on the pre-peak height: if $S(k_{\text{pre}}) \lesssim 2.7$ the system is in a state called 'intermediate range-order' fluid characterized by the presence of 'indistinct' cluster phases, i.e. states that consist of monomers, dimers, trimers, and so on where the cluster-size probability distribution decreases monotonically and shows no maximum. Furthermore, the average lifetime of such small clusters seems to be rather short, i.e. they frequently break and reform [201]. On the other hand, there is consensus about that a sufficiently strong signal in the static structure factor $S(k_{\text{pre}}) \gg 2.7$ is a indication for a 'mono-disperse' cluster phase, i.e. where the cluster-size probability function shows a clear maximum indicating a preferred mean-cluster size and only few free monomers.

We will now consider lower temperatures than those for which $g(r)$ and $S(k)$ are shown in Figs. 6.3 (a) and (b). Note that the gas-liquid critical point for $B = 0.2$, $z_1 = 1.0$ and $z_2 = 0.5$ is located at ($\eta_c = 0.123$, $k_BT_c/\varepsilon_c = 0.11$). For temperatures below $k_BT/\varepsilon \approx 0.25$ (at a packing fraction $\eta = 0.05$) we observe that $g(r)$ exhibits

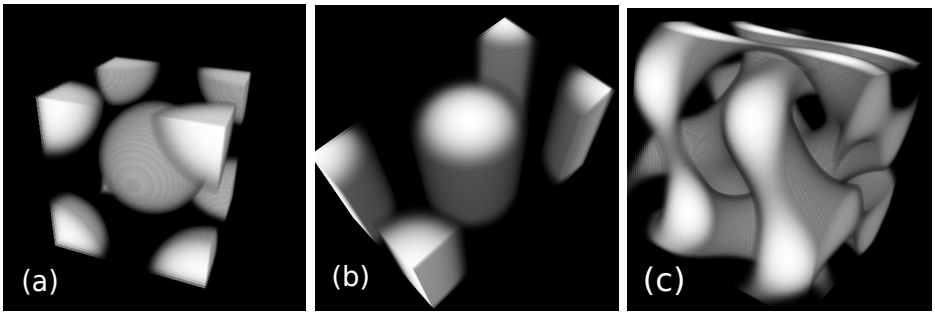

Figure 6.6 Three-dimensional density profiles of possible microphases found by minimizing the grand-potential at sufficiently low packing fraction (cf. Fig. 6.7). (a) Spherical micelles arranged on a BCC lattice, (b) 2D-hexagonal cylinders, and (c) the double-gyroid structure . White areas denote liquid-like high-density domains, black means zero density.

long-ranged oscillations that do not decay as $r \to \infty$, which is shown as the purple curve in Fig. 6.4. This means that there is a crossover from a disordered fluid state, where $g(r) \to 1$ as $r \to \infty$, to a periodically ordered microphase-separated state. The peaks in $g(r)$ correspond to spherical shells of high-density domains located around the reference particle at the origin (colored in red). Note that this particular form is the result of an artificially imposed spherical symmetry to the density profile $\rho(r)$ during the minimization procedure of the grand-potential functional.

Within mean-field DFT one finds an instability region in the $k_BT/\varepsilon - \eta$ phase diagram that is enclosed by a spinodal-like line, the so-called λ line. It is related to a divergence of the pre-peak in the static structure factor, i.e. $S(k_{\text{pre}}) \to \infty$. Physically, this means that the homogeneous bulk fluid is unstable with respect to arbitrary small density fluctuations, i.e. a periodically ordered microphase-separated state can be the equilibrium phase without the presence of any external field. We plot the λ line for $B = 0.2$, $z_1 = 0.1$ and $z_2 = 0.5$ in Fig. 6.5 as the short-dashed line along with the binodal (solid) and the spinodal (long-dashed). At low densities, in vicinity to yet outside of the λ line, the fluid exhibits unordered cluster phases manifested by prominent long-ranged, slowly decaying oscillations in $g(r)$, cf. our discussion above. At higher particle densities, these clusters may percolate to form system-spanning structures [182, 183]. We also indicate the regions of the 'intermediate range-order' fluid [86, 201] at higher temperatures, where the static structure factor $S(k)$ exhibits only a small pre-peak. At such statepoints, the fluid is characterized by the presence of mostly monomers and small transient clusters consisting of few particles.

In order to explore the structure of possible microphases, one has to perform three-dimensional DFT calculations. A detailed analysis revealed [89] that lamellar, cylindrical tubes arranged on a hexagonal lattice, gyroid-phases, and spherical micelles arranged on BCC lattice can be stable phases, depending on the state point in the $k_BT/\varepsilon - \eta$ phase diagram. In Fig. 6.6 we show the three-dimensional density profile of several structures that can exist as thermodynamically stable microphases at packing fractions $\eta \lesssim 0.15$. This includes (a) spherical micelles arranged on a BCC lattice, (b) 2D-hexagonal cylinders and (c) the double-gyroid phase. The white areas correspond to

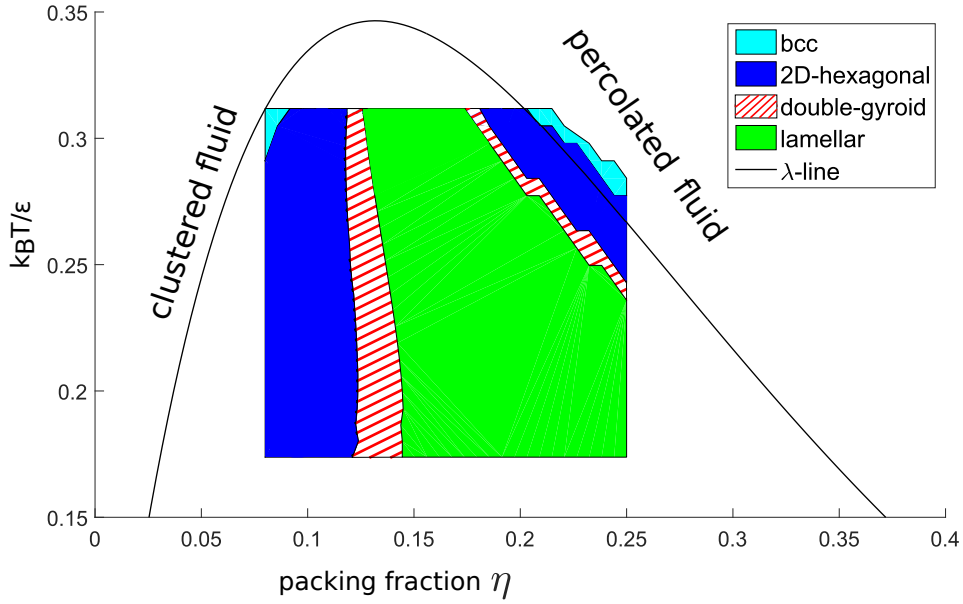

Figure 6.7 Thermodynamically stable microphases as predicted by mean-field DFT for the hard-core two-Yukawa fluid. Note that the structures at high packing fractions denote their inverse, i.e. low- and high-density domains are interchanged and the system forms periodically ordered percolated structures. Image adapted and modified from M. Edelmann and R. Roth, Phys. Rev. E **93**, 062146 (2016).

liquid-like high-density domains and black means zero density. The optimal side length L_0 of the corresponding unit cells ranges between $\approx 20\sigma - 30\sigma$ for the double-gyroid, $\approx 12\sigma - 20\sigma$ for e.g. the BCC structure and $\approx 7\sigma - 12\sigma$ for the lamellar phase. At high densities, one finds for instance that an inverted BCC phase can occur, i.e. where low- and high-density domains are interchanged. Other microphases (for instance spherical micelles on a FCC lattice) can also exist, but they are typically metastable with respect to the aforementioned structures.

The structures were obtained by numerically solving Eq. (2.66) in three dimensions massively in-parallel on graphics cards (Appendix A) via a standard Picard iteration scheme. One typically has to employ an initial guess $\rho_{\text{init}}(\mathbf{r})$ for the density that already resembles the desired microphase [89]. This is due to the fact that the free-energy landscape of a fluid with competing interactions can be very complex, i.e., within the region enclosed by the λ line there can exist a lot of metastable cluster states. This means that during the Picard iteration the system easily can become trapped in a local minimum, which may be far away from the desired structure when simply employing a random noise term above the bulk profile as an initial input. For instance, a suitable guess for the lamellar structure with density modulations along the x-axis reads $\rho_{\text{init}}(\mathbf{r}) = \rho_b(1+\gamma\sin(2\pi x/L_0))$, where γ controls the strength of the perturbation; typically $\gamma = 0.1$ is sufficient. For the gyroid phase, a more complex approximation based on Fourier-expansions has to be used; it can be found in Ref. 203. The optimal periodicity length L_0 of a specific microphase can be found by minimizing the grand

potential functional $\Omega[\rho]$ in Eq. (2.61) w.r.t. both the density $\rho(\mathbf{r})$ and the size of the unit cell [89].

The complete phase behavior within (and in vicinity to)[1] the λ line, as obtained from mean-field DFT, is shown in Fig. 6.7 (modified from Ref. 89). Note that essentially the same phase diagram is predicted by computer simulations [90]. In particular, the microphases exhibit an unique sequence as a function of the packing fraction η and constant temperature, which is the *same* as for diblock-copolymer melts [190, 191]. This remarkable result can be explained with work done by A. Ciach [193], who showed that the latter system and colloidal fluids with competing interactions can be described by the same Landau-type free-energy functional.

6.3 Anisotropic competing interactions[2]

In this section, we provide a DFT study of a fluid where the particles interact via an anisotropic attraction via four patches, described by the Kern-Frenkel potential (3.1), and an additional longer-ranged Yukawa repulsion. An illustration of this model is displayed in Fig. 6.8. The total pair-interaction potential between two particles 1 and 2 thus reads

$$\phi(\mathbf{r},\varpi_1,\varpi_2) = \phi_{\text{HS}}(r) + \phi_{\text{rep}}(r) + \phi_{\text{bond}}(\mathbf{r},\varpi_1,\varpi_2)\,, \tag{6.9}$$

where $\phi_{\text{HS}}(r)$ is the hard-sphere potential (1.6), $r = |\mathbf{r}| \equiv |\mathbf{r}_1 - \mathbf{r}_2|$ is the center-to-center distance between particles 1 and 2, and $\phi_{\text{bond}}(\mathbf{r},\varpi_1,\varpi_2)$ is the KF pair potential defined in Eq. (3.1). In this section, we define the repulsive Yukawa potential as:

$$\phi_{\text{rep}}(r) = \begin{cases} 0 & ; \quad r < \sigma \\ B\sigma \exp\left[-z(r/\sigma - 1)\right]/r & ; \quad r > \sigma \end{cases} \tag{6.10}$$

where B controls the repulsion strength and z its range. Note that here we do *not* extent $\phi_{\text{rep}}(r)$ down to the core as we only treat the repulsion with a mean-field functional:

$$\mathcal{F}_{\text{ex}}[\rho] = \mathcal{F}_{\text{ex}}^{\text{HS}}[\rho] + \mathcal{F}_{\text{ex}}^{\text{bond}}[\rho] + \frac{1}{2}\iint \mathrm{d}\mathbf{r}\,\mathrm{d}\mathbf{r}'\,\rho(\mathbf{r})\rho(\mathbf{r}')\phi_{\text{rep}}(|\mathbf{r}-\mathbf{r}'|)\,, \tag{6.11}$$

where the hard-sphere correlations are again described with the Rosenfeld functional [17], and the bonding contribution according to the original approach of Yu and Wu [72] (this was termed the 'FMT functional' in Ch. 4). We assume four patches per particle, i.e. $M = 4$, a range of the patch-patch pair potential of $\delta = 0.119$, and the

[1] Note that the λ line is a locus of mechanical instability of the homogeneous bulk fluid, i.e. periodic microphases may also occur outside the λ line, where the bulk phase is metastable w.r.t. the latter (but mechanically stable). This is the reason why in Fig. 6.7 e.g. the inverted-BCC phase also occurs slightly outside of the λ line.

[2] This section is reproduced from: D. Stopper and R. Roth, Phys. Rev. E **96**, 042607 (2017).

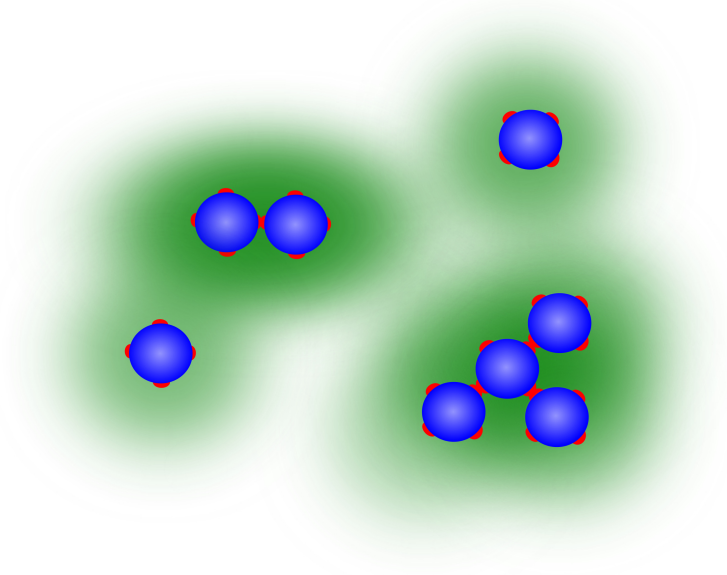

Figure 6.8 Schematic illustration of the considered model for anisotropic competing interactions. Patchy particles modeled as hard spheres (blue) with four attractive sites (red) and an additional spherically-symmetric hard-core Yukawa repulsion (green).

opening angle is fixed at $\cos(\theta_{\max}) = 0.895$. The total excess free energy per particle of the homogeneous fluid is given by:

$$\frac{\beta F_{\text{ex}}}{N} = \left[\frac{3\eta(2-\eta)}{2(1-\eta)^2} - \ln(1-\eta)\right] + M\left[\ln(X) - \frac{X}{2} + \frac{1}{2}\right] + \frac{\rho_b}{2}\int \mathrm{d}\mathbf{r}\, \beta\phi_{\text{rep}}(r)\,. \quad (6.12)$$

The probability X that an arbitrary patch is not bonded is defined in Sec. 3.2 in Eq. (3.19). In order to investigate whether this system exhibits a λ line, we need an expression for the static structure factor $S(k)$. Fortunately, the internal structure of FMT and the mean-field functional allow for an analytic solution for the Fourier transform of the bulk pair direct correlation function $\widehat{c}(k)$ and thus for $S(k)$. The former splits into three terms:

$$\widehat{c}(k) = \widehat{c}_{\text{HS}}(k) + \widehat{c}_{\text{bond}}(k) + \widehat{c}_{\text{rep}}(k)\,,$$

where

$$\widehat{c}(k) - \widehat{c}_{\text{rep}}(k) = -\sum_{\nu,\nu'} \left.\frac{\partial^2(\Phi_{\text{HS}} + \Phi_{\text{bond}})}{\partial n_\nu\, \partial n_{\nu'}}\right|_{\rho_b} \widehat{\omega}_\nu(\mathbf{k}) \cdot \widehat{\omega}_{\nu'}(-\mathbf{k})\,, \quad (6.13)$$

and

$$\begin{aligned}\widehat{c}_{\text{rep}}(k) &= -\beta\widehat{\phi}_{\text{rep}}(k) \\ &= -\frac{4\pi\beta B\sigma^3}{(k\sigma)^2 + z^2}\left(\cos(k\sigma) + \frac{z}{k\sigma}\sin(k\sigma)\right)\,. \end{aligned} \quad (6.14)$$

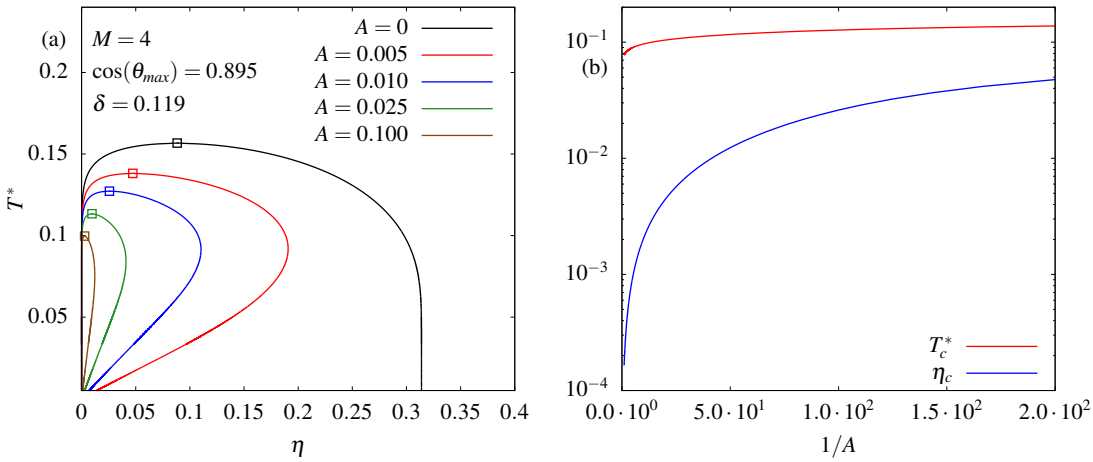

Figure 6.9 (a) Gas-liquid coexistence phase diagrams in the $T^* - \eta$ plane for $A = 0.005$ (red long-dashed), 0.01 (blue short-dashed), 0.25 (green dashed-dotted) and 0.1 (brown dotted). Open squares denote the critical points. (b) Critical temperature T_c^* and density η_c as a function of the inverse repulsion strength $1/A$. The parameter z controlling the range of repulsion is fixed at $z = 0.5$.

Here, the $\widehat{\omega}_\nu(\mathbf{k})$ are the Fourier-transforms of the FMT-type weight functions $\omega_\nu(\mathbf{r})$, which are known analytically (they can be found in Sec. A.2.1 of Appendix A). We do not show the full expression here as it would not provide much physical intuition.

6.3.1 Bulk phase diagrams

In this section, we discuss results for the gas-liquid binodals and the λ line. The former is determined by demanding chemical and mechanical equilibrium, and critical points are calculated by demanding that the first and second derivatives of the systems pressure p w.r.t. the density ρ_b vanish. All phase diagrams are displayed in the $T^* - \eta$ plane, where $T^* = k_B T/\varepsilon$ and ε is the patch-patch interaction energy. As in Sec. 6.2 we fix the amplitude ratio between attraction and repulsion, i.e. we assume $B = A\varepsilon$, where A denotes a dimensionless scaling factor.

Gas-Liquid phase separation. In Fig. 6.9 (a) we show results for gas-liquid binodals (lines) and critical temperatures (open squares) for distinct values of A. We display curves for $A = 0$ (black), $A = 0.005$ (red), 0.01 (blue), 0.025 (green) and 0.1 (brown). The value of z is fixed at 0.5 which is inspired by previous DFT studies of competing interactions [85, 89]. For $A = 0$, i.e. the pure patchy fluid, the liquid phase is characterized by elongated tetrahedral networks, where most of the patches are bonded (see also Secs. 3.3 and 3.4 for more details). Remarkably, we find that the topology of the gas-liquid binodals changes fundamentally for $A \neq 0$, where the liquid branch is squeezed to significantly lower packing fractions. Moreover, the values of the critical packing fraction η_c and temperature T_c^* decrease, and eventually are suppressed to the origin as $1/A \to 0$, see Fig. 6.9 (b). We also observe that the liquid-branch of the binodal exhibits a reentrant shape, i.e. when the temperature is lowered at

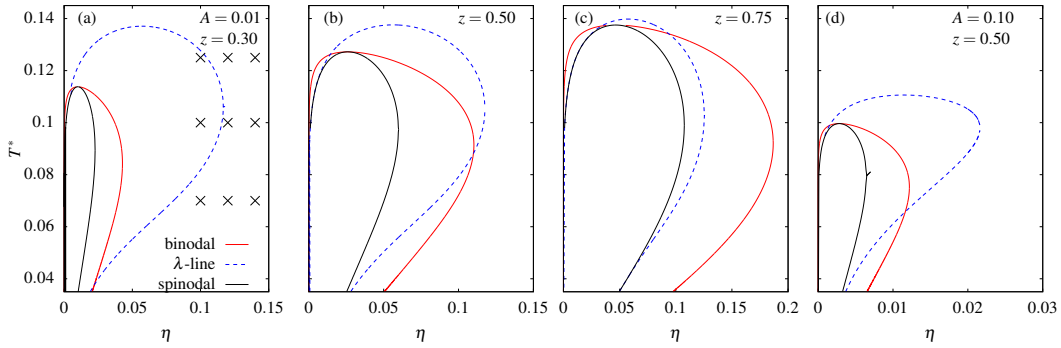

Figure 6.10 (a)–(d) show the binodal (red solid), spinodal (black dashed-dotted) and the λ-line (blue dashed) for a variety of parameters A and z. Note the small packing fractions η in (d) for $A = 0.1$ and $z = 0.5$ in comparison to $A = 0.01$ (a)–(c). Crosses in (a) denote state points shown in Fig. 6.11.

constant η, at some point one enters the two-phase region and subsequently reenters to a stable liquid state.

The effects leading to a reentrant phase diagram may be understood as the result of a competition between bond formation and the isotropic repulsion. Up on cooling, the latter increasingly influences bond formation between particles due to its long-range character. In order to minimize their configurational energy, the particles may tend to form elongated, chain-like structures rather than tetrahedral-like networks. As a result, with decreasing temperature, the phase-separated regime appears to shrink and vanishes for $T^* \to 0$, as a fluid of chains does not phase separate [47]. This physical picture is also consistent with that the critical point successively is suppressed to the origin as $A \to \infty$. Furthermore, we have verified that the reentrant shape of the binodal does not show up for a *temperature-independent* repulsion (i.e. constant B), whereas the critical point is still suppressed to the origin as $B \to \infty$.

Note that from a technical point of view the reentrant effect and vanishing of the critical point are the result of a competition between the rather complex density dependence of Eqs. (3.20) and (3.19) and the mean-field free energy accounting for the repulsion, which scales with $\sim \rho_b^2$. It therefore remains an open question to what extend a theory describing the repulsion beyond mean-field would impact the phase behavior. It is also interesting to note that the reentrant shapes of the binodal bear resemblance to the phase behavior found in systems with so-called $2AnB$ patchy colloids [154, 155]. There one places two sites of type A at the poles of each particle, and n patches of type B are placed along the equator. The particles are allowed to only interact via AA or AB bonds (with distinct interaction energies ε_{AA} and ε_{AB}), while BB bonds are forbidden. In these systems, a reentrant binodal is the result of a competition between AA bonds and AB bonds at finite temperatures if $\varepsilon_{AB} < \varepsilon_{AA}/2$. The latter condition ensures that the ground state at zero temperature will always consist of chains (which do not phase separate) rather than branched structures.

Microphase separation: λ line. We now focus on the λ line, which is determined by the value of the wavenumber $k = k_{\text{pre}}$ for which the static structure factor $S(k)$ diverges. In Figs. 6.10 (a) – (d) we show the λ lines (blue dashed), the binodals (red) and spinodals (black) for a selection of parameters A and z: $A = 0.01$, $z = 0.3$ (a), $z = 0.5$ (b), $z = 0.75$ (c), and $A = 0.1$ and $z = 0.5$ (d). Strikingly, the λ line also exhibits a reentrant topology which is fundamentally different to spherically-symmetric competing interactions [196, 89]. A feature satisfied by both the present system and two-Yukawa fluid is that the λ line converges to the spinodal for $T^* \to 0$ which here gives rise to the reentrant behavior of the λ line. In particular, the λ line stretches asymmetrically into the 'high-density regions' (the packing fractions are much lower than e.g. for the two-Yukawa fluid) and converges rather quickly to the spinodal close to the gas-liquid critical point. This may be due to the fact that a fluid consisting mainly of short chains or small clusters, as present in the gaseous phase, seems to be incommensurate with self-assembly into complex microphases. Hence, the reentrant topology is most likely a consequence of the directionality of the particle interaction.

By altering the tuple (A, z), it is possible to significantly tune the absolute location of the λ line in the phase diagram, as well as its relative location to the binodal. For instance, we find when A is kept fixed and z is varied, that the absolute extension of the λ line changes only slightly, whereas both the binodal and spinodal grow considerably as the range of repulsion is reduced – compare Figs. 6.10 (a), (b) and (c). We can also alter A and keep z fixed: compare Figs. 6.10 (b) where $A = 0.01$ and (d) where $A = 0.1$. In this case, we observe that the binodal and the λ line both can be changed on an absolute scale, whereas their relative location to one another is not affected dramatically. Generally, we can conclude that the λ line follows the overall behavior of the binodal and spinodal in the phase diagram as the relative strength of the repulsion (i.e. the parameter A) is increased: the region where microphase separation can occur is suppressed to very low packing fractions and temperatures which is a curious feature certainly not seen in fluids with spherically-symmetric competing interactions.

6.3.2 Structural properties

In this section we shall focus on (bulk) structural properties of our model system. More specifically, we calculate the fluid structure around a purely repulsive test particle. Strictly speaking this is not equivalent to the radial distribution function $g(r)$, but the density profile around the repulsive test particle will capture the dominating inter-particle correlations of the surrounding fluid. In order to obtain the (orientational averaged) density distribution, we minimize the grand potential $\Omega[\rho]$ in radial symmetry w.r.t.. to the density profile $\rho(\mathbf{r}) = \rho(r)$ using a standard numerical minimization scheme [70]. The potential $V_{\text{ext}}(r)$ exerted by the test particle to the surrounding fluid is set to

$$V_{\text{ext}}(r) = \begin{cases} \infty & ; \quad r < \sigma \\ \frac{A\varepsilon\sigma}{r} \exp\left(-z(r/\sigma - 1)\right) & ; \quad r \geq \sigma \end{cases} . \tag{6.15}$$

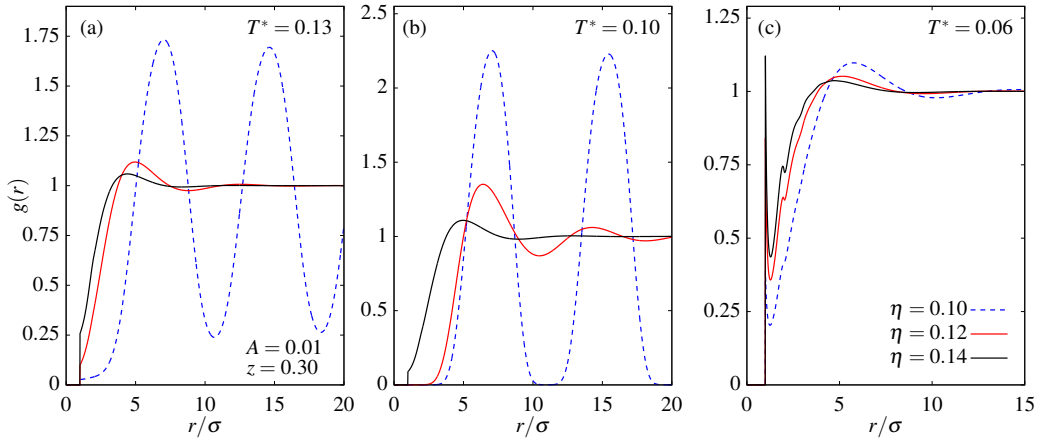

Figure 6.11 Radial distribution function $g(r)$ around a purely repulsive test particle for different values of the temperature $T^* = 0.13$ (a), 0.10 (b), and 0.06 (c). The packing fractions are $\eta = 0.10$ (blue dashed), 0.12 (red dotted) and 0.14 (black solid). The values of A and z correspond to the phase diagram shown in Fig. 6.10 (a), where the state points are marked with crosses.

In Figs. 6.11 (a) – (c) we show the resulting density profiles $\rho(r)$ for several values of $k_BT/\varepsilon = 0.13$ (a), 0.10 (b), and 0.06 (c) at constant packing fractions $\eta = 0.14$ (black solid), 0.12 (red dotted), and 0.10 (blue dashed). The parameters in $\phi_{\text{rep}}(r)$ are set to $A = 0.01$ and $z = 0.3$ corresponding to the phase diagram in Fig. 6.10 (a), where the considered state points are marked with crosses. For $\eta = 0.10$ and temperatures $T^* = 0.13$ and 0.10 we are inside of the instability region; in Figs. 6.11 (a) and (b) this is manifested by strong periodic density modulations in $\rho(r)$ that do not decay as $r \to \infty$. The lengthscale of these oscillations is $L_0 \approx 7 - 8\sigma$ which is fairly close to $2\pi/k_{\text{pre}}$, where $k_{\text{pre}}\sigma \approx 0.8$ is the wavenumber at which $S(k_{\text{pre}})$ diverges.

For densities $\eta = 0.12$ and 0.14, the state points are in vicinity to but located outside the λ line, and here we observe that long-ranged slowly-decaying cluster correlations emerge. Following our discussion of Sec. 6.2, these may be related to unordered cluster phases, which would not be recognizable in the bulk fluid (i.e. on statistical average the density is constant, $\rho(\mathbf{r}) = \text{const.}$) – in contrast to microphases inside the λ line. In particular, we observe that the cluster oscillations in $\rho(r)$ reflect the reentrant topology of the phase diagram: far away from the λ line (cf. Fig. 6.11 (a)) only weak oscillations can be seen; in its direct vicinity, cluster correlations are clearly visible, in particular for $\eta = 0.12$. By further lowering temperature (Fig. 6.11 (c)) cluster correlations in turn become less pronounced.

6.3.3 Inhomogeneous bulk phases

We will now investigate what kind of microphases can be stable within the regions of the phase diagrams that are enclosed by the λ line. Does the typical sequence (BCC-hexagonal-gyroid-lamellar-inverted gyroid-inverted hexagonal-inverted BCC) of mesophases that is found in fluids with spherically competing interactions, as a function of the density and constant temperature, change due to an anisotropic attraction?

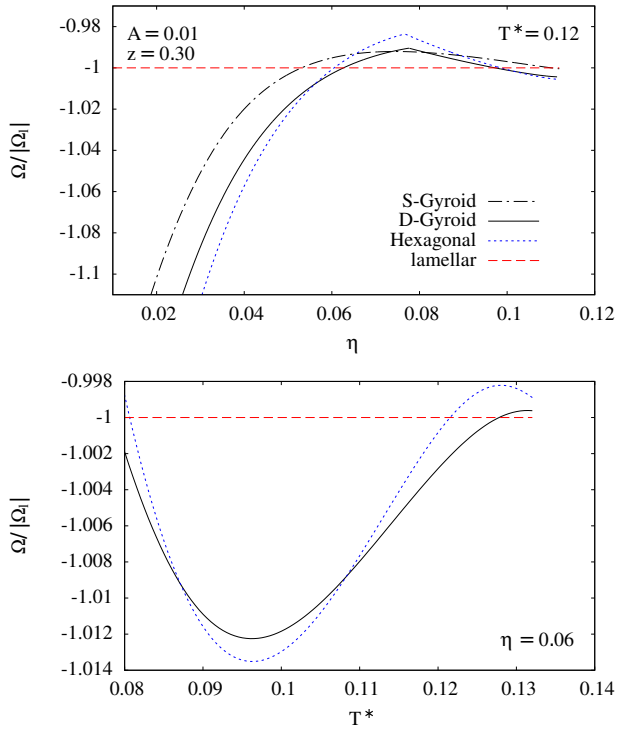

Figure 6.12 (a) The grand potential Ω normalized w.r.t. the lamellar phase (red dashed line) as a function of η at temperature $T^* = 0.12$ for several structures, including the single-gyroid (green dashed-dotted), double-gyroid (black solid), and 2D-hexagonal phase (blue dotted). (b) Same as in (a) but as a function of the temperature T^* at fixed packing fraction $\eta = 0.06$.

In Fig. 6.12 (a) we show $\Omega/|\Omega_l|$ normalized w.r.t. the absolute value of the lamellar phase Ω_l as a function of the reservoir packing fraction η for $A = 0.01$ and $z = 0.3$, corresponding to the phase diagram shown in Fig. 6.10 (a). The temperature is fixed at $T^* = 0.12$. For these parameters we observe the *same* sequence of structures as predicted for spherically-symmetric competing interactions (cf. Fig. 6.7): BCC-hexagonal-gyroid-lamellar-inverted gyroid-inverted hexagonal-inverted BCC. Note that for the sake of clarity the BCC phase is not displayed, as it occurs only in direct vicinity to the λ line. The kinks in the graphs corresponding to the double-gyroid and hexagonal phase indicate a first-order transition to their inverted structure, i.e., where low-density and high-density domains are interchanged. The lamellar and the single-gyroid structure are its own inverse, thus the grand potential of these structures is a smooth function of η.

Figure 6.12 (b) also pictures the behavior of the grand potential $\Omega/|\Omega_l|$, but now as a function of the temperature T^* at fixed packing fraction $\eta = 0.06$. Strikingly, we observe a reentrant effect: starting from a stable lamellar structure, the gyroid phase becomes stable between $T^* \approx 0.127$ and $T^* \approx 0.11$. Subsequently, this is followed by a region where the 2D-hexagonal structure corresponds to the global thermodynamic minimum, and at $T^* \approx 0.09$ the gyroid becomes the most stable structure again. For lower temperatures than displayed in the image, approaching the λ line, the lamellar phase is stable again. This behavior directly reflects the reentrant shape of the λ line, and is not compatible with the typical phase diagrams in systems with spherically

competing interactions, cf. Fig. 6.5. We have performed the same calculations also for the phase diagram in Fig. 6.10 (d), and found a similar behavior – although here the inverse structures (e.g. inverse double-gyroid or inverse BCC) seem to be unstable (despite a properly chosen initial perturbation $\delta\rho(\mathbf{r})$ one always ends up with an unspecific structure), which may be due to the fact that the (reservoir) packing fraction is too low in order to stabilize these structures.

Chapter 7

Patchy Models for Protein-Salt Mixtures

7.1 Introduction

Proteins are essential biological macromolecules, ubiquitously present in living organisms and cells, where they are crucial to and responsible for e.g. metabolism, the cell structure, or the transport of molecules such as oxygen. Proteins consist of amino acids connected via peptide bonds which defines their so-called primary structure. A single protein can unite several thousands of individual atoms, that primarily interact via covalent bonds, hydrogen bonds, and van der Waals forces. The non-covalent interactions control the so-called secondary, tertiary and quaternary protein structure and are typically much weaker compared to chemical bonds. Proteins can thus respond to chemical influences, such as exposure to acids, or to physical influences, such as temperature and pressure gradients with reversible or irreversible changes in their form and shape (unfolding and denaturation). An illustration of the most abundant protein in mammals, serum albumin, is pictured in Fig. 7.1.

Due to their inherent structure the interactions between proteins in solution are much more complex than that between two atoms or spherical colloids. The interactions among individual proteins include Coulomb forces, hydrogen bonds, van der Waals interactions, as well as solvent-mediated effects due to the presence of hydrophobic and hydrophilic zones on the proteins surface. Further levels of complexity are added due to inhomogeneous patterns of surface charge and the non-spherical shape of many proteins in general. All of this makes a quantitative physical description of proteins at the molecular level cumbersome and hence poses a large challenge for the statistical physics of soft matter. In particular, obtaining predictions for the macroscopic phase behavior based on atomistic simulations is at the very best extremely time-consuming and in many cases unfeasible. At the same time a profound understanding of the microscopic mechanisms in protein solutions is important to various fields ranging from biotechnology, biology, pharmacology and medicine, to environmental science and food

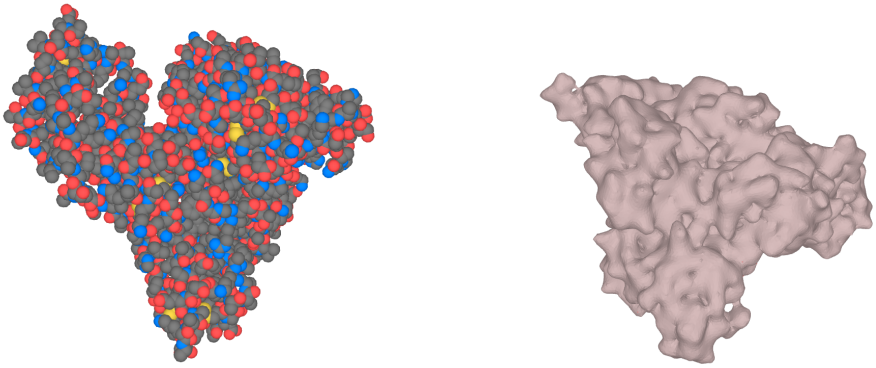

Figure 7.1 Left: Molecular picture of bovine serum albumin (BSA), where individual atoms are shown as spheres. Grey corresponds to carbon, blue to nitrogen, red to oxygen, and yellow to sulfur. The structure of the protein is the result of covalent- and hydrogen bonds, as well as van der Waal and Coulomb forces. Right: The structure of the BSA protein in surface representation. Images generated from https://www.rcsb.org/, PDB ID 3V03, K.A. Majorek *et al.*, Mol. Immunol. **52**, 174 (2012).

processing. For example, protein condensation and aggregation can be related to many diseases [204, 205] such as eye cataract [60] or Alzheimer's disease [61].

In 1977 Ishimoto and Tanaka [206] were the first who observed that protein solutions (lysozyme in salt water) can phase separate into protein-poor and protein-rich phases, in this context often termed liquid-liquid phase separation (LLPS). Many further studies on different types of proteins followed, see, e.g., Refs. 207–210 for detailed studies by Benedek and co-workers who investigated the formation of metastable (w.r.t. crystallization) liquid-liquid phase separation in aqueous γ-crystallin solutions, which plays a crucial role in mammal eye cataract. The occurrence of metastable LLPS regions is relevant to protein crystallization pathways: the presence of liquid-liquid critical points may enhance the formation of crystal nuclei in a 'two-step' process [211], where in a first instance a dense liquid droplet is formed from which then crystal structures can emerge [212]. A broader overview on the experimental history of research on the protein phase behavior is e.g. provided in Ref. 213.

Understanding and predicting the structure, dynamics and phase behavior of such complex macromolecules defines soft-matter science, and there is no simple recipe or general principle which tells us how to map a protein, or other complex materials as polymer melts, to a simple fluid as liquid argon [2]. It thus seems intriguing that various aspects of the experimental phase behavior of many distinct protein species, despite their differences in size, structure, or biological function, share intriguing similarities with a simple model of hard spheres and an additional short-ranged attraction outside their hard core [62, 214]. This model was first studied by Hagen and Frenkel [215] to model the phase behavior of colloid-polymer mixtures. Recall (see Sec. 1.2) that models of colloidal particles interacting via a short-ranged attraction exhibit a fundamentally different equilibrium phase behavior than those where the attraction is longer-ranged [31]: if phase separation into colloid-poor and colloid-rich occurs, then it is typically

metastable w.r.t. crystallization and the equilibrium phase diagram is as displayed in Fig. 1.2 (b). However, in contrast to protein solutions, in colloid experiments metastable liquid-liquid phase separation is often suppressed by particle aggregation and dynamically arrested gel phases [31, 33].

While the statistical physics of colloidal fluids consisting of spherical particles certainly is a valuable starting point, it is easy to grasp that proteins do not interact via purely isotropic (effective) pair potentials. Evidence for directional interactions between proteins is vast, starting from their non-spherical shape or the presence of hydrophobic and hydrophilic zones on their surface that may give rise to orientation-dependent forces. As regards the phase behavior, most notably the location of metastable critical points and liquid-liquid phase boundaries at rather low protein densities, such that the former are not frustrated by dynamic arrest, strongly suggest the presence of anisotropic attractive interactions between proteins in solution [65, 45] as a popular feature of patchy interactions is the tendency to render critical points at lower densities compared to isotropic pair potentials [47]. A promising framework to study the phase behavior of proteins is therefore formed by patchy particles [36, 59]. During the past two decades, many patchy particle models have been formulated to study features of protein solutions. In 1999, Sear [43] was the first who introduced a model based on Wertheim's perturbation theory that semi-quantitatively reproduced the phase diagrams of protein solutions. In 2001, Curtis *et al.* [67] argued that directional interactions need to be taken into account in order to reproduce experimental measurements of the second virial coefficient $B_2(T)$ in lysozyme solutions. In 2008, Gögelein *et al.* formulated an approach [45] to calculate the effects of sodium chloride on lysozyme solutions, were he employed a Barker-Henderson thermodynamic perturbation theory to describe patchy attractions, and a screened Coulomb potential to account for effects of the electrostatic repulsion. Results from computer simulations confirmed these theoretical ideas [44, 216] and provided further evidence for the importance of patchy attractions in protein solutions with other studies addressing the experimentally often observed two-step crystallization process [217, 218]. Furthermore, important aspects of protein solutions in presence of multivalent metal ions were successfully understood via simple colloidal models making use of patchy interactions [46, 144], where salt ions can bind to the protein surface and act as mediator for bonds between different proteins. In this chapter, we shall be concerned with these systems.

7.2 Protein-salt mixtures

Multivalent-metal ions have proven to be a powerful tool to induce a broad variety of interactions between proteins [68, 91]. Most importantly, these multivalent ions can trigger a so-called reentrant phase behavior as a function of the salt concentration. We shall now review the fundamentals of the experimental phase behavior of BSA and human serum albumin (HSA) in the presence of yttrium-III chloride (YCl_3) in some detail based on work of the Schreiber group [68, 91, 219, 220, 69, 213, 46], though an

Figure 7.2 Reentrant phase behavior of bovine serum albumin in the presence of yttrium chloride at constant protein concentration of $c_p = 50$ mg/ml and increasing salt concentration (from left to right). The clear regime at low salt concentration defines Regime I, a turbid solution Regime II, and a clear solution at high salt concentration Regime III (see text). Image from F. Zhang *et al.*, Phys. Rev. Lett. **101**, 148101 (2008) ©2008 American Physical Society

.

extensive review of all findings that have been gathered since more than a decade is clearly beyond the scope of this chapter; for more details, we refer to the aforementioned references, and references therein.

In pure water, without salt, both BSA and HSA carry a net-negative surface charge (its precise value depends on the pH value) and hence the protein solution is charge-stabilized. The addition of multivalent salt (in the following its concentration is denoted by c_s, typically given in millimolar (mM)) screens long-ranged repulsive electrostatic forces acting between the proteins. At the same time, positively charged multivalent cations (Y^{3+}) can bind to solvent-exposed carboxylic side chains on the protein surface and thereby change the net surface charge of the proteins. However, for sufficiently low salt concentrations the solution stays charge-stabilized and appear optically clear. In Ref. 68 this is called Regime I. Upon further increasing the salt concentration, the samples may become optically turbid at a specific salt concentration c^*, which, in turn, depends on the protein concentration c_p. This region is called Regime II in which the solution exhibits a very rich phase behavior, including a LLPS region, protein crystallization via different pathways, or aggregation of amorphous protein structures that at high densities form gel-like states. Further addition of salt leads to a reentrant effect (or reentrant condensation) above a certain concentration c^{**}, where the samples become optically clear again. This defines Regime III. An illustration of this reentrant condensation is shown in Fig. 7.2. We will discuss the three Regimes I, II and III in more detail subsequently where we complement the text with Figs. 7.3 and 7.4.

Regime I: $c_s < c^*$. With increasing salt concentration, approaching c^*, small-angle x-ray scattering (SAXS) experiments show [68] that the scattering intensities $I(q)$ exhibit a rapid increase for wavenumbers $q \to 0$ – see Figs. 7.3 (a) and (c) where $I(q)$ is shown for a protein concentration of $c_p = 100$ mg/ml and various salt concentrations

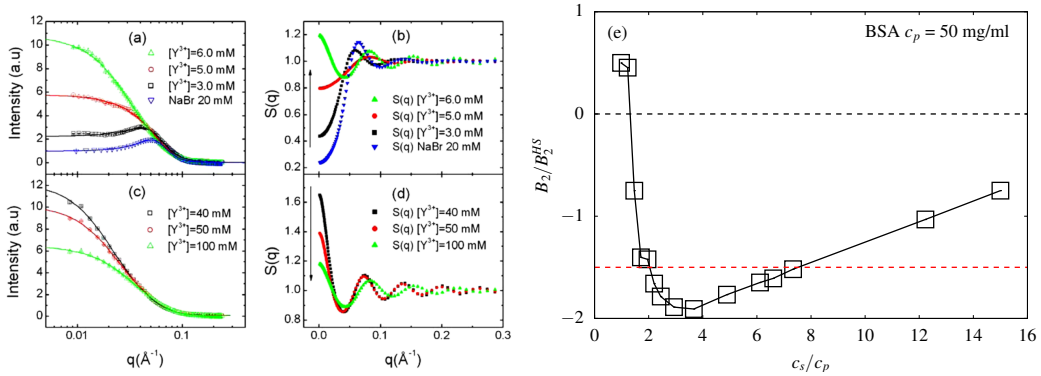

Figure 7.3 Left [(a) and (c)]: Results obtained from SAXS measurements of a BSA-YCl_3 solution at a protein concentration $c_p = 100$ mg/ml and various salt concentrations. Middle [(b) and (d)]: Corresponding structure factors obtained from fitting a (sticky) square-well model to the intensity. (e) Experimental results for the reduced second virial coefficient B_2/B_2^{HS} for $c_p = 50$ mg/ml as a function of salt concentration, where $B_2^{\mathrm{HS}} = 2\pi\sigma^3/3$ is the second virial coefficient for hard spheres, obtained by assuming a sticky hard-sphere pair potential acting between the proteins. The red, dashed line is a guide to the eye where $B_2/B_2^{\mathrm{HS}} = -1.5$, which is a phenomenological way to estimate the location of critical points in a wide class of simple fluids [123, 124]. The black dashed line shows $B_2/B_2^{\mathrm{HS}} = 0$, i.e. where attraction balances repulsion. Images (a)–(e) from F. Zhang *et al.*, Phys. Rev. Lett. **101**, 148101 (2008) ©2008 American Physical Society, data shown in (e) from M. Fries, *private communication.*

(below c^*). The corresponding[1] effective structure factors $S(q)$ are displayed in Figs. 7.3 (b) and (d): with increasing salt concentration, the values of $S(q)$ a low $q \to 0$ increase suggesting that attraction between the proteins starts to dominate over repulsion upon approaching the transition concentration c^*. By fitting known analytical expressions for the structure factor of the square-well fluid to the experimental results one learns that the range of protein-protein attraction is very short-ranged – a few per cent of the effective protein diameter [68].

In Ref. 69 Soraruf and co-workers provide a detailed study of Regime I for the BSA-YCl_3 system. In this work, the isothermal compressibility χ_T and the (OZ) correlation length ξ_{OZ} were measured using static (SLS)[2] and the time-dependent intensity auto-correlation function $g^{(2)}(q, t)$ was obtained from dynamic light scattering (DLS)[3]. The results from SLS experiments presented in Ref. 69 showed that upon approaching c^* the isothermal compressibility and the correlation length increase by several orders of magnitude, akin to a spinodal-like transition. These results are in

[1]Recall [57] that the scattering intensity is proportional to the static structure factor $S(q)$, $I(q) \propto P(q)S(q)$, where $P(q)$ is the form factor, a function that contains information about the geometric form of a particle (more precisely information about the spatial distribution of scattering centers). Assuming a spherical or ellipsoidal particle $P(q)$ is easily calculated. Thus, one can extract an effective structure factor $S(q)$, or, in turn, if a known analytical expression for $S(q)$ of some model is used, one can gather information about the effective protein pair interactions.

[2]In SLS experiments the low-density ($\rho_b \to 0$) and large wavelength ($q \to 0$) behavior of the static structure factor $S(q)$ can be measured:

$$S(q) \approx \frac{S(0)}{1 + \xi_{OZ}^2 q^2} \approx \frac{1}{(1 + 2B_2\rho_p)(1 + \xi_{OZ}^2 q^2)} \tag{7.1}$$

where $S(0)$ is approximated by $S(0) = (\partial\beta p/\partial\rho_p)^{-1} \approx 1/(1 + 2B_2\rho_p)$ and B_2 is the second virial coefficient. ρ_p denotes the number density of the proteins in the sample.

line with the strong increase of $I(q \to 0)$ obtained from the SAXS measurements. Furthermore, two decay times in $g^{(2)}(q,\, t)$ emerged upon coming close to the c^* line, pointing towards the presence of protein structures larger than monomers. Recently, Bleibel and co-workers found [144] a similar behavior upon approaching the fluid-fluid spinodal in a simple patchy model for proteins, where cluster formation (i.e. networks of bonded particles) was identified to be responsible for two decay times in the dynamic structure factor. In Ref. 69 it is stated that no qualitative changes were observed when repeating the SLS and DLS measurements after a few days using the same samples, suggesting that the protein clusters may correspond to a true equilibrium state. Interestingly, equilibrium clusters in protein solutions due to the presence of competing interactions had been reported earlier [84]. We will return to this in Sec. 7.5.

Regime II: $c^* < c_s < c^{**}$. The experimental results found in Ref. 69 for the compressibility and correlation length point towards the presence of a spinodal-like transition upon approaching c^*. But what mechanisms might cause the optical turbidity of the samples after crossing c^* in Regime II (the rather sharp transition from a clear to a turbid solution at salt defines c^*) ? From the perspective of equilibrium liquid-state theory, the occurrence of steeply increasing scattering intensities, diverging correlation lengths and an observable turbidity might lead to the conclusion that the system crosses an actual spinodal line at $c_s \approx c^*$, where the turbidity is associated with critical opalescence (density fluctuations on the scale of the wavelength of visible light). However, crossing the boundary c^* does not necessarily lead to macroscopically phase-separated protein phases – this requires sufficiently high protein and salt concentrations, see Figs. 7.4 (a) and (b). The coexisting protein-rich phases can form amorphous protein aggregates after several days to weeks and appear gel-like (Fig. 7.4 (e)) and we also show the typical behavior of the second virial coefficients B_2 crossing the LLPS region (calculated from a simple square-well model) in Fig. 7.3 (c) for a protein concentration of $c_p = 50$ mg/ml. It becomes clearly negative upon approaching c^*,

[3]With DLS experiments it is possible to investigate dynamic properties. The intensity auto-correlation function $g^{(2)}(q,\, t)$ can be written as

$$g^{(2)}(q,\, t) = 1 + \beta\, |f(q,\, t)|^2 \,, \tag{7.2}$$

where $f(q,\, t) \equiv F(q,t)/F(q,0)$ and $F(q,\, t) = \int \mathrm{d}\mathbf{r}\, \exp(-i\mathbf{q}\cdot\mathbf{r})\, G(r,\, t)$ is the spatial Fourier-transform of the van Hove function $G(r,\, t)$ termed the dynamic structure factor. β is an instrument dependent constant. Since the van Hove function can be split into self (s)- and distinct (d) parts $G(r,\, t) = G_s(r,\, t) + G_d(r,\, t)$ (see Ch. 5 for details) the same is true for the dynamic structure factor, i.e. $F(q,\, t) = F_s(q,\, t) + F_d(q,\, t)$. For mono-disperse systems it is known that $f_{s/d}(q,\, t)$ decays for fixed q and as a function of time as [57]:

$$f_{s/d}(q,\, t) \propto \exp(-D_{s/d}(q)\, q^2\, t) \,, \tag{7.3}$$

where $D_{s/d}(q)$ are (q-dependent) diffusion constants that provide information about self- and collective (distinct) structural relaxation over time. A second, typically slower time scale may emerge if structural correlations on a larger lengthscale influence the dynamics in the system, i.e. then one expects

$$f_{s/d}(q,\, t) = A^{(1)}_{s/d}(q) \exp(-D^{(1)}_{s/d}(q)\, q^2\, t) + A^{(2)}_{s/d}(q) \exp(-D^{(2)}_{s/d}(q)\, q^2\, t) \,, \tag{7.4}$$

with $D^{(2)}_{s/d}(q) < D^{(1)}_{s/d}(q)$ and q-dependent amplitudes $A^{(i)}_{s/d}(q)$.

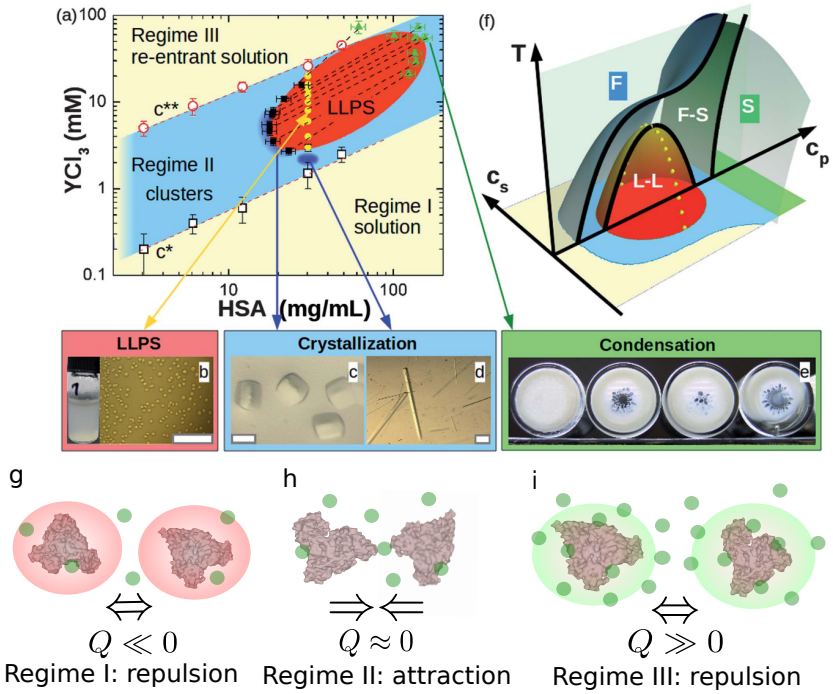

Figure 7.4 Figures illustrating the explanations of Regime I, II and III in the main text. (a) Reentrant phase behavior of HSA (similar for BSA) in the presence of YCl_3 in the $c_p - c_s$ plane at 20°C. (b) Under an optical microscope the LLPS region appears as slowly coalescing droplets of the protein-rich phase. (c) and (d) Growth of crystals observed from the protein-poor phases via two distinct crystallization processes: a non-classical two-step crystal [220] growth from the dilute protein phase via intermediate high-density droplets close to the LLPS and c^{**} phase boundary in (c) and via a classical one-step process in (d) (growth from a homogeneous solution). (e) Amorphous protein aggregates self-assemble after long times (after several weeks) from high-density protein phases, indicating a gel-like but non-arrested phase. (f) Sketch of the conjectured three-dimensional phase diagram for protein-salt mixture in $c_p - c_s - T$ space. (g) – (i) Sketch of the dominating protein interactions in Regimes I, II and III upon adding salt. Regime I: Electrostatic repulsion dominates in the solution, due to the strongly negative net surface charge ($Q \ll 0$) of HSA/BSA at neutral pH. Regime II: The trivalent positively charged Y^{3+} ions (green dots) screen the electrostatic repulsion and can bind to the protein surfaces. At the same time proteins start to form aggregates. Regime III: At high salt concentrations, over-charging ($Q \gg 0$) sets in leading again to an overall repulsive protein-protein interaction. Image is adapted and modified from Zhang *et al.*, Soft Matter **8**, 1313 (2012).

and decreases even below the value of -1.5, which in a wide class of simple fluids is an empirical value to estimate the critical temperature [123, 124].

We mentioned in the introduction 7.1 that a general feature in protein solutions is that the fluid-fluid coexistence is metastable with respect to crystallization, in analogy to the equilibrium phase behavior of colloidal fluids with a short-ranged attraction. Indeed, depending on the actual salt and protein concentration, crystals can nucleate via the classical pathway near the phase boundary c^*, or via a non-classical two-step mechanism close to the LLPS region and c^{**} boundary [91, 219, 220]. However note that there is strong evidence [221] that c^* does not coincide with the equilibrium fluid-solid boundary, as might be surmised from Fig. 7.4 (f); crystallization can also be observed below c^*, i.e. the (equilibrium) fluid-solid phase boundary must lie at lower salt concentrations. These experimental results point towards the fact that Regime II

is presumably located completely within the equilibrium solid-fluid coexistence region. Recall that crystallization in experiments with colloids that interact via a short-ranged attraction is often observed only in a narrow region close to the equilibrium gas-solid coexistence curve, and metastable non-equilibrium particle aggregation and gelation likely frustrates the true equilibrium phase coexistence of a low-density colloidal gas and a crystal phase, even at very low colloid packing fractions of $\sim 1\%$ [31, 33].

Given the close analogies found in the phase behavior of e.g. colloid-polymer mixtures and many protein solutions, a visible turbidity found outside of the LLPS region (cf. Figs. 7.2 and 7.4 (b)) might also be the result of non-equilibrium protein aggregation [221]. In fact, in contrast to states at salt concentration $c_s < c^*$ where experiments suggest [69, 222] that small protein clusters might correspond to an equilibrium state (see also Sec. 7.5), for $c_s > c^*$ it is observed that the aggregates tend to grow evidencing a non-equilibrium state [69]. Importantly, these metastable protein aggregates are believed to play a role in the above mentioned two-step crystallization process near the phase boundary c^{**} [220].

Regime III: $c_s > c^{**}$. At very high salt concentrations, the LLPS region and turbidity vanishes and the solution becomes clear again [68]. The system undergoes a charge inversion [68, 223, 213], i.e. the net surface charge of the proteins becomes positive. As a result, electrostatic repulsion again dominates over attraction. This manifests itself in decreasing values of $I(q)$ and $S(q)$ at low $q \to 0$, corresponding to increasing values of the (reduced) second virial coefficient B_2/B_2^{HS}. This behavior is called reentrant condensation and is defined by a second phase transition at salt concentrations $c_s = c^{**}$. As mentioned above, one also observes protein crystallization in vicinity to the latter, though the nucleation mechanism is different to that found at c^* [219].

7.3 Ion-activated patchy particles as a model for protein-salt mixtures

The existence of a reentrant LLPS region and protein condensation can be semi-quantitatively explained with a colloidal model of patchy particles [46] formulated within Wertheim's theory [73–77] (see also Ch. 3). The key point of the model is that the patch-patch interaction strength is controlled by the amount of salt (cations) present in the system. All repulsive interactions that occur and dominate the protein solution in Regimes I and III are mapped onto the hard-sphere pair potential. The patches represent solvent-exposed side chains on the protein surface which can be occupied by the yttrium ions, which yields an energy gain of ε_b. Two proteins can then be cross-linked if an occupied site meets a non-occupied one. In this case the interaction between the two proteins is *activated* by an ion, whereas it is *deactivated* otherwise. Note that protein bonds mediated by yttrium ions were observed in crystals

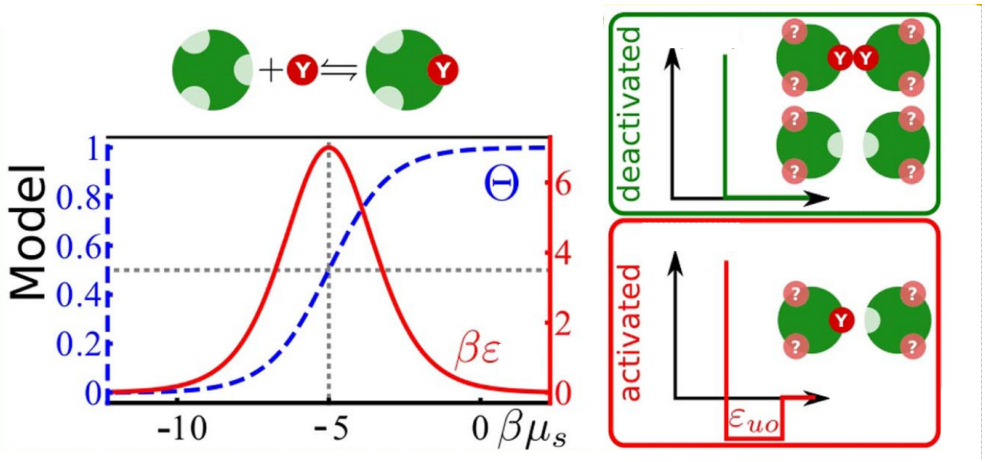

Figure 7.5 Proposed microscopic explanation for the formation of attractive protein interactions in the context of a patchy colloidal model [46]: multivalent cations can bind to unoccupied sites on the protein surface. The occupation probability Θ is defined in Eq. (7.5) and is shown as a function of the chemical potential μ_s of the salt (blue dashed line). A protein bond can be formed if an occupied site meets an unoccupied one ('activated') but no bond can be formed if two occupied or unoccupied sites meet ('deactivated'). The resulting patch-patch interaction energy is given by Eq. (7.7) and is displayed by the red curve as a function of μ_s. Image adapted and modified from Roosen-Runge *et al.*, Sci. Rep. **4**, 7016 (2014).

[219]. An illustration of the mechanism is provided in Fig. 7.5, taken and modified from Ref. 46).

The average occupancy Θ of a site by an ion may be written as the grand-canonical statistics of a two-state system:

$$\Theta(\mu_s) = \frac{1}{\exp(\beta(\varepsilon_b - \mu_s))}\,, \tag{7.5}$$

where μ_s is the chemical potential of the cations. As a result, the (average) patch-patch interaction energy ε may be written as

$$\varepsilon = \varepsilon_{uu}(1-\Theta)^2 + 2\varepsilon_{uo}\Theta(1-\Theta) + \varepsilon_{oo}\Theta^2\,. \tag{7.6}$$

The first term describes the interaction between two unoccupied sites. They meet with a probability of $(1-\Theta)^2$; the third term accounts for the interaction between two occupied sites, meeting with a probability of Θ^2. It is assumed that two unoccupied or two occupied patches do not interact, i.e. $\varepsilon_{uu} = \varepsilon_{oo} = 0$. Eventually, the effective patch-patch attraction becomes

$$\beta\varepsilon(\mu_s) = \frac{2\beta\varepsilon_{uo}\exp(\beta\varepsilon_b - \beta\mu_s)}{(1+\exp(\beta\varepsilon_b - \beta\mu_s))^2}\,, \tag{7.7}$$

and is thus controlled by the chemical potential μ_s of the salt, the binding energy ε_b between the cation and the proteins surface, and the interaction energy ε_{uo} between an occupied (activated) and unoccupied (deactivated) site meeting with probability $\Theta(1-\Theta)$. Note that the quantities ε_b and ε_{uo} may depend on the ion and protein

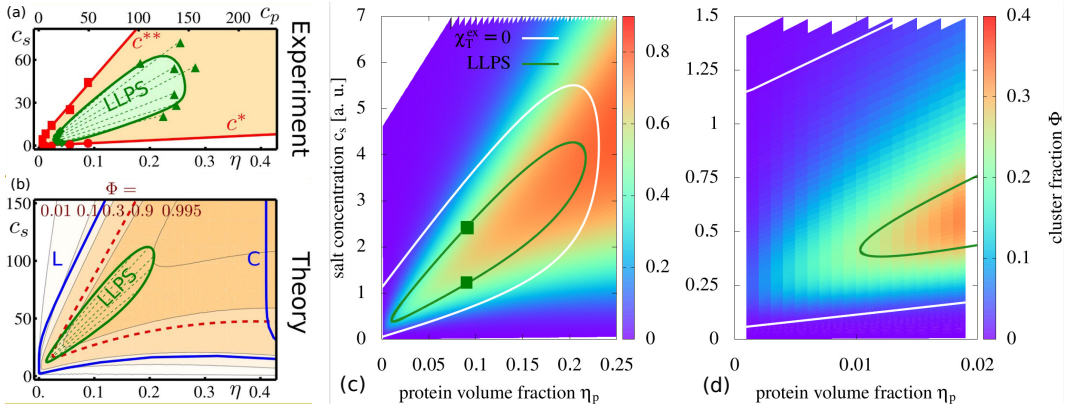

Figure 7.6 Theoretical phase diagram of the ion-activated patchy particle model [46] (see text for details) in the $\eta_p - c_s$ plane. (a) + (b) Comparison of the theoretical phase diagram to the experiments according to Roosen-Runge *et al.* [46]. The red-dashed line in the bottom left image (b) displays the percolation line according to Flory-Stockmeyer theory [149, 148] where the probability of bonding exceeds $p_b > 1/3$ in the case of four binding sites (patches) per protein (cf. Eq. (3.26)). (c) The model exhibits a closed-loop LLPS (green line) with two, upper and lower, critical points (squares). The white line enclosing the LLPS regime shows the locus where $\chi_T = \chi_T^{id}$, i.e. where $S(0) = 1$. According to Stopper *et al.* [136] (see also Sec. 2.4) the overall particle attraction dominates over repulsion within the region enclosed by this line. The colored heat map represents the number fraction Φ (cf. Eq. (3.27)) of proteins engaged in clusters, where the blue area corresponds to $\Phi \approx 0$, i.e. the presence of hard-sphere like monomers, and red to $\Phi \approx 1$, i.e. the presence of system-spanning networks. (d) A magnification of the phase diagram at low volume fractions (see text).

species, respectively, and can be considered as fixed quantities in a given experimental setup. They may be chosen inspired by experimental values [46]. Thus, the chemical potential μ_s controls the attraction between the proteins and takes the role of an effective temperature. For $\beta\mu_s \to \pm\infty$ it follows from Eq. (7.7) that $\beta\varepsilon(\mu_s) \to 0$, i.e. the proteins behave as hard spheres in the limit of no salt and at very high salt concentrations.

The resulting bulk phase diagram is displayed in Fig. 7.6 in the $\eta_p - c_s$ plane, where η_p denotes the protein volume fraction, and c_s the total salt concentration present in the system. The model assumes four binding sites per protein (i.e. $M = 4$), inspired by the number of cross-linked proteins in crystals [219] and $\beta\varepsilon_b = -5$ and $\beta\varepsilon_{uo} = 14$. It is also important to note that only the proteins are represented explicitly in this model. This, in turn, implies that c_s as a function of μ_s cannot be predicted self-consistently within this approach. However, we may assume [46] that c_s can be written as[4]

$$c_s(\mu_s) = \rho_p M \Theta(\mu_s) + \rho_s^r(\mu_s)\left(1 - \eta_p(1 + \sigma_s/\sigma_p)^3\right) \tag{7.8}$$

$$\equiv c_s^{\text{bound}}(\mu_s) + c_s^{\text{free}}(\mu_s) \tag{7.9}$$

where ρ_p is the protein number density, σ_p (σ_s) denotes the effective protein (salt ion) diameter, and $\rho_s^r(\mu_s) = C\exp(\beta\mu_s)$ is the number density of the salt ions in the reservoir, which are approximated as an ideal gas. However, the constant C cannot be determined self-consistently; in Figs. 7.6 (c) and (d) we have set $C \equiv 2$. The first term

in Eq. (7.8) accounts for the salt ions bonded to the protein surfaces and the second term describes the amount of free salt present in the system.

Comparing the theoretical predictions to the experimental phase diagram (Figs. 7.6 (a)+ (b), from Ref. 46), we see that the colloidal model accurately reproduces the closed-loop coexistence region (green lines) on a semi-quantitative level. In particular, the rather low values of packing fractions below 25% of the high-density protein phase and of the critical densities (squares) below 10% point towards the presence of highly anisotropic, patchy protein interactions. The red dashed line in Fig. 7.6 (b) corresponds to the percolation line (defined in Eq. (3.26)). The blue solid line is the fluid-solid boundary, where the solid is described within a cell model [43]. In accordance with experimental results, the LLPS regime is found to be metastable[5] w.r.t. crystallization [46]. The fraction Φ of proteins in clusters (or the degree of polymerization), cf. Eq. (3.27), displayed as a coarse contour plot in (b), is shown in a more detailed heat map in Figs. 7.6 (c) and (d). Blue areas correspond to the hard-sphere limit, i.e. $\Phi = 0$ whereas red corresponds to $\Phi = 1$ indicating the presence of system-spanning dense networks of proteins. In addition, we show as the white solid line where the isothermal compressibility takes its ideal-gas value, i.e. where attraction balances repulsion (see Sec. 2.4). The behavior of both, the degree of polymerization Φ and the line $\chi_T = \chi_T^{\mathrm{id}}$ fairly resemble the experimental lines c^* and c^{**}.

It is important to note that the model provides an effective and coarse description within a patchy colloidal picture, that itself is based on an approximate theoretical framework. We thus emphasize that e.g. the criterion $\chi_T = \chi_T^{\mathrm{id}}$ or the percolation line are not a direct quantitative measure for the experimental crossover lines c^* and c^{**}, but rather provide an idea of the essential physics in terms of a reentrant attraction as a function of the salt concentration. Recall that any form of repulsion is mapped onto the hard-sphere potential and any form of attraction is mapped onto the patchy interaction. Similarly, the theoretical model fails to satisfactorily explain the occurrence of a turbidity in experiments that is *visible by eye*. As mentioned earlier, a turbidity implies the presence of dense aggregates or droplets of proteins with sizes of the order of several hundreds of nanometers. The image Fig. 7.6 (c) displays a magnification of the theoretical phase diagram at low protein packing fractions. Here the fraction of proteins in clusters is predicted to range between 10% and at most 40%, which cannot quantitatively explain the presence of large and dense protein aggregates

[4]Note that in Eq. (7.8), and in the model in general, the unit of c_s is a number density, whereas in experiments the salt concentration is typically given in millimolar (mM). Similarly, the protein concentration c_p is e.g. given in mg/ml, whereas in the theoretical model reduced quantities such as the protein packing fraction $\eta_p = \pi\sigma_p^3\rho_p/6$ are used. Interconversion of these variables is straightforward. For instance, η_p can be calculated from c_p in mg/ml via: $\eta_p = \pi\sigma_p^3\,\rho_p/6 = \pi\sigma_p^3\,\left(c_p/M_{\mathrm{BSA}}\right)/6$, where $\sigma_p \approx 7$ nm is the effective protein diameter and $M_{\mathrm{BSA}} = 66$ kDa is the molecular weight of BSA. Note, however, that there is, of course, not a one-to-one correspondence between the experimental and theoretical phase diagram in terms of absolute values for the protein and salt concentrations.

[5]Wertheim's theory for patchy particles cannot describe solid (crystalline) phases. Thus 'metastable' in this context means that the Wertheim free energy of the fluid phase is larger than that obtained from the cell-model method. A potential future project could elucidate the precise location of the fluid-solid phase boundaries of the model with the help of computer simulations.

scattering visible light. In particular, if the protein aggregation in Regime II was a pure non-equilibrium phenomenon (cf. discussion in Sec. 7.2), no equilibrium theory would be able to describe the lines c^* and c^{**} on a quantitative level.

7.4 Protein adsorption at the solid-liquid interface[6]

Protein adsorption at solid-liquid interfaces occurs in many natural processes, and its understanding is crucial to many fields, ranging from biotechnology, biology, pharmacology, medicine to environmental science and food processing with relevance in many applications [224]. In particular, it is the first step in numerous biological processes, such as the blood coagulation cascade or transmembrane signaling and adhesion of particles (bacteria or cells) [224] and therefore plays a key role in biomedical devices, including biosensors, biochips, soft contact lenses and biomaterials for implants [225]. In this section, we demonstrate that experimentally observed salt-induced protein adsorption at a planar attractive substrate can be intuitively understood with the ion-activated patchy model (see Sec. 7.3). The adsorption experiments, carried out by the Schreiber group, were performed in presence of a planar silicium-dioxide (SiO_2) substrate at different salt (YCl_3) concentrations and constant protein (BSA) concentration of $c_p = 20\,\mathrm{mg/ml}$ corresponding to a packing fraction of $\approx 1\%$. This corresponds to taking a path in the experimental phase diagram as indicated by the red arrow in Fig. 7.7 (b). For further experimental details we refer to Ref. 161.

Experimental observation

As outlined in Sec. 7.2, protein solutions in presence of multivalent undergo a reentrant condensation (RC) phase behavior as a function of the total salt concentration. An aggregation Regime II occurs in between two (protein-density dependent) salt concentrations c^* and c^{**}, which is illustrated in Fig. 7.7 (b). The physical mechanisms behind the observed RC behavior are believed to be the inversion of protein charge (Fig. 7.7 (a)) and a cation-mediated anisotropic attraction. The laterally-averaged thickness d of the adsorbed protein layer was obtained from real-time ellipsometric data measurements. The experimental results (individual symbols) are plotted in Fig. 7.8 as a function of of the dimensionless quantity c_s/c_p. Note that both BSA and SiO_2 surfaces are net negatively charged in pure water without added salt. Under these conditions the electrostatic repulsion among the proteins as well as among proteins and the substrate dominates the solution, leading to an overall low adsorption. With increasing salt concentration c_s, a clear increase of the adsorbed amount of proteins at the substrate is observed (solid triangles in Fig. 7.8). In Regime II, the value of d reaches a maximum of $\approx 10\,\mathrm{nm}$ at $c_s = 4$ mM (empty diamonds in Fig. 7.8), evidencing that clearly more than one monolayer of proteins is adsorbed to the interface (the

[6]This section is partially reproduced from M. Fries, D. Stopper, A. Hinderhofer, F. Zhang, R. M. J. Jacobs, M. W. A. Skoda, R. Roth, and F. Schreiber. Phys. Rev. Lett., **119**, 228001 (2017).

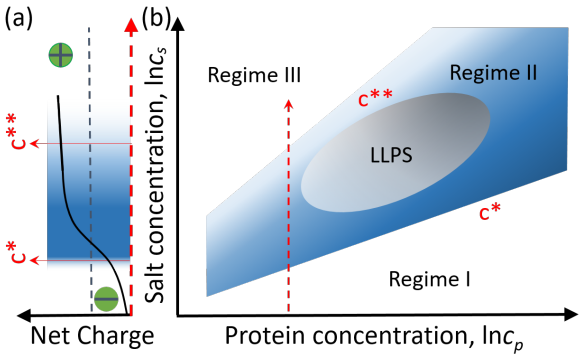

Figure 7.7 (a) Charge inversion of BSA as a consequence of adding trivalent yttrium ions. (b) Schematic of the bulk phase diagram of BSA and YCl_3 showing a liquid-liquid phase separation (LLPS) and reentrant condensation. The dashed red arrow indicates the path taken in the experiments.

effective diameter of BSA is ≈ 7 nm). Upon further increasing the salt concentration, the protein adsorption decreases down to a value of $d \approx 6$ nm when approaching the second transition line c^{**}. Note that in Regime II the bulk solution was centrifuged before performing the adsorption measurements, which results in a small jump of the adsorption at the transition from Regime II to III [161]. The centrifugation removed some of the largest protein aggregates, as an excessive amount of large protein clusters would cause a dramatic drop of the sensitivity of the ellipsometer due to massive light scattering. We show both data sets at $c_s/c_p = 40$ (centrifuged and non-centrifuged) to demonstrate the obtained difference, which, importantly, does not affect the overall adsorption trend. In Regime III, close to c^{**}, the value of d after (≈ 6 nm) and without centrifuging (≈ 7.5 nm) for $c_s = 12$ mM. At very high salt concentrations (solid squares in Fig. 7.8), deeply in Regime III, the value of d converges to a plateau value of ≈ 4.5 nm corresponding to slightly less than coverage by one full monolayer. Interestingly, there the proteins were found to irreversibly be bounded to the substrate (rinsing the sample with water did not reduce the measured layer thickness d) [161].

Theoretical modeling

In order to understand the experimental adsorption behavior, in a first instance it is helpful to understand that the latter is related closely to that of the second virial coefficient B_2 of the *bulk* protein solution (see inset of Fig. 7.8). Recall that B_2 is defined as

$$B_2 = 2\pi \int_0^\infty \mathrm{d}r\, r^2 \left[1 - e^{-\beta\, \phi_{\mathrm{eff}}(r)}\right] , \tag{7.10}$$

where $\phi_{\mathrm{eff}}(r)$ is the effective spherically-averaged protein-protein pair potential. In Regime II, the value of B_2/B_2^{HS}, where $B_2^{\mathrm{HS}} = 2\pi\sigma_p^3/3$ is the hard-sphere virial coefficient, is clearly negative indicating a strong overall attraction between proteins compared to Regime I and III; note that this is *not* the definition of the regimes nor its boundaries, but rather is an important observation: the net attraction between proteins is reflected by a sharp adsorption maximum. This observation indicates that the protein adsorption

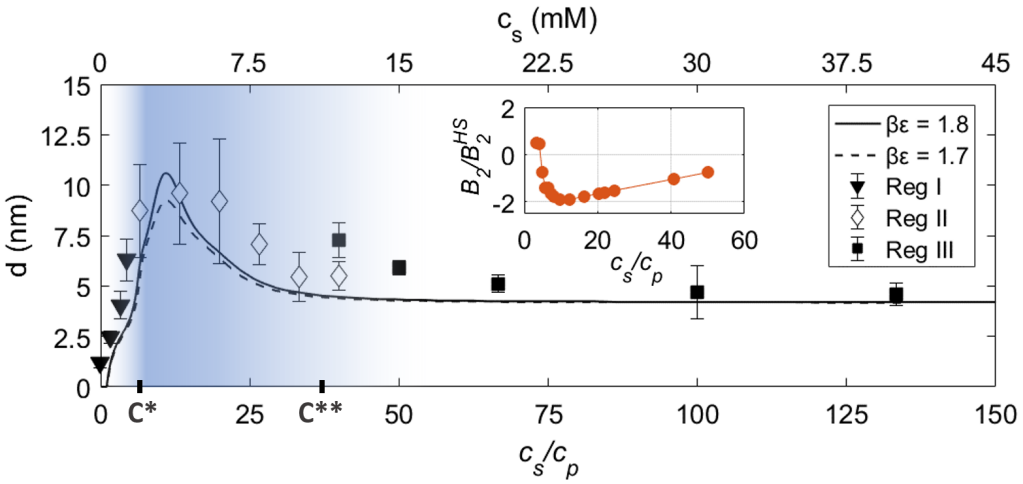

Figure 7.8 *Individual symbols*: Adsorbed protein layer thickness d extracted from ellipsometry as a function of c_s/c_p. c^* and c^{**} denote the phase transitions of the bulk solution [68], see also Fig. 7.7 (b). The top c_s-axis shows the absolute salt concentration c_s in mM (at $c_p = 20$ mg/ml). The blue shaded area indicates the approximate range where bulk turbidity occurs. *Solid and dashed lines*: Protein adsorption based on DFT calculations as borne out by the ion-activated attractive patch model, while neglecting long-range electrostatic forces, as a function of c_s/c_p for two different values of $\beta\varepsilon_w$ (see main text). *Inset*: The reduced second virial coefficient B_2/B_2^{HS} obtained from SAXS measurements.

in the system is closely related to the bulk behavior, which can successfully be accounted for by the model for ion-activated attractive patches as a mechanism for interactions in protein-salt mixtures, introduced in Sec. 7.3. While the experimental results suggest that the bulk behavior dominates the adsorption trend, another key point is the protein adsorption at a charged attractive planar wall, which implies breaking the translational symmetry of the system. We can make use of DFT in order to investigate inhomogeneous density distributions of proteins at the solid-liquid interface. More precisely, we employ the mFMT-DFT formulation of Wertheim's theory, discussed in detail in Ch. 4, to theoretically calculate the layer thickness d at the attractive substrate, where we incorporate the protein model from Sec. 7.3 within DFT.

The attraction mechanism between protein and substrate arises in the experiments as follows: the substrate is charged and strongly attracts yttrium ions, which in turn attract proteins towards the wall (Fig. 7.9 (a)). Effectively, this can be described by a short-ranged external potential $V_{\text{ext}}(z)$ acting on the proteins, where z is the distance normal to the SiO_2 wall. We set

$$V_{\text{ext}}(z) = \begin{cases} \infty & ; \quad z < 0 \\ -\varepsilon_w \Theta(\mu_s) h(z) & ; \quad z \geq 0 \end{cases} , \tag{7.11}$$

in order to represent a steric repulsion between proteins and the substrate for $z < 0$ and an attraction for $z > 0$. The function $h(z)$ accounts for the rather short-ranged attraction induced by the yttrium ions *condensed* on the wall – which is in-line with recent experimental observations [226]. Here, we employ a Gaussian form $h(z) =$

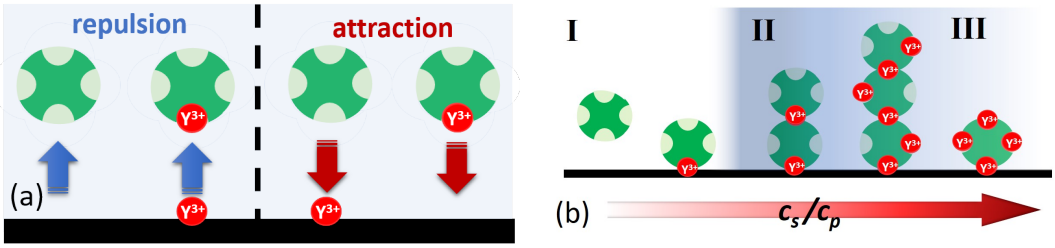

Figure 7.9 (a) Illustration of the different interaction mechanisms of the proteins, salt, and interface. (b) Sketch of protein adsorption on the attractive surface by increasing c_s/c_p.

$\exp(-2(z/\sigma_p)^2)$ with the range of attraction being roughly one protein diameter, which *effectively* accounts for the range of the screened electrostatic interactions between ions and the wall, and between ions and proteins.

The key point of the wall-fluid potential is: the strength of the external potential depends on μ_s, the chemical potential of the salt, via the occupation probability Θ of the protein binding sites. This form can be motivated by the following arguments. A sketch is presented in Fig. 7.9. At low c_s, when $\Theta \to 0$, only few proteins are subject to the attraction of the wall induced by ions. As c_s increases, more ions can mediate attractions between the wall and proteins. At the same time, the protein-protein attraction increases considerably, which in turn leads to an increase of the overall adsorption of proteins. At very high c_s ($\Theta \to 1$), the mechanism for the wall attraction remains, while the protein-protein interaction becomes weak since a majority of binding sites are occupied so that salt ions cannot induce anymore a patchy attraction between proteins. Therefore, one expects from the just outlined model ≈ 1 monolayer of proteins to be adsorbed on the wall at high salt concentrations.

In Fig. 7.8 (solid and dashed lines), we show the theoretical values of d in nm as a function of c_s/c_p for a packing fraction $\eta_p = \pi\rho_p\sigma_p^3/6 = 0.0078$, corresponding to a path in the theoretical phase diagram as illustrated by the red dashed arrow in Fig. 7.7 (b). This particular value for the packing fraction was chosen such that the relative distance between the path and LLPS boundary is the same as that in the experimental phase diagram[4]. Recall also that only the proteins are represented explicitly in the theoretical model, which implies that the salt concentration c_s as a function of μ_s cannot be predicted self-consistently within this approach. We use the location of the minimum of the experimentally determined value of B_2/B_2^{HS} in order to calibrate $c_s(\mu_s)$ which results in $C = 2$ in Eq. (7.8).

We furthermore choose four binding sites per protein (i.e. $M = 4$), $\varepsilon_b = -5$ and $\varepsilon_{uo} = 14$ in Eqs. (7.5) and (7.7) as in Ref. 46. The protein adsorption is then obtained from the inhomogeneous density profile $\rho_p(z)$, computed from DFT employing the ion-activated patch model. Recall that in Sec. 4.4 of Ch. 4 we have shown that the mFMT-DFT is fairly reliable for the case of four binding sites per particle. In order to compare with experiments, we define d as the distance from the wall where $\rho_p(z)$ is at least 50% higher than the bulk density ρ_p. For suitable values of $\beta\varepsilon_w$ (1.8 (solid curve), and 1.7 (dashed curve)), we find very good, semi-quantitative agreement between

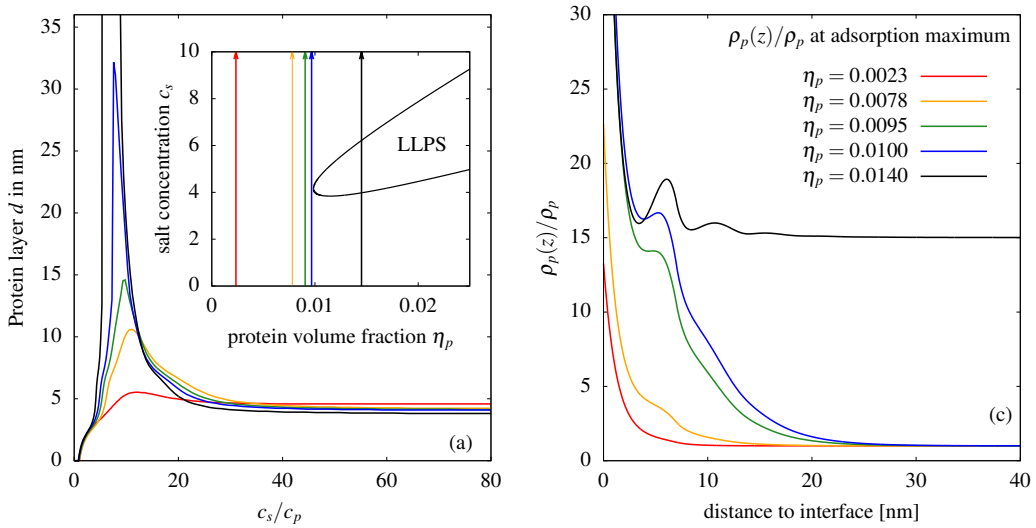

Figure 7.10 (a) Adsorption layer d in nm assuming a protein diameter of $\sigma_p = 7$ nm as obtained from the theoretical model upon approaching LLPS at several constant protein volume fractions η_p, where the orange curve corresponds to the black solid line in Fig. 7.8 with $\beta\varepsilon_w = 1.8$. The inset (b) demonstrates the paths taken relative to the low-density protein phase of the LLPS region. (c) Plots of the protein density $\rho_p(z)$ corresponding to the adsorption maxima shown in (a) and normalized to their asymptotic value for $z \to \infty$, where the same color code as in (a) and (b) is used.

theory and experiment. For high values of c_s, we find a value of d related to ≈ 1 monolayer coverage, similar to the experiments.

The theoretical results confirm that ion binding at the protein surface drives the experimentally observed non-monotonic adsorption behavior, thereby reflecting the underlying bulk interactions. In particular, the remarkable agreement between experiment and theory (considering in particular the few parameters involved) emphasizes that our model of ion-activated attractive patchy particles, subjected to an effective external wall potential, captures the essential effects of the protein adsorption at a charged surface in the presence of multivalent salt ions. Our model is kept intentionally simple with a minimum number of parameters, which helps us to identify the key mechanism responsible for the behavior of the system, namely the ion-activated patchy interactions of the proteins.

Enhanced protein adsorption upon approaching coexistence region

Importantly, using the DFT model we can easily explore the adsorption behavior of the system in different regions of the bulk phase diagram. The theoretical predictions for the layer thickness d, as a function of the dimensionless ratio c_s/c_p, are displayed in Fig. 7.10 (a) for several fixed protein volume fractions; the corresponding paths in the theoretical bulk phase diagram are shown in the inset (b). The model parameters are the same as in Fig. 7.8 and given above. In addition, we show the protein density distributions $\rho(z)$ obtained from DFT in Fig. 7.10 (c), corresponding to the maxima of

the adsorption layer d shown in Fig. 7.10 (a). Note that the curves are normalized with respect to the bulk value of the protein-poor phase.

The model predicts that the adsorption in Regime II is dramatically enhanced upon approaching the LLPS region. For the path crossing the coexistence region (black arrow) the attractive substrate is covered by a macroscopic film of the coexisting high-density protein phases, i.e. the layer thickness d diverges. The enhancement of adsorption at the solid-liquid interface, when approaching liquid-liquid coexistence from the dilute phase, is a well-known phenomenon in the statistical physics of simple liquids [57, 227]. It is related to wetting transitions, which can occur at bulk coexistence where the thickness of the adsorption layer diverges either continuously or discontinuously to form a macroscopically thick film above a certain so-called wetting temperature.

Our theoretical results suggest that interfacial phenomena such as wetting may also be formed in rather complex solutions of proteins, which would provide promising new perspectives for controlling protein adsorption at interfaces. In fact, exploiting the underlying bulk phase behavior and thermodynamic conditions offers an particularly efficient tool for tailoring a desired protein density at substrates in a controlled manner.

7.5 Simple extension for the protein model

In Sec. 7.2 we laid out the experimental phase behavior of proteins-salt mixtures in some detail. In this section, we discuss possible equilibrium cluster formation of proteins upon approaching the lower phase boundary c^* in Regime I. In fact, we would expect that upon approaching c^* there is a window where competing interactions (see Ch. 6) might be present as the surface charge of the proteins is reduced due to binding of positively charged cations to the protein surfaces, resulting in a weakening of the overall electrostatic repulsion between the proteins. At the same time, ion-mediated bonds between the latter lead to an effective short-ranged patchy attraction. While the existence of two-time scales in dynamic correlation functions provides some hints for cluster formation [69], according to our discussions given in Ch. 6, we would also expect the presence of a pre-peak in the static structure factor $S(q)$ at low wave numbers q.

In order to take electrostatic forces into account, the simplest extension of the protein model discussed in Sec. 7.3 is to assume a salt-dependent screened electrostatic repulsion, which may be described by the Derjaguin-Landau-Verwey-Overbeek (DLVO) theory. The latter was derived for the dilute limit of two charged hard spheres in the presence of monovalent salt, and thus should be applied with care to denser protein solutions in presence of multivalent salts; nevertheless it may provide qualitative insights into the essential physics. Let us thus consider a repulsive hard-core Yukawa-potential $\phi_{\text{rep}}(r) \equiv \phi_{\text{DLVO}}(r)$ in addition to the salt-dependent patchy attraction. The theoretical description within DFT is as described in Sec. 6.3. Theoretical results for the structure factor $S(q)$ are calculated via the Fourier transform of the direct pair correlation function $\widehat{c}(q)$, $S(q) = 1/(1 - \rho_b \widehat{c}(q))$, where the latter is obtained from taking two functional derivatives of the excess free energy functional given by Eq. (6.11).

Within DLVO theory, the repulsive part of the pair interaction reads:

$$\beta\phi_{\mathrm{DLVO}}(r) = \frac{A_{\mathrm{DLVO}}}{r/\sigma_p}\,\exp[-\kappa(r/\sigma_p - 1)]\,, \tag{7.12}$$

$$= \frac{\lambda_B/\sigma_p}{(1+\kappa/2)^2}\frac{Q_p^2}{r/\sigma_p}\,\exp[-\kappa(r/\sigma_p - 1)]\,, \tag{7.13}$$

where κ^{-1} is the reduced (dimensionless) Debye screening length and Q_p is the net protein surface charge in units of the elementary charge e. Both quantities, κ and Q_p, are in general salt- and protein concentration dependent. The inverse reduced Debye screening length may be written as

$$\kappa = \sigma_p\sqrt{4\pi\lambda_B\,(z^2 c_s^{\mathrm{free}} + \rho_p|Q_p|)}\,, \tag{7.14}$$

where c_s^{free} is the number density of the *free* ions (cf. Eq. (7.8)) and z is the valence number of the ions, i.e. $z = 3$. Furthermore, $\lambda_B = e^2/(4\pi\varepsilon_0\varepsilon_r k_B T)$ is the Bjerrum length ($\lambda_B \approx 0.7$ nm for water at room temperature). If we assume an effective protein diameter of $\sigma_p = 7$ nm [46] we thus have $\lambda_B/\sigma_p = 0.1$. The model framework for ion-activated patches leads to a simple expression for the net protein surface charge as a function of the salt-chemical potential:

$$Q_p(\mu_s) = -Q_0 + z\,M\,\Theta(\mu_s)\,, \tag{7.15}$$

where Q_0 is the surface charge without salt (we assume $Q_0 = -6$ as in Ref. 46), and $\Theta(\mu_s)$ is given by Eq. (7.5).

The key feature of the inverse screening length κ is its dependency on the salt concentration, $\kappa \propto \sqrt{c_s^{\mathrm{free}}}$ and the protein density, $\kappa \propto \sqrt{\rho_p}$. However, as mentioned above, we cannot expect Eqs. (7.14) and (7.12) to hold for multivalent salts on a quantitative level. We therefore introduce a scaled screening length, $\tilde{\kappa} \equiv \psi\kappa$ with a scaling factor ψ that is used to fit theoretical expressions to experimental results for the static structure factor.

Experimental results for $S(q)$. In Figs. 7.11 (a)–(d) we display the effective static structure factor as obtained from scattering intensities $I(q)$ measured in SAXS experiments for a BSA-$LaCl_3$ (lanthanum (III) chloride) mixture [222] at $c_p = 50$ mg/ml (a), 100 mg/ml (b), 150 mg/ml (c) and 200 mg/ml (d). The (reduced) salt concentrations are $c_s/c_p = 1.1$ (purple), 2.2 (green), 3.3 (blue), and 4.4 (yellow). All these state points are located within the clear Regime I. Note that $LaCl_3$ does not trigger LLPS, pointing towards an ion-induced attraction that is weaker than for YCl_3 [228]. However, a reentrant phase behavior is still observed, including Regimes I, II and III. At state points for $c_s/c_p = 1.1$ (purple lines) the solution is dominated by repulsion [222, 221]. In particular, at these state points, the first peak in $S(q)$ is not a signal indicating competition between attraction and repulsion; rather it indicates the presence of a longer-ranged repulsive component in the pair potential forcing the

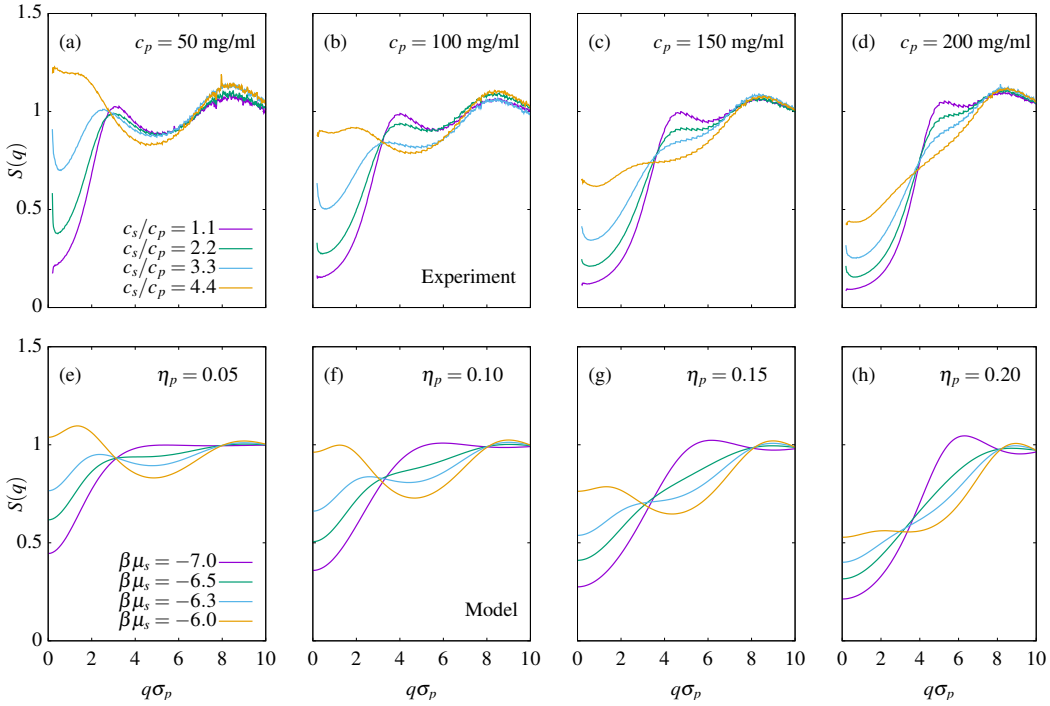

Figure 7.11 (a)–(d) Effective static structure factor $S(q)$ for BSA-$LaCl_3$ at $c_p = 50$ mg/ml (a), 100 mg/ml (b), 150 mg/ml (c) and 200 mg/ml (d) for reduced salt concentrations $c_s/c_p = 1.1$, 2.2, 3.3, and 4.4. Note that these state points are located below the transition boundary c^* in Regime I; the experimental data is replotted from Ref. 222. (e) – (h) Theoretical results for the static structure factor $S(q)$ at different protein volume fractions η_p as borne out by the extended protein model. The resulting phase diagram is displayed in Fig. 7.12. Note that there is no one-to-one mapping between the experimental and theoretical phase diagram in absolute numbers, so that the protein volume fractions in (e)–(h) do *not* precisely correspond to the protein concentrations shown in (a)–(d).

proteins to separate at distances larger than their effective diameter σ_p (recall that in a hard-sphere like fluid the main peak is located at $q\sigma \approx 2\pi$). We observe that the peak shifts (at constant $c_s/c_p = 1.1$) from initially $q\sigma_p \approx 3$ to higher values of $q\sigma_p \approx 2\pi$ with increasing protein concentration (it vanishes for $c_p \geq 300$ mg/ml, not shown). This is a consequence of the fact that the electrostatic repulsion depends on the protein density (the former gets screened at higher protein densities, i.e. its amplitude and range decrease, cf. Eq. (7.12)). This is also in line with findings of BSA solutions in the presence of monovalent sodium chloride [229].

Consider now the case of increasing salt concentration at fixed protein density. We make two observations: first, and as expected, the value of $S(q \to 0)$ clearly increases towards unity, indicating that attraction between the proteins starts to play a dominating role where the effect is more pronounced at lower protein densities. We furthermore observe that the first peak in $S(q)$ initially located at $q\sigma_p \approx 3$ starts to move towards lower values of q, most clearly visible in Figs. 7.11 (a) and (b). We note that such behavior is only known for systems where a short-ranged attraction competes with a longer-ranged repulsion, see e.g. Refs. 198, 86. It can be surmised from Figs. 7.11 (a) and (b) that this peak, however, will continue to move towards $q \to 0$ for

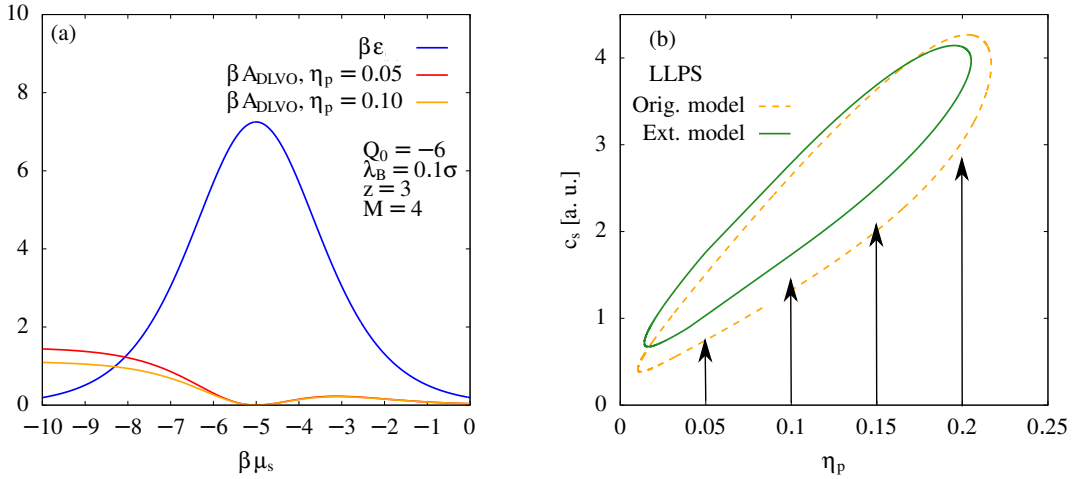

Figure 7.12 (a) Amplitude $\beta\varepsilon(\mu_s)$ of the patch-patch interaction energy (blue) defined in Eq. (7.7) to the amplitude $\beta A_{\mathrm{DLVO}}(\mu_s)$ of simple DLVO-type repulsion defined in Eq. (7.12) for $\eta = 0.05$ (red) and 0.10 (orange) as a function of the salt chemical potential μ_s. The scaling parameter is $\psi = 2$ (see main text). (b) LLPS region (green solid) as borne out of the extended model in comparison to the LLPS region according to the original model (orange dashed). The arrows indicate taken paths at constant protein density in Figs. 7.11 (e)–(h).

higher salt concentrations approaching c^*, where we know that the system undergoes a spinodal-like transition manifested by steeply increasing scattering intensities for $q \to 0$. At higher protein concentrations of $c_p = 150$ mg/ml (c) and 200 mg/ml (d) the overall effect is much less pronounced. This behavior is consistent: as mentioned above, both the amplitude and the range of the electrostatic repulsion should decrease with respect to a state point with lower protein density but the same value of c_s/c_p. As a result, with increasing protein concentration, the system behaves more similarly to a fluid where there is only a short-ranged attraction present between the particles, i.e. $S(q \to 0)$ increases as the salt concentration is increased, but no peak emerges at low q.

Comparison with theoretical results. Remarkably, if we choose $\psi = 2$, i.e. $\tilde{\kappa} = 2\,\kappa$, where κ is defined in Eq. (7.14), we can obtain qualitative similarities between the static structure factor $S(q)$ as borne out by the extended protein model (incorporated into DFT along the lines of Sec. 6.3) and the experimental results. This is displayed in Figs. 7.11 (e) – (h) for protein packing fractions $\eta_p = 0.05$ (e), 0.1 (f), 0.15 (g) and 0.2 (h); note that a constant value of the salt chemical potential $\beta\mu_s$ is similar to a constant ratio c_s/c_p in the experiments. Interestingly, a similar trend for $S(q)$ was observed in Ref. 230 where the author studied effects of a spherical DLVO-type repulsion on a patchy model for proteins based on the floating-bond model [143].

In Fig. 7.12 (a) we compare the amplitude of the attractive patch-patch interaction energy (blue line) in comparison to the amplitude A_{DLVO} of repulsion, defined in (7.12), as a function of the salt chemical potential $\beta\mu_s$. We show A_{DLVO} for a protein packing fraction $\eta_p = 0.05$ (red line) and 0.1 (orange). Similar to the attraction, the repulsion shows a reentrant effect, however, at high salt density its amplitude and

range are significantly damped. Interestingly, this qualitatively is consistent with the experimental behavior of the second virial coefficient (Fig. 7.3) which does not reach its initial values of Regime I upon approaching Regime III. The effects of incorporating a longer-ranged repulsion on the LLPS region (green line) in comparison to the original model (orange dashed) are displayed in Fig. 7.12 (b). The arrows indicate paths at constant chemical potential $\beta\mu_s$, illustrating the state points at which $S(q)$ is shown in Fig. 7.11.

The results of the extended model for protein-salt mixtures provide theoretical evidence that competing interactions play a role in Regime I upon approaching the phase boundary c^*. In particular, the original protein model, where no long-ranged repulsion is taken into account, does not predict any pre-peak in the corresponding structure factor. However, the presence of *equilibrium* protein cluster phases, defined in Refs. 199, 86, 87 as the presence of aggregates with a particular size (see also discussions in Ch. 6), cannot be verified – the signals in the experimentally measured structure factors $S(q)$ are too inconclusive. We might conclude that both structural and dynamical [69] results from experiments point toward some indistinctive form of protein cluster formation.

Chapter 8

Final Remarks and Outlook

In this final chapter, we will conclude by summarizing some of the key findings of this thesis and possible directions to future work. This work was generally concerned with the statistical physics of (classical) fluids whose physical properties are driven by the presence of highly-directional particle interactions. We chose to employ the framework of patchy particles, which is a generic model system for real fluids in which anisotropic interactions are present, equally applicable to molecular (e.g. water) and colloid and soft-matter systems (e.g. protein solutions). In this thesis we focused on the colloidal picture, i.e. mesoscopic particles that are immersed in an atomic solvent, and we employed modern tools of statistical mechanics, including classical density functional theory and computer simulations.

Chapter 2

In Ch. 2 we laid out fundamentals of liquid-state theory pertinent to our studies in the subsequent chapters. This on the one hand included the introduction of basic quantities such as the radial distribution function $g(r)$ and the bulk pair direct correlation function $c(r)$ (Secs. 2.1.2 and 2.1.4), as well as the theoretical framework of classical DFT (Secs. 2.2 and 2.3).

In Sec. 2.4 we introduced a novel concept for how to generally measure the balance between attractive and repulsive forces in a fluid. This is probably one of the oldest and most fundamental questions in liquid-state theory, as the competition between excluded volume effects and interparticle attraction governs the thermodynamic and structural properties of *any* fluid. We began Sec. 2.4 by recalling the importance of the second virial coefficient $B_2(T)$ for quantifying the balance between net repulsion and attraction that determines certain thermodynamic properties of fluids. The Boyle temperature T_B represents the simplest example of a crossover temperature identified by the vanishing of the excess pressure, $p - p^{\mathrm{id}}$, in a dilute gas. Here we have identified a more sophisticated criterion, pertinent to a dense fluid, that also reflects the competition between repulsive and attractive interactions. The new criterion also involves a thermodynamic excess function: the line in the phase diagram where

the excess isothermal compressibility $\chi_T^{\rm ex}$ vanishes describes crossover of the total pair correlation function $rh(r)$ from asymptotic damped oscillatory decay, dominated by repulsive forces and characteristic of hard-sphere systems, to monotonic decay, dominated by attractive forces and characteristic of dilute gaseous and near-critical fluid states. Our criterion corresponds to the condition $(\partial\beta p/\partial\rho_b)_T = 1$. In the limit $\rho_b \to 0$ this condition reduces to $B_2(T_B) = 0$, i.e. the definition of the Boyle temperature; however note that approximate theories do not necessarily yield the exact Boyle temperature. Generally, the condition corresponds to the static structure factor $S(k)$, at wave number $k = 0$, taking its ideal gas value: $S(0) = 1$. For the square-well fluid, which is an important model fluid in liquid-state theory, this new thermodynamic criterion yields a line in the $T - \eta$ phase diagram that lies close to the actual Fisher-Widom (FW) crossover line, as determined from a formal pole analysis of the asymptotic decay of the total correlation functio $h(r)$ [126, 57, 128, 129]. In the paper [136] we furthermore show that this holds also for other widely considered model fluids.

The new criterion is based on considering the attractive and repulsive contributions to the pair direct correlation function $c(r)$, see Sec. 2.4.2, for a range of thermodynamic states. It corresponds to the condition that the three dimensional integral of $c(r)$ in Eq. (2.125) vanishes. For the simple square well (SW) model the exact asymptotic result $c(r) = -\beta\phi(r)$ describes well the behavior of $c(r)$ outside the hard-core (see Fig. 2.4). The origin of the crossover from monotonic to damped oscillatory as the density increases is straightforward to grasp. Unfortunately, there are few simulation results in the literature, for models exhibiting both repulsive and attractive interactions, that display $c(r)$ at different state points. Ref. [135] for the truncated and shifted Lenard-Jones model is an exception and it is pleasing that the MC results for a fixed supercritical temperature also show the asymptotic formula for $c(r)$ holding outside the core region and the core contribution becoming more negative as the density increases. Without knowledge of $c(r)$ one cannot perform a careful pole analysis of the asymptotic decay required to determine the true correlation length and therefore the FW and W lines. One must resort to fitting simulation data for the decay of $\ln|rh(r)|$ to obtain decay lengths.

As a final remark to Sec. 2.4 we note that it is difficult to determine the FW and the W line in simulations because the true correlation length ξ is not easily computed. It requires knowledge of $h(r)$ with high precision out to large separations r, i.e. to ten particle diameters or more, to be able to make reliable fits to the decay lengths or to perform an accurate determination of $c(r)$ in order to determine poles. The $\chi_T = \chi_T^{\rm id}$ criterion is much easier to examine in simulations. As such this is a good starting point for investigating where in the phase diagram we expect the competition between repulsive and attractive interactions to lead to crossover in the asymptotic decay of correlations, i.e. to point to the location of a FW line. Experimentally χ_T is easily obtained from equation of state determinations or from extrapolation of small angle scattering data to zero wavenumber [57].

Chapter 4

Section 4.2

In Sec. 4.2 we employed classical DFT to address the bulk structure of patchy fluids with a maximum number of bonded neighbors equal to four. To this end, we made use of free energy density functionals incorporating Wertheim's first-order perturbation theory (Ch. 3), which is known to yield reliable results for bulk properties such as the degree of polymerization (Fig. 3.2) and other thermodynamic properties (Fig. 4.9); see also Refs. 77, 47, 154, 157.

Three density functional approaches have been considered which are commonly employed in the literature. The first is formulated within the framework of Tarazona's weighted-density approximation for hard spheres first suggested by Segura *et al.* [71]; the second approach is based on Rosenfeld's fundamental measure theory, as originally proposed by Yu and Wu [72]; the third functional that we considered was a slightly modified version of the latter, which we termed the 'mFMT functional' (see Sec. 4.1 and Secs. 2.3.1 and 2.3.2). We calculated density profiles around a test particle interacting via an attractive square-well with its surrounding (patchy) neighbors, thereby obtaining effective radial distribution functions. In order to classify the results given by these functionals, we first benchmarked the theoretical curves against simulation results for the radial distribution function $g(r)$ of tetrahedral patchy particles. It turned out that the mFMT functional was the only approach which was capable of satisfactorily matching simulation results, while the original FMT clearly underestimated correlations; the WDA functional completely failed to account for essential structural properties. However, upon lowering temperatures, even the mFMT approach could not quantitatively describe the height of the correlation peak emerging at $r \approx 1.75\sigma$ in the simulated radial distribution functions, which is a structural indicator of a strong tetrahedral arrangement of the particles (see Figs. 4.4 and 4.5). This may be attributed to approximations introduced by Wertheim's first-order perturbation theory (see Ch. 3). Most notably, the latter does not provide information about the geometrical arrangement of the patches and, moreover, all quantities are averaged over particle orientations. As a result, any weighted-density functional which employs the bulk Wertheim theory and makes use of purely spherical weight functions cannot depend on particle orientations – while this is accurate for a bulk theory describing thermodynamic properties of the homogeneous fluid, it will necessarily yield deviations between theory and simulations in (effective) inhomogeneous situations in which the geometrical arrangement of the interaction sites becomes important.

We also saw that the bulk pair direct correlation function $c(r)$ that one obtains from taking two functional derivatives of the mFMT functional did not satisfy the exact low-density result: $c(r) = f(r)$, where $f(r)$ is the orientational averaged Mayer-f function. As regards future work, it would thus be desirable to construct a functional which obeys the exact low-density limits Eqs. (4.8) and (4.9), and shows a similar performance than the present FMT-based functional. An obvious choice is to follow Tarazona's Mark I

DFT version for hard spheres [102], and introduce a suitable weighted density to be used in Eq. (3.20) which by construction yields Eq. (4.9). This can be achieved by defining a 'bonding' weight function

$$\omega_{\mathrm{bond}}(r) \equiv \frac{\langle f_{\mathrm{bond}}(r)\rangle}{\int \mathrm{d}\mathbf{r}\,\langle f_{\mathrm{bond}}(r)\rangle}\,,$$

leading to a new weighted density $n_{\mathrm{bond}}(\mathbf{r}) = \int \mathrm{d}\mathbf{r}'\,\rho(\mathbf{r}')\omega_{\mathrm{bond}}(|\mathbf{r}-\mathbf{r}'|)$. However, we found that this simple approach led to density profiles which are very poor compared to simulations, and thus more sophisticated approaches seem to be necessary for a consistent density functional theory for associating fluids.

Section 4.3

We began Sec. 4.3.1 by calculating Fisher-Widom (FW) and Widom (W) lines for the patchy fluid (Fig. 4.7) based on the density functional introduced in Sec. 4.2, where we considered four, three and two patches per particles. Interestingly, we found for all cases that the FW lines were not bounded by the spinodals at low temperatures, as is usually the case for fluids with spherically-symmetric pair potentials (see, e.g., Ref. 136 and references therein). This means that, outside of the gas-liquid instability region, the correlation length ξ remains finite for all temperatures, which complies with the fact that disordered states can exist in patchy fluids down to very low temperatures [50, 51]. We additionally calculated the line where the isothermal compressibility χ_T takes its ideal gas value, i.e. $\chi_T = (\rho_b k_B T)^{-1}$, or, equivalently $\chi_T^{\mathrm{ex}} = \chi_T - \chi_T^{\mathrm{id}} = 0$. In Sec. 2.4 we showed that this thermodynamic line approximates well the actual FW line for the square-well fluid, treated in mean-field DFT, and in Ref. 136 we validated this for other model fluids with short-ranged isotropic interactions. Importantly, we found in Sec. 4.3.2 that also for the patchy fluid the $\chi_T^{\mathrm{ex}} = 0$ lines lie rather close to the respective FW lines. This result evidences that the (static) correlation length ξ, within the Wertheim theory, remains finite for $T \to 0$ (as χ_T and ξ are related via Eq. (2.121)), although, of course, the system will be dynamically arrested as T approaches zero.

Subsequently, in Sec. 4.3.2 we put attention to the limit where the number of patches is exactly two and explored the question: what is leftover in the $T-\eta$ phase diagram in the limit of chain-forming fluids where phase coexistence has disappea?red? Recall that for every fluid in three dimensions the occurrence of a gas-liquid critical point and curves of phase coexistence (binodal) and mechanical instability (spinodal) are typically accompanied by a bunch of additional lines that may be drawn in the phase diagram, as for instance the FW and W lines, or the locus in the phase diagram at which the reduced isothermal compressibility $\overline{\chi}_T = \chi_T/\chi_T^{\mathrm{id}} = \rho_b k_B T \chi_T$ exhibits a local maximum (which we termed the $\overline{\chi}_T^{\mathrm{max}}$ line) – see Figs. 4.7 (a) – (c). As the Widom line, the latter diverges at the critical point. We demonstrated that although there is no gas-liquid binodal in the chain-forming patchy fluid, and hence no true critical point, one can still calculate lines of maximal correlation length and thermodynamic response functions all of which diverge upon approaching the *origin* at zero temperature

and density. This is curious. At finite densities, however, as mentioned above, both $\overline{\chi}_T$ (and hence χ_T) as well as the correlation length ξ remain finite down to zero temperature. Moreover, we found a fairly broad region in the phase diagram, around the origin, in which the decay of $h(r)$ is monotonic, i.e. we found FW crossover (as in the high-temperature limit, where the particles behave as hard spheres, there is always damped oscillatory decay of $h(r)$). In particular, we validated our theoretical results against computer simulations.

The results for the chain-forming patchy fluid are at odds with the typical situation for fluids with isotropic particle interactions, where a FW or W line is always accompanied by the presence of a (true, i.e. at finite temperatures) gas-liquid critical point. Our surprising results might thus be understood as the remnants of a pseudo-critical point suppressed to the origin at zero density and temperature.

Chapter 6

In Sec. 6.3 we presented a DFT study investigating systems with anisotropic competing interactions, where the anisotropic patchy attraction was accounted for within Wertheim's theory and the FMT functional due tu Yu and Wu [72], and the repulsion was described in a standard mean-field treatment. We calculated the respective gas-liquid coexistence regions, as well as the λ line, which encloses a region in the phase diagram where the bulk fluid is unstable w.r.t. density fluctuations and self-assembles into (periodic) microphases. This is a well-known phenomenon in systems with spherically-symmetric competing interactions, see Sec. 6.2. Importantly, we found that the topology of the phase diagram changes fundamentally in comparison to the case of isotropic competing interactions, including critical points at very low temperatures and densities as well as reentrant binodals. The λ line follows the form of the latter and also exhibits a reentrant behavior. In Sec. 6.3.2 we calculated the density profile $\rho(r)$ around a repulsive test particle having the same hard-core diameter as the surrounding particles. Here, we found that the bulk phase behavior of the system is reflected in the structure of the fluid – reentrant cluster correlations in $g(r)$ were visible along isochores in vicinity to the λ line. Subsequently, in Sec. 6.3.3 we investigated what kind of microphases could be stable within the λ line, and we found the same types of microphases as in systems with spherically-symmetric competing interactions (cf. Fig. 6.7), i.e. BCC structures, lamellar and gyroid phases as well as cylindrical tubes arranged on a hexagonal lattice. In line with the reentrant shape of the λ line, we observed that the occurrence of specific types of microphases showed a temperature-dependent reentrant effect (cf. Fig. 6.12), which is different to the phase diagram for the isotropic double-Yukawa fluid, where the location of microphases within the λ line depends only on the packing fraction η (see Fig. 6.5). It remains an interesting future task to sample through the phase diagrams displayed in Figs. 6.10 (a)–(d) and determine the sequence of stable structures, which we conjecture is different to those generated by isotropic competing interactions treated within mean-field DFT.

Chapter 7

In Ch. 7 we were concerned with the theoretical modeling of protein solutions in the presence of multivalent metal ions, based on earlier experiments [68, 91, 69] and theoretical work [46]. In Sec. 7.2 we outlined the rich bulk phase behavior which had been found in experiments; the rich phase diagram of human serum albumin (HSA), or bovine serum albumin (BSA), in the presence of yttrium chloride (YCl_3) is illustrated in Fig. 7.4. In Ref. 46 the phase behavior of proteins in the presence of multivalent salt was successfully described by a patchy colloidal model. We summarized the key aspects of this model in Sec. 7.3; it describes proteins as patchy particles, where the anisotropic attraction is mediated by ions that can chemically bind to the protein surface. A bond between two distinct proteins is only possible if an occupied patch meets an unoccupied one. The resulting phase diagram, calculated from the Wertheim theory, is in semi-quantitative agreement with the experiments. This includes reentrant condensation in terms of protein clusters and a closed-loop LLPS region (see Fig. 7.6).

Section 7.4

The Schreiber group carried out experiments investigating the adsorption behavior of proteins in the presence of multivalent salts at attractive solid substrates [231]. Importantly, a reentrant effect was observed in terms of the thickness of the adsorbed protein layer as a function of the salt concentration (at constant protein density), thereby reflecting the rich reentrant bulk behavior of protein-salt mixtures. In Sec. 7.4 we showed that the experimental data could be understood by theoretical calculations within the framework of classical DFT based on the model of ion-activated patchy model for proteins (Sec. 7.3). In addition to the fundamental implications of the first-time demonstration of the ion-activated patch model in the context of a symmetry break introduced by the presence of an interface, our approach and theoretical findings (Figs. 7.8 and 7.10) suggested furthermore an interesting and in fact efficient alternative to tune protein adsorption at substrates via benefiting from suitable thermodynamic conditions, i.e. conditions that favor a certain level of adsorption driven by the underlying bulk phase behavior. This is in contrast to 'common' approaches, where the underlying interaction mechanisms between proteins and solid surfaces are controlled by e.g. altering the surface chemistry of the interface. In future work, it would thus be fascinating to explore if adsorption phenomena such as wetting, well known in simple fluids, could be observed in a rather complex protein suspensions exhibiting LLPS in the presence of multivalent salt. The consequences might be important for the control and tailoring of protein adsorption, which, in turn, is relevant for biological or medical applications such as biosensors or better biocompatibility in dental implants, lenses and joints and might be extended to other biological systems such as DNA nanostars used in hydrogels [42].

Section 7.5

In Sec. 7.5 we proposed an extended model for protein-salt mixtures which includes effects of the Coulomb repulsion acting between the proteins, which in the simple model introduced by Roosen-Runge (cf. Sec. 7.3) is mapped in an effective manner onto the hard-sphere pair potential. The incorporation of an additional repulsion to the model is motivated by recent experimental data that suggests the formation of *equilibrium* protein clusters due to the presence of competing interactions [222] for state points close to yet below c^*. Indeed, upon approaching the latter, the surface charge of the proteins reduces due to binding of positively charged cations to the protein surfaces, thereby weakening the overall electrostatic repulsion between the proteins. At the same time, ion-mediated protein bonds introduce an short-ranged anisotropic attraction between the proteins. This presumably opens the window towards a region in the phase diagram where anisotropic competing interactions might play a role.

We described the electrostatic repulsion between the proteins via a DLVO-like theory, where the strength (Eq. (7.12)) and range (Eq. (7.14)) of the repulsion depend on both, the protein density and the amount of salt. The resulting model is therefore an application of the model fluid with anisotropic competing interactions, investigated in Sec. 6.3 of Ch. 6. The results of the extended protein model provided theoretical hints that the competition between a short-ranged attraction and a longer-ranged repulsion might favor the formation of equilibrium clusters at sufficiently low protein densities and salt concentrations in vicinity to the transition boundary $c_s < c^*$. In particular, the original protein model, where no longer-ranged repulsion is taken into account, does not predict a pre-peak at low wave numbers in the static structure factor $S(k)$. However, from the experimental data we cannot certainly conclude that there are equilibrium cluster protein phases, i.e. fluid states that are characterized by the presence of clusters with a certain average size, as is often observed in colloidal fluids with competing interactions [84, 199, 86, 87] (see also Sec. 6.2). Rather, the weak signals at low wavenumbers observed in the experimental structure factor $S(k)$ point towards what in the aforecited literature is referred to as the presence of an 'intermediate-range order', which refers to fluid states characterized by the equal presence of monomers and transient (small) clusters.

Appendix A

Classical Density Functional Theory on Graphics Cards[1]

A.1 Parallel minimization on graphics cards

A.1.1 Parallelization of DFT and FMT in D dimensions

From a numerical point of view, a scalar-field $f(\mathbf{r})$ depending on D cartesian spatial variables $\mathbf{r} = (x_1, \ldots, x_D)$ has to be windowed on a finite grid. This means that every variable x_m with $m = 1, .., D$, takes on discrete values only, and we can write $x_m = \xi_m(i_m, \Delta)$ with a suitable mapping-function ξ_m; the i_m enumerate all points in m-th direction, i.e. $i_m \in [0, N_m - 1]$ when N_m is the number of grid points in that direction. The quantity Δ denotes the spacing between grid points which we assume to be identical along each axis. It is straightforward to lift this restriction to different grid spacings Δ_m for different axes, equally spaced grids in each direction is essential for an efficient application of fast Fourier methods, which we employ In this chapter. In particular, we demand that the values of x_m are uniquely determined by their index i_m. For instance, if all coordinates are positive, we have $x_m(i_m) = \xi_m(i_m, \Delta) := i_m \Delta$ for all m. However, in the following it is convenient to map the tuple $(i_1, .., i_D)$ in row-major order onto a global index n,

$$n(i_1, ..., i_D) = \sum_{l=1}^{D} \left(\prod_{m=l+1}^{D} N_m \right) i_l \,, \tag{A.1}$$

and we can write $f(\mathbf{r}) = f(i_1, ..., i_D) \equiv f_n$ which simply is the value of f at each lattice point, and $n \in [0, N_1 \cdot ... \cdot N_D - 1]$. Note that row-major order conventionally is used by most programming languages to map multi-dimensional data onto linear arrays.

Recall that in DFT We start with considering the Picard iteration in order to solve Eq. (2.66) numerically. Starting from an initial guess for the density profile $\rho^{(k=0)}(\mathbf{r})$ (e.g. the corresponding ideal gas limit) the algorithm generates a new density profile

[1] This appendix is reproduced from D. Stopper and R. Roth, J. Chem. Phys. **147**, 064508 (2017) with the permission of AIP publishing

$\rho^{(k+1)}(\mathbf{r})$ given a density profile $\rho^{(k)}(\mathbf{r})$ of the k-th iteration step via

$$\rho^{(k+1)}(\mathbf{r}) = (1-\gamma)\rho^{(k)}(\mathbf{r}) + \gamma\tilde{\rho}^{(k)}(\mathbf{r})\,, \tag{A.2}$$

where (cf. Eq. (2.66))

$$\tilde{\rho}^{(k)}(\mathbf{r}) = \rho_b \exp\left[-\beta V_{\text{ext}}(\mathbf{r}) + c^{(1)}(\mathbf{r}\,;\,[\rho^{(k)}]) + \beta\mu_{\text{ex}}\right]\,. \tag{A.3}$$

The mixing parameter $\gamma \in [0,1]$ is introduced for stability reasons, since a 'bad guess' $\rho^{(0)}$ may result in divergences during subsequent iteration steps. Usually a good choice is $\gamma = 0.1$, which still guarantees for fast convergence, but we note that there exist more sophisticated ways how to choose values for the mixing parameter [70]. On a grid, the discrete counterparts of Eqs. (A.2) and (A.3) can be treated as a set of $N_1 \cdot ... \cdot N_D - 1$ decoupled equations

$$\rho_n^{(k+1)} = (1-\gamma)\rho_n^{(k)} + \gamma\tilde{\rho}_n^{(k)}\,, \tag{A.4}$$

$$\tilde{\rho}_n^{(k)} = \rho_b \exp\left[-\beta V_{\text{ext},n} + c_n^{(1)} + \beta\mu_{\text{ex}}\right]\,, \tag{A.5}$$

which *in principle* may all be computed in parallel.

Importantly, the structure of FMT for hard disks and spheres allows also for an parallel computation of the weighted densities $n_\alpha(\mathbf{r})$ and the direct correlation function $c^{(1)}(\mathbf{r})$. From a mathematical point of view, Eqs. (2.96) and (2.102) are convolutions which can be written as a simple multiplication in Fourier-space

$$\widehat{n}_\alpha(\mathbf{k}) = \widehat{\rho}(\mathbf{k})\;\widehat{\omega}_\alpha(\mathbf{k})\,, \tag{A.6}$$

$$\widehat{c}^{(1)}(\mathbf{k}) = -\sum_\alpha \widehat{\frac{\partial\Phi}{\partial n_\alpha}}(\mathbf{k})\;\widehat{\omega}_\alpha(-\mathbf{k})\,, \tag{A.7}$$

in which $\widehat{f}(\mathbf{k}) = \int \mathrm{d}\mathbf{r}\, f(\mathbf{r}) \exp(-i\mathbf{k}\cdot\mathbf{r})$ denotes the D-dimensional Fourier-transform of f. On a grid we have $\widehat{f}(\mathbf{k}) = \widehat{f}(\xi_1(i_1,\Delta_{k_1}),..,\xi_D(i_D,\Delta_{k_D})) \equiv \widehat{f}_n$ with Δ_{k_m} denoting the grid spacing of each axis in reciprocal space. The latter are connected to the spacing in real space via $\Delta_{k_m} = 2\pi/(N_m\Delta)$, which is the reason why we may have different spacings per axis although there is the same discretization of each axis in real space. We again obtain a set of independent equations,

$$\widehat{n}_n^\alpha = \widehat{\rho}_n\,\widehat{\omega}_n^\alpha\,, \tag{A.8}$$

$$\widehat{c}_n^{(1)} = -\sum_\alpha \widehat{\chi}_n^\alpha\,\widehat{\omega}_n^\alpha\,, \tag{A.9}$$

where we have set $\chi^\alpha = \partial\Phi/\partial n^\alpha$. The Fourier- and inverse-Fourier-transforms of functions defined on a lattice again allow for parallel calculation via Fast-Fourier methods (FFT). Generally, all Fourier-transforms of quantities that change during the Picard iteration have to be calculated numerically, whereas the Fourier-transforms $\widehat{\omega}_\alpha(\mathbf{k})$ of the weight functions do not change and are known analytically. Moreover, the

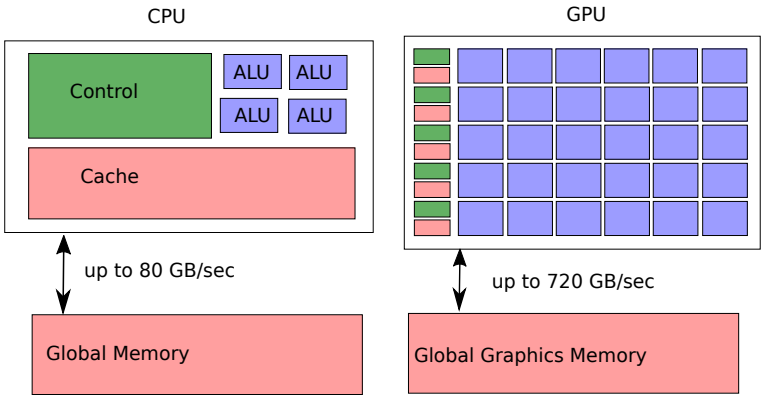

Figure A.1 Schematic illustration of the differences between a CPU (left) and a GPU (right). The arithmetic logical units (ALU, in the online-version blue) perform arithmetic operations on data; cache (red) is a fast but small memory. Instructions are scheduled by control units (green). CPU and GPU have access to (distinct) global memory.

partial derivatives allow for an analytical evaluation before applying FFT algorithms, cf. Sec. A.2.1.

A.1.2 Maximizing parallel-data operations

In order to maximize parallel-data operations, we make use of the hardware architecture of GPUs, which is fundamentally different from standard multi-core CPUs [232]. While a CPU is highly optimized for efficient memory management, process scheduling and arithmetic operations in serial, a GPU mainly is designed for massive data-parallel operations, as arising in graphics applications (e.g. pixel shading). A fundamental feature is that an single instruction invokes parallel processing on many (distinct) data elements; this is known as single-instruction-multiple-data pattern (SIMD). The difference in hardware architecture is pictured in Fig. A.1: A modern CPU (left) consists of a number (here: four) of arithmetic logical units (ALU, blue), also referred to as processor cores. Most focus is put on process scheduling and memory management (control (green) and cache units (red)). In contrast, a modern GPU contains up to thousands of processor cores, but relatively small cache and control units reflecting the design for heavy SIMD-type operations. However, since roughly one decade, CPUs also tend to increase SIMD-type operations, mainly as a result of fundamental physical limitations which prevent an unlimited increase in clock-frequency. Nowadays high-performance CPUs have up to $\sim$ 20 cores whereby each core can handle up to 32 floating-point operations (FLOPs) per clock-cycle, and this trend seems to increase in future.

Nevertheless, GPUs clearly outpace standard CPUs in both, single (SP) and double precision (DP) FLOPs since recent years. FLOPs per second can serve as a theoretical measure for the performance of a processor, and is obtained by the following equation

$$\frac{\text{FLOPs}}{\text{sec}} = \frac{\text{instructions}}{\text{clock-cycle}} \times \text{frequency} \times \text{cores}\,, \tag{A.10}$$

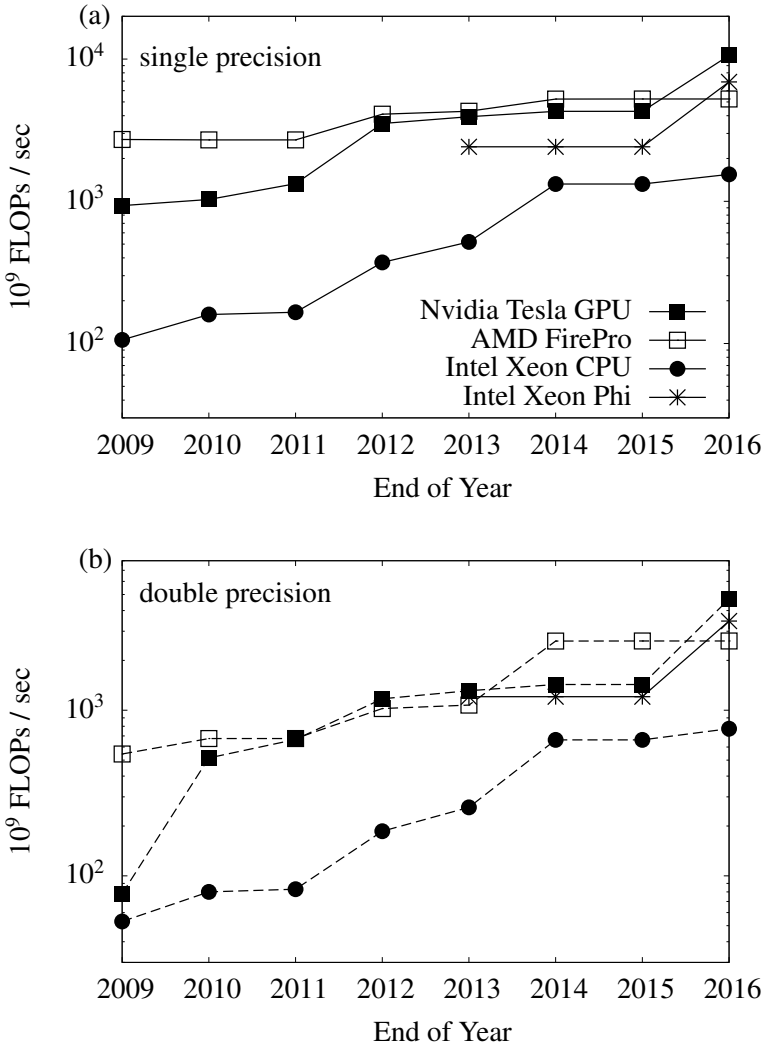

Figure A.2 Recent development of theoretical FLOPs per second (cf. Eq. (A.10)) in comparison between Nvidia Tesla series (filled squares), AMD FirePro series (open squares), Intel Xeon CPUs (points) and Intel Xeon Phi series (stars). (a) shows single-precision and (b) double precision performance.

where the processor frequency measures the number of clock-cycles per second, which commonly is in the Giga-Hertz regime. The quantity 'instructions/clock-cycle' can vary significantly, and e.g. depends on the hardware design. For instance, each core of a modern GPU can handle up to 2 floating-point instructions per clock-cycle in SP, and as mentioned above, each core of a recent CPU is capable of initiating up to 32 instructions per clock-cycle, where an instruction is either an additive or multiplicative arithmetic operation.

For illustration, in Fig. A.2 the theoretical FLOPs per second in single (a) and double (b) precision of recent generations of high-performance GPUs of the GPU-manufacturers Nvidia ('Tesla' series, filled squares) and AMD ('FirePro' series, empty squares) are compared to the most powerful CPU-series 'Xeon' of the CPU manufacturer Intel over the last years 2009 - 2016. Note that the Intel 'Xeon Phi' series has been published as a alternative to GPUs a few years ago, and is a (co-)processing unit where recent versions

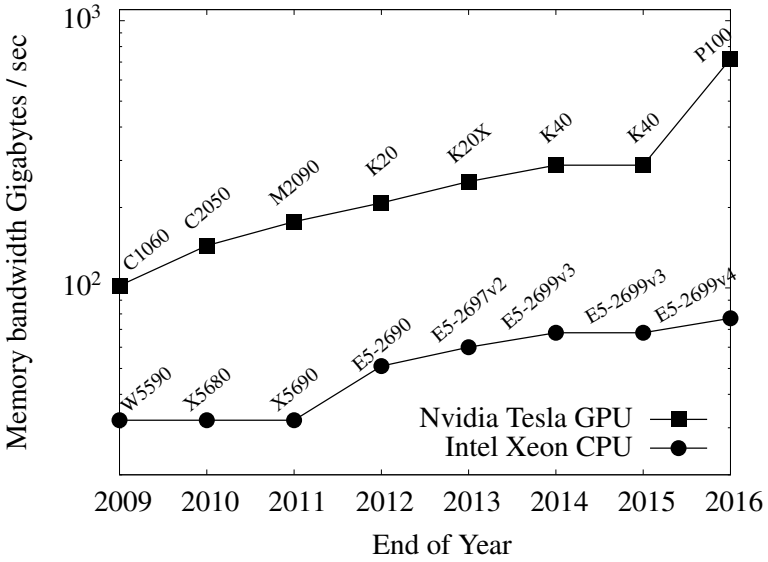

Figure A.3 Recent development of theoretical memory bandwidth in Gigabytes per second of Tesla GPUs and high-end Intel CPUs.

have up to 72 CPU-type cores. Interestingly, even latest high-performance CPUs clearly fall behind professional many-core devices by an order of magnitude. Moreover, the memory bandwidth of such hardware is significantly higher in comparison to CPUs, which is relevant for reading or storing data in global memory. In Fig. A.3, we compare the theoretical maximum bandwidth in Gigabytes per second between Intel Xeon, and Nvidias Tesla series. Additionally, we have labelled the specific hardware generations (which can also be applied to Fig. A.2). The memory bandwidths of AMDs GPUs and Intels Xeon Phi are comparable to those of Nvidia, and for clarity in the plot they are not pictured here. Note that standard consumer graphics cards such as the Nvidia 'Geforce' series reach similar values regarding single precision FLOPs and memory bandwidth, but have a rather poor double precision performance. This is in contrast to standard consumer CPUs (e.g. Intel i5 and i7 series), which mainly are limited in the number of cores and memory bandwidth in comparison to high-end processors.

The usage of many-core devices such as GPUs for scientific purposes mainly is limited by two major factors: (i) the problem under consideration must be efficiently parallelizable; (ii) the available amount of global graphics memory must be sufficient. In particular, (ii) impeded DFT calculations being executed on GPUs for long times, although the possibility of free-programmable graphics cards were already introduced. For instance, a simple 3D-FMT program computing hard spheres in a hard box with $(256)^3$ grid points allocates circa 1 Gigabytes of memory in single- and twice as much in double precision, but graphics memory has reached such domains just a few years ago. Therefore, massive data movement with low bandwidth between GPU and CPU would had been necessary, thereby completely compensating the performance gain of parallel-data processing. However, facing the recent escalation of available memory with high bandwidth, GPUs have become promising candidates for significantly speeding-up DFT calculations.

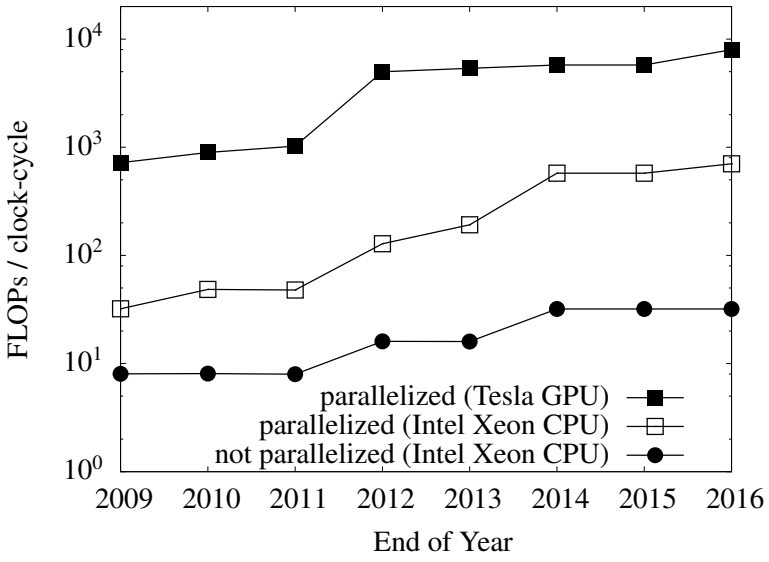

Figure A.4 Instructions/clock-cycle for each core of Intel Xeon CPUs compared to FLOPs/clock-cycle (i.e., instructions/clock-cycle × cores, see text) of Nvidia high-performance GPUs and Intel Xeon CPUs. This representation can be viewed as the theoretical performance gain of a parallelized versus a completely serial program execution at *same clock frequency*.

A rough theoretical estimate of speed-up can be given as follows. We assume that a standard DFT implementation typically runs completely sequential, i.e. it makes use of only one processor core. Hence, a measure for speed-up between serial and parallel execution is substantiated by considering instructions/clock-cycle of a single-core device (divide out frequency and cores in Eq. (A.10)) versus the FLOPs/clock-cycle of a multi-core device (where all processor units contribute, i.e. only divide out frequency in Eq. (A.10)). For illustration, we picture the resulting theoretical performance gain due to parallelization in Fig. A.4 for Nvidias Tesla series (filled squares) and Intel Xeon CPUs (open squares) relative to a sequantial program execution on a single CPU core (points). Clearly, similar considerations can also be done for CPUs of other manufactures (e.g. AMD) or standard-consumer GPUs (e.g. Nvidias Geforce or AMDs Radeon series), but the picture does qualitatively not change.

To provide an example oriented on the hardware used In this chapter (see Sec. A.2), consider a Tesla K40 having 2880 cores with 2 instructions per cycle each, and a standard-desktop CPU Intel i5-4570 with 4 cores allowing for 32 instructions/cycle for each core (both in SP). We obtain a speed-up factor of roughly 180; when taking clock-frequency into account, this advance will significantly be smaller since the CPU cores clock with a higher frequency of 3500 MHz, whereas the K40 reaches 745 MHz per core. Thus, we obtain an effective speed-up of 40. However, note that here effects of memory accesses are neglected completely; these numbers only provide an illustration of the orders of magnitude to which extent a parallel DFT executed on a recent (high-end) GPU might be faster in comparison to a DFT executed in serial on a CPU.

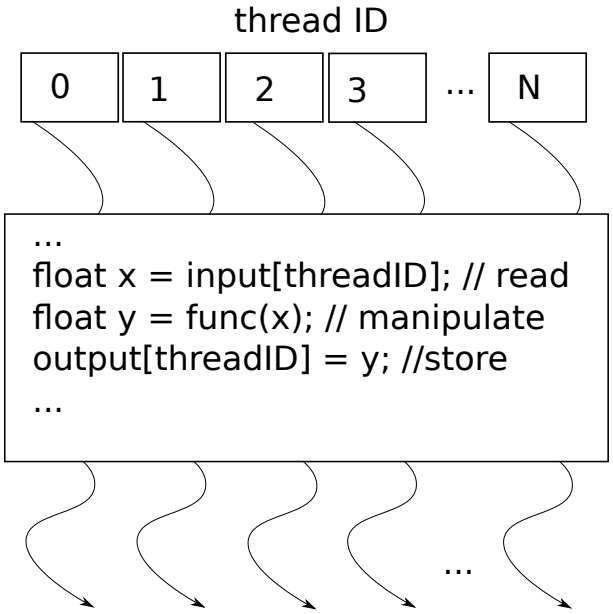

Figure A.5 Pseudo-code illustration of data processing in a CUDA application: The thread ID is used for loading and storing data. Arrows indicate instruction flow of each thread.

A.1.3 General purpose GPU programming: CUDA

In this chapter, we make use of the developer environment CUDA introduced by Nvidia in 2007. CUDA provides an extension of the programming language C/C++ in order to outsource parallelizable algorithms on Nvidia graphics cards. However note that while CUDA can be used only with Nvidia GPUs, there exist further multi-platform programming models such as the OpenCL standard which are also appropriate for GPGPU. We choose CUDA since it provides a wide range of features, including optimization tools and a library for performing GPU accelerated Fast-Fourier-transforms which is crucial for FMT applications.

A CUDA program starts a user defined number of so-called threads, which perform arithmetic operations on given data elements. Internally, these are divided into groups of 32, referred to as warps, and all threads of a warp are executed simultaneously by the cores of a multiprocessor. Hence, depending on the number of ALUs inside a multiprocessor, the latter can execute several warps in parallel. While in sequential code usually loop control variables serve as data indexer, in CUDA one accesses data depending on the thread identification number (thread ID), thus every thread can operate on distinct data elements which schematically is depicted in Fig. A.5. Note that there is no direct mapping between threads and available cores. Indeed, commonly a program is initiated with much more threads than ALUs are available in order to maximize performance. The reason is so-called latency hiding – access to global graphics memory is even with modern bandwidths relatively slow in comparison to arithmetic operations. If some threads of an executed warp are reading or storing data, the internal scheduler of the GPU switches to another (queued) warp to execute.

In practice, one has to decide on the basis of the given data structure and underlying

hardware how many threads are optimal to be started, i.e. to obtain best performance. However, these and further technical details regarding efficient GPU programming are well documented [233, 234] and shall not be discussed here in more detail.

A.2 Implementation details

In this section we discuss the systems which we consider in order to demonstrate the performance of GPU-accelerated DFT applications. Moreover, we discuss details regarding memory efficient implementations by making use of symmetries within FMT.

Toward this end, we investigate a two-dimensional ($D = 2$) system of hard disks, where we keep a 'test disk' fixed at the origin and determine the equilibrium density around that particle, but we have no further external field such as hard wall boundaries (which is the 2D radial distribution function $g_{2\mathrm{D}}(r)$ [92]). In $D = 3$ we consider hard spheres enclosed by a hard box (i.e., a hard slit in each spatial direction) and an additional test particle is located in the middle of the box. These two scenarios are later used as benchmark for performance measurements related to computational cost versus system size.
Additionally, we investigate for fixed volumes how the choice of the grid spacing Δ impacts the resulting density profile, and we compare the results of a quasi-1D situation with very high spatial resolution to full 3D calculations.

A.2.1 Model systems

In two dimensions a recent version of FMT [116] proposes an excess free-energy density as a function of four weighted densities: two weighted densities are scalar, one is vectorial and has in general two components, and the fourth one is a second-rank tensor-like weighted density with three independent components. Additional higher-ranked tensorial weight functions can be included in a systematic expansion of the Mayer-f function, but do not seem to be necessary for an accurate account of the fluid or solid structure [116]. The Fourier-transforms of the weight functions are given by

$$\widehat{\omega}_2(k) = 2\pi R J_1(kR)/k\,, \tag{A.11}$$

$$\widehat{\omega}_1(k) = 2\pi R J_0(kR)\,, \tag{A.12}$$

$$\widehat{\vec{\omega}}_1(\mathbf{k}) = -i\mathbf{k}\widehat{\omega}_2(k)\,, \tag{A.13}$$

$$\widehat{\overleftrightarrow{\omega}}^{(2)}_{ij}(\mathbf{k}) = -\frac{2\pi}{R}\frac{\partial}{\partial k_i}\frac{\partial}{\partial k_j}J_0(\sqrt{k_x^2 + k_z^2}R)\,, \tag{A.14}$$

where $J_i(x)$ is the i-th order Bessel function of the first kind. Here and in the following $k = |\mathbf{k}|$ is the absolute value of $\mathbf{k}$. Note that the derivatives of the Bessel functions can be calculated analytically. In addition there exists one more scalar weight function $\widehat{\omega}_0(k) = \widehat{\omega}_1(k)/(2\pi R)$.

In three dimensions, the free-energy density $\Phi(\{n_\alpha\})$ is a function of six weighted densities [17]. However, note that only three of them are linear independent and their

Fourier-transforms $\widehat{\omega}_\alpha$ are known analytically [235]

$$\widehat{\omega}_3(k) = 4\pi \left(\sin(kR) - kR\cos(kR)\right)/k^3\,, \tag{A.15}$$

$$\widehat{\omega}_2(k) = 4\pi R \sin(kR)/k\,, \tag{A.16}$$

$$\widehat{\vec{\omega}}_2(\mathbf{k}) = -i\mathbf{k}\widehat{\omega}_3(k)\,, \tag{A.17}$$

and $\widehat{\omega}_1(k) = \widehat{\omega}_2(k)/(4\pi R)$, $\widehat{\omega}_0(k) = \widehat{\omega}_2(k)/(4\pi R^2)$, $\widehat{\vec{\omega}}_1(\mathbf{k}) = \widehat{\vec{\omega}}_2(\mathbf{k})/(4\pi R)$. For simplicity, we employ the original Rosenfeld-functional

$$\begin{aligned}\Phi_{\mathrm{RF}}(\{n_\alpha\}) = -n_0\ln(1-n_3) + \frac{n_1 n_2 - \vec{n}_1\cdot\vec{n}_2}{1-n_3} \\ + \frac{n_2^3 - 3n_2\vec{n}_2\cdot\vec{n}_2}{24\pi(1-n_3)^2}\,,\end{aligned} \tag{A.18}$$

which is sufficient as long as no high-density peaks are present such as in crystals [107, 115] or strong-confining external potentials [118]. In such cases, the last term of Eq. (A.18) can lead to divergences, but empirical corrections [236] or more sophisticated approaches including tensorial weight functions can be applied [110] in order to describe strongly peaked density distributions. For the particle densities considered In this chapter (cf. Sec. A.3) we did not observe any divergences in the hard box using Eq. (A.18), but this may be different for higher densities.

A.2.2 Efficient DFT implementation

Following our considerations of Sec. A.1.1, we store all quantities depending on spatial and momentum-space variables in row-major order using linear floating-point arrays (single- or double precision). Every global array index n (i.e., thread ID) of such an array can then be remapped to two- or three-dimensional indices i_m by inverting Eq. (A.1).

Since memory on graphics cards is still the major limitation factor, we present a few suggestions of how to implement a DFT-FMT program using as less memory as possible. First, remind that the Fourier-transform of a function $f(\mathbf{r})$ with purely real values obeys Hermitian symmetry, i.e. $\widehat{f}^*(\mathbf{k}) = \widehat{f}(-\mathbf{k})$, where $\widehat{f}^*$ is the complex-conjugate of $\widehat{f}$ (this is a fact in all dimensions). As a result, in discrete multi-dimensional Fourier-transforms it suffices to store the positive frequencies of one axis in momentum-space [237], which halves the amount of allocated memory needed for storing Fourier-transforms. Hence we recommend to employ real-to-complex (R2C) and complex-to-real (C2R) transforms provided by the cuFFT library. Second, we make use of the fact that the Fourier-transforms of the weight functions ω_α in both $D = 2$ and $D = 3$, are purely real or imaginary. Therefore, it is convenient to store all $\widehat{\omega}_\alpha$ (in their analytical form) in simple single- or double-precision floating-point arrays instead of more memory intensive data-types representing complex numbers. Note further that the FFT-routines assume periodic boundary conditions, i.e. the negative frequencies of the $\widehat{\omega}_\alpha$ have to be stored in the second half of the array. To provide an example, in 3D the components of the

wave vector $\mathbf{k} = (k_{x_1}, k_{x_2}, k_{x_3})$ are calculated according to

$$k_{x_m} = \begin{cases} 2\pi i_m/(N_m\Delta) & \text{if } \; i_m \leq N_m/2 \\ 2\pi(N_m - i_m)/(N_m\Delta) & \text{else} \end{cases} , \tag{A.19}$$

for $m = 1, 2$ and

$$k_{x_m} = 2\pi i_m/(N_m\Delta) \, , \tag{A.20}$$

for $m = 3$ with $i_3 \in [0, ..., N_3/2]$. While the investigated scenarios In this chapter are compatible with the periodic boundary conditions of FFT, for systems that are very far from being periodic, FFT methods still can be applied in most cases in order to calculate convolution integrals by applying 'zero-padding'. This amounts to extend the array storing the density profile with zeros such that a periodic mixing of the input arrays (e.g. density and weight functions) is avoided in order to not introduce a false periodicity (note that the full result of a linear convolution is always longer than either of the two input arrays).

As a third point we note that it suffices to store at most the linear independent weight functions, since the remaining ones are obtained by multiplication with trivial geometric measures and can easily be calculated on the fly. In particular, this fact allows for a simplification when calculating the direct correlation function $c^{(1)}(\mathbf{r})$. For instance, in $D = 3$ rewriting the summation in Eq. (A.7) yields

$$\begin{aligned} -\widehat{c}^{(1)}(\mathbf{k}) = \widehat{\frac{\partial\Phi}{\partial n_3}}\widehat{\omega}_3 - \left(\widehat{\frac{\partial\Phi}{\partial\vec{n}_2}} + \frac{1}{4\pi R}\widehat{\frac{\partial\Phi}{\partial\vec{n}_1}}\right)\cdot\widehat{\vec{\omega}}_2 \\ + \left(\widehat{\frac{\partial\Phi}{\partial n_2}} + \frac{1}{4\pi R}\widehat{\frac{\partial\Phi}{\partial n_1}} + \frac{1}{4\pi R^2}\widehat{\frac{\partial\Phi}{\partial n_0}}\right)\widehat{\omega}_2 \, , \end{aligned} \tag{A.21}$$

i.e. it suffices to store combinations of the partial derivatives, and subsequently one numerically calculates the corresponding Fourier-transform. Regarding memory accesses we emphasize that data transfers between CPU and GPU as well as accesses to the global graphics memory should be minimized whenever possible [234].

A.2.3 Technical details

We performed the serial DFT calculations on an Intel Core i5-4570 CPU with 3200 MHz clock frequency per core with a maximal theoretical memory throughput of 25.6 Gigabytes/sec. It allows for 32 FLOPs per cycle in single precision (16 in double precision). The systems memory is 32 Gigabytes DDR3-RAM. All codes are compiled using the -O2 optimization level in GNU G++ compiler version 4.8.4 on Ubuntu 16.04 LTS.

The parallel DFT is executed on two GPUs: First, we use a standard low-stream consumer graphics card GeForce GT730 with 2 Gigabytes GDDR5-RAM (launched 2014) with a maximum theoretical memory bandwidth of 48 Gigabytes/sec. It contains 2 multiprocessors with 192 ALUs each, thus the total amount of processor cores is

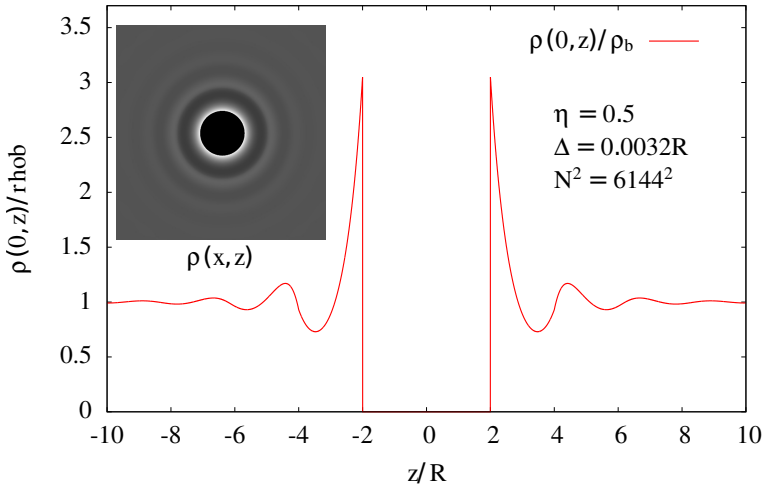

Figure A.6 Density profile of hard disks in 2D around a test particle calculated via the FMT outlined in Sec. A.2.1 on a GPU. The red line shows the density profile along the z-axis through the origin, whereas the inset pictures full density $\rho(x, z)$. White means high density, black zero density.

384 clocking with 902 MHz. This amounts to a theoretical peak performance of 693 Giga-FLOPs/sec in single precision (but only 28.9 in double precision).
Second, we employ the high-performance GPU Tesla K80, which basically unifies two Tesla K40s on a single board, which are connected via the PCI-Express 3.0 bus (15 Gigabytes/sec bandwidth). Every chip has 13 multiprocessors with 192 cores each, and has a total memory amount of 12 Gigabytes GDDR5-RAM with a bandwidth of 240 Gigabytes/sec. It reaches a theoretical peak performance of 4.36 Tera-FLOPs in SP (double 1.45) per chip with a maximum clock frequency of 875 MHz. Unfortunately, due to the internal structure of DFT and FMT, it is not possible to perform calculations on both chips at a time without mutual memory accesses via the PCI-Express bus, which clearly would limit the performance.

A.3 Results

A.3.1 Performance benchmarks

Two dimensions

We first present results for hard disks in two dimensions. As mentioned in Sec. A.2.1, we consider a system where a test particle is fixed at the origin and we calculate the density distribution $\rho(x, z)$ around that particle. For illustration, in Fig. A.6 we plot the density normalized with respect to bulk density ρ_b along the z-axis at $x = 0$ for a packing fraction of $\eta = \pi R^2 \rho_b = 0.5$ (red solid line). The density is initialized on the

grid as the corresponding ideal gas limit

$$\rho^{(0)}(i_1, i_2) = \begin{cases} 0 \ ; \ r < 2R \\ \rho_b \ ; \ \text{else} \end{cases} , \tag{A.22}$$

where $r = \Delta\sqrt{(i_1 - N/2)^2 + (i_2 - N/2)^2}$. The density subsequently is iterated 200 times according to Eqs. (A.2) and (A.3) using a mixing parameter $\gamma = 0.1$, irrespective of a complete convergence of the density profile corresponding to the thermodynamic minimum. We fix the system size at $V = (20R)^2$, and the number of grid points is $N^2 = 6144^2$ resulting in a fine grid spacing of $\Delta = 0.0032R$ in each spatial direction. The inset shows the full density profile, where black corresponds to lowest density and white means highest density. The calculation has been performed in single precision, where the peak value of resident memory reaches roughly 10 Gigabytes.

For the performance measurements, we investigate systems with $N^2 = 256^2$, 512^2, 1024^2, 1536^2, 2048^2, 2560^2, 3072^2, 4096^2, 5120^2 and 6144^2 grid points (note that the FFT routines require that the number of grid points can be written in the form $2^n \times 3^m \times 5^l \times 7^s$ along each axis where exponents are integers [237]). Hence, keeping the systems volume constant at $V = (20R)^2$ determines the corresponding grid spacing Δ. The packing fraction is fixed at $\eta = 0.3$. In Fig. A.7 (a) we compare the computation time of a serial DFT (filled squares) in single (full black lines) and double precision (dashed blue lines) to a parallel execution on the GT730 (empty squares) and a massively parallel execution on the Tesla K80 (stars). Here the distinction between 'parallel' and 'massively parallel' indicates the differences in the number of cores of the GPUs.

As mentioned in Sec. A.2.3, the employed CPU allows for each core for 32 FLOP instructions per clock-cycle in SP and 16 FLOPs in DP, but the differences are born out to be rather less than a factor of two. This may be due to the fact that memory bandwidth for reading and storing data limits the theoretical performance gain in single precision. While for the CPU implementation we do not run out of memory in both, SP and DP calculations, the picture is different on the GPUs. In particular, the low-stream GPU with 2 GB of memory allows only for system sizes up to 2048^2 in SP (1536^2 in DP), whereas employing the K80 the largest size is up to 6144^2 in SP and 4096^2 in DP, see also Fig. A.10 (a). However, regarding performance, even the slower GPU gives a significant speed-up factor of roughly 10 in SP compared to the serial code for all possible system sizes (cf. Fig. A.7 (b)), although performance dramatically breaks down when using double precision floating-point numbers; here the GT730 only yields a maximum speed-up between 2 – 4.

Running a massively parallel minimization, we obtain an enormous performance gain between 30 – 70 in SP and 20 – 40 in DP relative to the serial algorithm. The maximum speed-up factors are obtained for system sizes which can be written in the form 2^n with $n \in \mathbb{N}_+$, e.g. $N^2 = 1024^2$, 2048^2 or 4096^2. This is due to the fact that (parallel) FFT routines work most efficient for arrays with these dimensions [237]. For

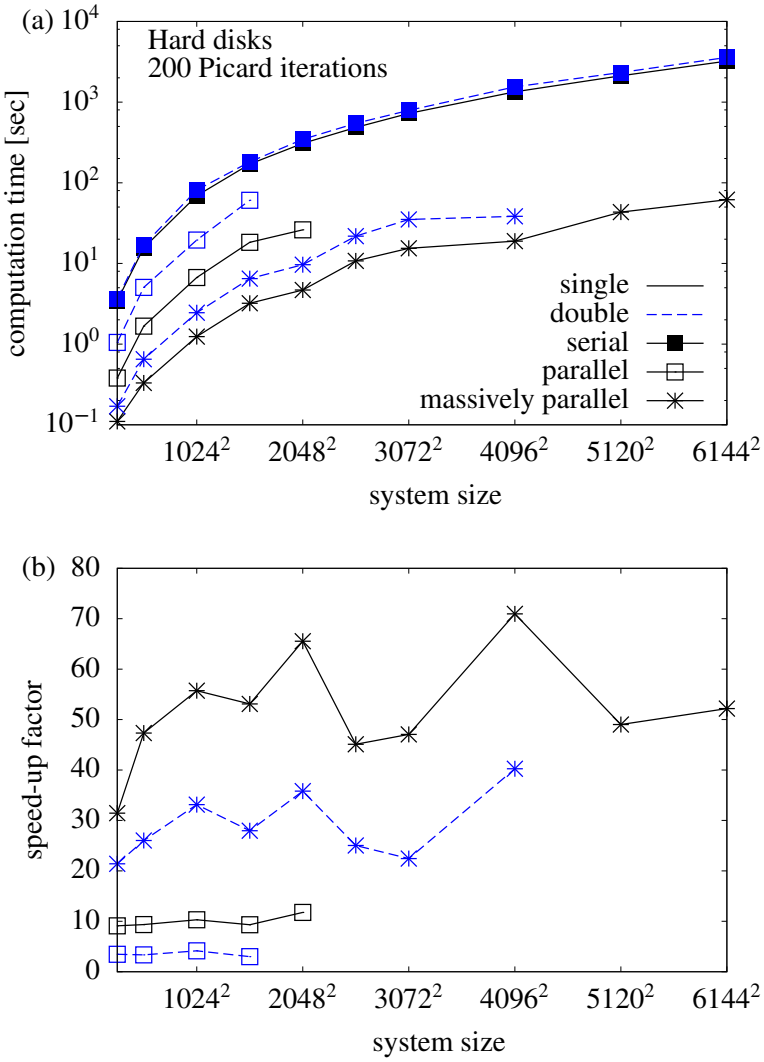

Figure A.7 (a) Total computation time needed for minimization of the grand potential for hard disks in single (full black) and double precision (dashed blue). Full squares show serial CPU results, open squares parallelized code on a low-stream GPU, and stars correspond to results born out by a high-performance GPU. Figure (b) demonstrates the obtained speed-up factor relative to the serial execution.

instance, considering a grid size of $N^2 = 4096^2$, the CPU code takes 1324 seconds whereas the massively parallel DFT runs only 19 seconds.

Three dimensions

We now focus on a full three-dimensional minimization of the grand potential for a system of hard spheres within a hard box. Additionally, as in $D = 2$, we keep a test particle fixed at the origin. For large enough systems, the density profile in vicinity to the test particle corresponds to the radial distribution function $g(r)$, and the contact value of the density at the center of a wall equals the bulk pressure. These relations can be used for internal consistency checks [70, 238], and we have verified that they are satisfied for the systems investigated In this chapter; further details are also given in the next Section A.3.2.

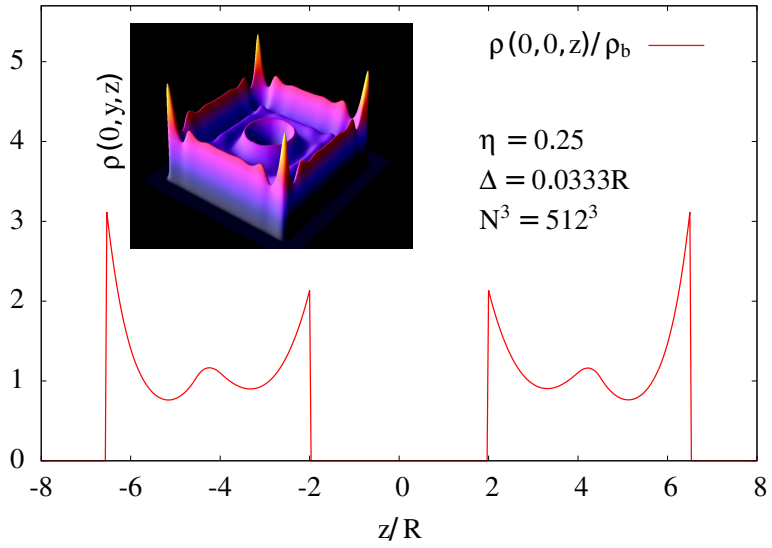

Figure A.8 Density profile of hard spheres in $D = 3$ in a cubic hard box at a packing fraction of $\eta = 0.25$. Moreover, we have fixed a test particle at the origin. As in Fig. A.6, red line corresponds to the density along the z-axis, and the inset pictures density in the y-z-plane at $x = 0$, where yellow means high density and blue low density.

In Fig. A.8 we plot the density divided by ρ_b along the z-axis at $x = y = 0$ for a 3D packing fraction of $\eta = 0.25$ using the Rosenfeld functional Eq. (A.18) (red solid line). Again, the density is initialized as the corresponding ideal gas limit. The total number of grid points is $N^3 = 512^3$ with a grid spacing of $\Delta = R/30$ yielding a volume of $V = (17.067R)^3$, and calculation is performed on the K80 in single precision. The inset pictures the density in the y-z-plane at $x = 0$, where yellow means highest and blue lowest density. We observe that the density is sharply peaked in the corners, which restricts the usage of standard FMT to low and intermediate packing fractions, since too strong confinement leads to divergences in the third term of Eq. (A.18). In situations with strong confinement and high densities one may use more sophisticated versions of FMT including tensorial weight functions [110].

As in two dimensions, we examine the computation time needed for 200 Picard iterations using a mixing parameter $\gamma = 0.1$. The system sizes are ranging from $N^3 = 64^3$, 96^3, 128^3, 160^3, 192^3, 224^3, 256^3, 288^3, 320^3, 384^3 to $N^3 = 512^3$, where the volume is kept constant at $V = (17.067R)^3$. Packing fraction is fixed at $\eta = 0.1$. Figures A.9 (a) and (b) show the same graphs as in Fig. A.7 but for hard spheres in $D = 3$: Filled squares correspond to the serial code, empty squares feature the parallel DFT on the slower GPU, and stars picture results which we obtain on the high-performance GPU. Again, the full black curves are the SP results, and dashed blue curves are DP results. As for the system of hard disks, the difference between single and double precision of the CPU version is measurable, though is less than a factor of two. The parallel execution increases performance by roughly a factor of 5 – 8 in SP and 2 – 4 in DP. For system sizes larger than 256^3 grid points in SP (224^3 in DP, respectively) the amount of necessary memory exceeds the limit of 2 Gigabytes. When running the massively parallelized DFT, the maximum number of grid points is

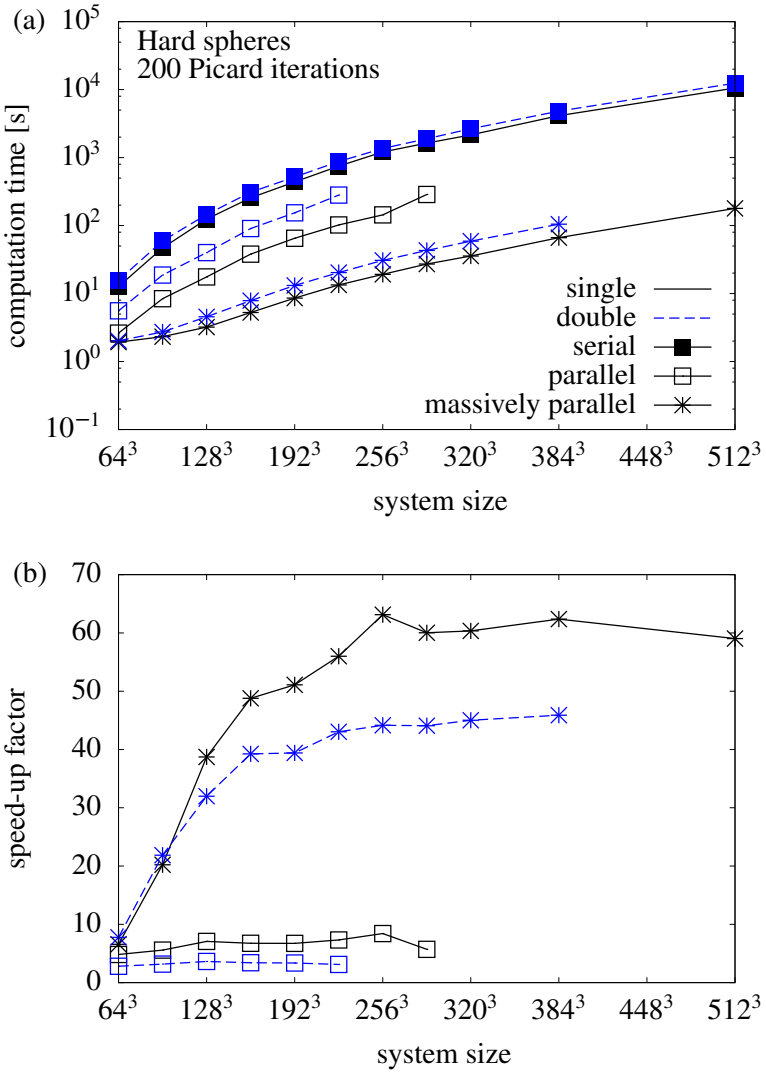

Figure A.9 Same as Fig. A.7 but for hard spheres in $D = 3$.

512^3 in SP (384^3 in DP), which also is shown in Fig. A.10 (b). Regarding performance, we find a peak speed-up factor of roughly 65 for 256^3 points in SP; for all remaining system sizes larger than 192^3 points speed-up ranges between 50 – 60 in SP, and 40 – 50 in DP.

To summarize, we can conclude that a massively parallel minimization of DFT-FMT in both, 2D and 3D situations, leads to enormous speed-up factors. However, it is important to note that the specific numbers clearly depend on the underlying hardware and software implementation. For instance, performing the same serial code on an older CPU with *higher* clock-frequency but less instructions per clock-cycle for each core, one may find increased speed-up factors, despite the higher clock-frequency. On the other hand, the advance of a GPU implementation will be less when employing a parallelized CPU code making use of all available processor cores, although for the CPU employed here we have found that using a multi-threaded version making use of all 4 cores only yields a speed-up of $\sim 1.5 - 2$ depending on the specific number of grid points.

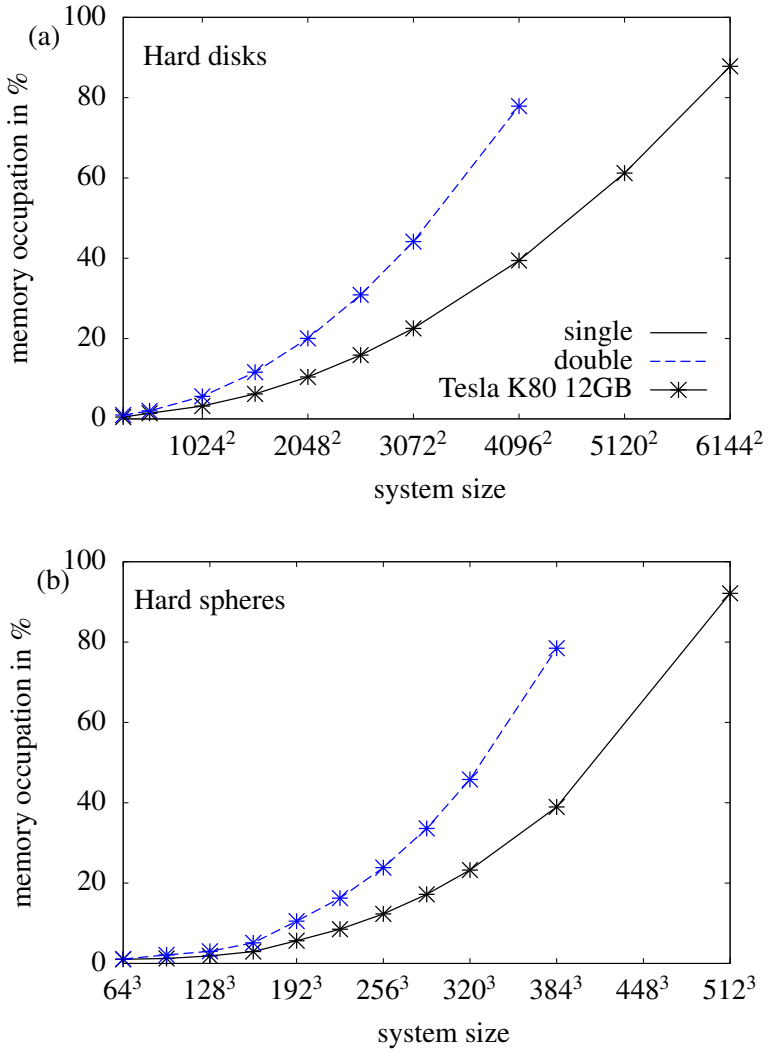

Figure A.10 Memory usage in % of one Tesla K80 chip as a function of system size for (a) hard disks and (b) hard spheres in single (full black) and double precision (dashed blue).

A.3.2 Convergence benchmarks

In the previous section we extensively studied the computational cost versus system size, i.e. the number of grid points used. While in Figs. A.6 and A.8 the grid spacing Δ is fine (~ 300 points per radius in 2D and 30 in 3D), we did not discuss whether for significantly coarser grid spacings (i.e., smaller number of grid points) the resulting density profiles are converged to the expected solution in thermal equilibrium.

In effective 1D situations, DFT calculations can be performed efficiently with very high spatial resolution. Hence, in this section we investigate the convergence of a full three-dimensional DFT result to the corresponding quasi-1D solution as a function of the number of grid points used for different volumes V. Specifically, we compare the density profile $\rho(z)$ confined in a slit-like hard pore of the effective 1D-system of hard spheres to the full 3D-results as a function of (i) number of grid points and (ii) computation time. The packing fraction is fixed at $\eta = 0.42$. Note that while the previously investigated 2D-system of hard disks can obviously also be reduced in

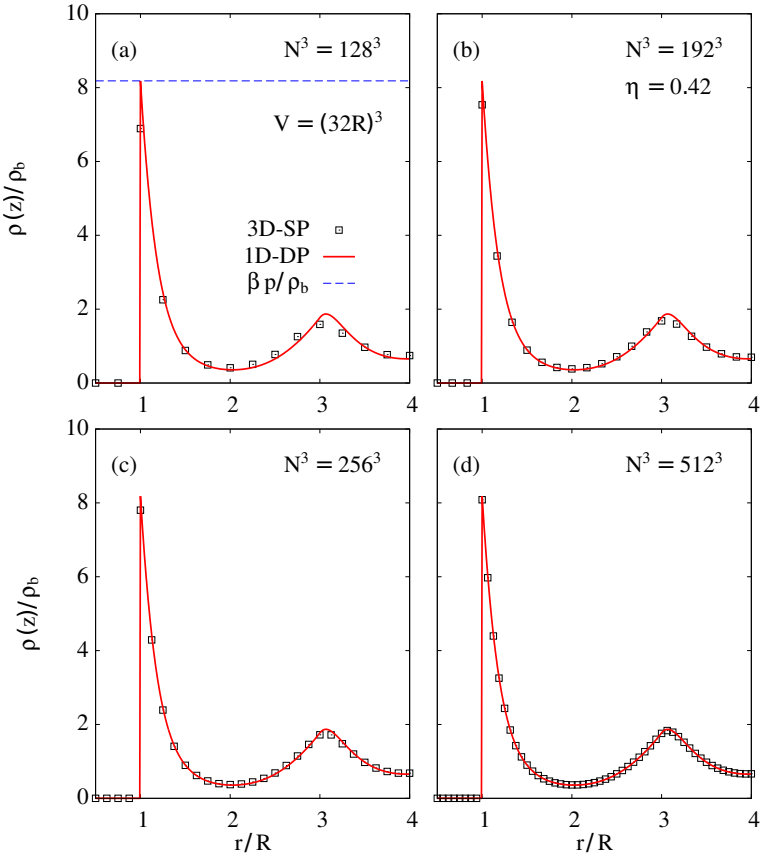

Figure A.11 Density profile of hard spheres in a slit-like pore of the quasi-1D system (red solid lines, double precision) with a fine grid spacing of 128 points per radius R at a packing fraction of $\eta = 0.42$. Additionally, in (a)–(d) the corresponding full 3D results (symbols, single precision) along an arbitrary axis parallel to the z-axis are pictured for numbers of grid points ranging from 128^3 (a) to $(512)^3$ (d).

dimensionality due to radial symmetry, here the reduction to 1D is only seemingly advantageous. First, in 2D it is possible to obtain a fine spatial resolution even for large systems along each axis with much less computational effort than in 3D. For instance, considering a volume of $V = (100R)^2$ and a total number of grid points of 2048^2, one obtains a grid spacing of ≈ 20 points per radius R which is sufficient even for quantitative accuracy, as we will see in the 3D case. Moreover, the resulting 1D FMT-equations on a standard linear grid no longer contain convolution integrals, and calculations become inefficient compared to using FFT-algorithms that can be applied in the full two-dimensional case.

In Figs. A.11 (a)–(d) we display the density $\rho_{1\mathrm{D}}(z)$ of the quasi-1D system (red solid line, in double precision) for a simulation volume of $V = (32R)^3$ (i.e., a length of $L = 32R$ in $D = 1$). The density is iterated 200 times, after which the relative change $\delta \equiv \int \mathrm{d}z\,(\rho^{k+1}(z) - \rho^k(z))^2$ to the previous density profile is $\delta < 10^{-15}$. Comparing the resulting contact density $\rho(R^+)$ to the Percus-Yevick bulk pressure $\beta p = \rho_b(1 + \eta + \eta^2)/(1 - \eta)^3$, we find excellent agreement (see blue dashed line in Fig. A.11) using a fine spatial resolution of 128 points per radius R. For illustration, on the CPU employed In this chapter, the serial code takes only 0.8 seconds in double

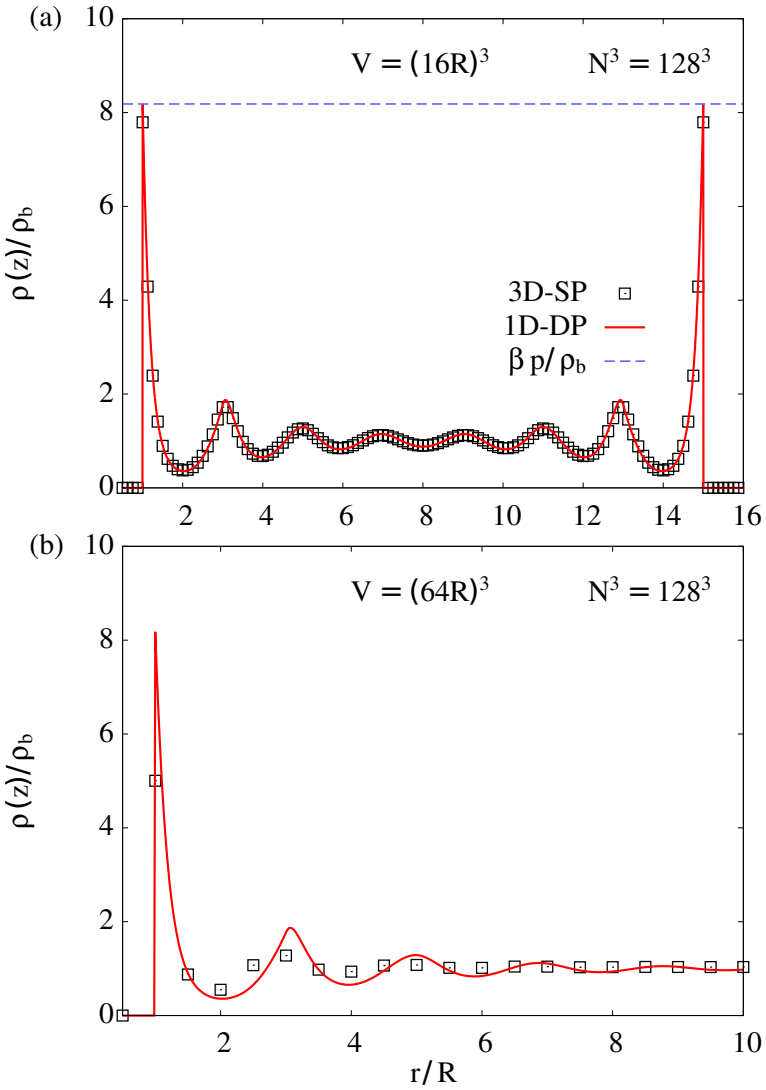

Figure A.12 Same as in Fig. A.11 but for a constant number of grid points $N^3 = 128^3$ and different volumes $V = (16R)^3$ (a) and $(64R)^3$ (b).

precision using 1D-FFT methods. We refer to Ref. [70] for further details regarding efficient 1D-DFT implementations.

Furthermore, in Figs. A.11 (a)–(d) we show the corresponding full 3D results (symbols) for numbers of grid points $N^3 = 128^3$, 192^3, 256^3 and 512^3 along an arbitrary axis parallel to the z-axis. For the volume $V = (32R)^3$ this corresponds to a grid spacing ranging from 4 to 16 points per radius. In order to achieve a situation corresponding to slit-like pore, in 3D the density is explicitly unconfined in the x- and y-direction, but confined in z-direction. Thus, for every constant point in the x-y-plane one obtains the identical density profile $\rho(x = \text{const}, y = \text{const}, z) \equiv \rho_{3D}(z)$. As expected, we observe that with increasing spatial resolution, the 3D result converges to the reference solution. On the scales shown in the plot, for the largest number of grid points studied here (512^3 in single precision, limited by the employed hardware) there is excellent agreement between the 3D- and 1D result, also in terms of the contact value. Moreover, still for 256^3 grid points the agreement is good, although slight deviations can be

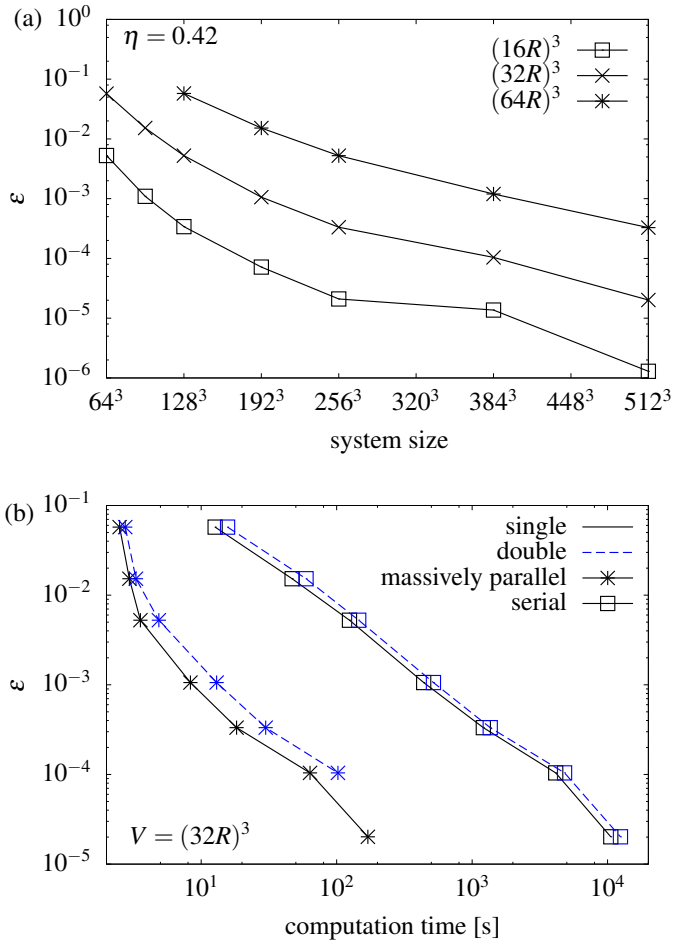

Figure A.13 (a) Convergence parameter ε of the three-dimensional density $\rho_{3D}(z)$ to the 1D-reference solution as a function of system size for three different simulation volumes $V = (16R)^3$ (open squares), $(32R)^3$ (crosses) and $(64R)^3$ (stars). (b) ε as a function of total computation time for the massively parallelized (stars) and serial DFT (open squares) in single (black solid) and double precision (blue dashed) for a simulation volume of $V = (32R)^3$.

observed; these are increasing with decreasing numbers of grid points (cf. Figs. A.11 (a) and (b)). Note that usage of single precision does not impact the density profiles presented here. In general we have verified that for all situations considered In this chapter, single precision is sufficient. However there are clearly situations such as the description of the crystal phase [115], where fluctuations beyond single precision may lead to unphysical results or numerical divergences .

In addition, we plot similar graphs for a smaller [$V = (16R)^3$) (a)] and a larger volume [$V = (64R)^3$, (b)] for $N^3 = 128^3$ grid points in Fig. A.12. While the large volume with 2 points per radius spatial resolution clearly fails to describe fundamental properties, the smaller system is satisfactory reflected using a relatively small number of grid points. Based on the present finding, we suppose that the grid spacing should not deceed the threshold of 8 – 10 points per particle (hard-core) radius in order to obtain reliable and meaningful results as long as the system is in the liquid state; for crystal-like states one may need to employ a rather more fine spatial resolution in

order to ensure that the desired properties of the system are described properly. As a direct measure of convergence, we consider the quantity

$$\varepsilon \equiv \int_0^L \mathrm{d}z \, \left(\rho_{3\mathrm{D}}(z) - \rho_{1\mathrm{D}}(z)\right)^2 \, , \tag{A.23}$$

which in Fig. A.13 (a) is shown as a function of system size for the three volumes shown in Figs. A.11 and A.12. This representation reflects the observed behavior of the density profiles: with increasing volume V, the number of grid points needs also to increase in order to obtain a similar level of accuracy compared to smaller volumes.

In Fig. A.13 (b) we show the accuracy as a function of computational cost for a massively parallel- (squares) and completely serial execution (stars) for $V = (32R)^3$. While increasing accuracy with a serial (or slightly parallelized on a standard consumer CPU) implementation rapidly becomes unproportional regarding computational effort, this is not the case for a heavy parallelized execution. Several further conclusion can be given. First, in situations that require a large volume in terms of the particle size (e.g. periodic cluster phases in systems with competing interactions [89]), a huge number of grid points is necessary in order to obtain reasonable accuracy. For instance, for $V = (64R)^3$, one already needs $(384)^3$ points in order to achieve a qualitative accuracy as in Fig. A.11 (b). Second, for smaller volumes, a massively parallelized DFT allows for the calculation with high spatial resolution – which can be mandatory, e.g. if the system is confined in an arbitrarily shaped cavity. Furthermore, due to the lack of a spatial direction, in 2D the investigation of large volumes with very high spatial resolution is applicable. These findings presented here demonstrate the need for a massively parallel implementation of a multi-dimensional DFT, as in such situations serial and slightly parallelized versions become highly infeasible.

Appendix B

Simulation Details

B.1 The open-source code *PatchyParticles*

All simulation results for patchy particles shown in this thesis were obtained from the open-source code *PatchyParticles* (PP) accompanying the nice paper *How to simulate patchy particles* by L. Rovigatti, J. Russo, and F. Romano [142]. It implements the Kern-Frenkel pair potential defined in Eqs. (3.1), (3.3), and (3.4). A documentation on how to use the PP code can be found on GitHub under https://github.com/lorenzo-rovigatti/PatchyParticles. At this point we also refer to the text book *Computer Simulation of Liquids* by Michael Allen and Dominic Tildesely which provides a general introduction to computer simulations [95].

The PP code implements the most important MC algorithms that are pertinent to simulations of patchy fluids, including simple roto-translations as discussed in Sec. B.2.1, AVB moves (Sec. B.2.3), but also more sophisticated cluster-move algorithms or techniques to calculate the free-energy landscape, which, however, we do not have employed in this work. Besides the canonical ensemble, the PP code can also run grand-canonical simulations which allows one to measure particle fluctuations.

Note that the PP code as available on the Internet does not calculate radial distribution functions or the density at a hard wall, but only provides basic measurements of e.g. the internal energy in canonical ensemble. We amended the original PP code to determine structural quantities.

B.2 Monte Carlo algorithms for patchy fluids

Consider a classical fluid of N particles with equal mass m. The Hamilton function H is given by

$$H = \sum_{i=1}^{N} \frac{|\mathbf{p}_i|^2}{2m} + \Phi(\mathbf{r}^N) + \underbrace{\sum_{i=1}^{N} V_{\text{ext}}(\mathbf{r}_i)}_{\equiv V}, \tag{B.1}$$

where $\Phi(\mathbf{r}^N)$ is a pair potential, i.e. $\Phi(\mathbf{r}^N) = \sum_{i<j} \phi(\mathbf{r}_i, \mathbf{r}_j)$. In a MC simulation one is typically concerned with calculating integrals of the form (for simplicity we consider

the canonical ensemble):

$$\langle \mathcal{A} \rangle = \int \mathrm{d}\Gamma \, \mathcal{A}(\Gamma) f_0(\Gamma) \tag{B.2}$$

$$= \frac{\int \mathrm{d}\mathbf{r}^N \, A(\mathbf{r}^N) \exp[-\beta(\Phi + V)]}{\int \mathrm{d}\mathbf{r}^N \, \exp[-\beta(\Phi + V)]} \tag{B.3}$$

$$\equiv \int \mathrm{d}\mathbf{r}^N \, A(\mathbf{r}^N) P(\mathbf{r}^N) \,, \tag{B.4}$$

where Γ is a point in phase space, and $f_0(\Gamma)$ is the probability distribution function in equilibrium, in case of the canonical ensemble given by Eq. (2.3). Furthermore, $\mathbf{r}^N = \{(\mathbf{r}_1, \varpi_1), ..., (\mathbf{r}_N, \varpi_N)\}$ denotes a set of tuples containing all particle positions and orientations, and $\int \mathrm{d}\mathbf{r}^N \equiv \int \mathrm{d}\mathbf{r}_1 \int \mathrm{d}\varpi_1 \cdots \int \mathrm{d}\mathbf{r}_N \int \mathrm{d}\varpi_N$.

Integrating out the momentum degrees of freedom in Eq. (B.2) yields (B.3) provided that $\mathcal{A}$ does not depend on the particle momenta $\mathbf{p}_i$, $i = 1, ..., N$. This leads to a reduced phase-space probability distribution $P(\mathbf{r}^N)$:

$$P(\mathbf{r}^N) = \frac{\exp[-\beta(\Phi + V)]}{\int \mathrm{d}\mathbf{r}^N \, \exp[-\beta(\Phi + V)]} \,. \tag{B.5}$$

Equations such as (B.4) may be approximated by employing stochastic (Monte-Carlo) integration schemes along with a technique called 'importance sampling', introduced in 1953 by Metropolis [96]: If we were able to generate a random sequence $\{\mathbf{r}_1^N, ..., \mathbf{r}_K^N\}$ of configurations (or samples) of length K in phase space, *according* to the phase-space probability distribution $P(\mathbf{r}^N)$, where $\mathbf{r}_j^N = \{(\mathbf{r}_1, \varpi_1)_j, ..., (\mathbf{r}_N, \varpi_N)_j\}$, $j = 1, ..., K$, then we could approximate Eq. (B.4) as:

$$\langle \mathcal{A} \rangle \approx \frac{1}{K} \sum_{j=0}^{K} \mathcal{A}_j \,, \tag{B.6}$$

where $\mathcal{A}_j = \mathcal{A}(\mathbf{r}_j^N)$. The obvious key task of a Monte-Carlo simulation is thus to generate a sequence $\{\mathbf{r}_1^N, ..., \mathbf{r}_K^N\}$ which samples the positional configuration space according to $P(\mathbf{r}^N)$.

B.2.1 Metropolis algorithm for patchy fluids

The Metropolis algorithm [96] is the most common method to generate samples according to the Boltzmann distribution (B.6). For a patchy fluid, the Metropolis algorithms involves the following steps (also called MC step or sweep): Starting from a given initial configuration $\mathbf{r}_0^N$, the $(j+1)$-th sample $\mathbf{r}_{j+1}^N$ is generated from $\mathbf{r}_j^N$ via the following iterative procedure:

1. Choose randomly a particle $s \in \{1, ..., N\}$ with coordinates $(\mathbf{r}_s, \varpi_s)_j$ from the configuration $\mathbf{r}_j^N$.

2. Perform a random roto-translation (trial move) of particle s, i.e. $(\mathbf{r}_s, \varpi_s)_{j+1} =$

$(\mathbf{r}_s + \delta\mathbf{r},\, \varpi_s + \delta\varpi)_j$, where $\delta\mathbf{r}$ denotes a small random translational displacement, and $\delta\varpi$ a small rotation around a randomly chosen axis $\mathbf{d}_\varpi$, respectively.

3. The above move generates an intermediate configuration that is given by $\widetilde{\mathbf{r}}^N_{j+1} = \{(\mathbf{r}_1,\, \varpi_1)_j, ..., (\mathbf{r}_s\,, \varpi_s)_{j+1}, ..., (\mathbf{r}_N\,, \varpi_N)_j\}$. Calculate now the change in configurational energy $\Delta E = (\widetilde{\Phi}_{j+1} + \widetilde{V}_{j+1} - \Phi_j - V_j)$ where $\widetilde{\Phi}_{j+1} \equiv \Phi(\widetilde{\mathbf{r}}^N_{j+1})$, $\Phi_j \equiv \Phi(\mathbf{r}^N_j)$ etc.

4. Accept the new intermediate configuration $\widetilde{\mathbf{r}}^N_{j+1}$ with probability

$$P_{j\to j+1} = \min\{1, \exp[-\beta\Delta E]\} \tag{B.7}$$

5. Repeat steps 1. to 4. for N times. This then defines the new configuration $\mathbf{r}^N_{j+1}$.

The translational displacement $\delta\mathbf{r} = (\delta x,\, \delta y,\, \delta z)^T$ is chosen uniformly from $[-\delta l,\, \delta l]\times [-\delta l,\, \delta l] \times [-\delta l,\, \delta l]$ where δl is the maximal displacement along each axis. A random rotation axis $\mathbf{d}_\varpi$ can be generated via $\mathbf{d}_\varpi = \left(\sqrt{1-\zeta^2}\cos(\varphi),\, \sqrt{1-\zeta^2}\sin(\varphi),\, \zeta\right)^T$ with $\zeta \in [-1, 1]$ and $\varphi \in [0,\, 2\pi)$ chosen uniformly. The rotation angle is chosen uniformly from $\delta\varphi \in [0,\, \delta\vartheta]$.

B.2.2 Equilibration and decorrelation

A simulation is typically initialized in a configuration that is far from equilibrium. Before starting to accumulate values of $\mathcal{A}_j$ according to the right-hand side of Eq. (B.6) by generating a sequence of configurations, it is important that the system is allowed to relax towards equilibrium for a sufficient number N_{eq} of MC steps (often called equilibration steps). A good estimate whether the system has reached equilibrium, is to monitor the instantaneous internal energy of the system as a function of MC steps and wait until systematic drifts have vanished. Furthermore, to ensure that the simulation has not entered a gas-liquid coexistence region, one should also monitor structural quantities such as $g(r)$. In a two-phase region, the $g(r)$ typically exhibits long-ranged oscillations that do not decay to the correct bulk value. In general it is difficult to say how many equilibration steps are necessary to approach equilibrium; in this work, we provide the number N_{eq} of equilibration steps prior to observable measurements in those sections where simulation results are presented.

A new configuration that has been generated from a previous one is in general highly correlated with the latter. This introduces bias to averages $\langle\mathcal{A}\rangle$ of observables. To minimize such correlations, one should allow for a certain number N_{decorr} of intermediate MC steps before calculating a new value $\mathcal{A}_{j+1}$ that enters Eq. (B.6). For the Metropolis algorithm this means that steps 1. to 4. are carried out for $N \times N_{\text{decorr}}$ times before a new value of $\mathcal{A}_{j+1}$ is recorded. The precise value of N_{decorr} depends on the number of particles N, the temperature T, packing fraction η. During the course of a simulation, in total $M \times N_{\text{decorr}} \times N_{\text{eq}}$ MC moves are performed; this number can be of order $\sim 10^{10}$ – 10^{12}.

The amount of necessary equilibration end decorrelation steps in some situations can be reduced significantly with clever MC algorithms. An important example, that we frequently employed in this work is the so-called aggregation-volume-bias (AVB) move.

B.2.3 Aggregation-volume-bias (AVB) moves

While roto-translations along with the Metropolis algorithm provide a suitable access to the behavior of patchy fluids at reasonable high temperatures and densities, it can be extremely difficult and demanding to sample the phase space at low densities and temperatures properly; at the same time, self-assembly of complex structures is often observed at very low temperatures and densities. For example, chain-formation in systems with two interaction sites becomes significant for $k_BT/\varepsilon \lesssim 0.08$ [154]. The probability to break an existing bond between two particles is proportional to $(k_BT/\varepsilon)^{-1}$; see Eq. (B.7). At these temperatures it typically requires $\sim 10^6$ – 10^8 trial moves to break a bond for simulations that make use of conventional Metropolis moves, which, in turn requires to run a very large number of equilibration and intermediate decorrelation steps.

The AVB algorithm proposes a method to significantly speed up phase-space sampling at such low densities and temperatures. This is achieved by performing two kinds of particle moves: (i) formation of a new bond between previously unbonded particles and (ii) breaking of an existing bonds between two particles by explicit separating. The precise steps involved can be found in Ref. [142]. The authors demonstrated that at low densities and temperatures, the AVB algorithm can speed up the sampling of phase space up to more than two orders of magnitudes compared to the standard Metropolis algorithm.

B.2.4 Calculating radial distribution functions

A key task throughout this work is to determine the radial distribution function $g(r)$ (and its dynamical analogue, the van Hove function) from a given set of configurations. This can be realized as follows. Due to the definition of $g(r)$, the mean number of particles $N(r)$ within a sphere of radius r centered around a reference particle can be written as

$$N(r) = 4\pi\rho_b \int_0^r \mathrm{d}r'\; r'^2 g(r') \;, \tag{B.8}$$

Differentiating both sides of Eq. (B.8) yields

$$\frac{\mathrm{d}N(r)}{\mathrm{d}r} = 4\pi r^2 \rho_b g(r) \;, \tag{B.9}$$

or, equivalently,

$$g(r) = \lim_{\Delta r \to 0} \frac{N(r+\Delta r) - N(r)}{4\pi\rho_b r^2 \Delta r} \approx \frac{N(r+\Delta r) - N(r)}{\frac{4\pi}{3}\rho_b[(r+\Delta r)^3 - r^3]} \,, \tag{B.10}$$

where $N_{\Delta r} \equiv N(r+\Delta r) - N(r)$ is the mean number of particles within the spherical shell between r and $r+\Delta r$. The quantity $N_{\Delta r}$ can be estimated by means of recording the distances of all particles surrounding a fixed reference particle into a histogram and then averaging over all (reference) particles and configurations. Hence, $g(r)$ is approximately given by

$$g(r) \approx \frac{\mathrm{hist}(r)}{\frac{4\pi}{3}\rho_b[(r+\Delta r)^3 - r^3]} \,, \tag{B.11}$$

where the histogram $\mathrm{hist}(r)$ is calculated via (the inner summation is an average over all particles)

$$\mathrm{hist}(r) = \frac{1}{NK}\sum_{i=1}^{K}\sum_{j=1}^{N}\sum_{k\neq j}^{N} \chi_{[r,r+\Delta r]}(|\mathbf{r}_{i,j} - \mathbf{r}_{i,k}|) \,, \tag{B.12}$$

in where $\mathbf{r}_{i,k}$ is the position of particle k within configuration $\mathbf{r}_i^N$, and $\chi_{[r,r+\Delta r]}(x)$ denotes the characteristic function on the interval $[r, r+\Delta r]$, i.e.

$$\chi_{[r,r+\Delta r]}(x) = \begin{cases} 1 & \text{if } \; x \in [r,\, r+\Delta r] \,, \\ 0 & \text{else} \,. \end{cases} \tag{B.13}$$

We used a spatial resolution of one hundred points per diameter, i.e. $\Delta r = 10^{-2}\sigma$.

B.2.5 Density at a hard wall

A hard wall can be modeled as a region where the particles cannot enter due to their hard core; respective configurations will be discarded by the MC algorithms during the course of the simulation. In this work, a hard wall with thickness 2σ was introduced at $z = 0$ in the x-y plane of the simulation box. Due to the symmetry induced by a planar hard wall, the equilibrium density profile will only depend on the z-coordinate and be translational invariant along the x- and y-axis. Similar to the derivation of Eq. (B.11), consider the number of particles at distance z to the wall:

$$N(z) = \int_0^{Lx} \mathrm{d}x' \int_0^{L_y} \mathrm{d}y' \int_0^{z} \mathrm{d}z'\, \rho(z') = L_x\, L_y \int_0^{z} \mathrm{d}z'\, \rho(z') \tag{B.14}$$

$$\Rightarrow \rho(z) = \frac{1}{L_x\, L_y}\frac{\mathrm{d}N(z)}{\mathrm{d}z} \approx \frac{1}{L_x\, L_y}\frac{N(z+\Delta z) - N(z)}{\Delta z} = \frac{1}{L_x\, L_y}\frac{\mathrm{hist}(z)}{\Delta z} \,, \tag{B.15}$$

wheren $\mathrm{hist}(z)$ is a histogram of the number of particles that are located between $[z,\, z+\Delta z]$ at distance z from the wall. It is given by

$$\mathrm{hist}(z) = \frac{1}{K}\sum_{i=0}^{K}\sum_{j=0}^{N} \chi_{[z,\, z+\Delta z]}(z_{i,j}) \,, \tag{B.16}$$

where $z_{i,j}$ is the distance of particle j to the wall in configuration $\mathbf{r}_i^N$.

B.3 Dynamic Monte-Carlo simulations

B.3.1 Methodology

The dynamic Monte Carlo (DMC) method [167, 168] is based on the standard Metropolis algorithm (see Sec. B.2.1) and mimics Brownian dynamics of colloidal particles immersed in a solvent in the limit of small displacements $\delta\mathbf{r}$. It is based on the observation that the mean square displacement of a free Brownian particle can be linked to the displacement distance in a MC simulation $|\delta\mathbf{r}| = \sqrt{(\delta x^2) + (\delta y)^2 + (\delta z)^2} \in [0,\, \delta r]$, where $\delta r = \sqrt{3}\,\delta l$. In a trial move, a randomly chosen particle is shifted by a random vector $\delta\mathbf{r}$ as described in Sec. B.2.1. Thus, the translational mean-square displacement per trial move is given by

$$\langle \delta\mathbf{r}^2 \rangle = \frac{1}{\delta r}\int_0^{\delta r} r^2 a(r)\ \mathrm{d}r \ \approx\ \frac{\bar{a}}{\delta r}\int_0^{\delta r} r^2\ \mathrm{d}r = \frac{\bar{a}}{3}\delta r^2. \tag{B.17}$$

Here the acceptance rate $a(r)$ of a trial move has been approximated by its average $\bar{a}$, which is exact only in the limit of infinitesimal displacements $\delta r \to 0$. Requiring Eq. (B.17) to be equivalent to the mean square displacement of an isolated Brownian particle, i.e.

$$\langle \delta\mathbf{r}^2 \rangle = 6D_0\Delta t = \frac{\bar{a}}{3}\delta r^2\ , \tag{B.18}$$

yields an explicit specification for δr:

$$\delta r(\Delta t) = \sqrt{\frac{18D_0}{\bar{a}}\Delta t} = \sqrt{\frac{18\sigma^2}{\bar{a}}\Delta t^*}\ , \tag{B.19}$$

where $\Delta t^* = \Delta t/\tau_B$, where $\tau_B = \sigma^2/D_0$ is the Brownian time. As a result the maximal displacement along each spatial direction is given by

$$\delta l\,(\Delta t) = \sqrt{\frac{6\sigma^2}{\bar{a}}\Delta t^*}\,. \tag{B.20}$$

The dependency on the acceptance ratio can be bypassed by redefining a MC step as performing roto-translations until N trial moves have been *accepted*; then the average acceptance probability of a trial move is $\bar{a} = 1$. Similar considerations [168] lead to an expression for the maximal angular displacement $\delta\vartheta$ per trial move. Taking all together we find:

$$\delta l\,(\Delta t^*) = \sqrt{6\sigma^2\Delta t^*}\quad ;\quad \delta\vartheta(\Delta t^*) = \sqrt{72\,\Delta t^*}. \tag{B.21}$$

In this thesis we have assumed a time step of $\Delta t^* = 10^{-4}$ which in case for hard spheres has proven to be sufficient for converging against Brownian dynamics [177]. It was moreover verified that the results obtained from DMC were insensitive to changes in Δt.

B.3.2 Measurements

The DMC method enables us to calculate means of time-dependent observables $\langle \mathcal{A} \rangle(t)$ in a colloidal fluid that is subject to Brownian motion, such as the mean-squared displacement or the van Hove function $G(r,\, t)$ (cf. Ch. 5). This amounts to calculate an average of $\mathcal{A}$ at several points in time. This is done as follows.

Starting with an equilibrium configuration $\mathbf{r}_0^N$, we perform a number of M_t Monte-Carlo steps according to the Metropolis algorithm discussed in Sec. B.2.1. It is important to note that here intermediate equilibration steps must not be allowed to ensure a convergence of the DMC method towards Brownian dynamics. The total simulation time $t_{\max}$ (in units of τ_B) is then given by $t_{\max} = K_t \Delta t^*$ with $K_t \in \mathbb{N}$. In order obtain reliable statistics, we have to repeat the above steps for K times; this then yields an estimate for $\langle \mathcal{A} \rangle(t)$. In order to minimize correlations, we choose the latest configuration $\mathbf{r}_{K_t}^N$ as initialization for the new run (which clearly can be done in bulk fluids).

The mean-squared displacement is calculated according to:

$$\left\langle [\mathbf{r}(t) - \mathbf{r}(0)]^2 \right\rangle = \frac{1}{N \cdot K} \sum_{i=1}^{K} \sum_{j=1}^{N} [\mathbf{r}_{i,j}(t) - \mathbf{r}_{i,j}(0)]^2 \,, \tag{B.22}$$

where $t \in \{0,\, t_{\max}\}$ and $\mathbf{r}_{i,j}(t)$ denotes the location of particle j in configuration $\mathbf{r}_i^N$ at time t.

Similar to the calculation of the radial distribution function $g(r)$, the self and distinct parts of van Hove function $G(r,\, t)$ can be obtained from:

$$G_d(r,\, t) = \frac{1}{\frac{4\pi}{3}\rho_b[(r+\Delta r)^3 - r^3]} \frac{1}{NK} \sum_{i=1}^{K} \sum_{j=1}^{N} \sum_{k \neq j}^{N} \chi_{[r,r+\Delta r]}(|\mathbf{r}_{i,j}(t) - \mathbf{r}_{i,k}(0)|) \,, \tag{B.23}$$

$$G_s(r,\, t) = \frac{1}{\frac{4\pi}{3}\rho_b[(r+\Delta r)^3 - r^3]} \frac{1}{NK} \sum_{i=1}^{K} \sum_{j=1}^{N} \chi_{[r,r+\Delta r]}(|\mathbf{r}_{i,j}(t) - \mathbf{r}_{i,j}(0)|) \,. \tag{B.24}$$

Bibliography

[1] V. Weisskopf, Trans. N.Y. Acad. Sci. II **38**, 202 (1977).

[2] R. Evans, D. Frenkel, and M. Dijkstra, Physics Today **72**, 38 (2019).

[3] J. G. Kirkwood and E. M. Boggs, J. Chem. Phys. **10**, 394 (1942).

[4] W. W. Wood and J. D. Jacobson, J. Chem. Phys. **27**, 1207 (1957).

[5] B. J. Alder and T. E. Wainwright, J. Chem. Phys. **27**, 1208 (1957).

[6] B. Widom, Science **157**, 375 (1967).

[7] J. D. Weeks, D. Chandler, and H. C. Andersen, J. Chem. Phys. **54**, 5237 (1971).

[8] J. A. Barker and D. Henderson, Rev. Mod. Phys. **48**, 587 (1976).

[9] *Proceedings of the Symposium on the Many-Body Problem* (New York, London, p. 498, 1963).

[10] J. K. G. Dhont, *An Introduction to Dynamics of Colloids* (Elsevier New York, 1996).

[11] H. Löwen, Phys. Rep. **237**, 249 (1994).

[12] P. Langevin, C. R. Acad. Sci. (Paris) **146**, 530 (1908).

[13] P. N. Pusey and W. van Megen, Nature **320**, 340 (1986).

[14] R. Piazza, T. Bellini, and V. Degiorgio, Phys. Rev. Lett. **71**, 4267 (1993).

[15] P. N. Pusey, W. van Megen, P. Bartlett, B. J. Ackerson, J. G. Rarity, and S. M. Underwood, Phys. Rev. Lett. **63**, 2753 (1989).

[16] R. Evans, Adv. Phys. **28**, 143 (1979).

[17] Y. Rosenfeld, Phys. Rev. Lett. **63**, 980 (1989).

[18] A. L. Thorneywork, R. Roth, D. G. A. L. Aarts, and R. P. A. Dullens, J. Chem. Phys. **140**, 161106 (2014).

[19] A. L. Thorneywork, J. L. Abbott, D. G. A. L. Aarts, and R. P. A. Dullens, Phys. Rev. Lett. **118**, 158001 (2017).

[20] A. L. Thorneywork, S. K. Schnyder, D. G. A. L. Aarts, J. Horbach, R. Roth, and R. P. A. Dullens, Mol. Phys. **116**, 3245 (2018).

[21] W. K. Kegel and A. van Blaaderen, Science **287**, 290 (2000).

[22] E. R. Weeks and D. A. Weitz, Phys. Rev. Lett. **89**, 095704 (2002).

[23] P. J. Lu, E. Zaccarelli, F. Ciulla, A. B. Schofield, F. Sciortino, and D. A. Weitz, Nature **453**, 499 (2008).

[24] C. P. Royall, S. R. Williams, T. Ohtsuka, and H. Tanaka, Nature Mater. **7**, 556 (2008).

[25] A. E. Bailey, W. C. K. Poon, R. J. Christianson, A. B. Schofield, U. Gasser, V. Prasad, S. Manley, P. N. Segre, L. Cipelletti, W. V. Meyer, M. P. Doherty, S. Sankaran, A. L. Jankovsky, W. L. Shiley, J. P. Bowen, J. C. Eggers, C. Kurta, T. Lorik, P. N. Pusey, and D. A. Weitz, Phys. Rev. Lett. **99**, 205701 (2007).

[26] E. A. G. Jamie, R. P. A. Dullens, and D. G. A. L. Aarts, J. Chem. Phys. **137**, 204902 (2012).

[27] U. Gasser, E. R. Weeks, A. Schofield, P. N. Pusey, and D. A. Weitz, Science **292**, 258 (2001).

[28] S. Asakura and F. Oosawa, J. Chem. Phys. **22**, 1255 (1954).

[29] A. Vrij, Pure Appl. Chem. **48**, 471 (1976).

[30] A. P. Gast, C. K. Hall, and W. B. Russell, J. Colloid Interface Sci. **96**, 251 (1983).

[31] V. J. Anderson and H. N. W. Lekkerkerker, Nature **416**, 811 (2002).

[32] S. Torquato and F. H. Stillinger, Rev. Mod. Phys. **82**, 2633 (2010).

[33] H. N. W. Lekkerkerker and R. Tuinier, *Colloids and the Depletion Interaction* (Springer Lecture Notes in Physics, 2011) p. 833.

[34] Z. Zhang and S. C. Glotzer, Nano Letters **4**, 1407 (2004).

[35] A. B. Pawar and I. Kretzschmar, Macromolecular Rap. Comm. **31**, 150 (2010).

[36] E. Bianchi, R. Blaak, and C. N. Likos, Phys. Chem. Chem. Phys. **13**, 6397 (2011).

[37] W. Bol, Mol. Phys. **45**, 605 (1982).

[38] W. R. Smith and I. Nezbeda, J. Chem. Phys. **81**, 3694 (1984).

[39] I. Nezbeda and G. A. Iglesias-Silva, Mol. Phys. **69**, 767 (1990).

[40] G. N. I. Clark, A. J. Haslam, A. Galindo, and G. Jackson, Mol. Phys. **104**, 3561 (2006).

[41] B. Ruzicka, E. Zaccarelli, L. Zulian, R. Angelini, M. Sztucki, A. Moussaid, T. Narayanan, and F. Sciortino, Nature Mater. **10**, 56 (2011).

[42] S. Biffi, R. Cerbino, F. Bomboi, E. M. Paraboschi, R. Asselta, F. Sciortino, and T. Bellini, Proc. Natl. Acad. Sci. **110**, 15633 (2013).

[43] R. P. Sear, J. Chem. Phys. **111**, 4800 (1999).

[44] N. Kern and D. Frenkel, J. Chem. Phys. **118**, 9882 (2003).

[45] C. Gögelein, G. Nägele, R. Tuinier, T. Gibaud, A. Stradner, and P. Schurtenberger, J. Chem. Phys. **129**, 085102 (2008).

[46] F. Roosen-Runge, F. Zhang, F. Schreiber, and R. Roth, Sci. Rep. **4**, 7016 (2014).

[47] E. Bianchi, J. Largo, P. Tartaglia, E. Zaccarelli, and F. Sciortino, Phys. Rev. Lett. **97**, 168301 (2006).

[48] D. de las Heras, J. M. Tavares, and M. M. Telo da Gama, J. Chem. Phys. **134**, 104904 (2011).

[49] F. Romano, E. Sanz, and F. Sciortino, J. Chem. Phys. **132**, 184501 (2010).

[50] F. Smallenburg and F. Sciortino, Nat. Phys. **9**, 554 (2013).

[51] F. Sciortino and E. Zaccarelli, Curr. Op. in Coll. and Int. Sci. **30**, 90 (2017).

[52] H. C. Andersen, J. Chem. Phys. **59**, 4714 (1973).

[53] I. Nezbeda, J. Kolafa, and Y. V. Kalyuzhnyi, Mol. Phys. **68**, 143 (1989).

[54] D. Ghongasi and W. Chapman, Mol. Phys. **79**, 291 (1993).

[55] M. W. Mahoney and W. L. Jorgensen, J. Chem. Phys. **112**, 8910 (2000).

[56] E. Sanz, C. Vega, J. L. F. Abascal, and L. G. MacDowell, Phys. Rev. Lett. **92**, 255701 (2004).

[57] J.-P. Hansen and I. McDonald, *Theory of Simple Liquids with Applications to Soft Matter* (Academic Press 4th Edition, London, 2013).

[58] F. H. Stillinger, Science **209**, 451 (1980).

[59] J. McManus, P. Charbonneau, E. Zaccarelli, and N. Asherie, Curr. Opin. Solid State Mater. Sci. **22**, 73 (2016).

[60] G. B. Benedek, Investig. Ophthalmol. Vis. Sci. **38**, 1911 (1997).

[61] A. Aguzzi and T. O'Connor, Nat. Rev. Drug Discov. **9**, 237 (2010).

[62] D. Rosenbaum, P. C. Zamora, and C. F. Zukoski, Phys. Rev. Lett. **76**, 150 (1996).

[63] G. Foffi, G. D. McCullagh, A. Lawlor, E. Zaccarelli, K. A. Dawson, F. Sciortino, P. Tartaglia, D. Pini, and G. Stell, Phys. Rev. E **65**, 031407 (2002).

[64] M. Muschol and F. Rosenberger, J. Chem. Phys. **107**, 1953 (1997).

[65] H. Liu, S. K. Kumar, and F. Sciortino, J. Chem. Phys. **127**, 084902 (2007).

[66] J. P. K. Doye, A. A. Louis, I.-C. Lin, L. R. Allen, E. G. Noya, A. W. Wilber, H. C. Kok, and R. Lyus, Phys. Chem. Chem. Phys. **9**, 2197 (2007).

[67] R. A. Curtis, H. W. Blanch, and J. M. Prausnitz, J. Chem. Phys. B **105**, 2445 (2001).

[68] F. Zhang, M. W. A. Skoda, R. M. J. Jacobs, S. Zorn, R. A. Martin, C. M. Martin, G. F. Clark, S. Weggler, A. Hildebrandt, O. Kohlbacher, and F. Schreiber, Phys. Rev. Lett. **101**, 148101 (2008).

[69] D. Soraruf, F. Roosen-Runge, M. Grimaldo, F. Zanini, R. Schweins, T. Seydel, F. Zhang, R. Roth, M. Oettel, and F. Schreiber, Soft Matter **10**, 894 (2014).

[70] R. Roth, J. Phys.: Condens. Matter **22**, 063102 (2010).

[71] C. J. Segura, W. G. Chapman, and K. P. Shukla, Mol. Phys. **90**, 759 (1997).

[72] Y.-X. Yu and J. Wu, J. Chem. Phys. **116**, 7094 (2002).

[73] M. Wertheim, J. Stat. Phys. **35**, 19 (1984).

[74] M. Wertheim, J. Stat. Phys. **35**, 35 (1984).

[75] M. Wertheim, J. Stat. Phys. **42**, 459 (1986).

[76] M. Wertheim, J. Stat. Phys. **42**, 477 (1986).

[77] G. Jackson, W. Chapman, and K. Gubbins, Mol. Phys. **65**, 1 (1988).

[78] C. De Michele, S. Gabrielli, P. Tartaglia, and F. Sciortino, J. Phys. Chem. B **110**, 8064 (2006).

[79] S. Roldan-Vargas, L. Rovigatti, and F. Sciortino, Soft Matter **13**, 514 (2017).

[80] A. J. Archer and R. Evans, J. Chem. Phys. **121**, 4246 (2004).

[81] A. J. Archer, P. Hopkins, and M. Schmidt, Phys. Rev. E **75**, 040501 (2007).

[82] D. Stopper, R. Roth, and H. Hansen-Goos, J. Chem. Phys. **143**, 181105 (2015).

[83] D. Stopper, A. L. Thorneywork, R. P. A. Dullens, and R. Roth, J. Chem. Phys. **148**, 104501 (2018).

[84] A. Stradner, H. Sedgwick, F. Cardinaux, W. C. K. Poon, S. U. Egelhaaf, and P. Schurtenberger, Nature **432**, 492 (2004).

[85] A. J. Archer, D. Pini, R. Evans, and L. Reatto, J. Chem. Phys. **126**, 014104 (2007).

[86] J. A. Bollinger and T. M. Truskett, J. Chem. Phys. **145**, 064902 (2016).

[87] J.-M. Bomont, D. Costa, and J.-L. Bretonnet, Phys. Chem. Chem. Phys. **19**, 15247 (2017).

[88] A. Ciach, Phys. Rev. E **78**, 061505 (2008).

[89] M. Edelmann and R. Roth, Phys. Rev. E **93**, 062146 (2016).

[90] Y. Zhuang, K. Zhang, and P. Charbonneau, Phys. Rev. Lett. **116**, 098301 (2016).

[91] F. Zhang, R. Roth, M. Wolf, F. Roosen-Runge, M. W. A. Skoda, R. M. J. Jacobs, M. Stzucki, and F. Schreiber, Soft Matter **8**, 1313 (2012).

[92] J. K. Percus, Phys. Rev. Lett. **8**, 462 (1962).

[93] J. K. Percus, J. Stat. Phys. **15**, 505 (1976).

[94] T. K. Vanderlick, H. T. Davis, and J. K. Percus, J. Chem. Phys. **91**, 7136 (1989).

[95] M. P. Allen and D. J. Tildesley, *Computer Simulation of Liquids* (Oxford University Press, 2nd Edition, Oxford, 2017).

[96] N. Metropolis, A. W. Rosenbluth, M. N. Rosenbluth, A. H. Teller, and E. Teller, J. Chem. Phys. **21** (1953).

[97] J. K. Percus and G. J. Yevick, Phys. Rev. **110**, 1 (1958).

[98] M. S. Wertheim, Phys. Rev. Lett. **10**, 321 (1963).

[99] N. Carnahan and K. Starling, J. Chem. Phys. **51**, 635 (1969).

[100] T. V. Ramakrishnan and M. Yussouff, Phys. Rev. B **19**, 2775 (1979).

[101] P. Hopkins, A. Fortini, A. J. Archer, and M. Schmidt, J. Chem. Phys. **133**, 224505 (2010).

[102] P. Tarazona and R. Evans, Mol. Phys. **52**, 847 (1984).

[103] G. P. Brenan and R. Evans, Mol. Phys. **73**, 789 (1991).

[104] P. Tarazona, Phys. Rev. A **31**, 2672 (1985).

[105] S.-C. Kim, M. Calleja, and G. Rickayzen, J. Phys.: Condens. Matter **7**, 8053 (1995).

[106] J. L. Lebowitz, Phys. Rev. **133**, A895 (1964).

[107] Y. Rosenfeld, J. Chem. Phys. **98**, 8126 (1993).

[108] Y. Rosenfeld, M. Schmidt, H. Löwen, and P. Tarazona, J. Phys.: Condens. Matter **8**, L577 (1996).

[109] Y. Rosenfeld, M. Schmidt, H. Löwen, and P. Tarazona, Phys. Rev. E **55**, 4245 (1997).

[110] P. Tarazona, Phys. Rev. Lett. **84**, 694 (2000).

[111] G. Mansoori, N. Carnahan, K. Starling, and J. T.W. Leland, J. Chem. Phys. **54**, 1523 (1971).

[112] R. Roth, R. Evans, A. Lang, and G. Kahl, J. Phys.: Condens. Matter **14**, 12063 (2002).

[113] H. Hansen-Goos and R. Roth, J. Phys.: Condens. Matter **124**, 154506 (2006).

[114] H. Hansen-Goos and R. Roth, J. Phys.: Condens. Matter **18**, 8413 (2006).

[115] M. Oettel, S. Görig, A. Härtel, H. Löwen, M. Radu, and T. Schilling, Phys. Rev. E **82**, 051404 (2010).

[116] R. Roth, K. Mecke, and M. Oettel, J. Chem. Phys. **136**, 081101 (2012).

[117] S.-C. Lin and M. Oettel, Phys. Rev. E **98**, 012608 (2018).

[118] F. Gußmann and R. Roth, Phys. Rev. E **95**, 062407 (2017).

[119] P. Vargas, E. Munoz, and L. Rodriguez, Physica A **290**, 92 (2001).

[120] A. Archer and R. Evans, J. Chem. Phys. **118**, 9726 (2003).

[121] A. de Hek and A. Vrij, J. Colloid. Interface Science **88**, 258 (1982).

[122] M. Wolf, F. Roosen-Runge, F. Zhang, R. Roth, M. W. Skoda, R. M. Jacobs, M. Sztucki, and F. Schreiber, J. Mol. Liq **200**, 20 (2014).

[123] G. A. Vliegenthart and H. N. W. Lekkerkerker, J. Chem. Phys. **112**, 5364 (2000).

[124] M. G. Noro and D. Frenkel, J. Chem. Phys. **113**, 2941 (2000).

[125] D. J. Ashton, N. B. Wilding, R. Roth, and R. Evans, Phys. Rev. E **84**, 061136 (2011).

[126] M. E. Fisher and B. Widom, J. Chem. Phys. **50**, 3756 (1969).

[127] R. Evans and J. R. Henderson, J. Phys.: Condens. Matter **21**, 474220 (2009).

[128] R. Evans, J. R. Henderson, D. C. Hoyle, A. O. Parry, and Z. A. Sabeur, Mol. Phys. **80**, 755 (1993).

[129] R. Evans, R. J. F. Leote de Carvalho, J. R. Henderson, and D. C. Hoyle, J. Chem. Phys. **100**, 591 (1994).

[130] L. Xu, P. Kumar, S. V. Buldyrew, S.-H. Chen, P. H. Poole, F. Sciortino, and H. E. Stanley, Proc. Natl. Acad. Sci. **102**, 16558 (2005).

[131] V. V. Brazhkin, Y. D. Fomin, V. N. Ryzhov, and E. E. Tsiok, Phys. Rev. E **89**, 042135 (2014).

[132] J. R. Henderson and Z. A. Sabeur, Mol. Phys. **82**, 765 (1999).

[133] J. G. Kirkwood and E. Monroe, J. Chem. Phys. **9**, 514 (1941).

[134] A. J. Archer, B. Chacko, and R. Evans, J. Chem. Phys. **147**, 034501 (2017).

[135] M. Dijkstra and R. Evans, J. Chem. Phys. **112**, 1449 (2000).

[136] D. Stopper, H. Hansen-Goos, R. Roth, and R. Evans, J. Chem. Phys. **151**, 014501 (2019).

[137] M. Schmidt, H. Loewen, R. Evans, and J. Brader, Phys. Rev. Lett. **85**, 1934 (2000).

[138] G. Orkoulas and A. Z. Panagiotopoulos, J. Chem. Phys. **110**, 1581 (1999).

[139] R. Roth, J. Phys. Chem. B **122**, 3556 (2018).

[140] M. C. Walters, P. Subramanian, A. J. Archer, and R. Evans, Phys. Rev. E **98**, 012606 (2018).

[141] R. Evans and R. J. F. Carvalho, *Chemical Applications of Density Functional Theory, ACS Symposium* (edited by B.B. Laird, R.B. Ross, and T. Ziegler. ACS, Washington, DC, 1996) p. 166.

[142] L. Rovigatti, J. Russo, and F. Romano, Eur. Phys. J. E **41**, 59 (2018).

[143] E. Zaccarelli, F. Sciortino, and P. Tartaglia, J. Chem. Phys. **127**, 174501 (2007).

[144] J. Bleibel, M. Habiger, M. Lütje, F. Hirschmann, F. Roosen-Runge, T. Seydel, F. Zhang, F. Schreiber, and M. Oettel, Soft Matter **14**, 8006 (2018).

[145] B. D. Marshall, *Thermodynamic Perturbation Theory for Associating Fluids: Beyond First Order* (Rice University, PhD thesis, 2014).

[146] W. Zmpitas and J. Gross, Fluid Ph. Equilibria **428**, 121 (2016), theo W. de Loos Festschrift.

[147] H. C. Andersen, J. Chem. Phys. **61**, 4985 (1974).

[148] E. Bianchi, P. Tartaglia, E. Zaccarelli, and F. Sciortino, J. Chem. Phys. **128**, 144504 (2008).

[149] P. Flory, J. Am. Chem. Soc. **63**, 3083 (1941).

[150] F. Sciortino, E. Bianchi, J. F. Douglas, and P. Tartaglia, J. Chem. Phys. **126**, 194903 (2007).

[151] E. Bianchi, P. Tartaglia, E. La Nave, and F. Sciortino, J. Phys. Chem. B **111**, 11765 (2007).

[152] H. Hansen-Goos, *private communication* (2019).

[153] G. Foffi and F. Sciortino, J. Phys. Chem. B **111**, 9702 (2007).

[154] J. Russo, J. M. Tavares, P. I. C. Teixeira, M. M. Telo da Gama, and F. Sciortino, Phys. Rev. Lett. **106**, 085703 (2011).

[155] J. Russo, J. M. Tavares, P. I. C. Teixeira, M. M. Telo da Gama, and F. Sciortino, J. Chem. Phys. **135**, 034501 (2011).

[156] F. Sciortino and E. Zaccarelli, Curr. Opin. Solid State Mater. Sci. **15**, 246 (2011).

[157] P. Teixeira and J. Tavares, Curr. Op. in Coll. and Int. Sci. **30**, 16 (2017).

[158] C. J. Segura, E. V. Vakarin, W. G. Chapman, and M. F. Holovko, J. Chem. Phys. **108**, 4837 (1998).

[159] N. Gnan, D. de las Heras, J. M. Tavares, M. Telo da Gama, and F. Sciortino, J. Chem. Phys. **137**, 084704 (2012).

[160] A. Oleksy and P. I. C. Teixeira, Phys. Rev. E **91**, 012301 (2015).

[161] M. R. Fries, D. Stopper, M. K. Braun, A. Hinderhofer, F. Zhang, R. M. J. Jacobs, M. W. A. Skoda, H. Hansen-Goos, R. Roth, and F. Schreiber, Phys. Rev. Lett. **119**, 228001 (2017).

[162] A. Bymaster, A. Dominik, and W. G. Chapman, J. Phys. Chem. C **111**, 15823 (2007).

[163] J. Hughes, E. J. Krebs, and D. Roundy, J. Chem. Phys. **138**, 024509 (2013).

[164] L.-Y. Wang, F. Gu, H.-J. Wang, and Z.-L. Sun, J. Phys. Chem. B **121**, 2142 (2017).

[165] J. Horbach and W. Kob, Phys. Rev. B **60**, 3169 (1999).

[166] I. Saika-Voivod, F. Smallenburg, and F. Sciortino, J. Chem. Phys. **139**, 234901 (2013).

[167] E. Sanz and D. Marenduzzo, J. Chem. Phys. **132**, 194102 (2010).

[168] F. Romano, C. De Michele, D. Marenduzzo, and E. Sanz, J. Chem. Phys. **135**, 124106 (2011).

[169] U. Marconi and P. Tarazona, J. Chem. Phys. **110**, 8032 (1999).

[170] D. Stopper, R. Roth, and H. Hansen-Goos, J. Phys.: Condens. Matter **28**, 455101 (2016).

[171] L. van Hove, Phys. Rev. **95**, 249 (1954).

[172] Y. Gao and M. L. Kilfoil, Phys. Rev. Lett. **99**, 078301 (2007).

[173] A. L. Thorneywork, D. G. A. L. Aarts, J. Horbach, and R. P. A. Dullens, Soft Matter **12**, 4129 (2016).

[174] C. P. Royall, J. Dzubiella, M. Schmidt, and A. van Blaaderen, Phys. Rev. Lett. **98**, 188304 (2007).

[175] A. J. Archer, A. M. Rucklidge, and E. Knobloch, Phys. Rev. E **92**, 012324 (2015).

[176] H. M. Al-Saedi, A. J. Archer, and J. Ward, Phys. Rev. E **98**, 022407 (2018).

[177] D. Stopper, K. Marolt, R. Roth, and H. Hansen-Goos, Phys. Rev. E **92**, 022151 (2015).

[178] J. Reinhardt and J. M. Brader, Phys. Rev. E **85**, 011404 (2012).

[179] T. Schindler, R. Wittmann, and J. M. Brader, Phys. Rev. E **99**, 012605 (2019).

[180] A. J. Archer, J. Phys.: Condens. Matter **17**, 1405 (2005).

[181] J. A. Leegwater and G. Szamel, Phys. Rev. A **46**, 4999 (1992).

[182] A. J. Archer and N. B. Wilding, Phys. Rev. E **76**, 031501 (2007).

[183] Y. Zhuang and P. Charbonneau, J. Phys. Chem. B **120**, 7775 (2016).

[184] A. I. Campbell, V. J. Anderson, J. S. van Duijneveldt, and P. Bartlett, Phys. Rev. Lett. **94**, 208301 (2005).

[185] D. Pini and A. Parola, Soft Matter **13**, 9259 (2017).

[186] E. R. Dufresne, H. Noh, V. Saranathan, S. G. J. Mochrie, H. Cao, and R. O. Prum, Soft Matter **5**, 1792 (2009).

[187] V. Saranathan, C. O. Osuji, S. G. J. Mochrie, H. Noh, S. Narayanan, A. Sandy, E. R. Dufresne, and R. O. Prum, Proc. Natl. Acad. Sci. **107**, 11676 (2010).

[188] C. P. Royall, Soft Matter **14**, 4020 (2018).

[189] Y. Zhuang and P. Charbonneau, J. Chem. Phys. **147**, 091102 (2017).

[190] S. Foerster, A. K. Khandpur, J. Zhao, F. S. Bates, I. W. Hamley, A. J. Ryan, and W. Bras, Macromolecules **27**, 6922 (1994).

[191] M. W. Matsen and M. Schick, Phys. Rev. Lett. **72**, 2660 (1994).

[192] D. Stopper and R. Roth, Phys. Rev. E **97**, 062602 (2018).

[193] A. Ciach, J. Pekalski, and W. T. Gozdz, Soft Matter **9**, 6301 (2013).

[194] R. P. Sear and W. M. Gelbart, J. Chem. Phys. **110**, 4582 (1999).

[195] A. Imperio and L. Reatto, J. Phys.: Condens. Matter **16**, S3769 (2004).

[196] A. J. Archer, C. Ionescu, D. Pini, and L. Reatto, J. Phys.: Condens. Matter **20**, 415106 (2008).

[197] N. W. Ashcroft and J. Lekner, Phys. Rev. **145**, 83 (1966).

[198] Y. Liu, L. Porcar, J. Chen, W.-R. Chen, P. Falus, A. Faraone, E. Fratini, K. Hong, and P. Baglioni, J. Phys. Chem. B **115**, 7238 (2011).

[199] P. D. Godfrin, N. E. Valadez-Pérez, R. Castañeda-Priego, N. J. Wagner, and Y. Liu, Soft Matter **10**, 5061 (2014).

[200] J.-L. Bretonnet, J.-M. Bomont, and D. Costa, J. Chem. Phys. **149**, 234907 (2018).

[201] S. Das, J. Riest, R. G. Winkler, G. Gompper, J. K. G. Dhont, and G. Nägele, Soft Matter **14**, 92 (2018).

[202] A. Shukla, E. Mylonas, E. Di Cola, S. Finet, P. Timmins, T. Narayanan, and D. I. Svergun, Proc. Natl. Acad. Sci. **105**, 5075 (2008).

[203] H. G. von Schnering and R. Nesper, Zeitschrift für Physik B Condensed Matter **83**, 407 (1991).

[204] D. P. J. Gunton, A. Shiryayev, *Protein Condensation: Kinetic Pathways to Crystallization and Disease.* (Cambridge University Press, 2007).

[205] Y. Shin and C. P. Brangwynne, Science **357**, 1253 (2017).

[206] T. Tanaka, C. Ishimoto, and L. Chylack, Science **197**, 1010 (1977).

[207] J. A. Thomson, P. Schurtenberger, G. M. Thurston, and G. B. Benedek, Proc. Natl. Acad. Sci. USA **84**, 7079 (1987).

[208] P. Schurtenberger, R. A. Chamberlin, G. M. Thurston, J. A. Thomson, and G. B. Benedek, Phys. Rev. Lett. **63**, 2064 (1989).

[209] M. L. Broide, C. R. Berland, J. Pande, O. O. Ogun, and G. B. Benedek, Proc. Natl. Acad. Sci. **88**, 5660 (1991).

[210] C. R. Berland, G. M. Thurston, M. Kondo, M. L. Broide, J. Pande, O. Ogun, and G. B. Benedek, Proc. Natl. Acad. Sci. **89**, 1214 (1992).

[211] O. Galkin and P. G. Vekilov, Proc. Natl. Acad. Sci. **97**, 6277 (2000).

[212] P. R. ten Wolde and D. Frenkel, Science **277**, 1975 (1997).

[213] F. Zhang, F. Rosen-Runge, A. Sauter, M. Wolf, R. M. Jacobs, and F. Schreiber, Pure Appl. Chem. **86**, 191 (2014).

[214] N. Asherie, A. Lomakin, and G. B. Benedek, Phys. Rev. Lett. **77**, 4832 (1996).

[215] M. H. J. Hagen and D. Frenkel, J. Chem. Phys. **101**, 4093 (1994).

[216] H. Liu, S. K. Kumar, and F. Sciortino, J. Chem. Phys. **127**, 084902 (2007).

[217] S. Whitelam, Phys. Rev. Lett. **105**, 088102 (2010).

[218] D. Fusco and P. Charbonneau, Phys. Rev. E **88**, 012721 (2013).

[219] F. Zhang, G. Zocher, A. Sauter, T. Stehle, and F. Schreiber, J. Appl. Cryst **44**, 755 (2011).

[220] F. Zhang, F. Roosen-Runge, A. Sauter, R. Roth, M. W. A. Skoda, R. M. J. Jacobs, M. Sztucki, and F. Schreiber, Faraday Discuss. **159**, 313 (2012).

[221] F. Zhang, *private communication* (2019).

[222] A. Girelli, *Proteins interactions and cluster formation in presence of multivalent ions* (Master's thesis, University of Tübingen, 2018).

[223] F. Roosen-Runge, B. S. Heck, F. Zhang, O. Kohlbacher, and F. Schreiber, J. Phys. Chem. B **117**, 5777 (2013).

[224] M. Rabe, D. Verdes, and S. Seeger, Adv. Colloid Interface Sci. **162**, 87 (2011).

[225] D. G. Castner, Biointerphases **12**, 02C301 (2017).

[226] S. S. Lee, M. Schmidt, N. Laanait, N. C. Sturchio, and P. Fenter, J. Phys. Chem. C **117**, 23738 (2013).

[227] S. Dietrich, *Wetthing phenomena* (Academic Press, London, 1988) pp. 1–218.

[228] O. Matsarskaia, F. Roosen-Runge, G. Lotze, J. Möller, A.Mariani, F. Zhang, and F. Schreiber, Phys. Chem. Chem. Phys. **20**, 27214 (2018).

[229] F. Zhang, M. W. A. Skoda, R. M. J. Jacobs, R. A. Martin, C. M. Martin, and F. Schreiber, J. Chem. Phys. B **111**, 251 (2007).

[230] F. Hirschmann, *Brownian dynamics and Monte Carlo simulations of a patchy particle model system for protein solutions* (Master's thesis, University of Tübingen, 2019).

[231] M. Fries, *Tuning protein adsorption using multivalent ions* (Master's thesis, University of Tübingen, 2016).

[232] J. Nickolls and W. Dally, IEEE Micro **30**, 56 (2010).

[233] NVIDIA, *CUDA C PROGRAMMING GUIDE* (NVIDIA Corporation, 2016).

[234] NVIDIA, *CUDA C BEST PRACTICES GUIDE* (NVIDIA Corporation, 2016).

[235] Y. Rosenfeld, Phys. Rev. A **42**, 5978 (1990).

[236] Y. Rosenfeld, M. Schmidt, H. Löwen, and P. Tarazona, Phys. Rev. E **55**, 4245 (1997).

[237] NVIDIA, *cuFFT library user's guide* (NVIDIA Corporation, 2016).

[238] P. Bryk, R. Roth, K. Mecke, and S. Dietrich, Phys. Rev. E **68**, 031602 (2003).

Acknowledgements

First, I would like to express my sincere gratitude to my supervisor Prof. Roland Roth for his extraordinary support on this thesis project. His knowledge, enthusiasm and kindness were a continuous source of motivation and a great help in all the time of research and writing. I thank him furthermore for all additional financial support which made possible very pleasant stays at various conferences and in particular my unforgettable visit at the University of Bristol with Profs. Bob Evans and Nigel Wilding from April to July 2019. At this point I gratefully acknowledge financial support by the Carl-Zeiss-Stiftung during the three years of my doctorate.

I am also very grateful to my second supervisor Martin Oettel. Many helpful advises and discussions contributed in many ways to this thesis, as well as several chats with his enthusiastic students Frank Hirschmann, Malte Lütje and Shang-Chun Lin.

My special thanks go to my office mate Dr. Hendrik Hansen-Goos for continuous support, encouragement and fruitful discussions on research but also non-research topics such as the future of E-mobility.

I furthermore would like to thank Prof. Frank Schreiber and Madeleine Fries for our fruitful collaboration between theory and experiments which was driven by their enthusiasm and motivation. I also thank Frank Schreiber for inviting me as 'special guest' to the annual retreat of his group in Oberjoch. Special thanks also go to Olga Matsarskaia for proof-reading parts of this thesis and funny chats at work and during our occasional jogs in the woods of Tübingen.

Last but not least, many others contributed in diverse ways to making the time of my doctorate unforgettable: My parents, my brother, my partner Lucca, my friends Anja, Lukas, Elke, Markus, Nico, Hans-Martin and his wife Jacky.